

Development of an IH-DTL Injector for the Heidelberg Cancer Therapy Project

Dissertation
zur Erlangung des Doktorgrades
der Naturwissenschaften

vorgelegt beim Fachbereich Physik
der Johann Wolfgang Goethe-Universität
in Frankfurt am Main

von

Yuanrong Lu
Peking University, P. R. China

Frankfurt am Main
2005

Vom Fachbereich Physik der
Johann Wolfgang Goethe-Universität als Dissertation angenommen.

Dekan:	Prof. Dr. Wolf Aßmus
Erster Gutachter:	Prof. Dr. Ulrich Ratzinger
Zweiter Gutachter:	Prof. Dr. Alwin Schempp
Datum der Disputation:	22. Juli 2005

Zusammenfassung

Krebserkrankungen gehören mit zu den häufigsten Todesursachen. Die Krebstherapie mit Schwerionenstrahlen (Heidelberg Heavy Ion Cancer Therapy HICAT) hat das Potenzial, eine wichtige und wirkungsvolle Behandlungsmethode zu werden – sowohl wegen der günstigen Bragg-Peak-Charakteristik als auch wegen der Beobachtung des Bestrahlungsverlaufs mittels Positronenemissionstomografie (PET).

Das Heidelberger Projekt zur Tumorthherapie mit schweren Ionen umfasst zwei EZR (Elelektron-Zyklotron-Resonanz)-Quellen, einen Hochfrequenzlinearbeschleuniger, ein Synchrotron und drei Bestrahlungsplätze. Als maximal gelieferte Strahlteilchen pro Synchrotronzyklus sind $4 \cdot 10^{10}$ p, $1 \cdot 10^{10}$ He, $1 \cdot 10^9$ C bzw. $5 \cdot 10^8$ O-Ionen spezifiziert, bei Strahlenergien zwischen 50 und 430 AMeV.

Der Hochfrequenzlinearbeschleuniger mit einer Betriebsfrequenz von 217 MHz besteht aus einem 400 AkeV Hochfrequenzquadrupol sowie einem sehr kompakten 7 AMeV-Driftröhrenbeschleuniger vom Interdigitalen H-Typ (IH-Struktur).

Die Entwicklung der IH-Struktur innerhalb dieses HICAT-Projekts ist eine große Herausforderung im Vergleich zum bisherigen Stand der Technik auf diesem Gebiet:

- Es ist die bisher höchste Betriebsfrequenz realisiert.
- Das resultierende Längen- zu Durchmesser Verhältnis dieses Tanks von etwa 11 liegt deutlich über bisher realisierten Werten.
- Die Kavität trägt drei interne magnetische Quadrupoltriplettlinsen.
- Es handelt sich bei 5.5 MV/m mittlerer Beschleunigungsrate zwischen den Endflanschen um den höchsten jemals angesetzten Beschleunigungsgradienten aller Strukturen in diesem Energiebereich.
- Die Strahlanpassung zwischen RFQ und Driftröhrenstruktur (Drift Tube Linac DTL) besteht nur aus einem Quadrupoldublett mit xy-Steerern und kompakter Strahldiagnose. Mit 205 mm ist sie extrem kompakt und bedienungsfreundlich.

Entwicklung und Aufbau der IH-Struktur für HICAT führten bisher zu folgenden Ergebnissen:

- Die Anwendung der KONUS-Strahldynamik in den Teilchensimulationsrechnungen mit dem Code LORASR führte zu einer 'Ein Tank-Lösung', welche die Anforderungen des HICAT-Synchrotrons am Einschusspunkt erfüllt. Die Rechnungen wurden zunächst mit künstlich generierten, homogenen Teilchenverteilungen am IH-Eingang, später auch mit realistischen, aus RFQ-Simulationsrechnungen (A. Schempp) gewonnenen Verteilungen im 6-dimensionalen Phasenraum durchgeführt. Die longitudinale 95% Emittanz am IH-Ausgang bleibt demnach unter 2 AkeVns , die transversalen, normierten Emittanzen betragen 0.77 mm mrad in xx' bzw. 0.62 mm mrad in yy' , die Emittanzzuwächse vom RFQ-Elektrodenende bis zur Kohlenstoff-Stripperfolie im Transferkanal zum Synchrotron betragen dabei 24 %, 18 % und 5 % in den entsprechenden Ebenen.
- Von den transversalen Strahlenveloppen ausgehend wurde ein verbessertes Design der RFQ-internen Rebuncher-Driftröhren erarbeitet, das für dieses innovative Bauteil am RFQ-Ausgang bessere Feldqualität und bessere Laufzeitfaktoren anbietet. Eine optimale effektive Rebuncher-Spannung von 45 kV für minimales Emittanzwachstum entlang der IH-Struktur wurde mittels Simulationsrechnungen ermittelt. Es wurden dabei im wesentlichen nur Auswirkungen auf die longitudinale Emittanz beobachtet.
- Es wurden 6 verschiedene Konzepte zur Abstimmung der Spannungsverteilung über den 56 Beschleunigungsspalten parallel genutzt, um das HF-Modell im Maßstab 1:2 erfolgreich einzustellen.
 - 'Volumenabstimmung': Dabei wird der Tankquerschnitt und damit die lokale Induktivität pro Länge so eingestellt, dass der lokale kapazitive Belag sich zur Resonanzfrequenz ergänzt. Dieses Endabstimmungskonzept ist vor allem bei großer β -Variation nützlich und wurde für HICAT erstmals eingesetzt.
 - 'Zusatzkapazitäten an der Driftröhrenstruktur': Diese Methode ist zum Vorabstimmen nützlich. Für den endgültigen Einsatz wurde eine Version entwickelt, bei der massive Kupferkörper gegenüber von Driftröhren in die Nutschienen der Driftröhrenstrukturträger (Rippen) eingeschraubt werden.
 - 'Linsenkopplung' bezeichnet die Kapazität zwischen den Rippen des Tankmittelrahmens und den Quadrupollinsengehäusen. Der über den betreffenden geometrischen Abstand festzulegende Kapazitätsbelag bestimmt die Kopplung der benachbarten Driftröhrensektionen.

- 'Driftröhrenabstimmung' ist das bewährte Feinabstimmungskonzept für IH-Strukturen. Durch individuelle Wahl des Spalt-zu-Periodenlängen-Verhältnisses für jeden Spalt kann bei gegebenem β -Profil der Kapazitätsbelag entlang der Kavität lokal optimiert werden.
- 'Rippeninduktoren' (Undercuts) ermöglichen die Realisierung des 'O-Mode' für H-Strukturen durch resonante Endzelligeometrie. Dabei werden die Rippen des Mittelrahmens an den Enden hinterfräst. Diese Flächen werden vom HF-Magnetfeld durchflutet und so wird Induktionsspannung in die Rippenenden 'gepumpt'.
- Bewegliche Tauchkolben an bestimmten Orten entlang der Kavität erlauben die endgültige Einstellung der Spannungsverteilung sowie die Resonanzfrequenzregelung im Betrieb (Standardkonzept für alle vielzelligen Strukturen). Bei den Abstimmarbeiten am Modell wurde insbesondere ein starker Einfluss der Linsenfußgeometrie festgestellt. Am Modell konnten schließlich die maximalen Spaltspannungsabweichungen zu den Sollwerten auf unter 5 % gedrückt werden.
- Zur technisch bequemen Umsetzung wurde ein näherungsweise rechteckiger Tankquerschnitt konzipiert. Die bewährte Aufteilung in obere und untere 'Tankhalbschale' sowie den Mittelrahmen wurde beibehalten. Jedoch sind die 'Halbschalen' jetzt in 60 mm hohe, ausgefräste Platten verwandelt worden. Die Ausfräsungstiefe kann entlang der Kavität variiert werden, an der planen Innenkontur können Verdrängungskörper bei guter HF-Kontaktierung und Kühlung eingebracht werden. Auf der unteren Deckelplatte können die Linsen präzise und stabil befestigt werden. Dies ist eine erhebliche Vereinfachung gegenüber bisherigen Konzepten. Nach diesen Vorarbeiten konnte die Bestellung der IH-Leistungskavität erfolgen.
- Simulationsrechnungen zu den elektromagnetischen HF-Feldern wurden mit dem kommerziell erhältlichen Code Microwave Studio durchgeführt. Einerseits konnten die Modellmessungen bestätigt werden. Auch die Parameterabhängigkeiten der longitudinalen Oberschwingungen H_{11n} , insbesondere ihre Resonanzfrequenzen, konnten untersucht werden. Andererseits war bei einer Gitterzahl von 2.3 Millionen die Leistungsgrenze des verfügbaren 2.4 GHz DELL PC mit Pentium4-Prozessor und 2.096 GRAM Speicherplatz erreicht. Jede Rechnung dauerte etwa 15 Stunden,

Geometrieänderungen konnten nicht immer mit der erforderlichen Genauigkeit untersucht werden.

Der simulierte Shuntimpedanzwert liegt um 15 % über dem aus laufenden IH-Strukturen extrapolierten Wert (195,8 M Ω /m absolut) und bestätigt damit die bisherigen Erfahrungen.

Damit erwartet man eine HF-Leistung von 755 kW für C⁴⁺-Betrieb. Die unbelastete Güte liegt dann bei 15600.

- Während der Fertigung der Leistungskavität wurden viermal Messungen zur Frequenz und zur Spannungsverteilung beim Hersteller durchgeführt.

Danach konnte die Anlieferung zur GSI-Verkupferungsanlage freigegeben werden.

Es wird erwartet, dass die verbliebenen Abweichungen zu den Sollwerten schließlich nach dem Verkupfern des Tanks mittels der Methode 'Zusatzkapazitäten an der Driftröhrenstruktur' und einer 'Volumenabstimmung' in Driftröhrensektion 2 bei korrekter Resonanzfrequenz beseitigt werden können.

To my parents, my family,
and the people
who love the life and are fighting against cancers.

Contents

Chapter One Introduction	1
1.1 Cancer and Radiation Therapy	1
1.2 The Development of Medical Accelerators	1
1.3 Worldwide Therapy Facilities	4
1.4 Multiple Beam Facility at Heidelberg	9
 Chapter Two RF Capabilities of the IH-DTL	 14
2.1 H-Mode and RF Structure of the IH-DTL	14
2.2 Particle Acceleration within One Gap	18
2.3 Longitudinal Single Particle Motion	21
2.4 Transverse Motion	23
 Chapter Three KONUS Beam Dynamics and LORASR Code	 26
3.1 Concept of KONUS Beam Dynamics	27
3.2 LORASR—KONUS Beam Dynamics Simulation Code	29
3.3 KONUS Beam Dynamics Example	33
 Chapter Four Beam Dynamics of the HICAT IH-DTL	 36
4.1 The Challenge of the HICAT IH-DTL Design	36
4.2 The LORASR Beam Dynamics Simulations	38
4.2.1 The Determination of Effective Gap Voltage Distributions	38
4.2.2 The Input Particles Distribution of the IH-DTL	41
4.2.3 The IH-DTL Simulation Results of LORASR	43
4.3 Motivation for a Redesign of the Buncher Drift Tubes	48
 Chapter Five The RF tuning of the IH-DTL 1:2 model cavity	 51
5.1 Measuring System for the IH-DTL Model Cavity	51
5.1.1 The Theory of Bead Pull Measurement	52
5.1.2 Back Ground Subtraction and Performed Calculations	53
5.1.3 Electric Field Distribution and Gap Voltage Distribution	53
5.2 Tuning Experience on the Model Cavity	54
5.2.1 Volume Tuning	55
5.2.2 Additional Capacitance Plate Tuning	58
5.2.3 Tube Tuning	59
5.2.4 Lens Coupling Tuning	63
5.2.5 The Undercut Tuning	65
5.2.6 The Plunger Tuning	67

5.3 The Effects of Lens Supporting Stems	71
5.3.1 The Initial Tuning Result of IH Model Cavity in 2002	71
5.3.2 The Field Distribution Influence of Triplet Supporting Stems	73
5.4 The Final End Flanges and Tuning Results	77
5.5 The Field Distribution of Higher Order Modes	79
5.6 Comparison of the Different Tuning Techniques	81
 Chapter Six The Final Proposal of IH Medical Power Cavity	 82
6.1 Geometry of the IH Medical Power Cavity	82
6.2 Calculations of IH cavity parameters	86
6.3 RF Feeder Design	87
 Chapter Seven Microwave Studio Simulation of IH Cavity	 90
7.1 Introduction of the Simulation Software	90
7.2 Simplification of the IH cavity for the Microwave Studio Simulation	90
7.3 The Field Distribution for the 1:2 Scaled IH Model and Power Cavity	94
7.4 Shunt Impedance and RF Power Dissipation for IH Real Power Cavity Simulated by MWS	100
7.5 The Simulations of Higher Order Modes	101
 Chapter Eight The RF measurements of the IH-DTL Power Cavity	 104
8.1 Assembling of IH Power Cavity at PINK Company	104
8.2 The Initial RF Measurements of the IH Power Cavity	106
8.3 The Second RF Investigation	108
8.4 The Third RF Investigation	113
8.5 The Fourth RF Investigation	117
 Summary	 120
References	123
Lists of the Figures	127
Acknowledgments	132
Curriculum vitae of the author	133
Publications of the author	135

Chapter One

Introduction

1.1. Cancer and Radiation Therapy

Cancer is becoming one of the most dangerous diseases all over the world. In 1982 there were 1.2million new indications in the countries of the European Community. 750 000 deaths were attributed to cancer in 1985. An increasing trend of fatal cancer cases is still observed^[1.1]. In developed countries about 30% of the patients suffer from cancer and half of these die from cancer^{[1.2] [1.3]}. ACS (American Cancer Society) in 2003 provided a statistics, which showed over 17millions new cancer cases have been diagnosed in USA since 1990, estimated about 1,334,000 new cancer cases would be diagnosed in USA in 2003 and about 556,500 patients would be dead of cancer, that was more than 1,500 death per day. In the same report, they said “Cancer is the second leading cause of death in the US, exceeded only by heart disease. In the US, 1 of 4 deaths is from cancer”.

Up to now, there are various cancer treatments: surgical removals of the tumor tissue, radiotherapy, chemotherapy and immunotherapy, the first two are becoming crucial importance at present. Surgery and radiotherapy alone are successful in 22% and 12% of cases, respectively. When combined they account for another 6% of the cases, so that radiotherapy is involved in almost half of the curative treatments of loco-regional type. For 18% of all cancer patients the local control of the primary tumor without metastasizing fails. These patients could be cured successfully if improved local or loco-regional treatment techniques were available. Among these improved treatment modalities is the application of proton and ion beams in radiation therapy. There is ample space for improvements here, because 37% of the tumors are metastasized at the moment of the diagnosis and couldn't be cured with loco-regional treatments alone. Thus, there is a strong clinical demand for ion beam therapy facilities in the entire world.

1.2. The Development of Medical Accelerators

It is a strong actual clinical demand that boosts the development of particle accelerators. However, the development of medical accelerators should be dated back to the history of particle accelerators. Since Roentgen (1901 Nobel Prize) discovered tube rays in 1895^[1.4], which are called after him and which he

nicknamed “x-rays” because he didn’t know what the rays are, J.J. Thomson measured the ratio of charge to mass of x-rays in 1897^[1.5] and concluded x-rays are free electrons, scientists realized its applications in clinical diagnostics and in therapeutic purposes gradually. In 1905 A. Einstein published the theory of special relativity. It was also at that time; almost every scientist was very interested in the nuclear structure. They were eager to use accelerated electrons to excite atoms, James Franck and Gustav Hertz did the first experiment in 1913 (1925 Nobel prize). One year later Marsden produced first proton beam irradiating paraffin with alpha particles. At the same year Greinacher built the first cascade generator (actually it is a voltage multiplier). An increasing trend of producing different kinds of particles with higher energy to replace the natural radioactive isotopes pushed scientists to develop various particle accelerators.

The earliest accelerators were vacuum x-ray tubes; it was operated at a peak voltage around 150kV with a 5mA electron current. At that time it was not so easy to get higher voltage, which was the main reason why scientists wanted to use alternating RF field to accelerate particles. In 1924, Gustav Ising from Stockholm proposed the first accelerator that used time-dependent fields, consisting of a straight vacuum tube and a sequence of metallic drift tubes with holes for the beam^[1.6]. The particles were to be accelerated from the pulsed voltages that were generated by a spark discharge and applied across the adjacent drift tubes. Synchronism of the applied pulses with the beam particles was to be attained by introducing transmission lines, chosen to delay the pulse from the voltage source to the drift tubes. This concept proposed by G.Ising was not tested at that time, but it influenced another young Norwegian student, Rolf Wideroe.

It was Rolf Wideroe who conceived and demonstrated the first RF linear accelerator experimentally in 1927 at Achen, Germany^[1.7]. The result was reported in a paper that is one of the most important in the history of particle accelerators and which inspired E.O. Lawrence to the invention of the cyclotron^[1.8].

The classical cyclotron has constant magnetic field magnitude and also constant RF frequency. Beam energy is limited by relativistic effects, which destroy synchronization between particle orbits and RF fields. Therefore, the cyclotron is useful only for ion acceleration. Cyclotrons are characterized by large-area magnetic fields to confine ions from zero energy to the output energy. After that, the Azimuthally-Varying-Field (AVF) cyclotron was a major improvement over the uniform-field cyclotron. The separated-sector cyclotron is

a special case of the AVF cyclotron. The azimuthally field variation results from splitting the bending magnet into a number of sectors. The advantages of the separated sector cyclotron are (1) modular magnet construction and (2) the ability to locate RF feeds and acceleration gaps between the sectors. The design of separated-sector cyclotrons is complicated by the fact that particles cannot be accelerated from low energy. This feature can be used to advantage; beams with lower emittance (better coherence) are achieved if an independent accelerator is used for low-energy acceleration.

The synchrocyclotron is a precursor of the synchrotron. It represents an early effort to extend the kinetic energy limits of cyclotrons. Synchrocyclotrons have a constant magnetic field with geometry similar to the uniform-field cyclotron. The main difference is that the rf frequency is varied to keep the synchronization of accelerated particle into the relativistic energy region. Synchrocyclotrons are cyclic machines with a greatly reduced time-averaged output flux compared to a cyclotron. Kinetic energies for protons to 1 GeV have been achieved. In the sub-GeV energy range, synchrocyclotrons were supplanted by AVF cyclotrons, which generate a continuous beam. Synchrocyclotrons have not been extended to higher energy because of technological and economic difficulties in fabricating the huge, monolithic magnets that characterize the machine. However, the investigations of phase equation in the synchrocyclotron lead to the concept of phase stability^{[1.9] [1.10]}.

Synchrotrons are the present standard accelerators for particle physics research. They are also cyclic machines. Both the magnitude of the magnetic field and the rf frequency are varied to maintain a synchronous particle at a constant orbit radius. The feature of constant-radius is very important; bending and focusing fields need only a small ring-shaped volume. This minimizes the cost of the magnets, allowing construction of large-diameter machines for ion energies up to several tens of TeV. Synchrotrons are used to accelerate both ions and electrons, although electron machines are limited in energy by emission of synchrotron radiation. The main limits on achievable energy for ions are the cost of the machine and availability of real estate. Cycling times are long in the largest machines, typically many seconds. Electron synchrotrons and proton boosters cycle at frequencies in the range of 15 to 60 Hz. Early synchrotrons used weak focusing. The bending magnets were shaped to produce a field with an index n in the range of $0 < n < 1$ (called CGS: Constant Gradient Synchrotron). All modern synchrotrons use transverse focusing systems composed of strong lenses in a focusing-defocusing array. The magnets have alternate positive and negative field gradient with $n \gg 1$ (AGS:

Alternating Gradient Synchrotron). The combination of focusing and defocusing in the horizontal and vertical directions leads to net beam confinement. It is similar with the optical effects of the better fitted focusing and defocusing optical lenses. Strong focusing minimizes the beam cross-section and reduces the magnet size.

The first hospital-based accelerator was a 1MeV air-insulated Van de Graff machine that was installed in Harvard Medical School in Boston and used to produce x-rays for treating cancerous tumors in 1937. The second machine, a pressure-insulated 1.25MeV machine, was installed in 1940 at the Massachusetts General Hospital (MGH) also in Boston. At the very beginning, particle accelerators were not widely used in medical science because of their high irradiation costs and enormous maintenance. Dramatic increase was made possible by the development of Betatron, by D.W. Kerst, who suggested using it as a radiation tool in 1943. Up to 1977, 45 Betatrons were in operation in the USA. The Siemens company produced more than 70 Betatrons in the same period and in the early 1970's about 200 Betatrons were in medical use all over the world.

Betatrons have played a significant role in the development of radiation therapy since they deliver x-rays with far better properties. However, the Betatrons' major disadvantages, such as its weight, the relatively low intensity of the x-ray beam, as well as the small treatment field area have caused the production end in the mid-1970's.

Development of military microwave generators during the Second World War made it possible to accelerate electrons for medical applications by using traveling wave structures. In 1946, the first traveling wave linear accelerator was demonstrated by D.W. Fry in England. Up to now there are about 7000 electron linacs used in various hospitals all over the world. Because of the advanced technology, its small dimensions and low treatments prices, there are still a lot of companies active in this field. Meanwhile, RF and microwave technology pushed also enormously the development of proton and ion beam linear accelerators. The circular high energy cyclotrons, synchrocyclotrons and synchrotrons were developed very fast and gradually and widely used in the medical science. This will be discussed in the next subdivision.

1.3. Worldwide Therapy Facilities

The "Father of Proton Therapy" was Robert Wilson, who published "Radiological Use of Fast Protons" in 1946^[1.11], the article established the fundamental principles and techniques that are being followed today at Loma

Linda's Proton Treatment Center and at other proton therapy facilities around the world.

The main goal of radiation therapy is to match an effective dose to a given tumor volume, while the surrounding healthy tissue as well as the skin and entrance and exit channels are irradiated as weak as possible. The dose is determined by the energy deposition of injected particles. The energetic heavy ions and protons are slowed down mainly by numerous ionizing collisions with the atomic electrons of the irradiated medium. The Linear Energy Transfer (LET) quantitatively characterizes the energy deposition. The dependence of the relative dose on the injection depth is called Bragg peak, the position of the Bragg peak can be adjusted by the energy of the injected particles. The comparison of Bragg peaks for different radiation sources is shown in figure 1.1. Actually, tumor tissue has an arbitrary volume, but the different injected beam energies and beam currents allow to form a homogenous dose distribution within the tumor volume. Carbon was chosen by GSI (Gesellschaft fuer SchwerIonenforschung, Germany) following a study of the biological efficiency of all ions from protons to uranium and being encouraged by the results gained at the Berkeley Bevatron before. The radiation damage it causes is repairable to a large extent in the entrance channel of the beam, and becomes irreparable only at the end of the beam's range within the tumor itself.

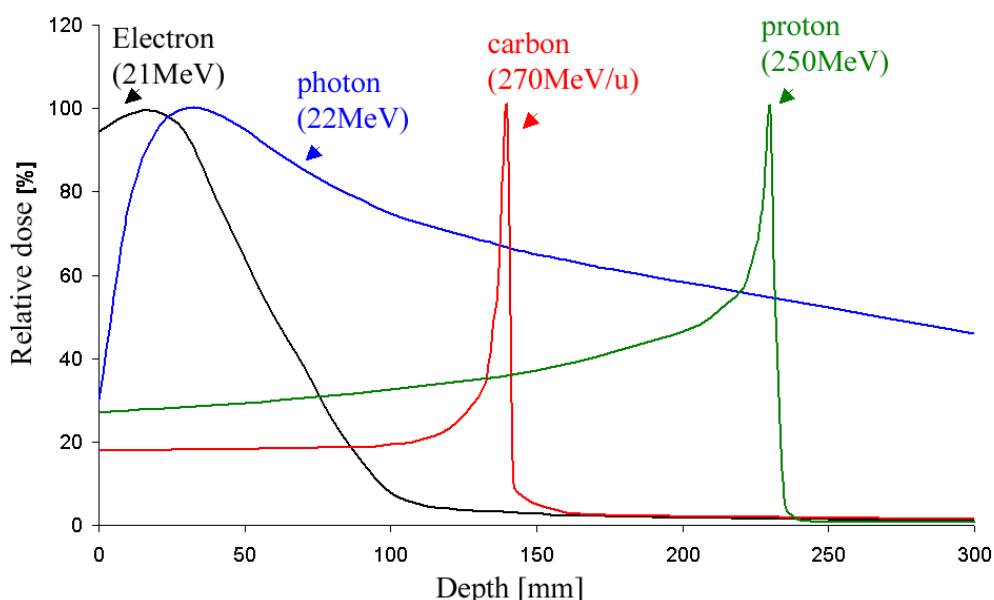


Fig.1.1 The Bragg peak for different radiation sources (after^[1,3])

The crucial difference arises from the damage caused on the cell DNA. Cancer cells and healthy cells alike die when their DNA sustains irreparable

damage. In general, this means both DNA strands being broken since the cell can frequently repair single strand breaks. The studies of GSI showed that lighter particles such as protons, whilst depositing their energy in the Bragg peak, cause far fewer double-strand breaks than heavier ones like carbon. Moreover, the boundary between single and double-strand damage is particularly sharp with carbon which, coupled with GSI beam delivery system, allows extremely precise targeting of the tumor a factor which has been incorporated into GSI treatment planning system.

Another advantage is that carbon ions do not scatter as much as lighter particles. This allows higher degrees of conformity to be achieved. Heavier ions, such as neon, were rejected because they tend to fragment. Carbon shows fragment action to some extent, but the fragmentation products include positron-emitting carbon 10 and 11. Positron Emission Tomography, PET, then allows the radiotherapist to observe "live" the position of the beam in the patient with a resolution of 2.5 millimeters. The GSI facility is the first to use PET to give on-line control of a carbon beam during irradiation. This is essential for irradiation of tumors close to critical structures like the brain stem or spinal chord. The Rossendorf Research Center in Dresden provided GSI's PET cameras.

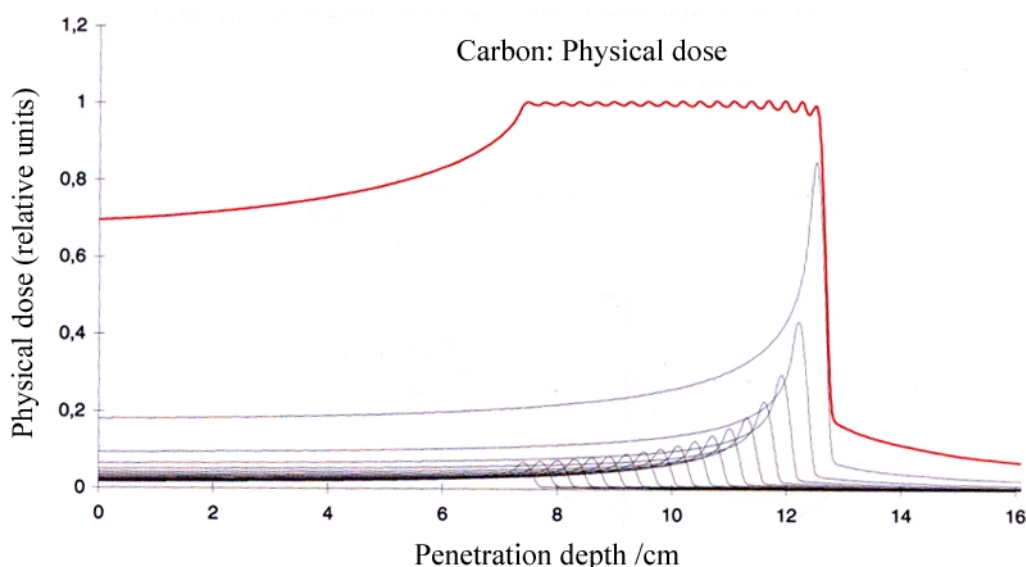


Fig.1.2 Covering a target volume by stacking several individual Bragg peaks of different carbon beam energy and intensity^[1.3]

Carbon ions open up the possibility of treating a range of hitherto difficult tumors, and complement established proton therapy techniques. Protons, however, will remain important at many treatment centers for many kinds of

cancer as well as for treatment of benign tumors. Figure 1.2 shows an example of a physical dose distribution composed by existing carbon beam energies and intensities.

Table 1. 1 Existing proton therapy facilities worldwide*

Who	Accelerator	Energy /AMeV	Treated Patients*	Date of the first/Last treatment	Beam delivery system
First generation of research proton and/or ion therapy facilities					
Donner Lab., Berkeley, USA	Synchrocyclotron	340	2517	1954-1993	horizontal
Werner Inst. Uppsala, Sweden	Cyclotron	185	220	1957-76	horizontal
Harvard Cycl. Lab., USA	Cyclotron	160	9116	1961-2002	horizontal
JINR, Dubna, Russia	Synchrocyclotron	90-200	124	1964-1974	Horizontal
ITEP, Moscow, Russia	Synchrotron	70-200	3539	1969	horizontal
LJIF, St. Petersburg, Russia	Synchrocyclotron	70-1000	1029	1975	horizontal
NIRS, Chiba, Japan	cyclotron	70	145	1979	horizontal
PMRC, Tskuba, Japan	Synchrotron	250	576	1983	Vertical, horizontal
PSI, Villigen, Switzerland	Isochronous cyclotron	70-590	3712	1984-2002	1 horizontal, 1 gantry
JINR, Dubna, Russia	Synchrocyclotron		154	1987	horizontal
TSL, Uppsala, Sweden	Cyclotron	200	311	1989	horizontal
NIRS, Chiba, Japan (HIMAC)	Synchrotron	400(C)	389	1994	1 horizontal, 1 vertical
TRUMPF, Canada	Cyclotron	180-520	77	1995	horizontal
Second generation of proton and/or ion research therapy facilities					
Clatterbridge, UK	Isochronous cyclotron	62	1201	1989	horizontal
UCL, Louvain-la-Neuve, Belgium	Cyclotron	90	21	1991-1993	horizontal
CAL, Nicea, France	Cyclotron	65	1951	1991	horizontal
CPO Orsay, France	Synchrocyclotron	70-200	2157	1991	horizontal
NAC, South Africa	Cyclotron	200	263	1991	horizontal
MPRI, IN, USA	Cyclotron	200	34	1993	horizontal
UCF-CNL, USA	Cyclotron	200	448	1994	horizontal
PSI, Villigen, Switzerland	Cyclotron	200	99 ^[1.12]	1996	1 eccentric gantry, spot scanning
GSI, Darmstadt, Germany ^[1.13]	Synchrotron	C: 80-430	200 ^[1.14]	1997	horizontal, raster scanning
HMI, ISL, Berlin, Germany	Cyclotron	70	300 ^[1.15]	1998	horizontal
Dedicated proton and/or ion therapy centers					
LLUMC, Loma Linda, USA	synchrotron	70-250	8000	1990	1 horizontal, 3 gantries
NCC, Kashiwa, Japan	Cyclotron	235	77	1998	1 horizontal, 2 gantries
HHTC, Hyogo, Japan ^[1.16]	synchrotron	p: 230 C: 320	6	2001	1 horizontal, 2 gantries 1 horizontal, 1 45deg.
PRMC, Tsukuba, Japan ^[1.17]	synchrotron	250	700	2001	1 horizontal, 2 gantries
WERC, Wakasa-Wan, Japan ^[1.17]	synchrotron	200		2002	1 horizontal, 1 Vertical
SCC, Shizuoka, Japan ^[1.17]	synchrotron	230		2002	1 horizontal, 2 gantries
Total				About 36767 treated patients	

*Treated patients by the beginning of 2003 (after ^[1.3] ^[1.19] ^[1.20])

Table 1. 2 The planed or proposed hadrontherapy facilities.

Who	Country	Planed first treatment	Comments
HICAT Heidelberg	Germany	2007	Protons, ions, synchrotron, 2 gantries, raster scanning
Shandong	China	2007 ^[1.21]	IBA 230MeV proton Cyclotron
PSI, Villigen	Switzerland	2007	Super-conducting Cyclotron, made by ACCEL company
Muenchen Privat Hospital	Germany	2007	Super-conducting Cyclotron, made by ACCEL company
Beijing	China	2007	70-230MeV proton synchrotron
CNAO, Milan and Pavia	Italy	2007	Protons, ions, synchrotron, 2 gantries, 1 fixed beam room, 1 experimental room
AUSTRON	Austria		2 proton gantries, 1 ion gantry, 1 fixed proton, 1 fixed ion, 1 experimental room
IMP, Lanzhou	China	2009	900MeV/u at CSR, protons, ions, clinical treatment, biological research, no gantry, shifted patients
Central Italy	Italy		Cyclotron, 1 gantry, 1 fixed beam room
Clatterbridge	UK		Upgrade using booster linear accelerator to 200MeV
TOP project	Italy		70MeV proton linac, expand to 200MeV
Moscow	Russia		320MeV compact proton accelerator
RMTC	USA		Combined medical radioisotope production complex and proton therapy facility using SSC linac
PTCA, Tenet Health System	USA		Several system throughout USA
NAI, IL	USA		300MeV protons, therapy and lithography

Proton and ion beam therapy centers are mainly located in the USA, Russia, South Africa, Japan and Europe. Almost all the centers utilize clinical beams with the energy varying from 60AMeV to 250AMeV and corresponding depths

of penetration in tissue ranging from 3.1cm to 38cm, suited for the treatment of both eye and deep-seated tumors. The three types of the accelerators designed specifically to operate in the hospitals, are the cyclotron, the synchrotron and the linear accelerator. Table 1.1 lists existing proton and ion beam therapy facilities. Table 1.2 shows the proposed or planned hadrontherapy projects.

1.4. Multiple Beam Facility at Heidelberg

An accelerator facility for radiotherapy of cancer tumor with protons and heavy ion beams was proposed for the Radiologische Universitätsklinik in Heidelberg in 1998^[1,3], it was anticipated that full operation could be started in the year 2007. Fig.1.3 shows the layout of the Heidelberg therapy project. The accelerator consists of ion sources, LEBT (Low Energy Beam Transport line), RFQ (Radio Frequency Quadruple), an IH-DTL (Interdigital H-type Drift Tube Linac) and the synchrotron.

Table 1.3 Specifications of the Heidelberg Therapy Facility (after^[1,3])

Ion Source	
Ion Source	ECR
Number	2
Frequency	14.5GHz
Extraction Energy	8AkeV
Intensity (DC, eμA)	>120(¹² C ⁴⁺), 600(He ²⁺), 1200(p)
Emittance (normalized)	<0.4 mm mrad
LEBT	
Bending Magnet	90°, 26.5° Edge focusing
m/q resolution	≈300
Intensity variation	RF Chopper
RFQ (<u>R</u>adio <u>F</u>requency <u>Q</u>uadruple)	
Type of RFQ	4-Rod
Input energy	8AkeV
Output energy	400AkeV
Frequency	216.816MHz
Electrode length	1.28m
Acceptance	1.0 mm mrad
Cavity length	1.40m
Cavity diameter	250mm

Beam matching	
Longitudinal	2 gap rebuncher (within RFQ cavity)
Transverse	Quadruple Doublet
IH-DTL	
Gap Number	56
Input energy	400Akev
Output energy	7AMeV
Frequency	216.816MHz
Transverse acceptance	1.0 mm mrad (norm.)
Long. acceptance	2.0 AkeV ns
Cavity length	3.76m
Transverse cavity dimensions	260mm*344mm
Stripper and beam parameters before injection	
Stripper foil thickness	50 $\mu\text{g}/\text{cm}^2$
Beam diameter	2.0mm
Ion species for synchrotron	P, He ²⁺ , C ⁶⁺ , O ⁸⁺
Beam pulse duration	$\leq 200\mu\text{s}$, $\leq 5\text{Hz}$
Beam emittance (normalized)	≤ 0.8 mm mrad
Energy spread	$\pm 0.15\%$
Synchrotron	
Injection turns	15
Injection energy	7AMeV
Hor. acceptance	100 mm mrad (absolute)
Vert. acceptance	25 mm mrad (absolute)
Magnetic rigidity	0.38—0.76Tm
Ring diameter	$\approx 20\text{m}$
Tuning factor: Horizontal Q_h	1.674
Vertical Q_v	1.221
Bending magnets: Number	6
Bending angle	60°
Radius	4.4m
B_{max}	1.50T
Aperture	$A_h=180\text{mm}$, $A_v=70\text{mm}$
Quadruple magnets: Number	12
Effective length	0.5m
Maximum gradients	5.5T/m
Sextuple magnets: Number	4

Effective length	0.2m
Maximum gradients	7.0T/m
Extracted beam parameters from synchrotron	
Beam energy	50—430AMeV
Beam intensity (particles per synchrotron cycle)	Protons: $4 \cdot 10^{10}$
	He: $1 \cdot 10^{10}$
	C: $1 \cdot 10^9$
	O: $5 \cdot 10^8$
Magnetic rigidity	1.03—6.60Tm
Exit emittance, hor. and vert.	5 mm mrad (absolute)
Energy spread	$\pm 0.1\%$

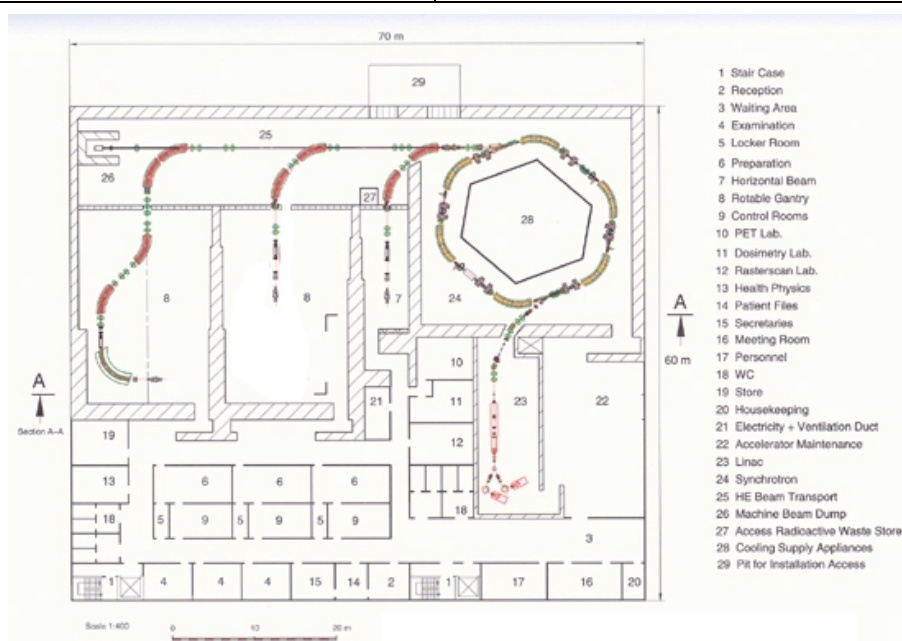


Fig.1.3 The layout of the Heidelberg Therapy Facility

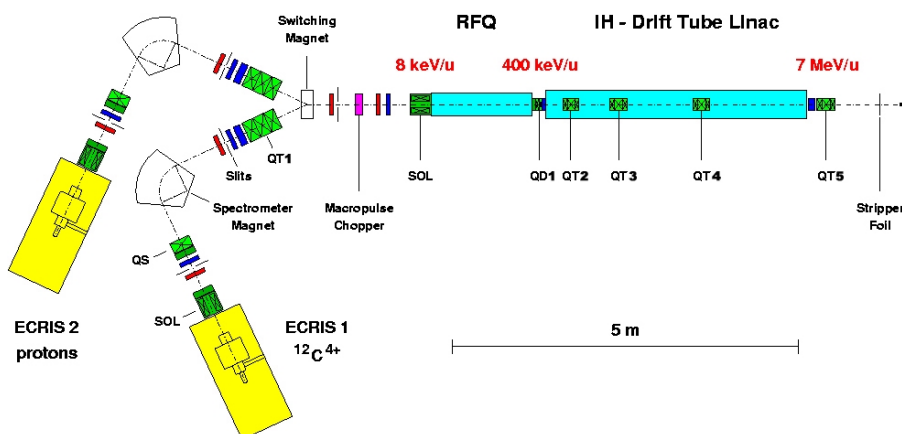


Fig.1.4 The HICAT injector ^{[1.3][1.27]}

The HICAT (Heidelberg Heavy Ion Cancer Therapy) injector chain is shown in Fig.1.4. ECR (Electron Cyclotron Resonance) ion sources have been chosen because of their excellent performance stability and long lifetime^[1.22]. Two identical ECR ion sources will deliver proton and $^{12}\text{C}^{4+}$ beams at an energy of 8AkeV. The switching time between two different ion species can be realized in between two synchrotron pulses. Great experience with ECR ion sources exists for a large spectrum of ion species and in particular for the production of carbon ions like for the GSI heavy ion therapy pilot project^[1.13]^[1.23]. A four-rod RFQ will accelerate protons or ions to 400AkeV. The length of RFQ electrodes is 1.28m; the electrodes are supported by 16 stems mounted in a distance of 85mm on the ground plate. The operating frequency is 216.816MHz. The designed inter-vane voltage is 70kV, the tank inner diameter is 250mm, and the calculated transmission efficiency is 99%. A compact RFQ internal buncher has been designed and installed at the exit of the RFQ cavity^[1.24-26].

The IH-DTL will accelerate the ions from 400AkeV to 7AMeV. Only one quadruple doublet (QD) is needed to realize the beam matching between RFQ and IH-DTL^[1.27-28]. The beam dynamics simulation software LORASR was developed and has been verified in earlier projects like the GSI high current project or the CERN 101/202MHz linac 3. Three quadruple triplets are placed in the IH cavity to divide the IH cavity into four accelerating sections^[1.27-29]. This triplet channel optimized the transverse focusing along KONUS structures (see Chapter 3 and Chapter 4). The principle of an IH-DTL cavity will be discussed in chapter 2. The development of the IH-DTL will be discussed in the following chapters. Chapter 3 will describe the basis of a KONUS beam dynamics design including one example. Chapter 4 will present the design results of the IH-DTL for the Heidelberg Heavy Ion Cancer Therapy project (HICAT). The IH-DTL tuning concepts and results will be shown in chapter 5. Chapter 6 describes the geometry of the IH cavity. Chapter 7 shows the Microwave Studio simulation results for the IH cavity. Chapter 8 will discuss the measurements of the HICAT IH-DTL power cavity.

After IH-DTL, $^{12}\text{C}^{4+}$ will be stripped to $^{12}\text{C}^{6+}$, injected into the synchrotron and accelerated up to 430AMeV at a momentum spread of $\pm 0.1\%$ ^[1.3]. The super periodicity is 2 (See Fig.1.5). The synchrotron consists of 6 bending magnets with a deflecting angle of 60 degree and a curvature radius of 4.4m. The maximum flux density of 1.5T, the circumference of the synchrotron is 63.246m, and the magnet rigidity ranging from 1.03 to 6.60Tm. There are 12 quadruples used, the maximum gradient is 5.5T/m at an effective length of

0.5m. There are those of 4 sextuple magnets, effective length is 0.2m with maximum gradient of 7T/m (see Fig.1.5).

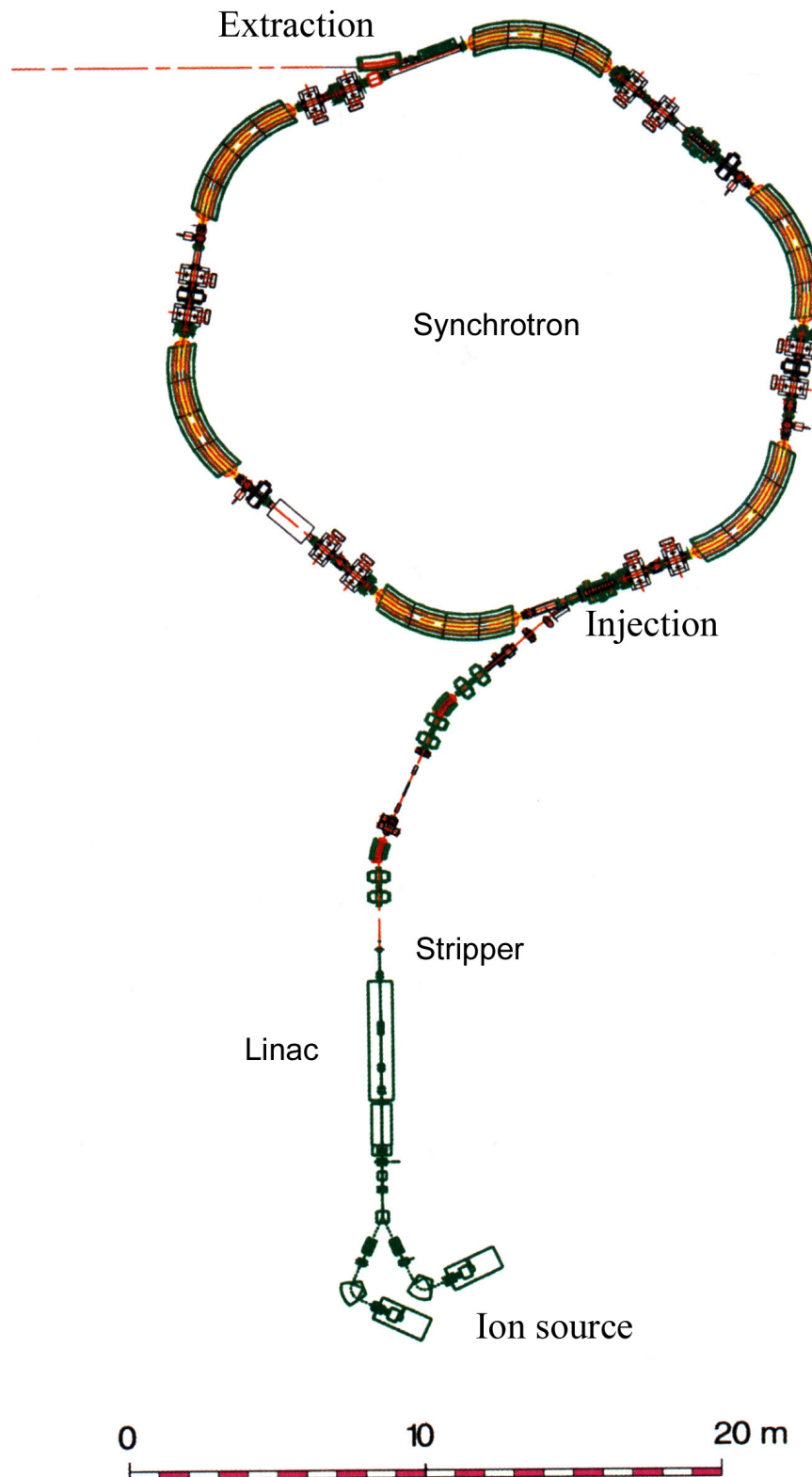


Fig.1.5 Accelerator components of the Heidelberg radiation facility ^[1.3]

Chapter Two

RF Capabilities of the IH-DTL

RF linear accelerator development was driven by basic research projects so far, while recently projects with a high potential for applied physics give strong additional impact. Examples of that kind of facilities are SNS (Spillation Neutron Source), which is now under construction at Oak Ridge in USA, the ESS (European Spillation neutron Source), ADS (Accelerator Driven System), IFMIF (International Fusion Materials Irradiation Facility) as well as the Proton and Ion beam therapy facilities all over the world. The potential applications of high power proton accelerators especially push the development of RF linear accelerators. The next generation of e^-e^+ colliders will also be realized in linac technology. Recent studies at the IAP Frankfurt show, that low and medium β , multi-cell H mode cavities can provide attractive capabilities as well for room temperature as for superconducting cavity designs^[2.1].

H-mode cavities were developed during last 25 years successfully to serve for a large variety of applications in the field of ion acceleration. The IH-DTL is efficient for an energy range from 100AkeV to 15AMeV, especially when combined with the KONUS beam dynamics. Room temperature IH-DTLs even can compete with existing superconducting linacs up to beam energies around 2AMeV in plug power consumption. This chapter will discuss the H mode and RF structure of the IH-DTL, the acceleration of a RF drift tube gap, and the particle stability in longitudinal and transverse directions. KONUS beam dynamics and simulation tool LORASR for IH-DTL will be discussed in chapter 3.

2.1 H-Mode and RF Structure of IH-DTL

Most RF cavity resonators used in linacs can be derived from the simple cylindrical or pillbox cavity. There are two different modes, which are often used in the linac, so called TE mode (Transverse Electric mode) and TM mode (Transverse Magnetic mode). TM mode (also called E-mode) is widely used in the Alvarez cavity. TE mode hasn't the longitudinal electric E_z component, so it is also called H-mode. IH-DTL (Interdigit H-mode Drift tube linac) and CH-DTL (Cross Bar H-mode DTL) linac use H-mode to create the required RF field.

The IH-DTL (H_{11} -mode) was mentioned as an attractive solution for proton acceleration up to 30MeV already at the 1956 CERN Symposium by J.P.Blewett^[2.2]. Several groups had studied the capabilities of that structure, and

important improvements and innovations were achieved during the design phase of many H-linac projects^[2.3-11].

There is a well-known analytic H-mode solution for cylindrical cavities with radius of R_T and length of L_c . Solving the Maxwell equations by postulating $E_z=0$, the general field expressions for the H-modes are

$$\begin{aligned}
 E_z &= 0 \\
 E_r &= j\omega \frac{ma^2}{x'_{mn}{}^2 r} B_0 J_m(k_{mn} r) \sin m\phi \sin \frac{p\pi z}{l_c} \exp(j\omega t) \\
 E_\phi &= j\omega \frac{a}{x'_{mn}} B_0 J'_m(k_{mn} r) \cos m\phi \sin \frac{p\pi z}{l_c} \exp(j\omega t) \\
 B_z &= B_0 J_m(k_{mn} r) \cos m\phi \sin \frac{p\pi z}{l_c} \exp(j\omega t) \\
 B_r &= \frac{p\pi}{l_c} \frac{a}{x'_{mn}} B_0 J_m(k_{mn} r) \cos m\phi \cos \frac{p\pi z}{l_c} \exp(j\omega t) \\
 B_\phi &= -\frac{p\pi}{l_c} \frac{ma^2}{x'_{mn}{}^2 r} B_0 J_m(k_{mn} r) \sin m\phi \cos \frac{p\pi z}{l_c} \exp(j\omega t)
 \end{aligned} \tag{2.1}$$

The general dispersion relation is $\omega^2/c^2 = k_{mn}^2 + k_z^2$, where $k_{mn} = x'_{mn}/R_T$ and $k_z = 2\pi/\lambda_{guide} = p\pi/l_c$, $p=1,2,3\dots$ the x'_{mn} are the zeros of the derivatives of the Bessel functions. The nomenclature of the TE_{mnp} modes is defined as follows. The subscript m ($m=0,1,2\dots$) is the number of full-period variations in ϕ of the field components. The subscript n ($n=1,2,3\dots$) is the number of the zeros of the axial field component in the radial direction in the range $0 < r \leq R_T$, excluding $r=0$. The subscript p ($p=1,2,3\dots$) is the number of half-period variations in z of the fields.

Because of $E_z=0$, the H mode in the empty cylinder couldn't be used to accelerate particles. In order to introduce the accelerating electric field along the structure, the drift tubes must be set into the cylinder cavity. But the electric capacitance between every gap makes the cavity frequency very much lower than that of the above theory. As an example, Fig.2.1 shows us the RF structure of CERN IH-DTL lead linac^[2.12]. The electric and magnetic fields are also shown in the figure. The averaged cavity diameter is 335mm and the length 1.42m. The H_{111} -mode of the corresponding empty cylinder has a resonance frequency of 535.3 MHz, but the measured frequency is only 202.56MHz. The ratio of frequencies is only 37.8%. It is the capacitance that makes the cavity frequency so low. By the way, after the drift tubes are set into the empty cavity, the electric and magnetic fields are no longer similar to the empty cylinder. After good tuning of an accelerator cavity, there is even a flat gap voltage distribution (zero mode) possible, which doesn't exist for the empty cylinders ($p>0$ in equat. 2.1), so it is called as $H_{11(0)}$ mode.

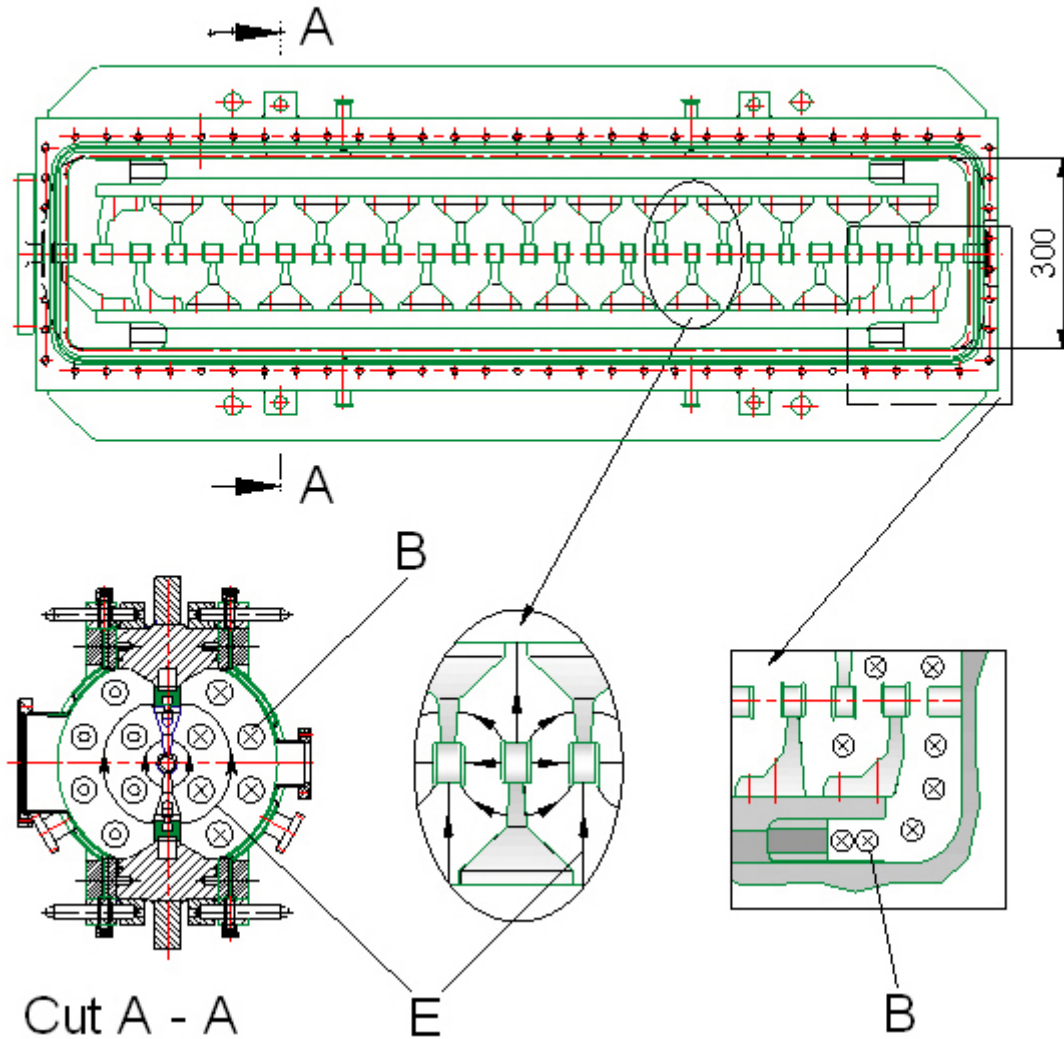
IH - Cavity, $H_{11(0)}$, 202 MHz


Fig.2.1 Top view on the 202 MHz drift tube structure of the CERN Pb^{25+} IH-DTL, tank 2. Below a cross sectional view of this cavity as well as the electric and magnetic field distributions at characteristic regions are plotted.^[2.12]

Fig.2.2 shows the cross section of IH-DTL. The cavity inductance per length can be derived from the Maxwell equations. We assume that magnetic induction B is homogeneous^[2.12], then the inductance can be derived as

$$L' = \frac{\mu_0 (R_2^2 - R_1^2) (\phi_2 - \phi_1)}{2} \quad (2.2)$$

It is proportional to the cross sectional area of the cavity^[2.13]. The parameters are explained by Fig.2.2. The electric capacitance per unit length consists of two parts: The first is the capacitance of the drift tube structure; this can be calculated by the formula^[2.1]

$$C'_d = \frac{\epsilon_0 \pi a^2}{2g_e(g+d)} \left[2 + \frac{4g_e}{\pi r_a} (\ln 2 + F_d(x)) \right] \quad (2.3)$$

with $F_d(x)$ was defined by the Equation (2.4) (see reference [2.14]).

$$F_d(x) = (1+x)\ln(1+x) - x\ln(x) \quad ; \quad x = \frac{d_e}{2g_e} \quad (2.4)$$

The symbols in Equations (2.3) and (2.4) are explained by Fig.2.3.

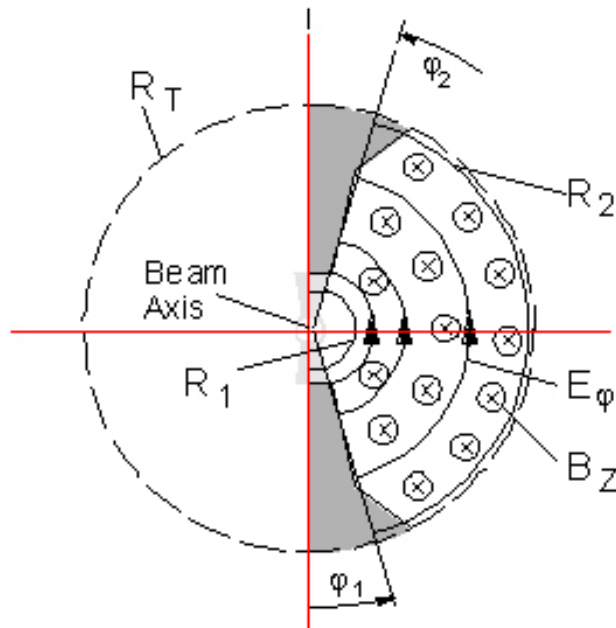


Fig.2.2 The cross section of the IH-DTL and parameters relevant for the analytical field approach

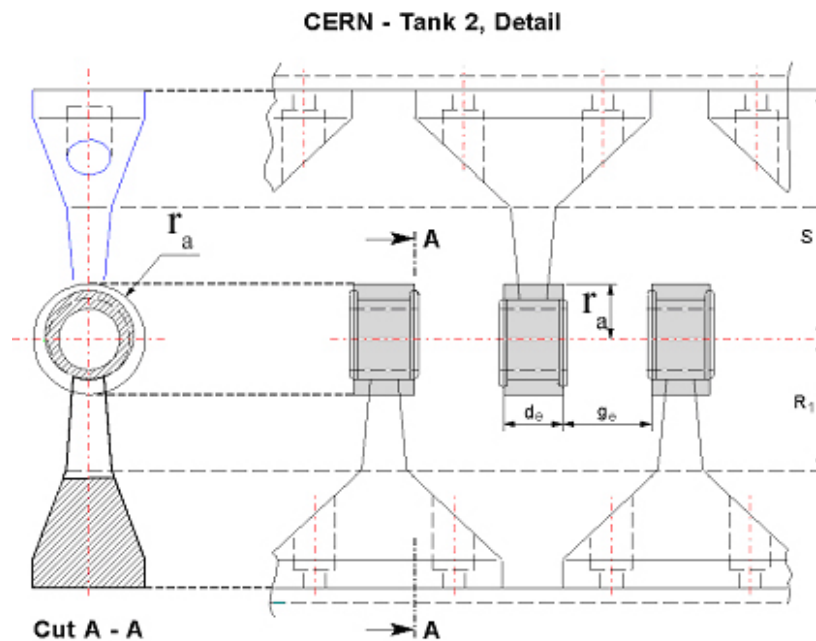


Fig.2.3 CERN IH-DTL structure and equivalent geometry to calculate the capacitance load

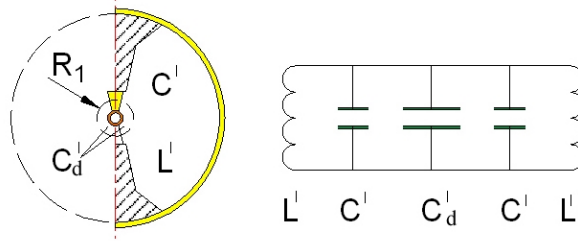


Fig.2.4 Equivalent circuit of IH-DTL

The second is the distributed capacitance between the tube support stems, girders and RF cavity walls. For the different designs, this capacitance $2C'$ can range from 0.5 to 2 times of C'_d . So the equivalent capacitance, inductance per unit length and angular frequency of IH-DTL cavity ^[2.1] are

$$C'_{IHD} = 2C' + C'_d$$

$$C' = \epsilon_0 \frac{R_2^4 \left[\ln \frac{R_2}{R_1} + \frac{2F-3}{4} \right] + R_2^2 R_1^2 (1-F)}{(R_2^2 - R_1^2)^2 (\phi_2 - \phi_1)}$$

$$L'_{IHD} = \frac{L'}{2} \left(\frac{R_2^2}{R_2^2 - R_1^2} \right)$$

$$\omega_{IHD} = \frac{1}{(L'C')^{1/2}} \left(\frac{2C'}{2C' + C'_d} \right)^{1/2} \cdot \left(\frac{R_2^2 - R_1^2}{R_2^2} \right)^{1/2}$$
(2.5)

Here F is the area correction factor in the cavity center (see Fig. 2.2 and Fig.2.3). The unit of the C'_{IHD} and L'_{IHD} is F/m and Hm, correspondently. The equivalent capacitance and inductance of the IH-DTL can be rewritten as:

$$C_e = C'_{IHD} l, \quad L_e = L'_{IHD} / l, \quad f = 1 / (L_e C_e)^{1/2}$$
(2.6)

2.2 Particle Acceleration Within One Gap

When a particle, with rest mass of m and charge of q , passes a gap on the paraxial with the RF phase ϕ , excited by the amplitude voltage U_0 , the kinetic energy gain ΔW

$$E_z(r, z, t) = E_z(r, z) \cos(\omega t + \phi)$$

$$\Delta W = q U_0 T(r, k) \cos \phi$$

$$U_0 = \int_{-L/2}^{L/2} E_z(0, z) dz$$
(2.7)

$$T(r, k) = \frac{\int_{-L/2}^{L/2} E_z(r, z) \cos(2\pi z / \beta \lambda) dz}{\int_{-L/2}^{L/2} E_z(0, z) dz}$$

Where U_0 is the amplitude gap voltage, T is the transit time factor, L is the periodic length, $L = v \cdot T_{rf} / 2 = \frac{1}{2} \beta c T_{rf} = \frac{1}{2} \beta \lambda$, if the periodic length $L = g$, then the transit time factor on the axis

$$T = \frac{\sin\left(\frac{\pi g}{\beta \lambda}\right)}{\frac{\pi g}{\beta \lambda}}$$

If the gap length is 0, then T becomes 1. However other aspects must be taken into account to determine the optimum gap geometry design, such as the risk of RF breakdown and RF power efficiency.

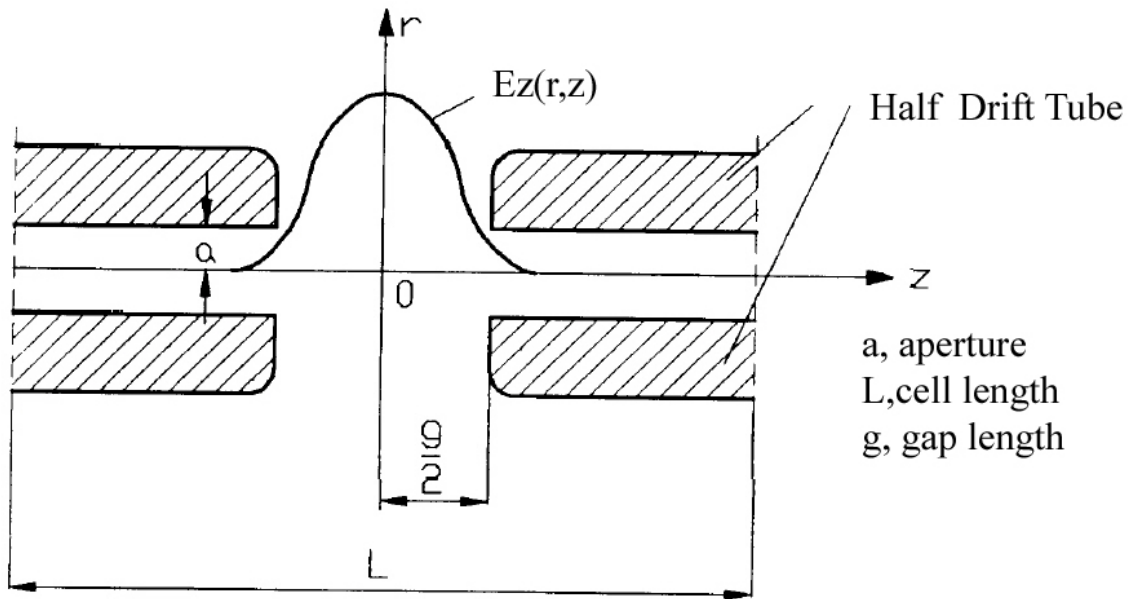


Fig.2.5 RF drift tube gap for the particle acceleration

For the thick walled drift tube gap with the large ratio of the gap length to drift tube length and/or large ratio of drift tube inner diameter to the drift tube length, the electric field penetrates into the drift tube. Then the transit time factor should be modified by the Bessel functions^[2.15].

$$T = \frac{J_0(2\pi a / \lambda) \sin(\pi g_c / \beta \lambda)}{I_0(k_s a) \pi g_c / \beta \lambda} \quad (2.8)$$

Where J_0 is the Bessel function of order zero, I_0 is the modified Bessel function of order zero. Here $k_s = 2\pi / (\gamma_s \beta_s \lambda)$, $g_c = g + 0.85\rho$, ρ is the chamfer radius of the drift tube ends.

The unloaded quality factor of the cavity is defined as

$$Q = \frac{\omega W}{P}$$

$$W = \frac{1}{2} C_e U_a^2, \quad U_a = \frac{1}{N_g} \sum_{i=1}^{N_g} V_{ia} \quad \text{or} \quad W = \frac{1}{2} L_e I^2 \quad (2.9)$$

where P is the dissipation power and W is the stored energy in the cavity, U_a is the averaged amplitude voltage, V_{ia} is the i_{th} gap amplitude voltage, I is the driven current.

The shunt impedance of the cavity characterizes the efficiency of the structure in providing the high accelerating field for a given RF power dissipation in the structure. It is defined as

$$Z_0 = \frac{(\int_0^l |E_z(0, z)| dz)^2}{Pl}$$

The relevant formula for the IH-Structures as published by the U.Ratzinger [2.1] is

$$Z_0 \cong \frac{\mu_0^{3/2} \kappa^{1/2} R_2^3 (\phi_2 - \phi_1)^2 \omega^{7/2}}{\sqrt{2\pi^2 c^2 N_m (\phi_2 - \phi_1 + 2c_1) c_2 \bar{\beta}^2}}, \quad \text{with} \quad (2.10)$$

$$\bar{\beta} = ((\beta_i^3 + \beta_f^3) / 2)^{1/3}, \quad \kappa_{cu} = 5.6 \cdot 10^7 [S / m]$$

$$Q \approx \frac{\pi^2 C_e Z_0 \bar{\beta}^2 c^2}{2\omega} \quad (2.11)$$

where c_1 and c_2 are the constants related with the structure, β_i and β_f are the relative velocity factor of the input and output particles, $\bar{\beta}$ is the averaged relative velocity of the particles in the cavity. Other parameters are shown in Fig.2.2, Fig.2.3 and Equation (2.5).

The effective shunt impedance in the accelerating cavity relates the equivalent effective voltage gain through the cavity to the power dissipated in the cavity wall

$$Z_{eff} = Z_0 T^2 \quad (2.12)$$

H-mode cavities have very high efficiency [2.1], especially at low beam velocities. This is shown in Fig.2.6 very well. The effective shunt impedance of the conventional $\beta\lambda/2$ -DTL structures are less than $50 M\Omega/m$, but that of IH-DTL reaches about $250 M\Omega/m$. Linac no. (3) and (4) haven't focusing elements inside the cavities; no. (6) uses conventional dynamics (synchronous phase $\phi_s = -30^\circ$) with quadruples in every second drift tube ($\phi_a = 100\text{mm}$). The line no.7 marks the estimated shunt impedance of the HICAT IH cavity. The more detailed estimations will be shown in the Chapter six and Chapter seven. The 700MHz CCDTL and BCDTL structures in Fig.2.6 were proposed by Los Alamos. Because of the high efficiency of H type structures, it shows the possibility to make the length of LINAC shorter and shorter.

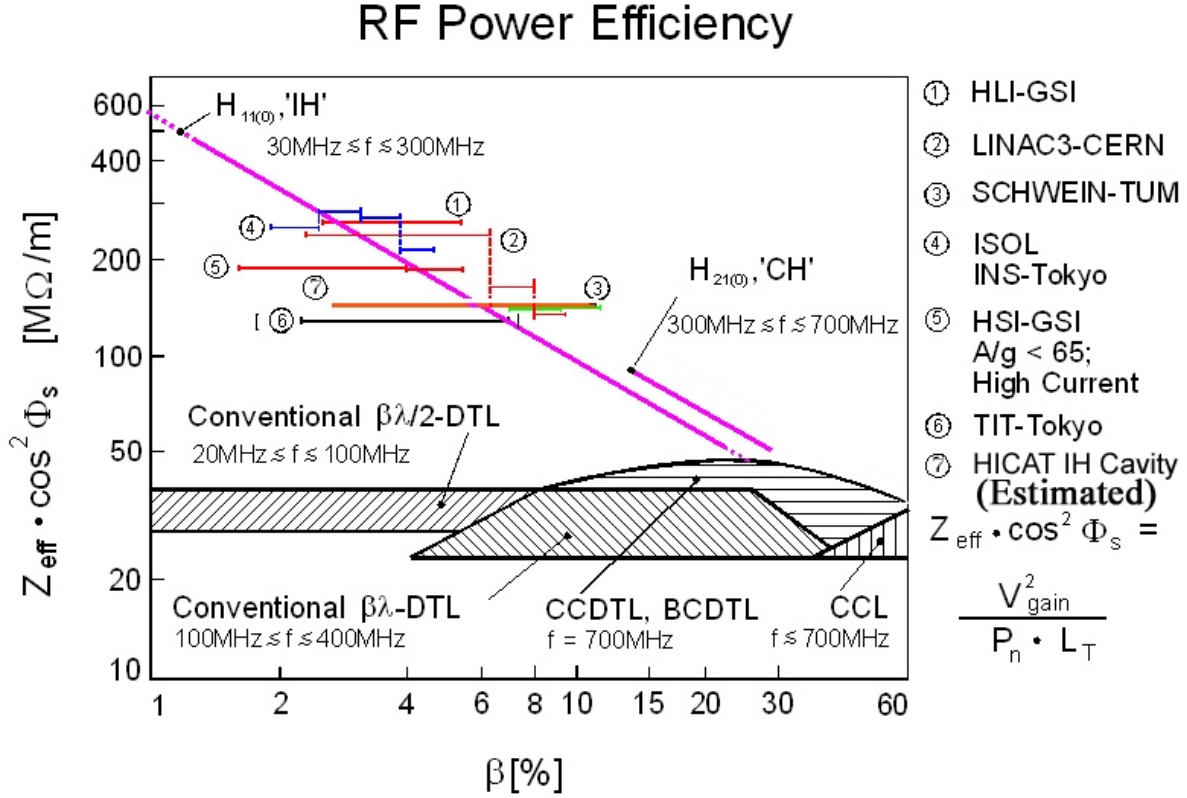


Fig.2.6 RF power efficiency of H-mode cavities (after ^[2.1])

2.3 Longitudinal Single Particle Motion

We consider the longitudinal motion of the particle, which has rest mass of m and charge of q and passes through a sequence of drift tubes and RF accelerating gaps. Starting from the Equation (2.7) and Fig.2.7, if the synchronous energy is changed very slowly, that $E_0 T$, β_s , γ_s , ϕ_s are nearly constant, the longitudinal equations can be written as^[2.16]

$$\frac{d^2(\phi - \phi_s)}{ds^2} = -\frac{2\pi q E_0 T}{mc^2 \lambda \beta_s^3 \gamma_s^3} (\cos \phi - \cos \phi_s) \quad \text{or}$$

$$\frac{d^2 \Delta \phi}{ds^2} = \frac{2\pi q E_0 T}{mc^2 \lambda \beta_s^3 \gamma_s^3} \sin \phi_s \Delta \phi \quad \text{or} \quad (2.13)$$

$$\frac{d^2 \phi}{ds^2} = -\frac{2\pi q E_0 T}{mc^2 \lambda \beta_s^3 \gamma_s^3} (\cos \phi - \cos \phi_s)$$

The second form of Equation (2.13) tells us the phase motion is stable as long as $\sin\phi_s < 0$, so the synchronous phase ϕ_s for DTL linear accelerator should satisfy: $-\pi < \phi_s < 0$. Recalling that there is an acceleration for $-\pi/2 \leq \phi_s \leq \pi/2$, one obtains simultaneous acceleration and potential well when $-\pi/2 \leq \phi_s \leq 0$. The behavior of $\Delta\phi$ looks like a resonance vibration, but resonance angular frequency will be decreased with $(\beta_s \gamma_s)^{3/2}$, resonance amplitude for phase oscillation will also be decreased, until ϕ reached to ϕ_s .

Using $ds = \frac{d\phi}{\phi'}$, multiplying the third form of Equation (2.13) by ϕ' , and after integrating, we get the potential energy term

$$V_\phi = \frac{qE_0 T}{mc^2} (\sin\phi - \phi \cos\phi_s) \quad (2.14)$$

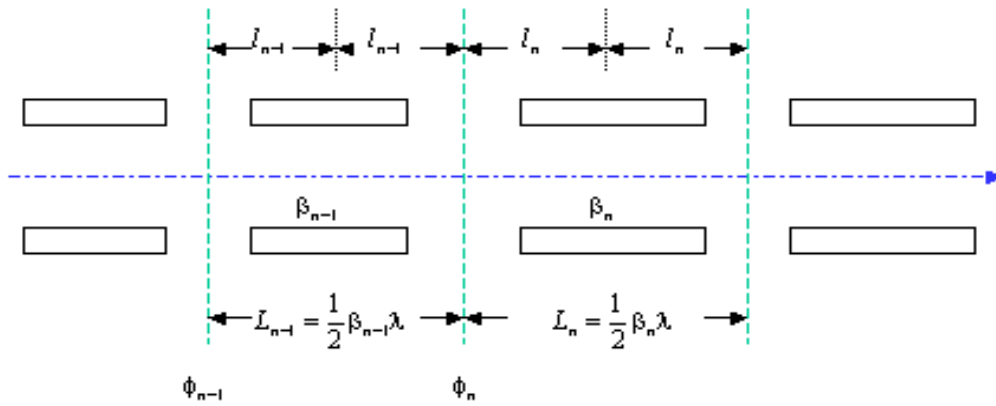


Fig.2.7 Accelerating cells for describing the longitudinal motion

This is so called potential well function. From the Equations (2.13), (2.14), we can draw the Fig.2.8. It will tell us the following information for a traditional linac design to a given synchronous phase ϕ_s :

- 1, the stable phase range for arbitrary particles: $-2|\phi_s| \leq \phi \leq |\phi_s|$, the smaller ϕ_s is, smaller the stable phase range is. For example, if $\phi_s = -30^\circ$, then stable phase ranges from -60° to 30° , if $\phi_s = -90^\circ$, then stable phase range can reach full 360° . But one should care less synchronous phase means large energy gain per acceleration and less stable phase range;
- 2, allowable maximum energy spread is happened at ϕ_s , it is given by the following

$$\Delta W_{\max} = \sqrt{\frac{2qE_0 T \beta_s^3 \gamma_s^3 \lambda mc^2}{\pi}} (\phi_s \cos\phi_s - \sin\phi_s) \quad (2.15)$$

3, because of the relation between the momentum and kinetic energy, the momentum spread is also given.

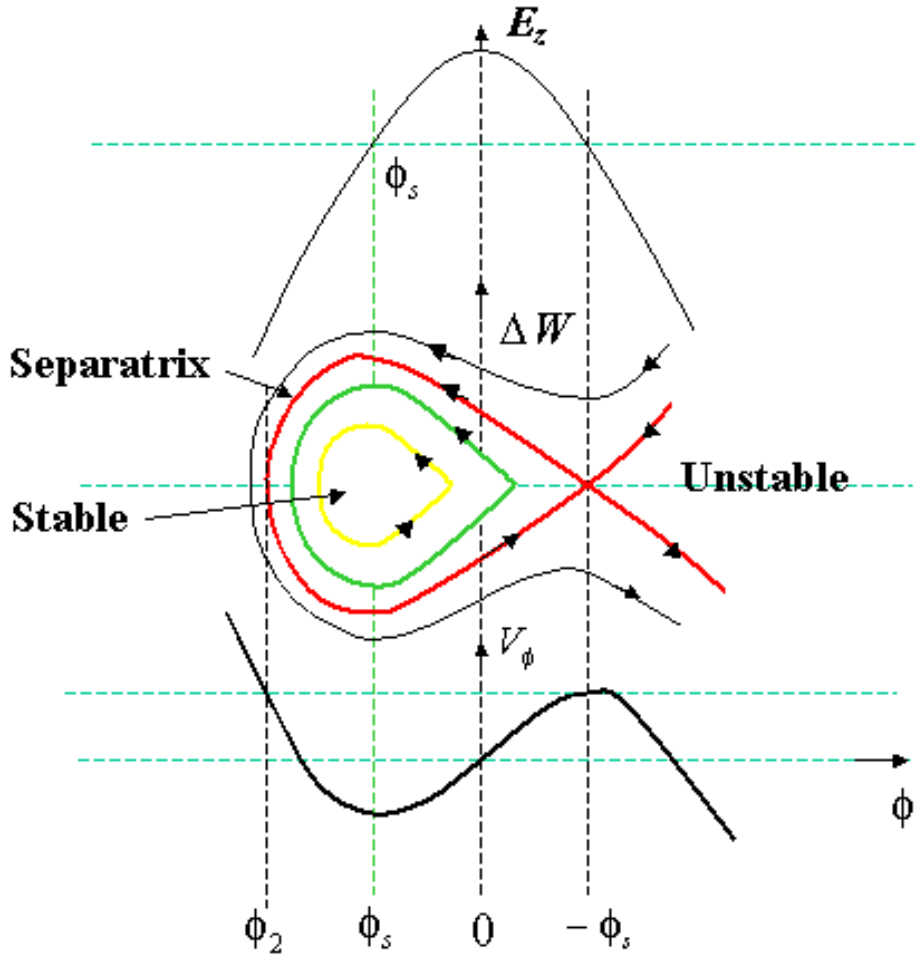


Fig.2.8 Longitudinal phase space and potential well

2.4 Transverse Motion

We concentrate particle transverse motion in this subdivision. First we can write the radial force in cylinder coordinate:

$$F_r = q(E_r + v_\phi B_z - v_z B_\phi) = q(E_r - v_z B_\phi) = q(E_r - \beta c B_\phi) \quad (2.16)$$

From the Maxwell's equations, we obtain:

$$\frac{1}{r} \frac{\partial}{\partial r} (r E_r) + \frac{\partial E_z}{\partial z} = 0 \quad (2.17)$$

$$\frac{1}{r} \frac{\partial}{\partial r} (r B_\phi) = \mu_0 \epsilon_0 \frac{\partial E_z}{\partial t} \quad (2.18)$$

We assume that near the axis the E_z is approximately independent with radial displacement, after integrating the Equation (2.17) and (2.18), we have

$$E_r = -\frac{r}{2} \frac{\partial E_z}{\partial z} \quad (2.19)$$

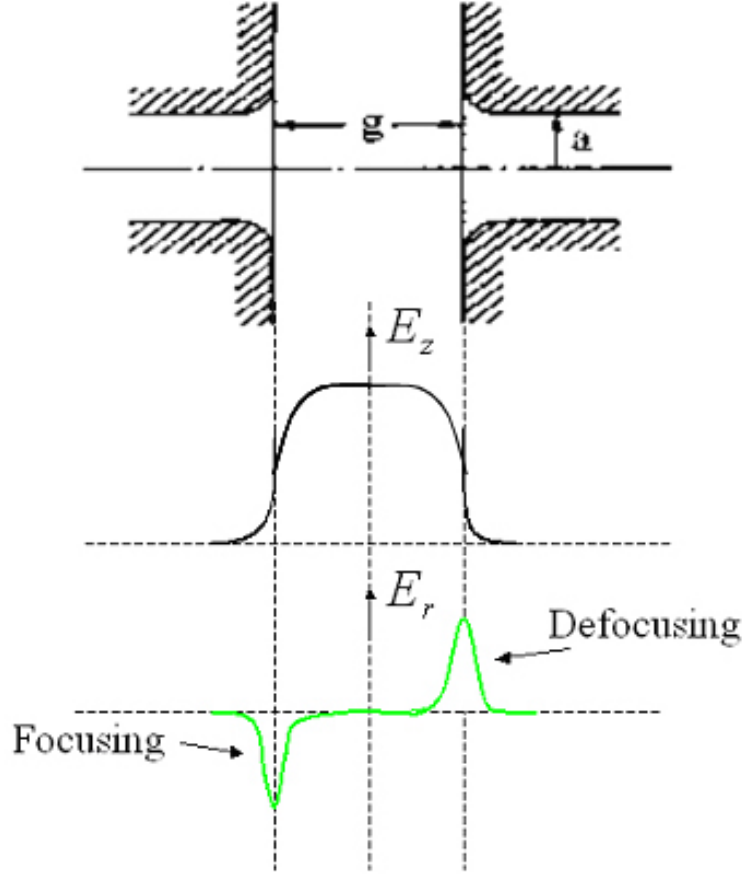


Fig.2.9 Longitudinal and radial electric field in an RF gap

$$B_\phi = \frac{r}{2} \mu_0 \epsilon_0 \frac{\partial E_z}{\partial t} = \frac{r}{2c^2} \frac{\partial E_z}{\partial t} \quad (2.20)$$

Using $F_r = \frac{\Delta p_r}{\Delta t}$ and $dt = (\beta c)^{-1} dz$, from the Equation (2.16), the radial momentum impulse is

$$\Delta p_r = q \int_{-L/2}^{L/2} (E_r - \beta c B_\phi) \frac{dz}{\beta c} = -\frac{q}{2} \int_{-L/2}^{L/2} r \left(\frac{\partial E_z}{\partial z} + \frac{\beta}{c} \frac{\partial E_z}{\partial t} \right) \frac{dz}{\beta c} \quad (2.21)$$

Substituting $\frac{\partial E_z}{\partial z} = \frac{dE_z}{dz} - \frac{1}{\beta c} \frac{\partial E_z}{\partial t}$ into the above equation, integrate it, we get

$$\Delta p_r = -\frac{qr\omega}{2\gamma^2\beta^2c^2} \int_{-L/2}^{L/2} E_z(0,z) \sin(\omega t + \phi) dz \quad (2.22)$$

Consider a particle at the origin at time $t=0$, $\omega t = kz$, $k = 2\pi/(\beta\lambda)$, $\phi = \phi_s$, using $\sin(\omega t + \phi) = \sin \omega t \cos \phi + \cos \omega t \sin \phi = \cos kz \sin \phi_s$, then it becomes

$$\Delta p_r = -\frac{qr\omega}{2\gamma^2\beta^2c^2} \sin \phi_s \int_{-L/2}^{L/2} E_z(0,z) \cos kz dz = -\frac{q\pi E_0 TL \sin \phi_s}{\gamma^2\beta^2c\lambda} r \quad (2.23)$$

Using the $r' = \frac{dr}{dz} = \frac{p_r}{p_z}$ so $p_r = mc\beta\gamma r'$, we can rewrite (2.23) as

$$\Delta(\beta\gamma r') = -\frac{q\pi E_0 TL \sin \phi_s}{mc^2\gamma^2\beta^2\lambda} r \quad (2.24)$$

From the Equation (2.24), we see the particle transverse motion is unstable for stable longitudinal synchronous phase $-\pi/2 \leq \phi_s \leq 0$. Even though the particle get the radial focusing because of $\frac{\partial E_z}{\partial z} > 0$, then $E_r = -\frac{r}{2} \frac{\partial E_z}{\partial z} < 0$, at the entrance of drift tube gap, and defocusing at exit of drift tube gap (See Fig.2.9). For the electrostatic effects, the particles are focused because of defocusing force has less impacting time. However, in RF drift tube linac, in order to keep the longitudinal focusing (stable), the synchronous phase ϕ_s must be ranged from $-\pi/2 \leq \phi_s \leq 0$, the accelerating field in this region is rising in time, although the particle is focused in the first half gap, the particle has more larger defocusing force in the second half gap, so phase or time effects has more defocusing force in the radial motion. This is very important confliction that characterizes the difficulties of RF DTL design. The introduced transverse focusing elements in the traditional DTL drift tubes increase the diameters of drift tubes and leads to very heavy capacitance load and large power dissipation and lower cavity shunt impedance. These problems are reduced by the KONUS beam dynamics for DTL structures and will be discussed in the next chapter.

Chapter Three

KONUS Beam Dynamics and LORASR Code

A main design problem to be solved for every RF linac is the transverse defocusing action of accelerating fields which have to provide longitudinal bunch focusing (comparing equations 2.13 and 2.24). In current opinions, there were two ways at that moment: the standard way is to keep the synchronous phase at a negative constant value, so longitudinal motion is stable. With setting quadruple magnetic lenses inside the drift tubes the radial focusing is provided. This way was adopted in many Alvarez cavities (See Fig.3.3a). The disadvantage is that a large capacitive load was introduced because of enlarging of outer drift tube diameters. This increases RF power dissipation and makes RF shunt impedance of cavity lower; another way is to use the APF (Alternative Phase Focusing) concept to improve the radial defocusing. The APF concept was developed since last 1950's by many authors^{[3.1]-[3.5]}. Up to now there are still some researchers who are interested in such machines^{[3.6]-[3.7]}. But the efficiency of APF depends very much on the correct configuration of each focusing section; there is no theory that could be applied to the optimisation of the drift tube array so far. The emittance growth was a main problem for the APF drift tube linac design. The stability of small oscillations can be explored with Mathieu-Hill equations, but only for one harmonic or for a step function approximation of the focusing force. One can investigate non-linear oscillations by using the smooth approximation method, but only for a small phase advance per focusing period.

A breakthrough was achieved by the idea of "KONUS" beam dynamics for the IH-DTL linac. It is completely different from above two ways. "KONUS" is deduced from German "Kombinierte Null Grad Struktur", which means "Combined Zero Degree Structure", developed by U.Ratzinger in 1988. Pre-investigations towards this achievement were done during the development of the Munich RF post accelerator SchweIN behind of the MP Tandem and especially by designing and realizing a new buncher system for SchweIN^[3.8]. The first clear description, KONUS beam dynamics simulation and successful experimental results were published in 1988^[3.9]. Since 1988, there are several projects which have been designed, manufactured and operated successfully by using KONUS beam dynamics, for example, GSI High Charge state Injector (HLI), High Current Injector (HSI)^{[3.10]-[3.11]}, CERN lead linac^[3.12], TRIUMF ISAC in Vancouver, CERN REX-ISOLDE^[3.13] project and so on. Many projects are well planned to build H-type DTL linacs and KONUS beam dynamics

simulations have been done, for example, IFMIF project^[3.14], Super-conducting CH cavity^[3.15], XADS^[3.16] project among others.

3.1 Concept of KONUS Beam Dynamics

From the equation (2.24), if the synchronous phase ϕ_s is near 0 degree from a bit positive (but not large positive phase as APF), the radial momentum impulse will be negative, the radial motion will be focused, meanwhile longitudinal motion isn't focused (see Fig.2.8 and equation (2.13)), but the instability isn't so large, this was verified by transformation of a particle pulse shape inside Munich 2f-booster with cavity length of 5m, which consists of 27gaps and 26 drift tubes with inner diameter of 30mm and outer diameter of 42mm^[3.9]. The cavity is shown in Fig.3.1, there are no radial focusing elements inside the tank, so the construction is rather simple and costs are low, only a quadrupole doublet was installed in front of the tank. One of the goals was to investigate whether such a type of multi-gap cavity can be used as a unit in a "long" heavy ion linac. The transformation of the beam $^{58}\text{Ni}^{22+}$ was shown in Fig.3.2, injection energy $E_i=150\text{MeV}$, output energy $E_a=280\text{MeV}$, 2f booster was operated at $f_{rf}=160\text{MHz}$. It is obvious that the pulse centre has less energy gain than the synchronous particle and has moved from positive to negative RF phases, while the pulse contour didn't change significantly. Therefore we can continue the acceleration process by adding another cavity with favourable length and with a suitable new 0° synchronous particle.

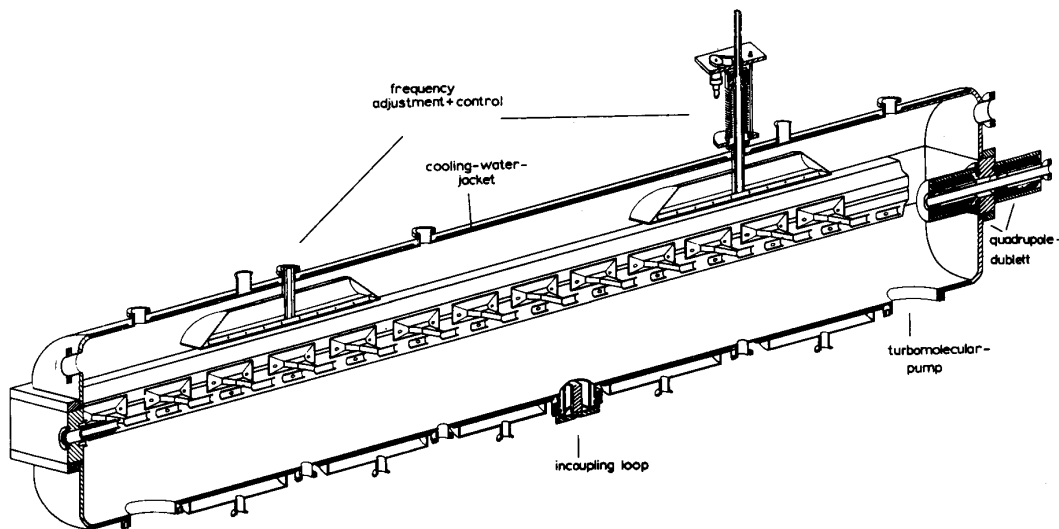


Fig.3.1 Sectional view of 2f cavity in Munich Post-accelerator

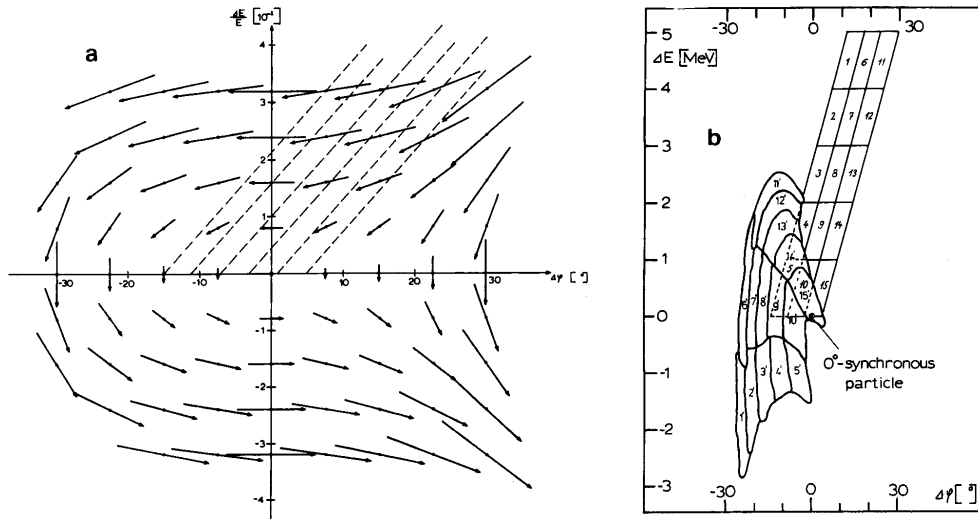


Fig.3.2 Particle velocity relative to 0° synchronous particle in the longitudinal phase space (a) and its transformation in $\Delta E/\Delta\phi$ plane by passing through a 0° synchronous particle of finite length.

The results are encouraging; they tell us that we can use finite length to accelerate particles as much as possible by setting 0° synchronous particle phase, until the accumulated radial defocusing force needs to be compensated by the quadrupole lenses (see Fig.3.3b), in order to ensure the particle are safety in longitudinal motion, before 0° acceleration section, the particles needs to be rebunched at about -30° synchronous phase for two or three cells to have enough longitudinal focusing for the 0° acceleration section length (See Fig.3.3c). This concept is shown in Fig.3.3.

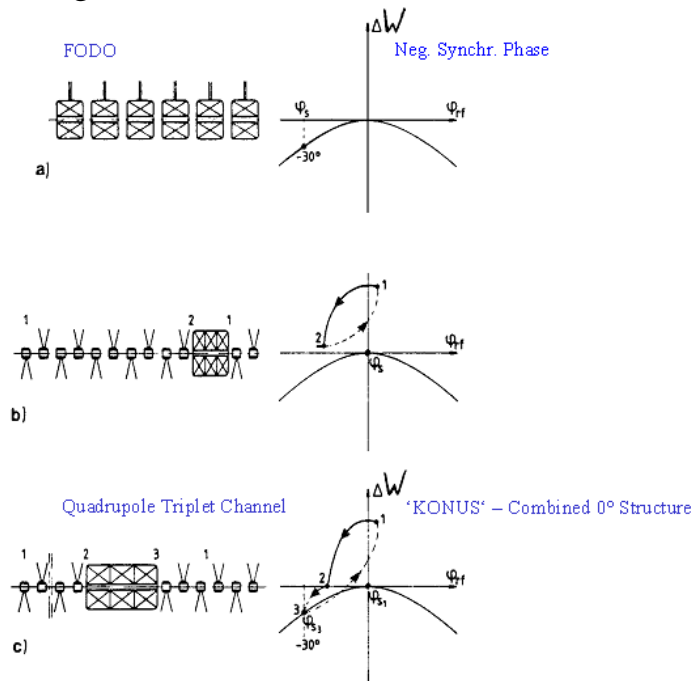


Fig.3.3 Concept of KONUS Dynamics Design^[3.17]

3.2 LORASR—KONUS Beam Dynamics Simulation Code

LORASR is abbreviated from German “**L**ongitudinale und **R**adiale **S**trahldynamikrechnungen mit **R**aumladung”^[3.18], which means longitudinal and radial beam dynamics simulation including space charge effect. The initial version LORAS didn’t include the space charge effect; the first project is “Munich SchweIN”, as was discussed in the last chapter. The simulation was tracing each particle in 6 dimensional phase space (See Fig.3.2)^[3.9]. From 1987 to 1991, the code was further developed for the design of “GSI HLI project” and “CERN lead linac”, because of the special requirements of low injection beam energy. The space charge effect was included in the LORASR by a particle in cell routine, additionally from the simulation and measured drift gap field distribution results; the drift gap field distribution was improved^[3.19]. For the GSI “Superlens” design, the RFQ routine was also included and the data plot function was improved. Now the software of LORASR has two versions, one is operating on LINUX machines; another is a PC version for windows 9X and windows 2000 /XP. This version of LORASR was compiled by Lahey Fortran95. It has friendly interface and functions are further improved in the future. Fig.3.4 shows the schematic sketch of the LORASR subroutine structure.

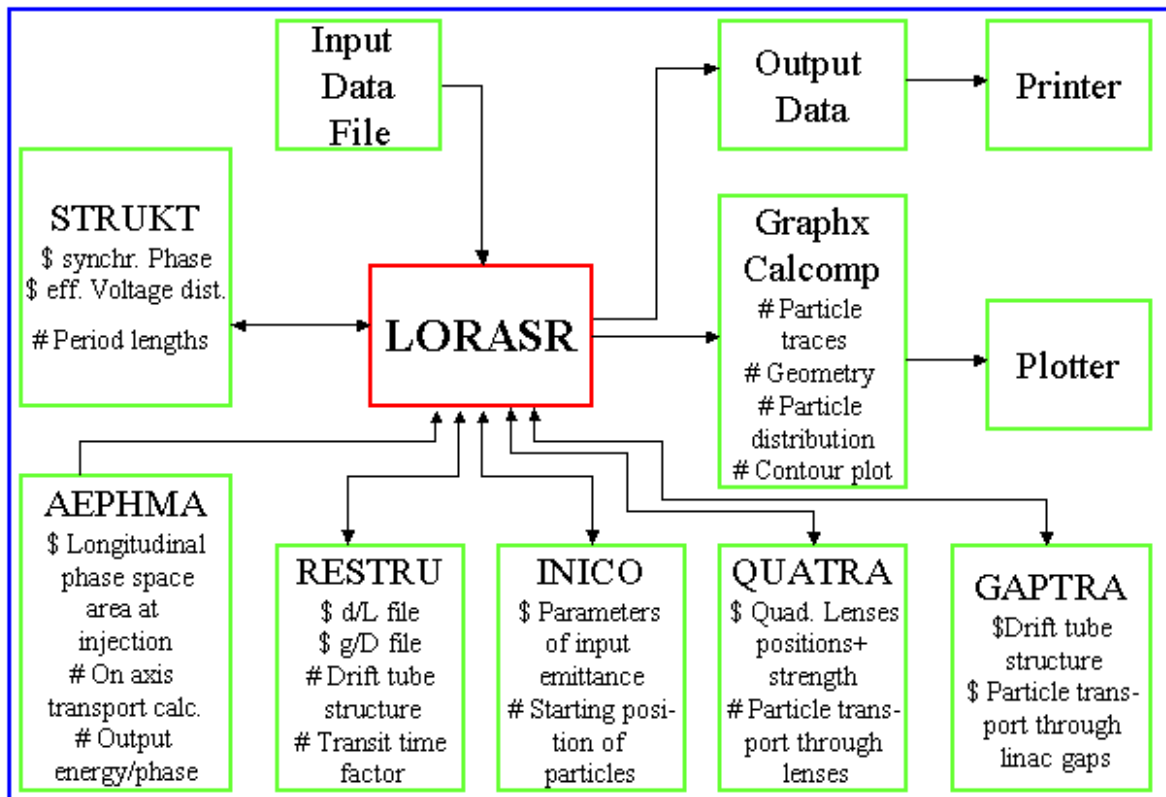


Fig.3.4 Schematic sketch of the LORASR structure (\$: Input parameters /data; #: Output parameters / data)

STRUKT (STRUCTure): Calculate the table of period lengths from the synchronous rf phase and the effective gap voltage of the synchronous particle. The synchronous particle is used to generate the drift tube structure. Along the linac, the synchronous particle may be replaced by another one. RF phase, injection energy and synchronous phase of the synchronous particle can be redefined at the entrance of each gap.

AEPHMA (Exit Energy PHase MATrix): Calculate the output energy and rf phase on the input rf phase and input energy matrix and hence determine the longitudinal $\Delta\phi$ - ΔW phase space acceptance. Calculations are done on the basis of a one step per gap calculation along the beam axis.

RESTRU (REal STRUcture): It calculates the geometry of the drift tubes and of the gap lengths. The input parameters required for calculation are the d/L (drift tube length to the periodic length) and the g/D (gap length to the inner diameter of the drift tubes) ratios. Alternatively the drift tube structure can be given by the data set 'FIST'. The electric gap field distribution and the transit time factors are determined. The according field distribution parameters are to be given by the data set 'FEVE'.

QUATRA (QUAdrupole TRAnsport): Subroutine QUATRA calculates the dynamics of the beam particle through the quadruple lenses. The input data required for the calculations are the geometry and the magnetic field gradient (Gauss/cm) of the quadruples.

GAPTRA (GAP TRAnsport): Calculates the transport of single particle along the drift tube sections. The dependence of the transit time factor is included according to the particles transversal position at each gap entrance.

GRAPHX (GRAPHics): This subroutine displays on a graphics terminal or on plotters using the library subroutines CALCOMP. The possible plots are:

- 1) Contour plot of output energy on input phase/input energy area.
- 2) Exit phase/energy distribution of input area studied in plot 1.
- 3) Single particle trace in real space.
- 4) Emittance plots of the injected beam in the transverse and longitudinal plane.
- 5) Single particle traces in longitudinal space (i.e., phase and energy of single particle relative to the synchronous particle).
- 6) Emittance plots in the transverse and longitudinal plane at the linac exit.
- 7) Geometry and aperture of the drift tube array and of the quadruple lenses.

READ&CARD: Input data are read in the free format by this subroutines as well as commands to determine the sequence of calculations.

Some useful beam transport matrixes:

Free space drift, M_{0T}

$$\begin{pmatrix} x_2 \\ x_2' \end{pmatrix} = \begin{pmatrix} 1 & l \\ 0 & 1 \end{pmatrix} \begin{pmatrix} x_1 \\ x_1' \end{pmatrix} = M_{OT} \begin{pmatrix} x_1 \\ x_1' \end{pmatrix} \quad (3.1)$$

Free space drift, M_{OL}

$$\begin{pmatrix} \Delta\phi_2 \\ \Delta W_2 \end{pmatrix} = \begin{pmatrix} 1 & P_l \\ 0 & 1 \end{pmatrix} \begin{pmatrix} \Delta\phi_1 \\ \Delta W_1 \end{pmatrix} = M_{OL} \begin{pmatrix} \Delta\phi_1 \\ \Delta W_1 \end{pmatrix} \quad (3.2)$$

where $P_l = \frac{-\omega L}{mc^3\beta^3\gamma^3}$.

Focusing quadruple, M_{QF}

$$\begin{pmatrix} x_2 \\ x_2' \end{pmatrix} = \begin{pmatrix} \cos\sqrt{kl} & \frac{1}{\sqrt{k}}\sin\sqrt{kl} \\ -\sqrt{k}\sin\sqrt{kl} & \cos\sqrt{kl} \end{pmatrix} \begin{pmatrix} x_1 \\ x_1' \end{pmatrix} = M_{QF} \begin{pmatrix} x_1 \\ x_1' \end{pmatrix} \quad (3.3)$$

where $k = \frac{qB'}{\beta\gamma m} > 0$, called quadruple focusing strength, B' called magnetic gradient. The dimension of B' is T/m. Unit of length is metre. One should notice LORASR uses Gauss as a unit of magnetic induction strength. Effective length is in cm.

Defocusing quadruple, M_{QD}

$$\begin{pmatrix} x_2 \\ x_2' \end{pmatrix} = \begin{pmatrix} \cosh\sqrt{kl} & \frac{1}{\sqrt{k}}\sinh\sqrt{kl} \\ \sqrt{k}\sinh\sqrt{kl} & \cosh\sqrt{kl} \end{pmatrix} \begin{pmatrix} x_1 \\ x_1' \end{pmatrix} = M_{QD} \begin{pmatrix} x_1 \\ x_1' \end{pmatrix} \quad (3.4)$$

where $k = \frac{qB'}{\beta\gamma m} < 0$.

For the traditional design, the transversal matrix M_{GT} for a RF accelerating gap:

$$\begin{pmatrix} x_2 \\ x_2' \end{pmatrix} = \begin{pmatrix} 1 & 0 \\ F_t & 1 \end{pmatrix} \begin{pmatrix} x_1 \\ x_1' \end{pmatrix} = M_{GT} \begin{pmatrix} x_1 \\ x_1' \end{pmatrix} \quad (3.5)$$

where $F_t = \frac{qE_0\pi T \sin(-\phi_s)}{2mc^2\beta^2\gamma^3}$, called radial focusing strength.

The longitudinal matrix M_{GL} for a RF accelerating gap:

$$\begin{pmatrix} \Delta\phi_2 \\ \Delta W_2 \end{pmatrix} = \begin{pmatrix} 1 & 0 \\ F_l & 1 \end{pmatrix} \begin{pmatrix} \Delta\phi_1 \\ \Delta W_1 \end{pmatrix} = M_{GL} \begin{pmatrix} \Delta\phi_1 \\ \Delta W_1 \end{pmatrix} \quad (3.6)$$

where $F_l = qE_0TL \sin(-\phi_s)$.

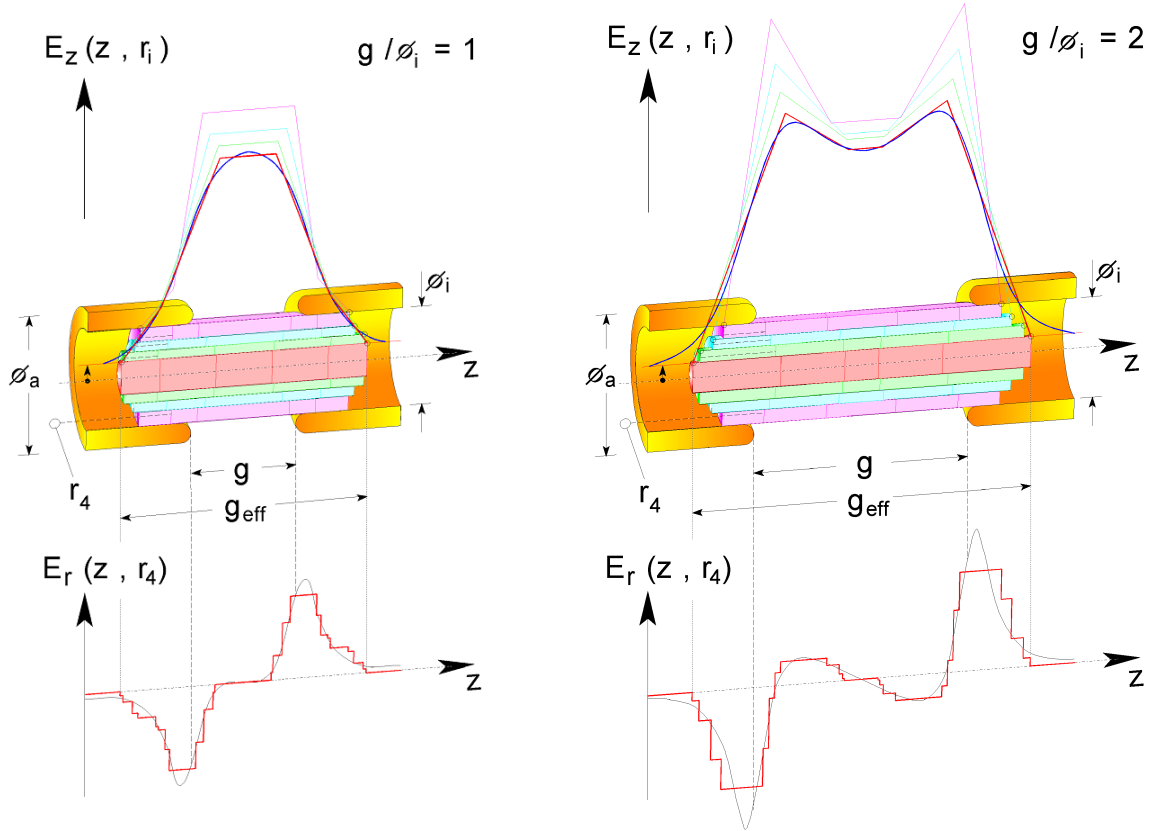


Fig.3.5 The approximated field distributions and comparison with simulations for two different gap lengths

But in the LORASR, the beam simulation for the RF accelerating gap is rather different from the equations (3.5) and (3.6). In order to determine the real voltage distribution and transit time factor, the effective gap length has been divided into 30 steps in five different zones in LORASR. The real voltage distribution in different zones is calculated by using the linear fit to the longitudinal gap field distribution (see Fig.3.5). The accurate calculations of transit time factor, RF phase of synchronous particles and energy gain was according to the real field and voltage distribution in different zones, every zone has been divided into 6 steps for more accurate calculations. This process is shown in Fig.3.6.

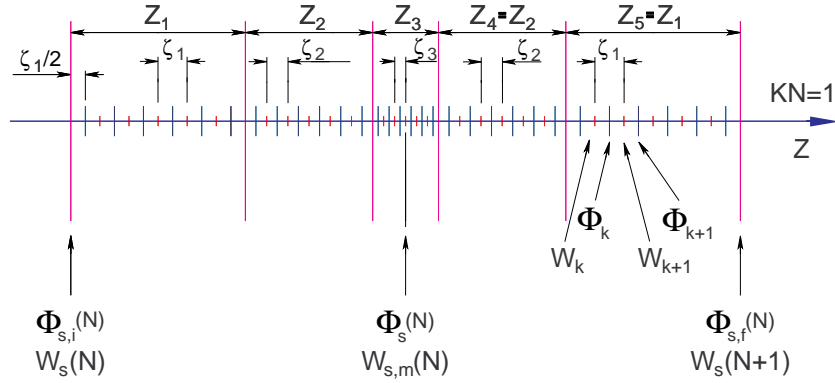


Fig.3.6 One gap is divided into 5 zones; every zone is divided into 6 steps

The motion of the particle in the k -th zone with the amplitude voltage of ΔV_k and phase of Φ_k (see Figure 3.5) can be traced by the following^[3.20]:

$$\begin{aligned}
 \Delta W_k &= q \Delta V_k \text{COS} \Phi_k ; \\
 W_{k+1} &= W_k + \Delta W_k ; \\
 x' &= x'_k \beta_k / \beta_{k+1} ; x_m = x_k + x' \zeta / 2 ; \\
 R_m &= (x_m^2 + y_m^2)^{1/2} ; W_m = \frac{W_{k+1} + W_k}{2} ; \Delta t = \frac{\zeta}{\beta_m c} ; \\
 \Delta v_r &= q E_r (R_m, z) \text{COS} \Phi_k \zeta (mc \beta_m \gamma_m)^{-1} ; \Delta s = \Delta v_r \frac{\Delta t}{2} ; \\
 x_{k+1} &= x_k + x' \zeta + \Delta s \cdot x_m / R_m ; \\
 x'_{k+1} &= x' + \frac{2 \cdot \Delta s \cdot x_m}{\zeta \cdot R_m} ; \\
 \Phi_{k+1} &= \Phi_k + 360^\circ \cdot \frac{\zeta}{\beta_{k+1} \cdot \lambda}
 \end{aligned} \tag{3.7}$$

Here, $E_r(R_m, z)$ is the transverse electric field, it can be expressed as:

$$E_r(R_m, z) = \frac{1}{R_m} \int_0^{R_m} -r \frac{dE_z(r, z)}{dz} dr \tag{3.8}$$

With the above formulas and the traditional beam transport matrixes for the free space and quadruple lenses, the particle trajectory in the six dimensional phase spaces along the structure can be simulated by the LORASR code.

3.3 KONUS Beams Dynamics Example

Fig.3.7 shows one KONUS beam dynamics design example. GSI HLI project was designed to use an IH-DTL cavity for the acceleration of $^{238}\text{U}^{25+}$ from

0.3MeV/u to 1.4MeV/u. The operating frequency is 108MHz. It has three KONUS sections (see sections I, II and III in Fig.3.8 separated by the green line), each KONUS section consists of a negative synchronous particle phase (-30°) rebuncher (from green to black), a 0° acceleration (from black to red) and of a transverse focusing triplet lens (from red to green). There are two quadrupole triplets (from red to green) are installed inside the cavity. The length of QT1 is about $4\beta\lambda$, that of QT2 is about $3\beta\lambda$, magnetic field gradient is about 78T/m. The inner aperture of QT is 24mm, that of drift tubes are changed from 18 to 20mm for different sections. The beam envelopes are shown in Fig.3.8. This machine has been operated successfully more than ten years. The special MEBT was designed to realize the beam matching between RFQ and IH-DTL.

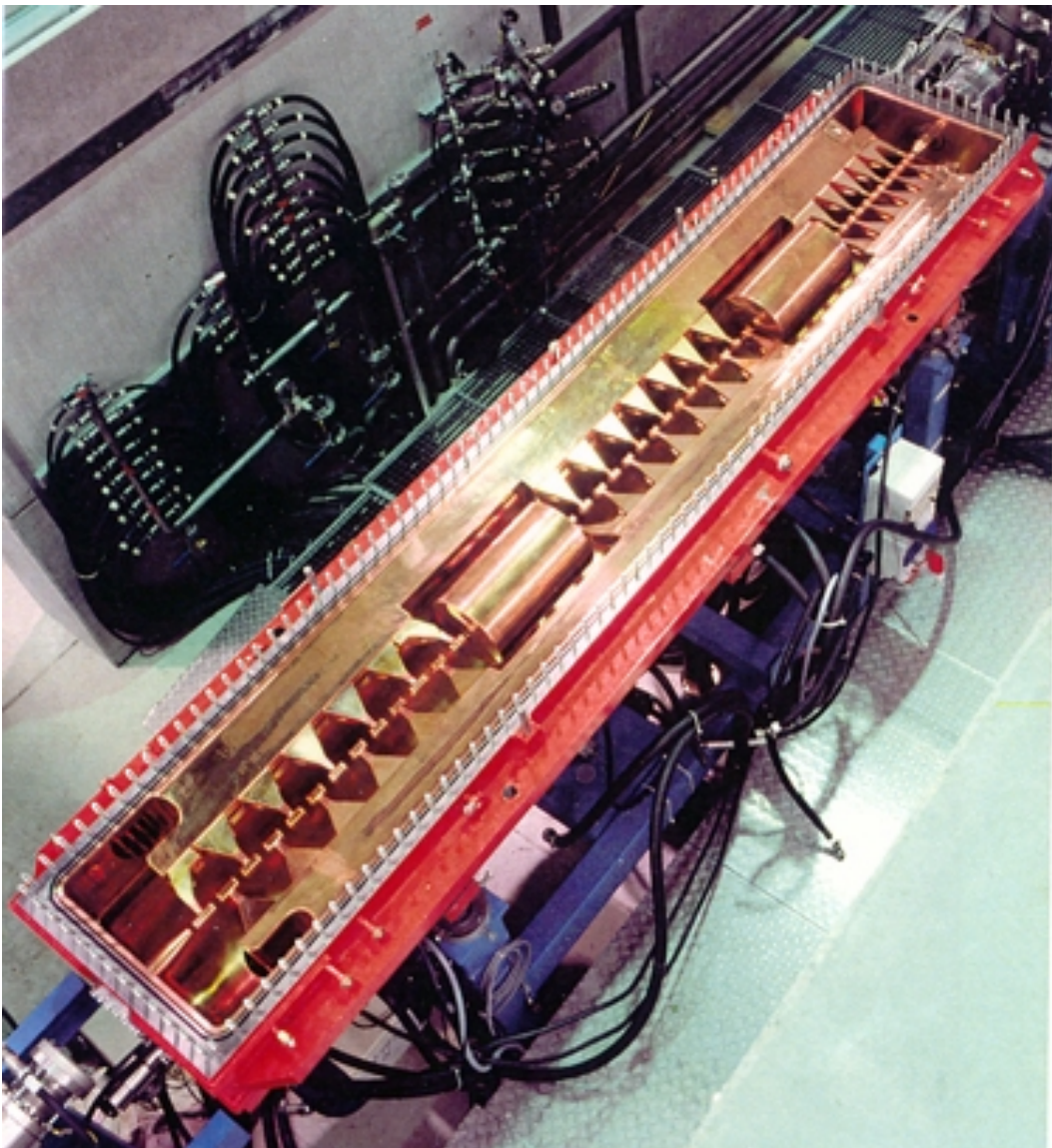


Fig.3.7 IH-DTL structure for GSI HLI project ^[2.1]

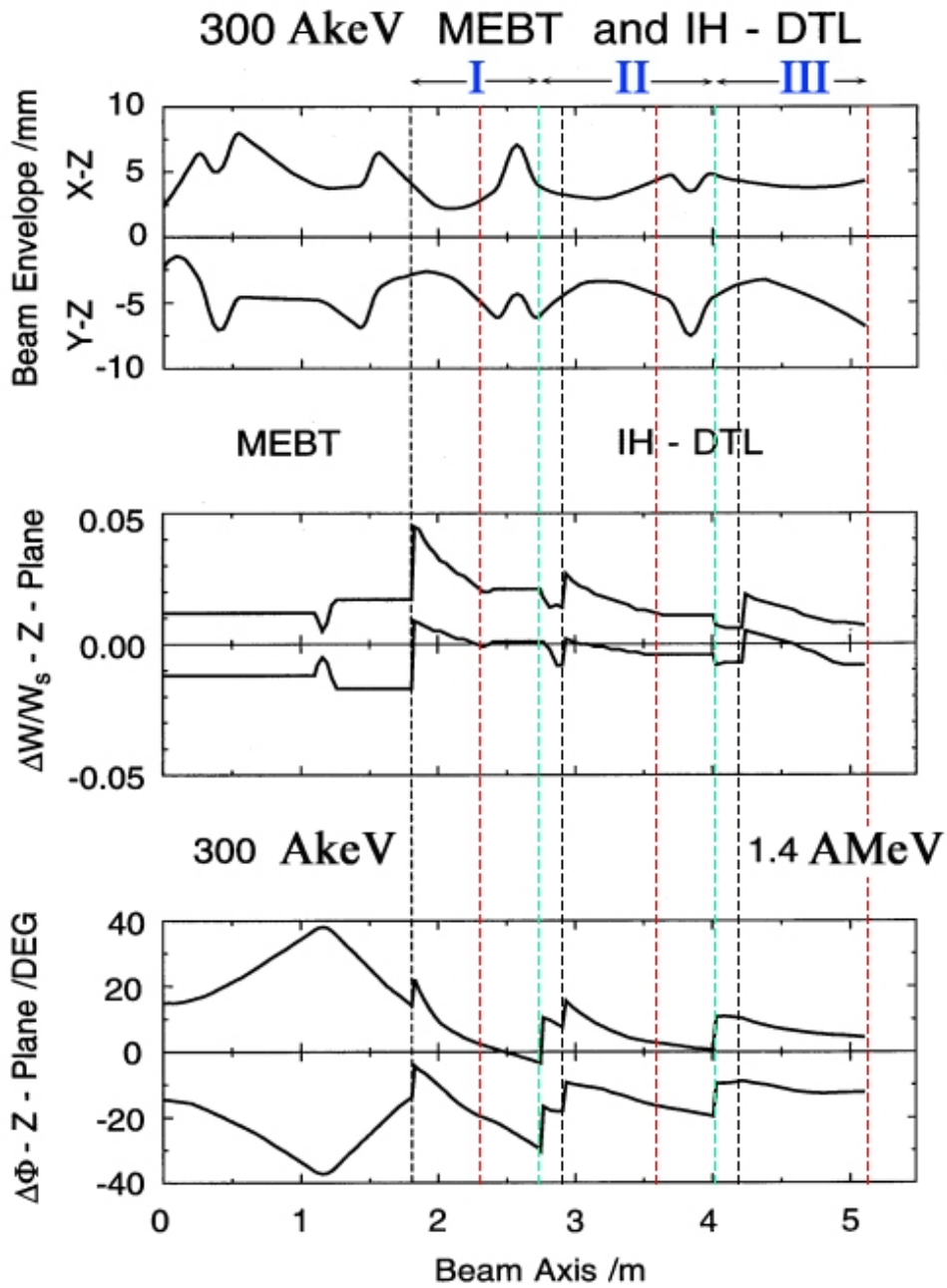


Fig.3.8 Beam envelopes of IH-DTL for GSI HLI project

First black to right: IH-DTL cavity;
 black to red: 0° acceleration section;
 red to green: quadrupole triplet;
 green to black: -30° rebuncher section

The next chapter will present all the design results of IH-DTL linac for Heidelberg cancer therapy project.

Chapter Four

Beam Dynamics of the HICAT IH-DTL

The HICAT linac injector consists of a four-rod RFQ, a short MEFT and of an IH-DTL linac. The RFQ will accelerate proton, oxygen and carbon ions to 400AkeV, the IH-DTL will reach 7AMeV at the exit. This chapter will discuss the beam transport properties in the IH-DTL cavity by using the concept of KONUS beam dynamics and simulation software LORASR.

4.1 The Challenge of the HICAT IH-DTL Design

Comparing to the existing IH-DTL cavities, there are the following topics in the HICAT IH-DTL cavity, which are real big challenge and should be taken into account more carefully in beam dynamics and the IH cavity geometry design.

- RF internal buncher in the RFQ cavity exit
- Very short MEFT design for the beam matching
- Highest operating frequency of IH-DTL cavity to be realized
- Highest effective voltage gain per meter
- IH-DTL with three internal triplets
- Extreme large ratio of cavity length to diameter

RF internal buncher was made by RFQ group at the IAP and is installed at the RFQ cavity end. By the bead pull measurements the effective buncher voltage can be adjusted from 60 to 110kV by changing the stem height. The required phase width $\leq \pm 15^\circ$ can be reached by an optimised buncher voltage. Fig.4.1 shows the buncher structure, Fig.4.2 shows the relation of bunched phase width with the effective bunch voltage^{[4.1][4.2]}.

Photo from A.Bechtold Dissertation

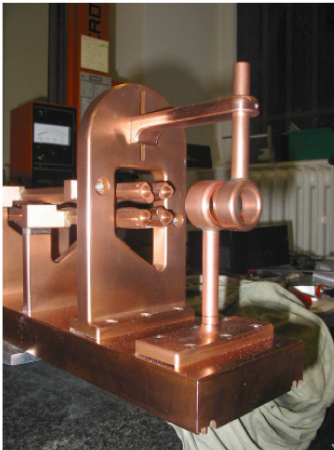


Fig.4.1 RF internal buncher

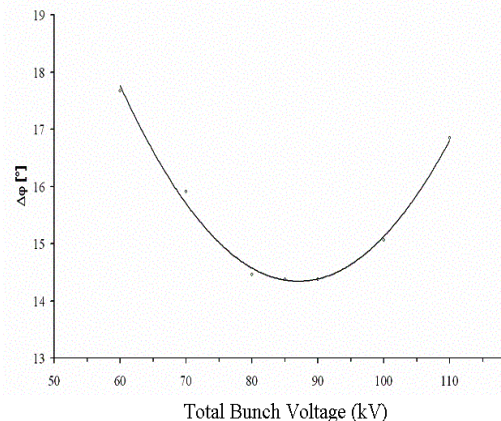


Fig.4.2 Bunched phase width vs. effective bunch voltage^[4.2]

The table 4.1 lists the parameter of the RFQ internal buncher^[4.3]. New MEBT geometry is shown in Fig.4.3. Table 4.2 shows the parameters of quadrupole doublet (see Fig.1.4 and Fig.4.3).

Table 4.1 The main parameters of the RFQ internal buncher^[4.3]

Distance between RFQ and first drift tube (mm)	40.8
First drift tube length (mm)	16.9
First gap length (mm)	7.0
Second tube length (mm)	13.4
Second gap length (mm)	7.0
Drift length between second gap and RFQ end(mm)	10.7
Thickness of RFQ end cover (mm)	27.3

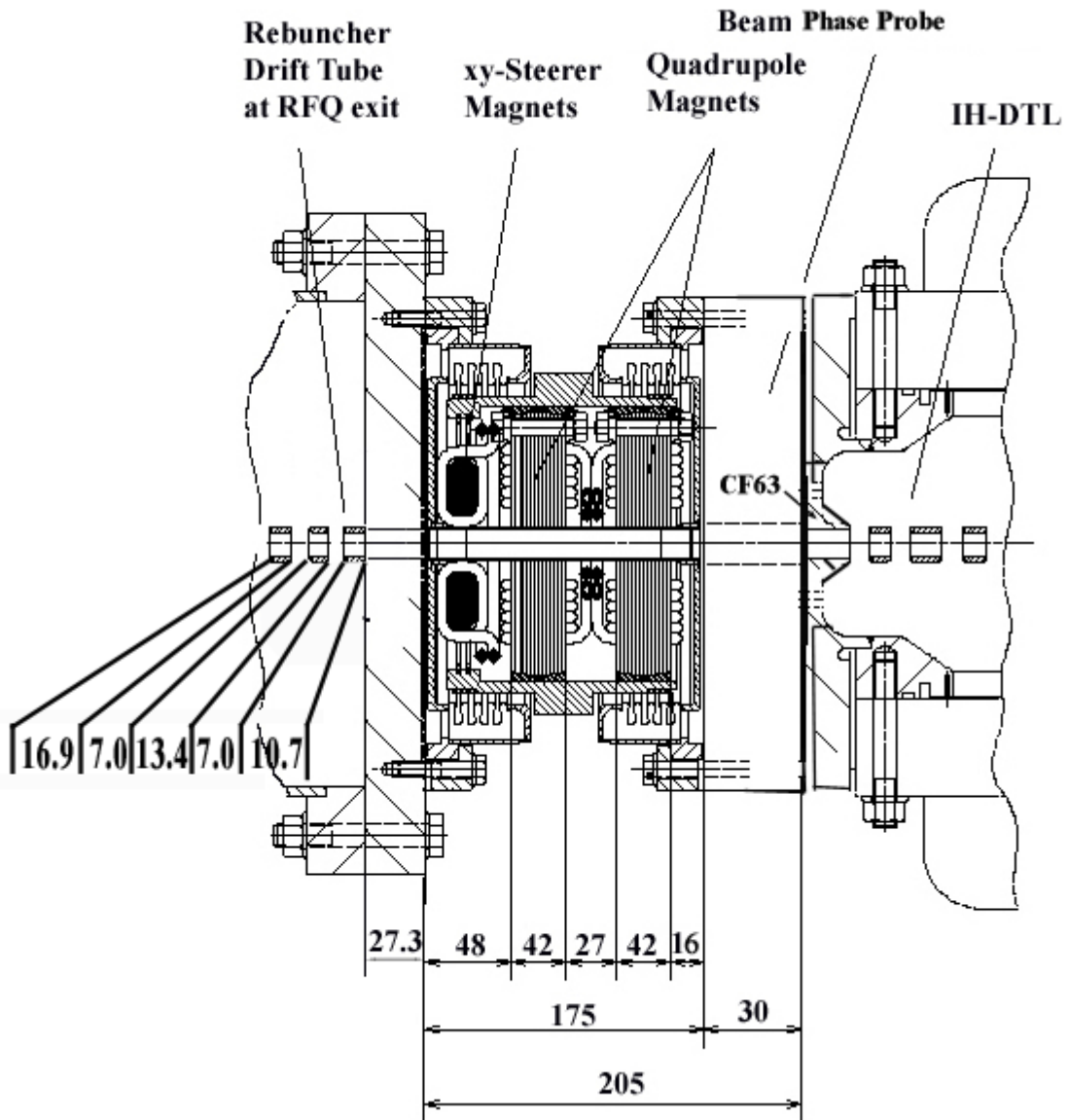


Fig.4.3 New MEBT geometry^[4.3]

Table 4.2 The parameters of the quadrupole doublet (QD)
(see Fig.1.4 and Fig.4.3)^[4.3]

	Mech. Length(mm)	Effective length(mm)
From RFQ Exit to QD11	48.0	44.0
QD11	42.0	50.0
From QD11 to QD12	27.0	19.0
QD12	42.0	50.0
From QD12 to IH entrance	16.0	12.0

4.2 The LORASR Beam Dynamics Simulations

Since the project was proposed, the pioneering designers were U.Ratzinger, S.Minaev and B.Schlitt^[1.27-29]. According to the experience of the existing IH-DTL projects, safety RF operation and higher RF efficiency, the electric field distributions along the structure is always kept the uniform, then the gap effective voltage distributions, drift tube and gap parameters can be predicted and set to the LORASR software to make the simulation. The initial design result of LORASR beam dynamics for the IH-DTL injector can be referenced in GSI internal report in 2000^[4.4]. Based on this design, one 1:2 scaled IH-DTL model cavity was manufactured for the tuning investigation and the final real effective voltage distributions of the beam dynamics design.

4.2.1 The Determination of Effective Gap Voltage Distributions

The RF tuning of the 1:2 scaled IH-DTL cavity was done at the RF laboratory of IAP in Frankfurt University in the summer of 2002. Six different tuning concepts have been used for approaching the effective gap voltage of IH-DTL cavity^{[4.4][4.5]}. The detailed discussions about the tuning concepts will be presented in the next chapter. Fig.4.4a shows the length changes of drift tubes (orange) and gaps (blue). Fig.4.4b shows the gap capacitance of the drift tube structure per unit length before and after tube changes, which are calculated by the equations (2.3) and (2.4). (See Fig.2.3., r_a is the radius of drift tube, factored by 1.450). It is changed from 38pF/m at entrance to 14pF/m at exit of IH-DTL. Fig.4.4c shows the on axis transit time factors for every gap as simulated by LORASR. Fig.4.4d and Fig.4.4e show the measured field distribution and voltage distribution, respectively. Fig.4.4f shows the effective voltage difference from the original design.

The sum of every section effective voltage deviation divided by the total effective cavity voltage gain are listed on the top of Fig.4.4f. Comparing the

designed against the measured effective voltage distribution in Fig.4.4f , the maximum difference occurred around the last magnetic quadrupole lens. Meanwhile from the Fig.4.4b, we can see decreasing the gap length has enhanced the capacitance in this area. It is very difficult to reach the designed effective voltage at these gaps, especially in gaps 37 and 40.

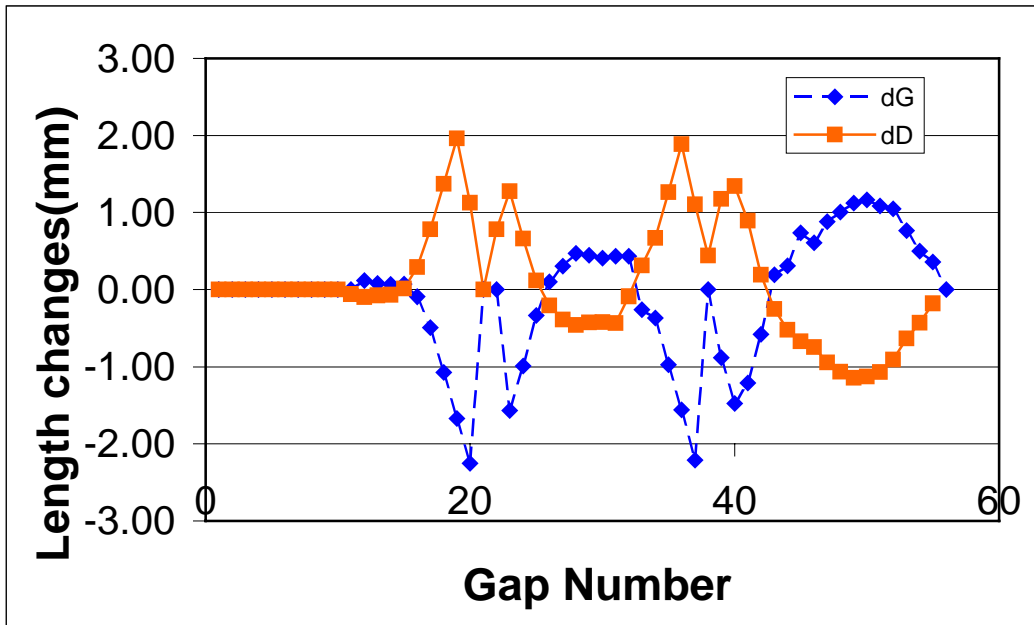


Fig.4.4a The length changes of drift tubes and gaps

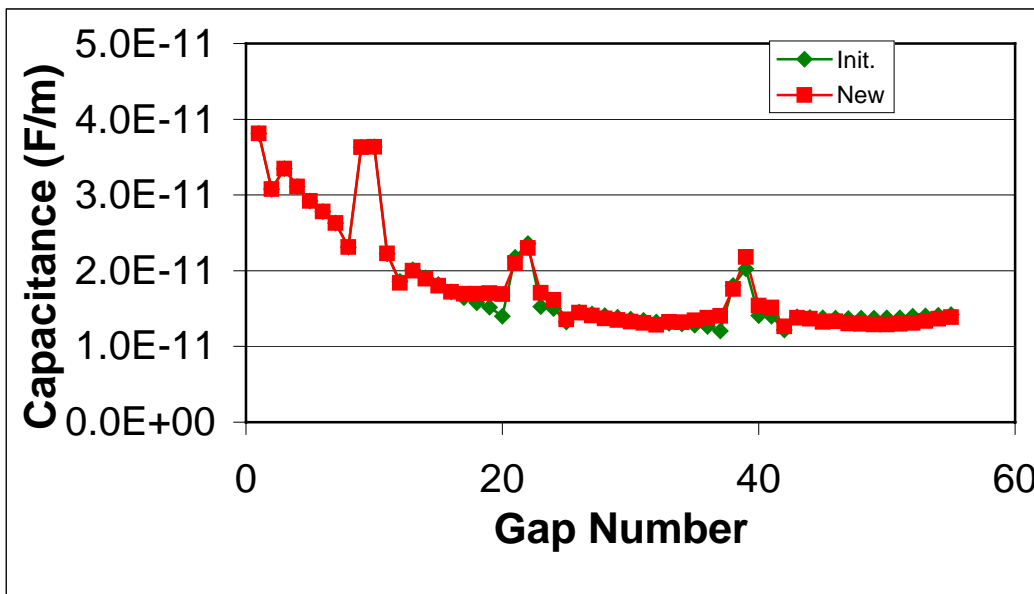


Fig.4.4b Capacitance of the drift tube structure per unit length

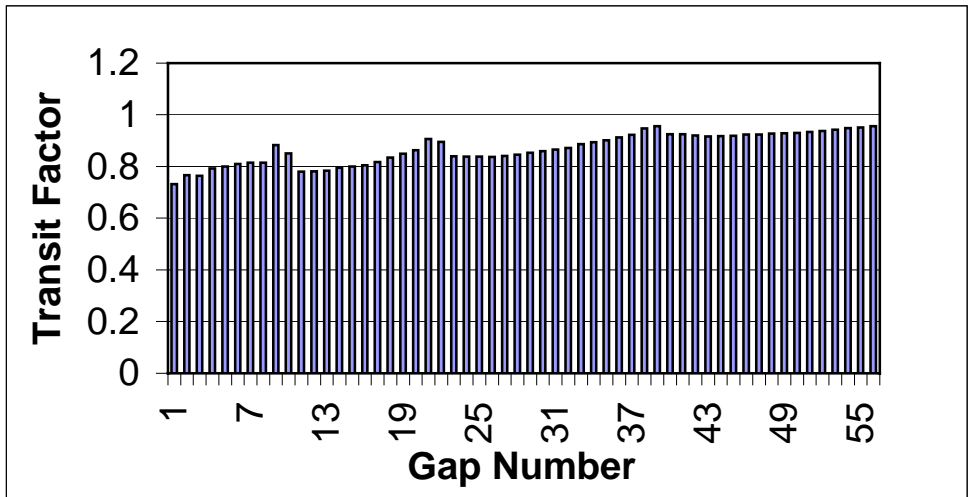


Fig.4.4c New transit time factor distribution

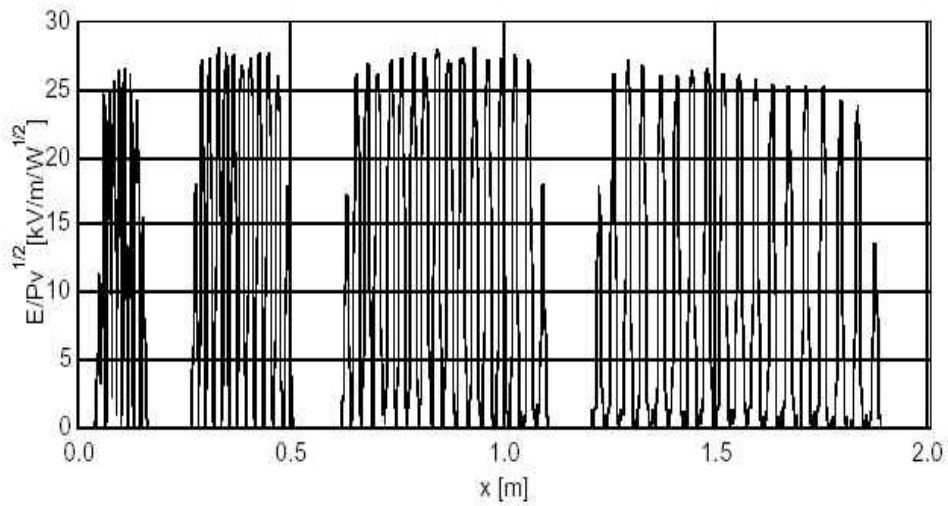


Fig.4.4d Measured electric field distribution

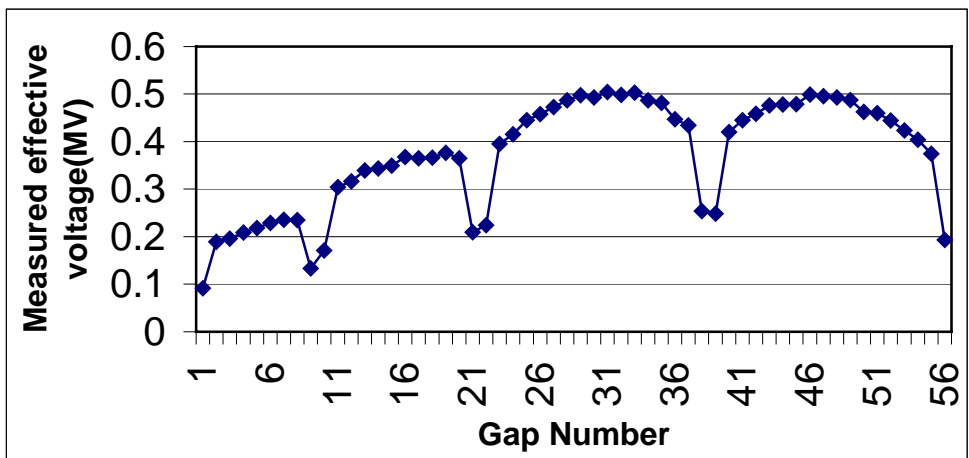


Fig.4.4e Measured effective voltage distribution

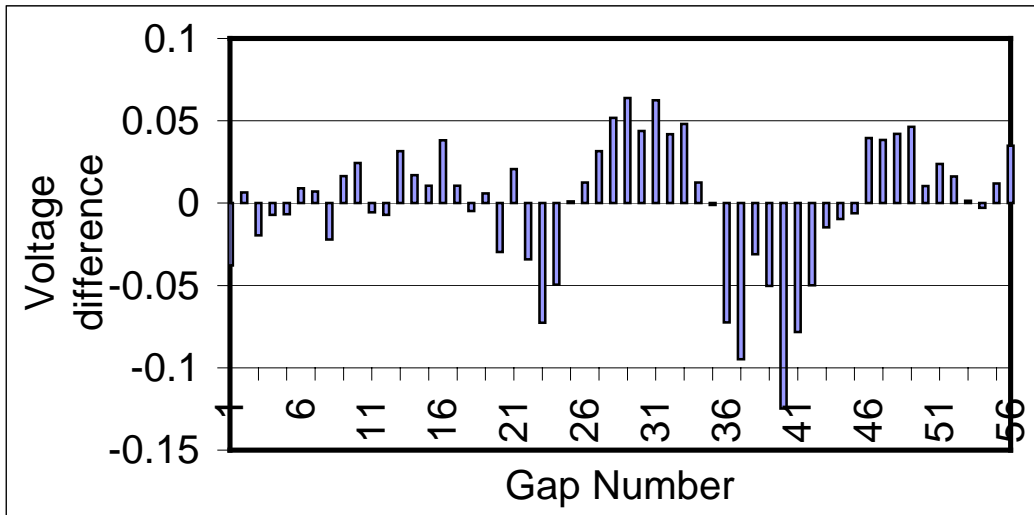


Fig.4.4f Effective voltage difference between theory and experiment

The Figure 4.4f shows the reason why the designed effective voltage around the last magnetic triplets was modified to optimise the LORASR redesign. Figure 4.5 shows the measured and new designed effective voltage distributions. The new effective voltage distribution will be realized for the IH-DTL power cavity.

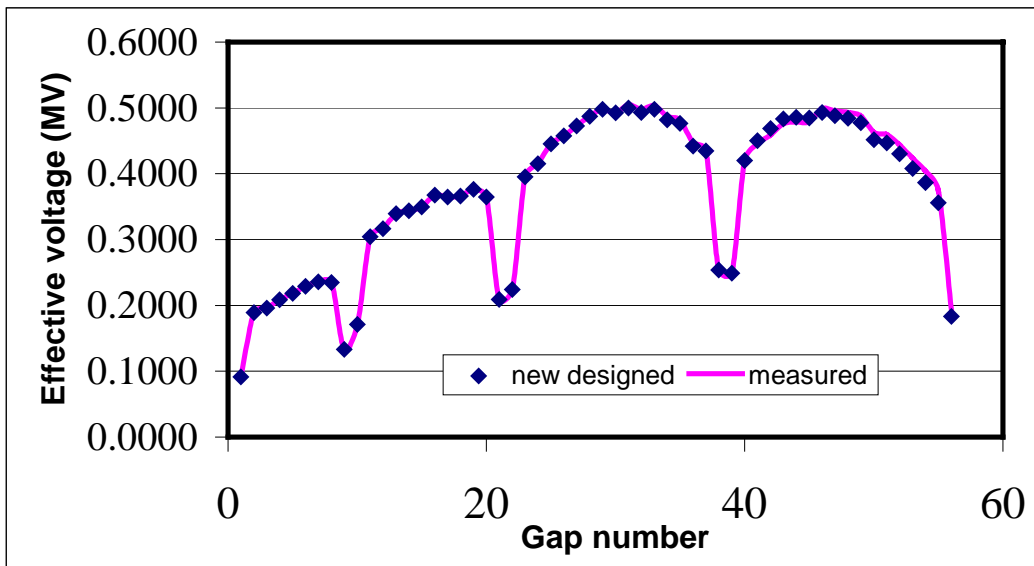


Fig.4.5 New designed effective voltage distributions

4.2.2 The Input Particle Distribution of the IH-DTL

The LORASR beam dynamics simulation for the IH-DTL injector has been designed for a homogeneous input beam and for actual particle distributions at the exit of RFQ accelerator. The input particle distribution for the IH-DTL is

shown in Fig.4.6, which was provided by Dr. A.Bechtold, as result of the simulations with the PARMTEQ code. It includes 3949 particles, only 51 particles are lost in the RFQ, the particle distribution is located at the middle of the first buncher drift tube. According to these parameters shown in figure 4.6, the longitudinal and transversal elliptical parameters for LORASR are listed in table 4.3.

Table 4.3 The input beam parameters of IH-DTL

Longitudinal emittance (95%)	1.57AkeVns
Transversal emittance (95%)	x-x': 0.58mrad y-y': 0.58mrad
Ellipse orient (see Fig.4.6)	x: -0.93mm y: 2.80mm Φ : -16.5°
Pulse center	Input energy: 1.200MeV Phase: 0°

RFQ GSIM, F=216.816 MHz, U=70KV
NCELL=219 , NPOINT=3949 , NTOTAL=4000 , lin=0 mA

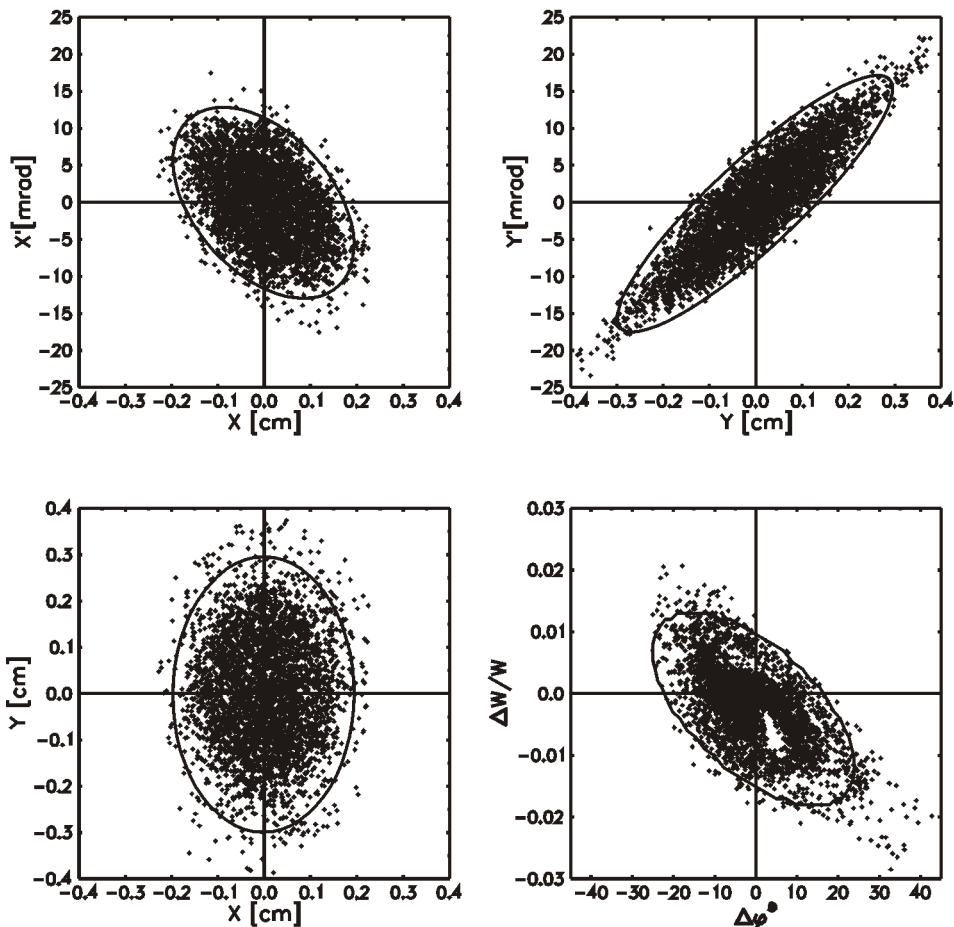


Fig.4.6 RFQ output beam parameters at the middle of first drift tube

The detailed LORASR input data set for the IH-DTL cavity is referenced in IAP-ACCC-181203. All parameters are explained in the literature^[4,6]. In order to shorten this thesis, only the simulation results for the real RFQ output particle distribution of PARMTEQ will be presented in the following.

4.2.3 The IH-DTL Simulation Results of LORASR

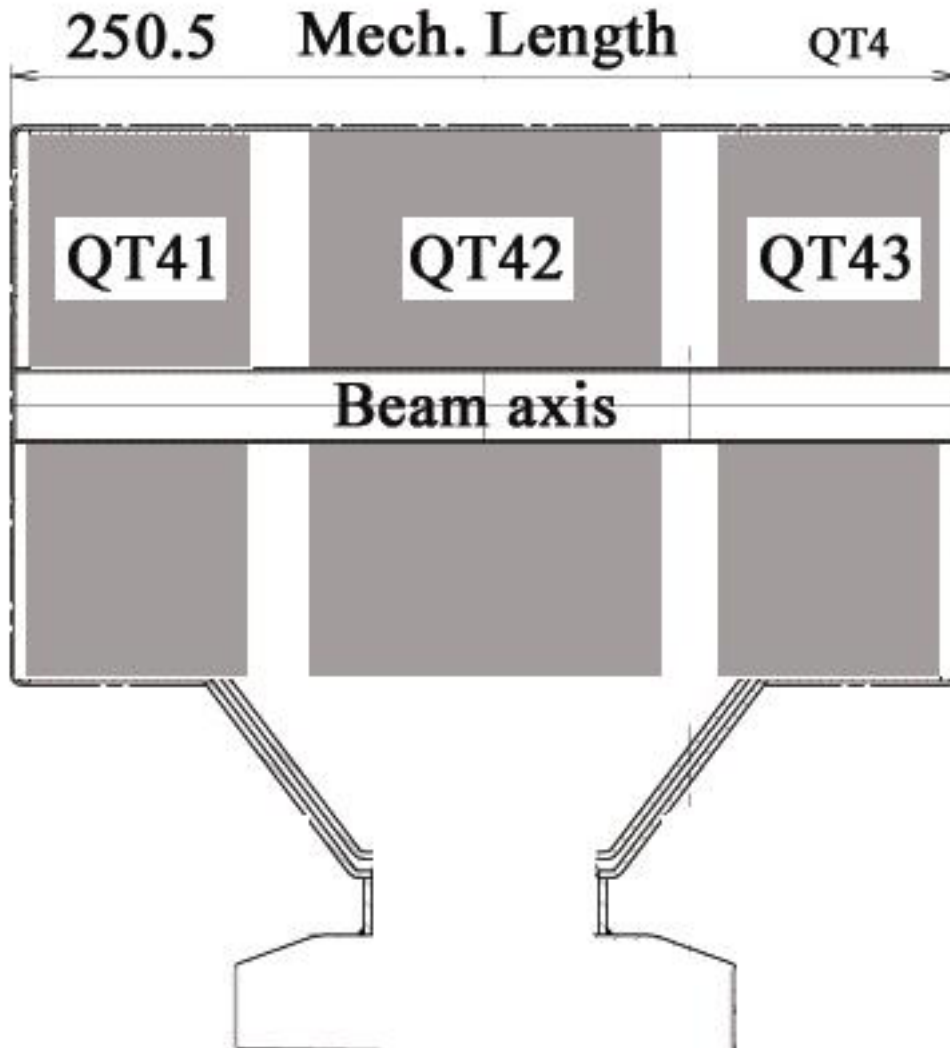


Fig.4.7 Geometry parameters of triplet

In order to realize the beam matching from the RFQ into the IH-DTL, a quadrupole doublet is used. The geometry was shown in Fig.4.3 and table 4.2, the magnetic gradients for QD11 and QD12 are 8280Gauss/cm and 8540Gauss/cm, respectively. The parameters of magnetic quadrupole triplet lenses for the IH-DTL are listed in table 4.4^[4,3]. It lists also the needed magnetic gradients of triplet lenses. The beam aperture diameter of the triplets is 18mm. Fig.4.7 shows the geometry of triplet QT4, all other triplets used in the IH-DTL have similar geometry.

Table 4.4 The triplet lenses for the IH-DTL^[4.3]

	Eff. Focal Lengths (mm)	Eff. Space	Mech. Length (mm)	Gradient (T/m)
QT2	49/74/49	20/20	236.9	97.20/99.50/97.20
QT3	56/88/56	20/20	264.0	85.70/96.00/87.50
QT4	49/88/49	20/20	250.5	102.50/106.30/102.50
QT5	56/104/56	20/20	Out of IH cavity	92.50/90.50/92.50

After editing the needed parameters for the IH-DTL in the LORASR code, the simulations were done starting at the RFQ internal buncher and done until to the injection point of the synchrotron. The magnetic gradient for every doublet and triplet is optimized as well as the RFQ internal buncher effective voltage. Finally the following design result is optimized at the effective bunch voltage 90.8kV, all the parameters of the quadrupole triplets have been optimized to get the lowest longitudinal emittance.

Fig.4.8a and b show the transverse envelopes (98% , 3949 particles) of IH-DTL, it is simulated from the PARMTEQ distribution at the RFQ exit. Fig.4.8c shows the longitudinal phase width of 98% bunched particles along the beam axis. From Fig.4.8a and Fig.4.8b, one can see the maximum beam size (12.3mm) is at the entrance of the quadrupole doublets in yz direction. The output beam of RFQ accelerator in yz direction is defocused so rapidly. But the inner diameter 18mm of matching quadrupole doublets can stand the actual beam size (12.3mm) at this position. Fig.4.8c shows 98% phase envelopes along the Φ -z plane. Fig.4.9 tells the energy spread and longitudinal phase envelopes against the structure defined synchronous particles. The blue line in Fig.4.9b shows the phase distribution of central particle, which is also very important ideas of KONUS beam dynamics. Fig.4.10 gives the results of normalized emittance growth, which is less than 30%.

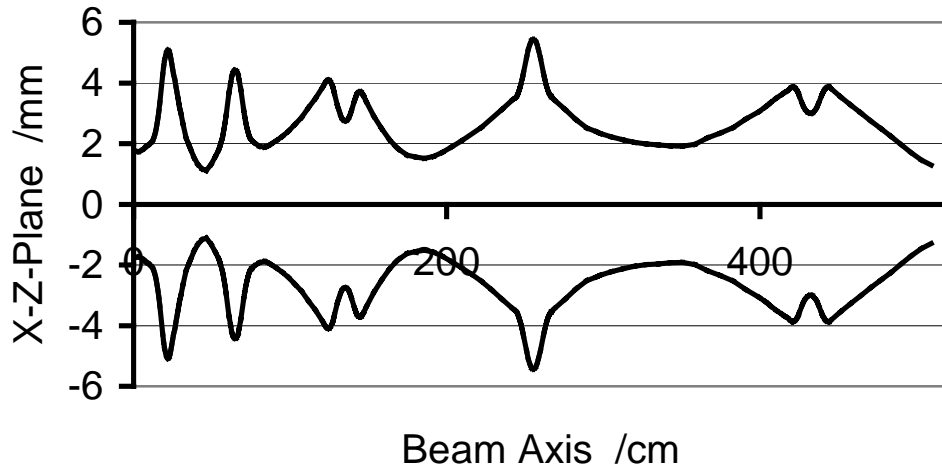


Fig.4.8a 98% envelopes (3949 particles) in xz direction

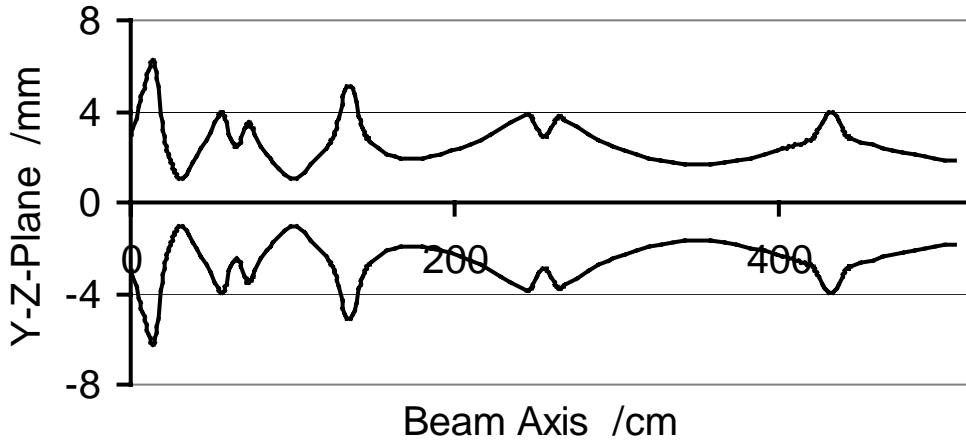


Fig.4.8b 98% envelopes (3949 particles) in yz direction

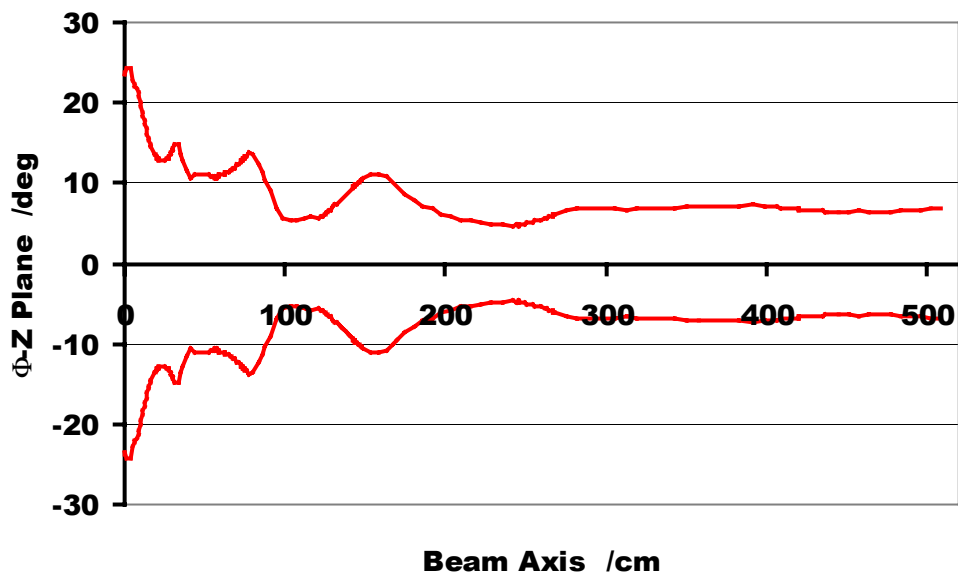


Fig.4.8c 98% envelopes at Φ -z plane. It shows the 98% phase width of the bunch along the beam axis.

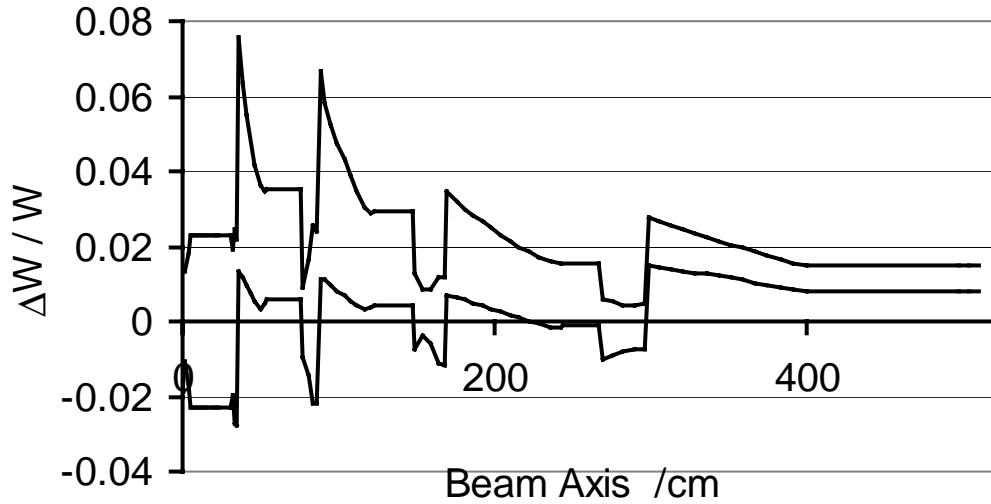


Fig.4.9a Longitudinal envelopes (98%,3949 particles)

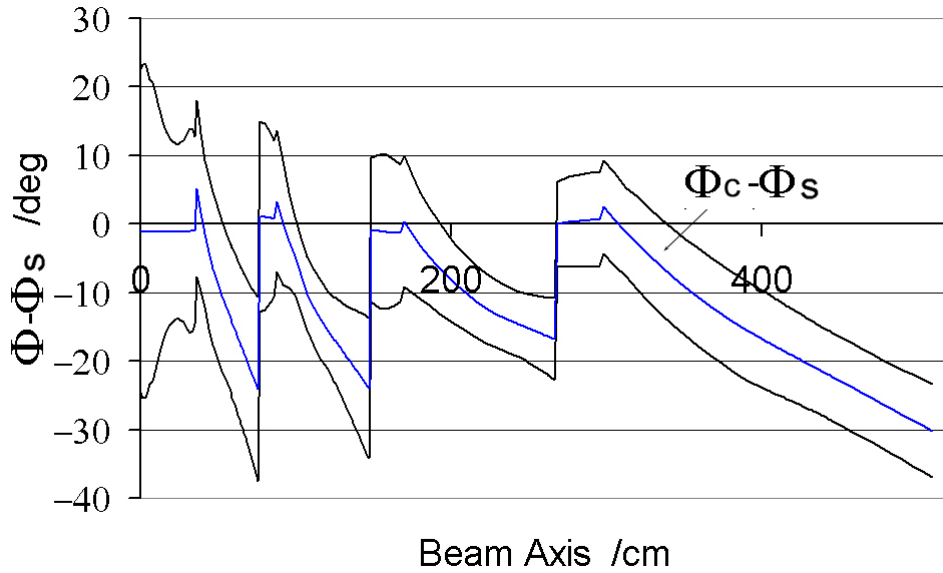


Fig.4.9b Longitudinal phase envelopes along the IH cavity (98%)
(plotted against the synchronous particles)

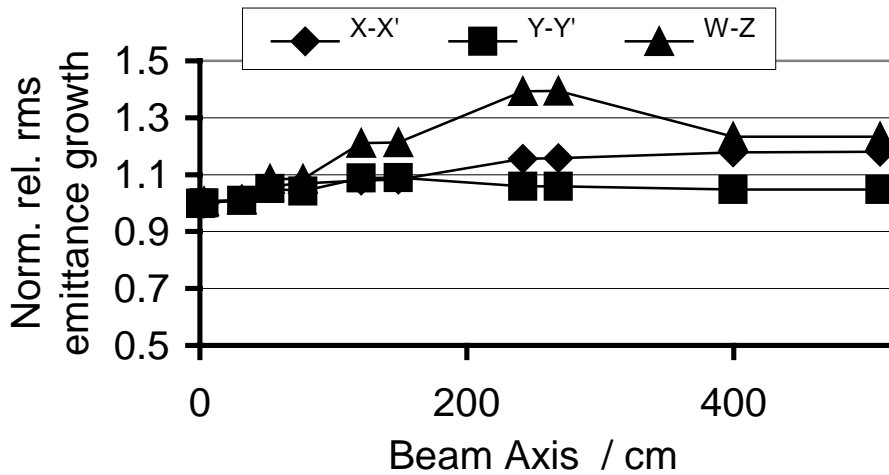


Fig.4.10 Normalized relative rms emittance growth.

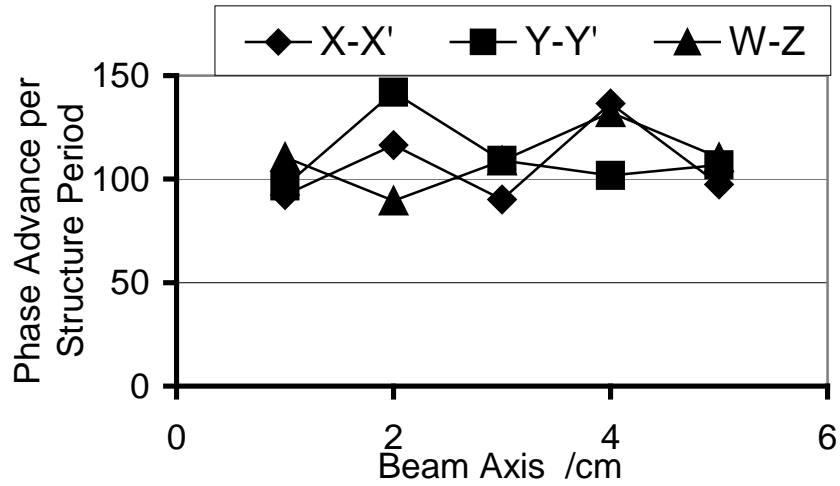


Fig.4.11 Phase advance per structure period.

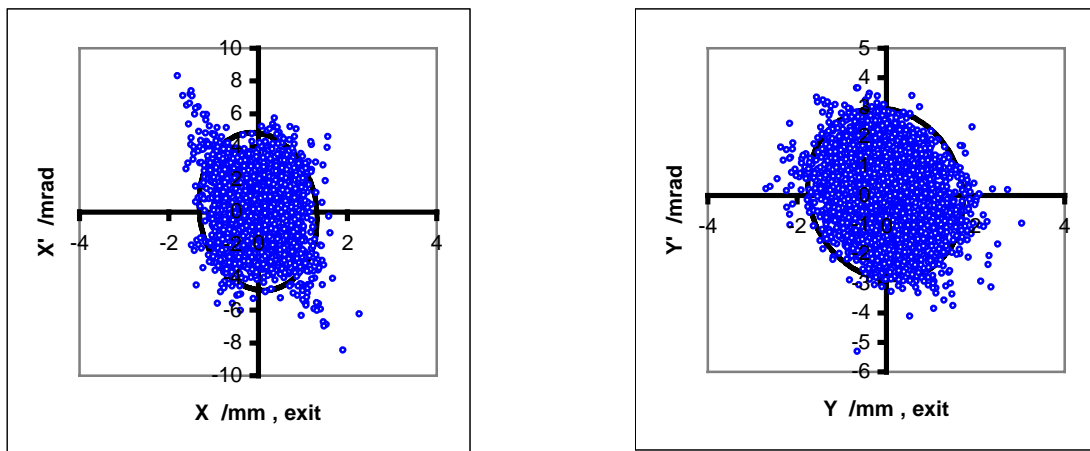
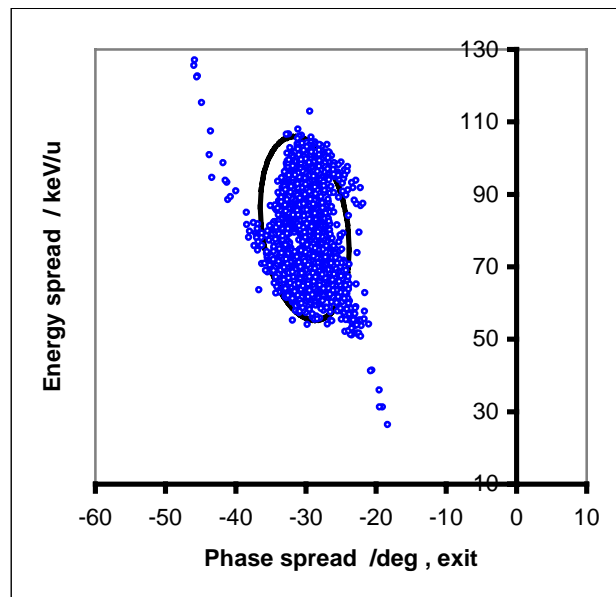


Fig.4.12 Normalized output emittance (with 95% particles)
 $\epsilon_x=0.77$ mmmrad, $\epsilon_y=0.62$ mmmrad



Output emittance $\epsilon_z=2.00146$ keV/u*ns

Fig.4.13 95% output longitudinal beam emittance ellipse for an injected emittance of 1.57AkeV*ns

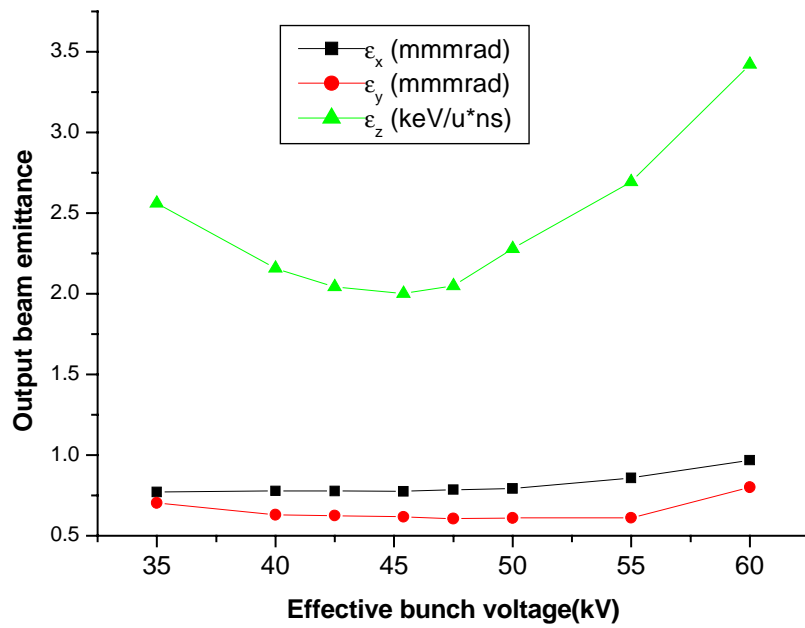


Fig.4.14 Dependence of the emittance values on the RFQ- internal buncher voltage

From last figure, the best effective bunch voltage should be 45.4kV. But when the effective bunch voltage is changing from 42.5kV to 47.5kV, the output emittance in three direction are changed not so much, that means if the effective bunch voltage is set around 45.4kV, it has the advantage to get less output emittance.

4.3 Motivation for a Redesign of the Buncher Drift Tubes

LORASR software is very suitable to simulate the transit time factor for larger D/L (tube length/periodic length) and smaller g/Φ_1 (gap length/inner diameter of drift tubes). Larger transit time factor means a smaller bunch voltage amplitude. From last section, the dynamics design shows the best effective bunch voltage of 45.4kV. From the design of A.Bechtold, the diameter of drift tubes is 2.0cm. The Fig.4.15a and b show the beam transport from the output of RFQ to the exit of doublet. The beam sizes are much smaller than 20mm, it allows to decrease the inner diameter of bunch drift tubes. The distance from the middle of the first bunch drift tube to the entrance of the doublet is 73.85mm (see table 1, $73.85=16.9/2+7.0+13.4+7.0+10.7+27.3$), the diameter of the beam in x direction is less than 4mm, while the beam diameter in y is less than 10mm. The suggested buncher tube inner diameter is 15mm. Due to the short periodic length and larger inner diameter of RFQ internal buncher drift tubes, it is better to use the formula (2.13) and (4.1) to simulate the transit time factor of thick walled drift tubes.

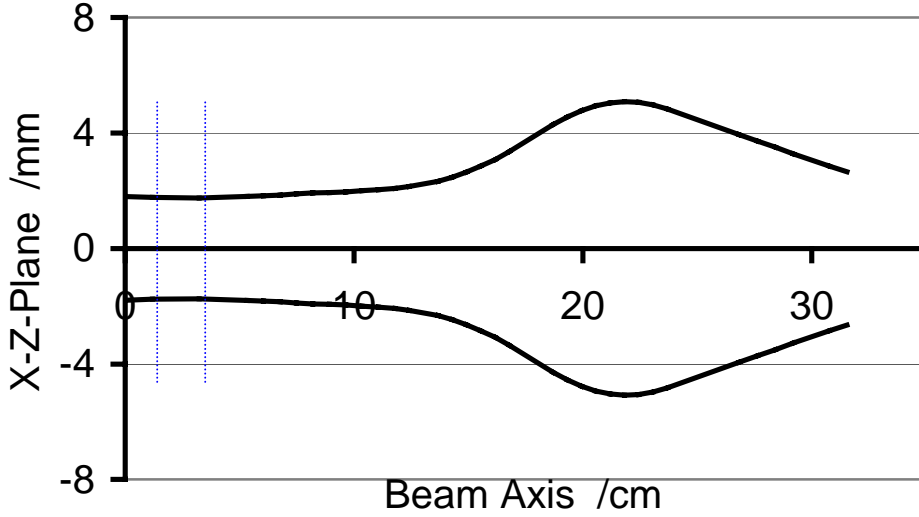


Fig.4.15a

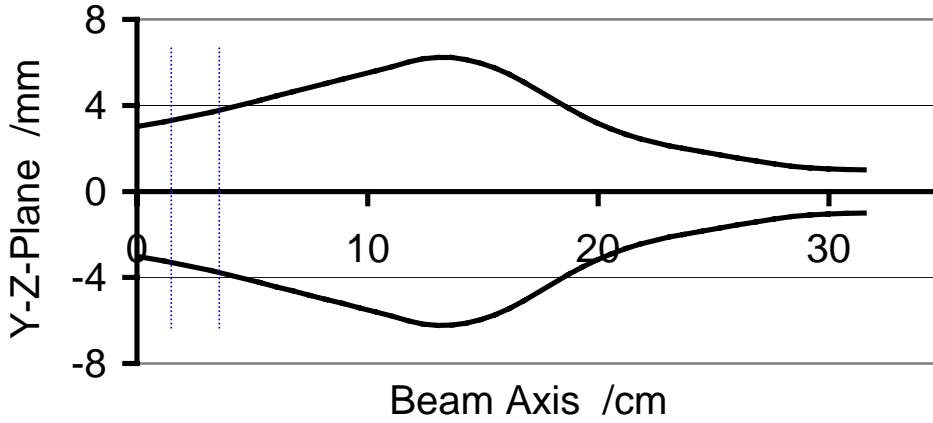


Fig.4.15b

Fig.4.15 Beam envelopes from the first drift tube center of RFQ internal buncher to the exit of doublet
 (a: x-z, b: y-z, two dot lines are first (1.175cm) and second (3.235cm) bunch gap center positions)

$$\beta\lambda = 0.04055, g = 0.007, g_c = g + 0.85\rho_i = 0.008275, \rho_i = 1.5 * 10^{-3} \text{ m}$$

$$\gamma = \frac{931.448 + 0.4}{931.448}, \quad k = \frac{2\pi}{\gamma\beta\lambda}, \quad \frac{\sin(\pi g_c / \beta\lambda)}{\pi g_c / \beta\lambda} = 0.9329$$

$$TF = \frac{J_0(2\pi a / \lambda) I_0(kr) \sin(\pi g_c / \beta\lambda)}{I_0(ka) \pi g_c / \beta\lambda}, \quad V_a = \frac{V_{eff}}{TF(r=0)} \quad (4.1)$$

Here, a is the inner radius of the bunch drift tube, ρ_i is the chamfer radius of drift tubes, $J_0(2\pi a / \lambda)$ is the Bessel function and $I_0(kr)$, or, $I_0(ka)$ is the modified Bessel functions of order zero, V_a is the bunch voltage amplitude. Table 4.5 lists transit

time factors at different radius r for three different inner diameters Φ_i of buncher drift tubes. Fig.4.16 shows the buncher drift tubes geometry. The chamfer radius is 1.5mm as discussed before, the suggested tube thickness is 4mm.

Table 4.5 Transit time factors at different radii and resulting bunch voltage amplitude at a fixed $V_{\text{eff}}=45.4\text{kV}$ for different tube diameters

Φ_i (mm)	$\text{TF}_{(r=0)}$	$\text{TF}_{(r=3\text{mm})}$	$\text{TF}_{(r=6\text{mm})}$	V_a (kV)
20.0	0.550	0.580	0.676	82.6
15.0	0.682	0.719	0.838	66.6
12.0	0.760	0.802	0.933	59.8

Table 4.5 shows that the on axis transit time factor for a tube with a inner diameter of 15mm is about 1.24 times higher than that for a tube with a inner diameter of 20mm. To achieve 45.4kV effective bunch voltage, the bunch voltage amplitude for a 15mm tube is also about 16kV lower than that for a 20mm inner diameter tube. With respect to the beam envelopes (Fig.4.15a and 4.14b), an inner diameter of 15mm tube seems ok. With respect to the errors in field simulation and analysis, the large tube diameters are not treated well enough in LORASR, so we would like to suggest the smaller tube diameter for a final realization also for this reason.



Fig.4.16 Buncher drift tube geometry (chamfer radius 1.5mm, tube thickness 4mm)

Chapter Five

The RF tuning of the IH-DTL 1:2 model cavity

The main task of the RF tuning of the 1:2 scaled IH-DTL model cavity was to demonstrate that this design could be realized. All the RF tuning results and concepts are presented and discussed in this chapter. The motivations for measurements were the following:

- A: Coupling of the fundamental cavity mode along the structure
- B: Balancing of contributions from different tuning concepts to approximate the design voltage distribution in a technical realistic way
- C: Recalculation of the effective gap voltage distribution to get an acceptable approximation after one or two iterations
- D: Fine tuning concepts for cavity operation.

5.1 Measuring System for the IH-DTL Model Cavity

The measuring system is composed of the IH-DTL model cavity, HP 8719C Network analyser, bead pull driving system, in/out coupling loop, GPIB-422CT interface and Macintosh computer. The IH model cavity is shown in Fig.5.1.1.

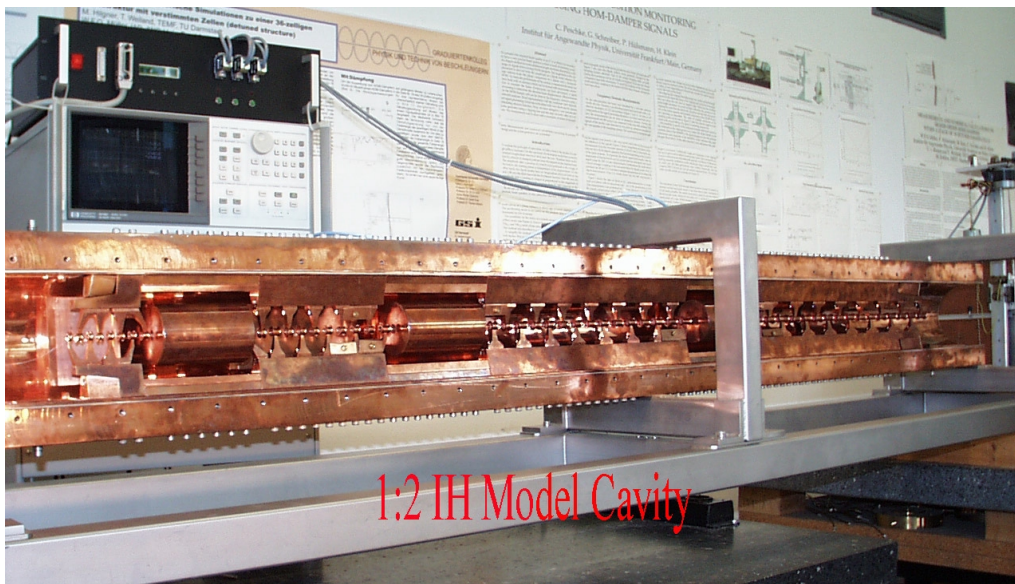


Fig.5.1.1 IH model cavity for Heidelberg Cancer Therapy Project

The first version of bead pull measuring software was written by C. Peschke^[5.1] and further developed at the first half of 2002 based on Igor Pro Macintosh version and Macintosh computer. It includes the following functions: the ground level correction of perturbation phase, electric field distributions

along longitudinal gaps or position or measuring points, gap voltage distribution, gap voltage difference from theoretical design, shunt impedance, data saving and diagram displaying functions. The basic of data processing will be discussed in the following subdivision.

5.1.1 The Theory of Bead Pull Measurement

Based on the general perturbation theory for RF resonant cavity^[5.2], we assume the quality factor of cavity is Q , stored energy W , Power losses P , angular frequency ω , radius of bead ball r_1 , being measured electric field E and magnetic field H , the relative permittivity ϵ_r and permeability μ_r , the shifted frequency $\Delta\omega$ caused by perturbation:

$$\frac{\Delta\omega}{\omega^2} = \left[\frac{-1}{QP} \cdot \pi \cdot r_1^3 \right] \cdot \left[\epsilon_0 \cdot \frac{\epsilon_r - 1}{\epsilon_r + 2} \cdot E^2 + \mu_0 \cdot \frac{\mu_r - 1}{\mu_r + 2} \cdot H^2 \right], \quad (5.1.1)$$

For small phase shift angels:

$$\Delta\Phi = \frac{2Q}{\omega} \cdot \Delta\omega \quad (5.1.2)$$

At last one can get:

$$\Delta\Phi = \left[\frac{-2\omega}{P} \cdot \pi \cdot r_1^3 \right] \cdot \left[\epsilon_0 \cdot \frac{\epsilon_r - 1}{\epsilon_r + 2} E^2 + \mu_0 \cdot \frac{\mu_r - 1}{\mu_r + 2} H^2 \right] \quad (5.1.3)$$

Two cases are of interests:

(i) Dielectric perturbing bead:

$$\mu_r=1, \text{ then } \Delta\Phi = \left[\frac{-2\omega}{P} \cdot \pi \cdot r_1^3 \right] \cdot \left[\epsilon_0 \cdot \frac{\epsilon_r - 1}{\epsilon_r + 2} E^2 \right] = -\omega\alpha_e E^2 / P \quad (5.1.4)$$

where $\alpha_e = 2\pi r_1^3 \cdot \epsilon_0 \cdot \frac{\epsilon_r - 1}{\epsilon_r + 2}$.

(ii) Metallic bead:

$\epsilon_r=\infty, \mu_r=0$ (diamagnetic due to the induced currents), for the IH cavity, the measured magnetic field $H \sim 0$ when bead ball moves on the axis of IH cavity.

$$\Delta\Phi = \left[\frac{-2\omega}{P} \cdot \pi \cdot r_1^3 \right] \cdot \epsilon_0 E^2 = -\omega\alpha E^2 / P \quad (5.1.5)$$

where $\alpha = 2\pi r_1^3 \cdot \epsilon_0$, which can be calibrated by a pillbox cavity. P denotes the RF power losses on the cavity wall:

$$P = \int \frac{1}{2} (H_{\text{surf}})^2 R_{\text{surf}} dA \quad (5.1.6)$$

where A =surface area, R_{surf} surface resistance of the cavity.

From the equations (5.1.4 and 5.1.5), dielectric and metallic perturbation balls are all suitable for IH cavity measurements. The shifted phase $\Delta\Phi$ (in degree) caused by a perturbation ball can be measured directly by HP8719C network analyzer; one can get the electric field distribution along the cavity

structure by moving a perturbation ball along the beam axis.

$$\frac{E(z)}{\sqrt{P}} = \left(\frac{-\Delta\Phi(z)}{\omega \cdot \alpha} \cdot \frac{\pi}{180} \right)^{\frac{1}{2}} \quad (5.1.7)$$

5.1.2 Back Ground Subtraction and Performed Calculations

The perturbation measurement software shows us two ways of ground level correction: one is linear correction; another is manual ground level correction. Linear ground correction is widely used in the pillbox and short cavity measurements, the ground level of measuring perturbing phase is rising up or going down monotonously. By setting the slope of ground line, one can easily correct the perturbing phase. The software will modify the measured data according to new linear ground line. But it is not very suitable for the long cavity measurement, especially for the measurement of the cavity with a large ratio of cavity length to cavity diameter; such a cavity is very sensitive, random noise will influence the measuring accuracy. On the other way, the bead pull measurement couldn't be done very fast to avoid the vibration of the perturbation line, every measuring process takes several minutes, the ground level during the measurement isn't changing monotonously, and even it goes up and down several times. That is the reason to apply manual ground level correction. From the initial measured perturbing phase, one can easily set the ground level line by clicking the ground points, the experimental value between any two ground level points can be corrected linearly. The whole measured RF phase curves will be modified by subtracting the correspondent background. The software finally allows for the integration of measured electric field values to get the gap voltage distribution.

5.1.3 Electric Field Distribution and Gap Voltage Distribution

After modifying the measured RF phase and set the related parameters in the formula (5.1.7), one can get the electric field distribution very conveniently. The perturbation constant should be calibrated for the absolute electric field measurements. For the IH-DTL cavity measurements, we could use the metal perturbation ball to get large rf phase signal and decrease the noise signal. After getting the electric field distribution, one can set the starting and ending points of integration range to get every gap voltage distribution. In order to enhance the integration accuracy, the average electric field strength of neighboring two measuring points is used to make the integration to get every gap voltage. The resulting LORASR transit time factors are used to get the effective gap voltage distribution along the structure. The difference between the measured and

designed effective gap voltage distributions is then reduced by cavity tuning until one gets accepted effective gap voltage distributions. Finally the effective shunt impedance for whole cavity can be deduced from the effective gap voltage distribution.

5.2 Tuning Experience on the Model Cavity

Six different tuning methods will be discussed in this subdivision (see Fig.5.1.1 and Fig.5.2.2). For every tuning method, several examples will be given to show what the effects are. After the IH model cavity components were delivered to Frankfurt University, it was assembled according to the preliminary design parameters. The first measurement was done on 24th of June. The result is shown in Fig.5.2.1a, 5.2.1b, 5.2.1c.

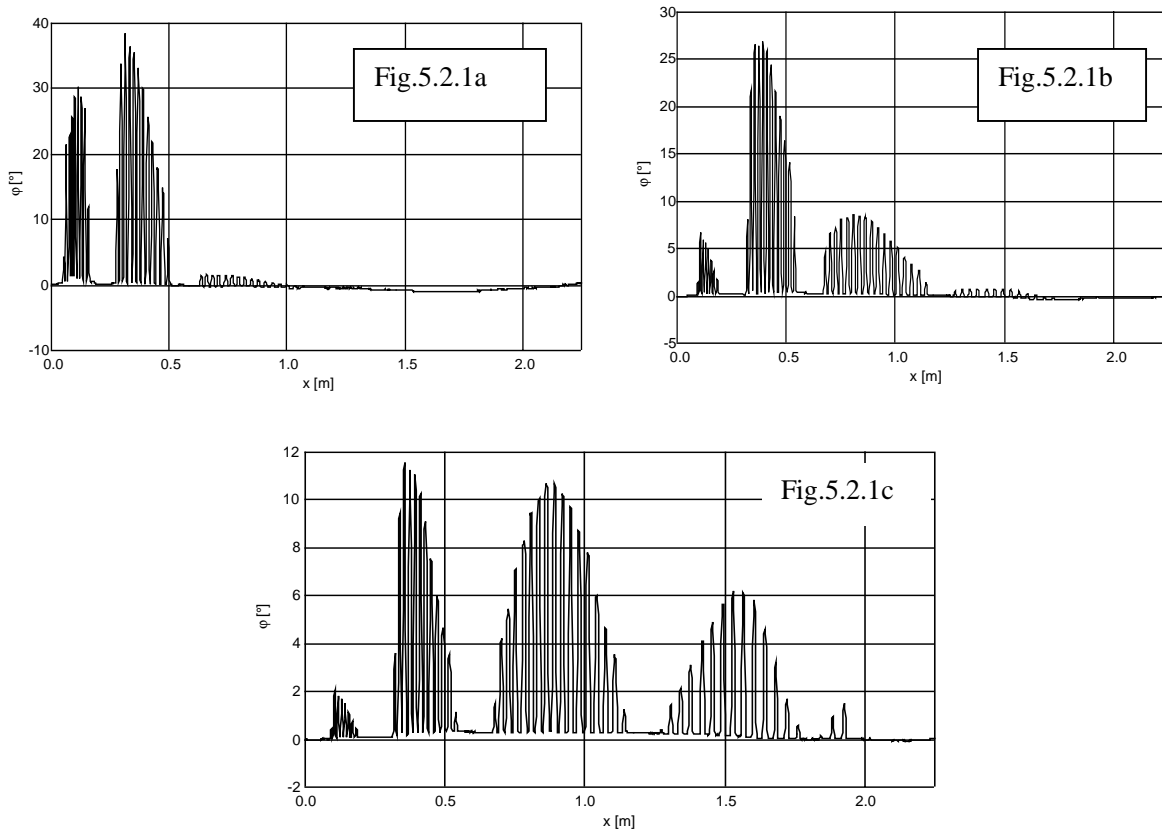


Fig.5.2.1 Phase distribution from the first bead pull measurements
 $f_1=428.73\text{MHz}$ (a), $f_2=436.1\text{MHz}$ (b), $f_3=445.4\text{MHz}$ (c)

The result is unexpected because there is no field distribution along the whole cavity for the fundamental mode f_1 in Fig.5.2.1a. Fig.5.2.1b shows the second harmonic mode distribution. The section 3 has a bit more field and section 4 has very less field. The reasonable explanation is: section 3 and section 4 have less capacitance, the local frequency is higher; Quadruple magnetic lenses have divided the cavity into four drift tube sections, every part having its own

resonance. The coupling between neighboring sections is weak, so the four parts are not resonating together. Fig.5.2.1c shows the phase response for the third cavity resonance. It also proves our explanation.

This phenomenon was never seen so drastically before in the existing GSI HLI and CERN IH cavities. They have only two lenses. It is a bit easier for these three parts to resonate at correct H_{110} mode. But in Heidelberg IH cavity, IH cavity will operate at 216.816MHz that is the highest IH operating frequency, the diameter of the cavity will be smaller than CERN and GSI HLI cavities; meanwhile the effective voltage gain per meter achieves 5.5MV/m, the cavity length is 3.77m, so the ratio of the cavity length to the diameter is the highest ever realized, this makes the cavity voltage distribution very sensitive. The three triplets are needed inside of the IH cavity to give the particles enough radial focusing force. In order to avoid possible RF sparking between magnetic lenses and drift tubes, the triplets are mounted on the ground level, the stems are oriented under 90° against the drift tube structure. The space between triplet and girder is larger, the coupling is so weak, the magnetic flux just goes through these windows, and every part has its own H mode resonance, while the total cavity couldn't be excited by one frequency. That is why the IH model cavity needs some additional blocks to close the windows a little bit between lens and the girder (halter) to increase the RF coupling (so called **lens coupling tuning**). But the electric field in this area should be kept in safe level; otherwise it will make RF sparking.

The six different tuning concepts, which are investigated in the HICAT IH-DTL cavity, are listed here and will be discussed in the following paragraphs individually.

Volume tuning

ACP tuning (Additional Capacitance Plate tuning)

Tube tuning

Lens coupling tuning

Undercut tuning

Plunger tuning

5.2.1 Volume tuning

Volume tuning means a variation of the cavity cross sectional area. It was realized in the HICAT IH-DTL model cavity, which consists of two half shells and one central frame, by installing copper blocks on the walls of the cavity half shells (Fig.5.2.2a).

The four volume tuning blocks are installed in sections 1 and 2. The parameters of the identical two volume tuning blocks in section 1 are

90mm(Length) *105.0mm(Height) * 25.0mm(Thickness). In section 2 the corresponding parameters are 120mm(L)*85.0mm(H)*15.2mm(T) (see Fig.5.2.2b). The volume tuning blocks in sections 1 and 2 are symmetric in both cavity half shells (Fig.5.2.2a and Fig.5.2.2b). The curvature of these blocks corresponds to the half shell radius $R_{cav}=68.0\text{mm}$. The volume blocks in section 2 are installed close to first magnetic quadrupole lens. The longitudinal positions of the volume tuning blocks can be seen from Fig.5.2.2b.

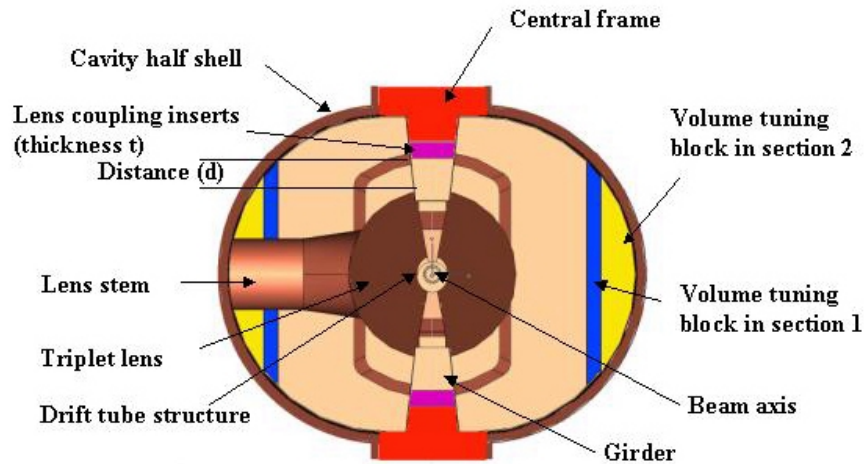


Fig.5.2.2a Cross sectional view of IH model cavity

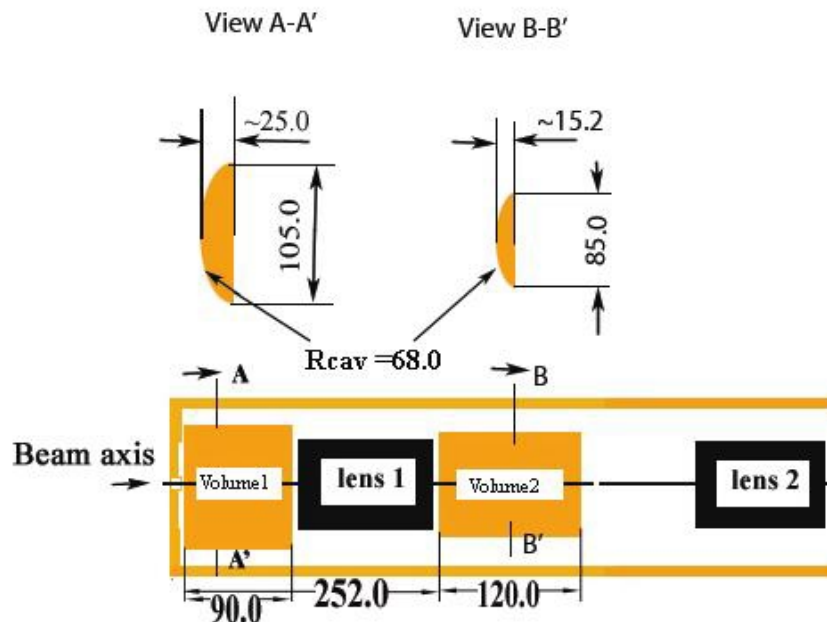


Fig.5.2.2b Volume tuning blocks position and cross section at the low energy end of the cavity

Fig.5.2.3a and Fig.5.2.3b show the bead pull measurement without and with

volume tuning in section 2. The volume tuner blocks in section 1 were shown in Fig.5.2.2a. The volume tuning blocks in section 2, which is 200(L)*85.0(H)*15.0(T), brings the field in sections 3 and 4 up very much, while it makes the fields in sections 1 and 2 extremely down. That means the size of volume tuning blocks in section 2 should be decreased.

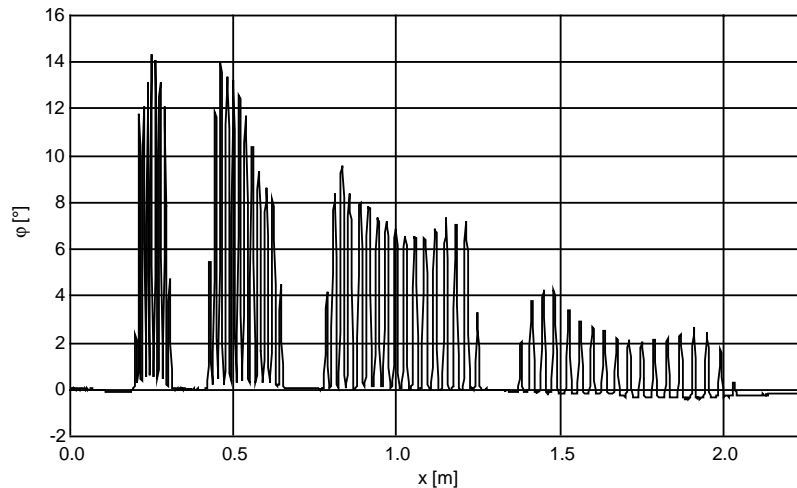


Fig.5.2.3a Without volume tuning in section 2, $f=419.16\text{MHz}$

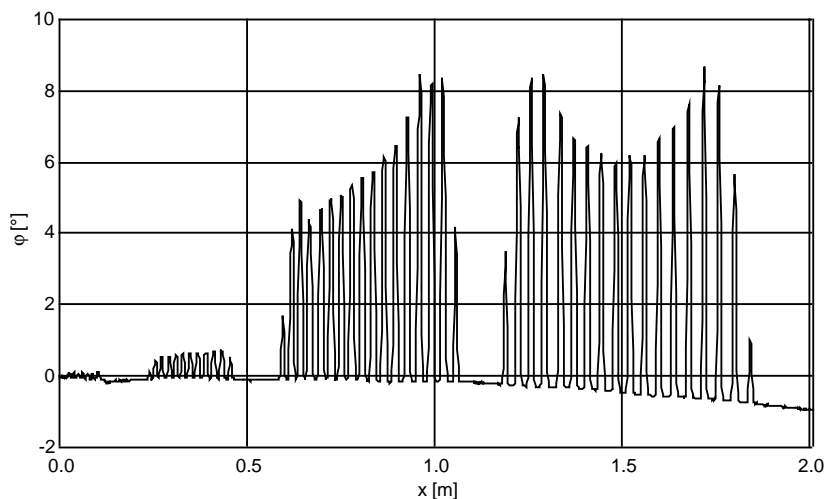


Fig.5.2.3b with volume tuning in section 2, $f=420.72\text{MHz}$

After several other tuning concepts were tested, it is proved that the size of tuning blocks in section 2 must be decreased. Fig.5.2.4a and Fig.5.2.4b show the influence before and after the lengths of volume tuning blocks in section 2 are shorted from 200.0mm to 120.0mm. It makes the field in sections 3 and 4 much lower than before. From the last several figures, the volume tuning concept gives the big chance to balance the field distribution in whole the cavity. The adding volume tuning blocks in sections 1 and 2 enhances the local frequency, because they decrease the

local cavity cross section area i.e. the local cavity inductance per unit length (see chapter 2). So it can change the field distributions in different sections very efficiently.

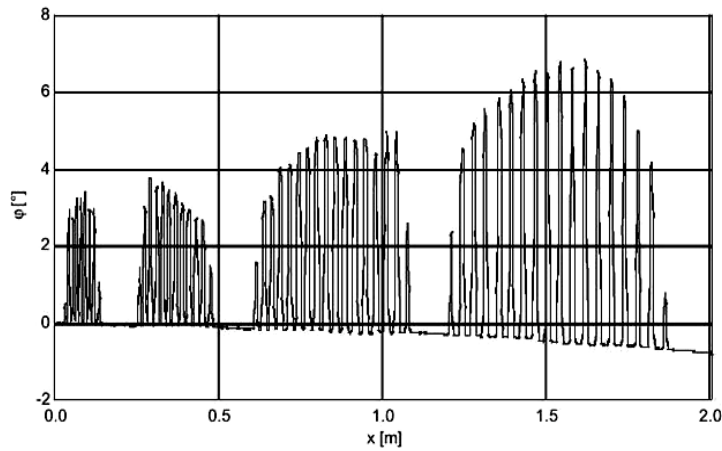


Fig.5.2.4a Length of volume tuning blocks in section 2: 200.0mm, HE undercut insert length 80mm, $f=430.94\text{MHz}$

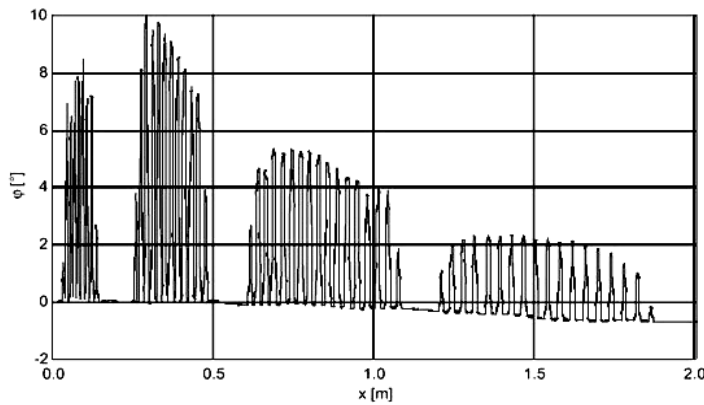


Fig.5.2.4b Length of volume tuning blocks in section 2: 120mm, HE undercut insert length 80mm, $f=429.95\text{MHz}$

5.2.2 Additional Capacitance Plate Tuning



Fig.5.2.5 ACP tuning

The additional capacitance plate tuning concept was only used at the

beginning of the RF tuning research. It is very convenient to know where the structure needs more capacitance per unit length, and it is also the way of tuning that can keep the drift tube and gap parameters. But this way won't be used for real cavity, because it will make the shunt impedance lower and increase the RF power dissipation, meanwhile it also increases the unreliability if the RF connection is not good enough. Fig.5.2.5 shows the mounting of ACP tuning. Fig.5.2.6 shows the effect of this tuning. The field distribution has been improved at the end of section 3 by three ACP clamped copper plates.

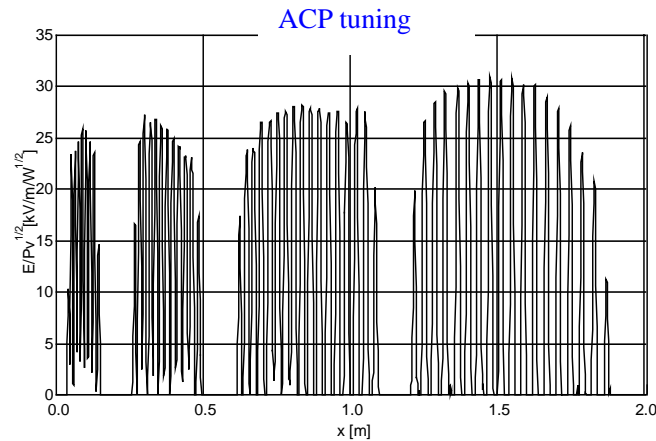


Fig.5.2.6 Field distribution tuned by ACP

5.2.3 Tube Tuning

Tube tuning is a standard tuning concept for IH cavities. It is a variation of the gap lengths along the cavity in such a way, that the distance between gap mid planes is conserved to keep the β -profile. On the other hand, the absolute drift tube lengths are chosen in such a way, that the resulting capacitance distribution lead to the desired voltage distribution along the cavity.



Fig.5.2.7 Lengthened tubes after soldering

One can use silver coating layer to lengthen drift tubes. When the silver layer is coated on the end surface of the tube, it can be 0.1—0.15mm longer once time, then it should be waited for another 20 minutes to let the coated silver layer be

completely dry, then another silver layer could be made. Of course it is easier to cut the tubes to be shorter. When the silver coated tubes were mounted on the stems, one should be very carefully not to damage the layer, especially when one made the gap length measurement. After several failures, soldering method was invented to lengthen the tubes. This is shown in Fig.5.2.7, even it is easier to make a tube 2mm longer by soldering. The inner and outer diameters were carefully made and kept close to the original tube shape. The end surface of the tubes was polished.

Table.5.2.1 Tube tuning (example 1)

Nr.	17 th Sept. G/mm	17 th Sept. D/mm	19 th Sept. G/mm	19 th Sept. D/mm
39	6.733	25.1	6.733	25.4
40	11.798	23.2	11.298	23.7
41	11.38	23.7	11.056	24.0
42	11.888	31.2	11.512	31.6
43	12.542	23.6	12.184	23.8
44	12.343	24.2	12.243	24.3
45	12.322	24.9	12.322	24.9
46	12.103	25.6	12.103	25.5
47	12.059	26.2	12.259	26.0
48	11.87	26.9	12.17	26.6
49	11.705	27.6	12.105	27.2
50	11.449	28.3	11.949	27.8
51	11.297	29.0	11.797	28.5
52	11.043	29.7	11.543	29.2
53	10.772	30.4	11.272	29.9
54	10.499	31.0	10.999	30.5
55	10.327	32.0	10.827	31.7

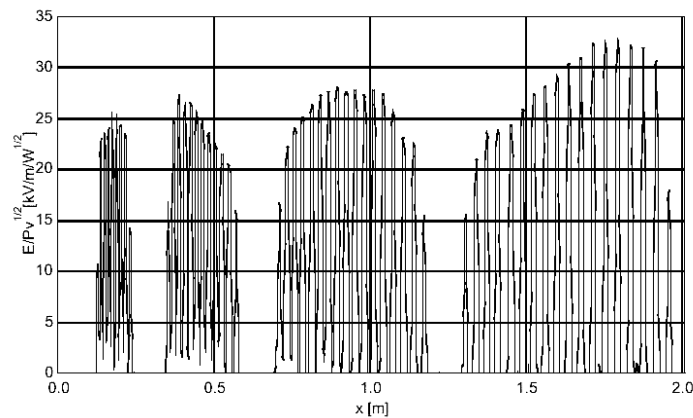


Fig.5.2.8a The field distributions according to drift tube structures listed in table 5.2.1 (a, 17th Sept.)

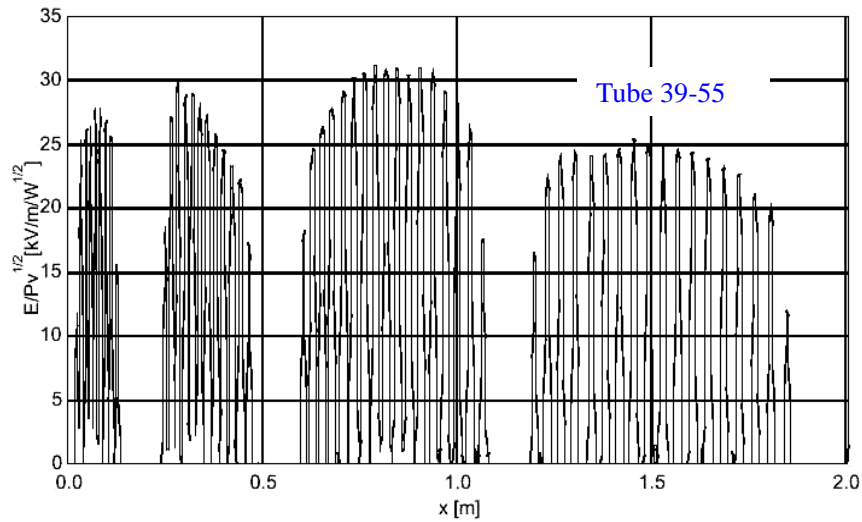


Fig.5.2.8b The field distributions according to drift tube structures listed in table 5.2.1 (b,19th Sept.)

Fig.5.2.8a and Fig.5.2.8b show the effect of tube tuning. The table 5.2.1 lists the tube parameters before and after changing. In this example, most of the tubes in section 4 were shortened and the gaps were enlarged. So the field distribution in 4th section goes down and is uniform.

Next example of tube tuning is how the field in 3rd section (Fig.5.2.8b) can be flattened and also be reduced. For this purpose, the tube lengths should be reduced 0.06—0.25mm and the gap lengths should be enlarged correspondently. The old (19th Sept.) and new (25th Sept.) tube parameters are listed in table 5.2.2. The new field distribution is shown in Fig.5.2.9. Comparing it to the Fig.5.2.8b, the effects are very clear.

Table.5.2.2 Tube tuning (example 2)

	19 th Sept.	19 th Sept.	25 th Sept.	25 th Sept.
	G/mm	D/mm	G/mm	D/mm
24	12.42	12.72	12.42	12.66
25	12.46	18.23	12.58	18.07
26	12.50	13.81	12.70	13.59
27	12.50	14.55	12.75	14.30
28	12.48	15.26	12.73	15.03
29	12.51	15.93	12.73	15.73
30	12.54	16.62	12.73	16.43
31	12.52	17.32	12.73	17.11
32	12.52	18.30	12.73	18.10
33	11.89	19.37	12.09	19.17
34	11.69	20.20	11.90	20.09

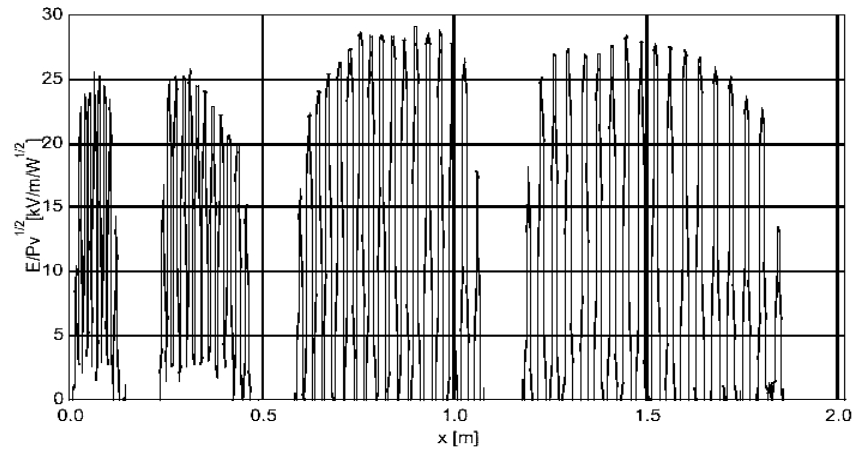
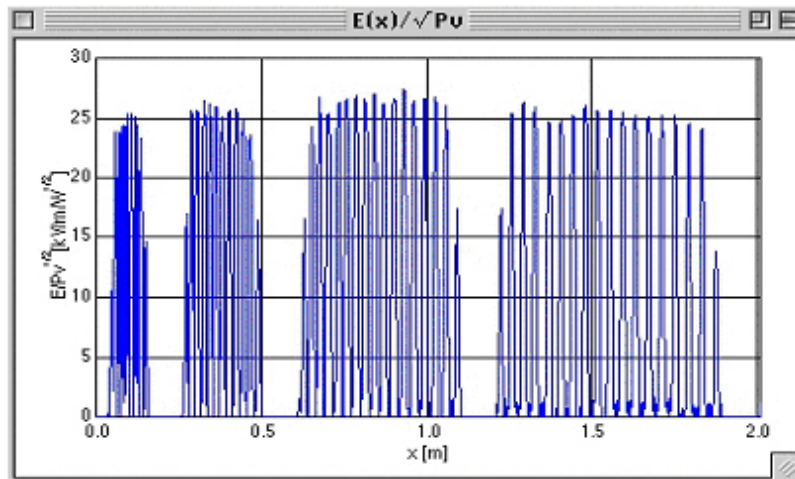
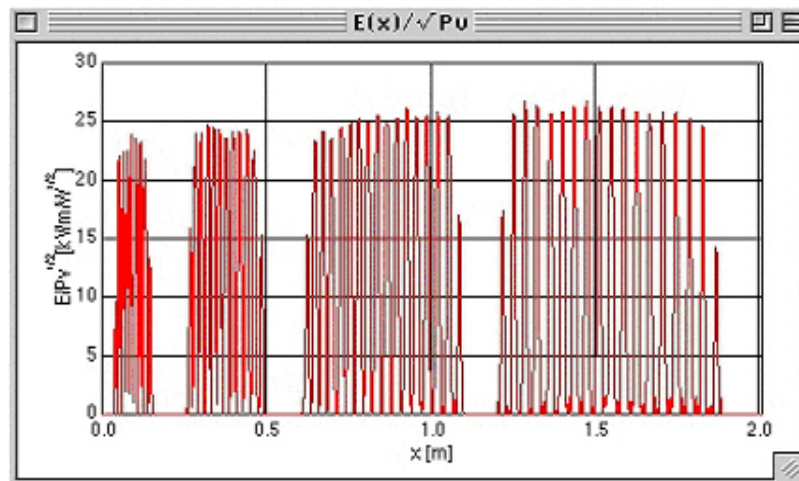


Fig.5.2.9 Tube tuning effects in 3rd section (example 2), comparing to the Fig.5.2.8b



a, 31st Oct., before changing



b, 7th Nov. after changing tube

Fig.5.2.10 Example 3 of tube tuning

Tube tuning is the most important tuning and also the standard tuning concept for IH model cavity. It is not for real power cavity tuning. When the adaptable

tubes and gaps parameters are determined from the model cavity tuning, they won't be changed any more for the real power cavity.

Table.5.2.3 Tube tuning parameters (example 3)

Nr.	31 st Oct.	31 st Oct.	7 th Nov.	7 th Nov.
	G	D	G	D
17	10.30	10.77	10.30	10.77
18	10.00	11.73	10.00	11.83
19	9.85	12.68	9.65	12.93
20	9.55	14.59	9.25	14.74
22	7.76	14.54	7.76	14.69
23	11.10	13.21	10.80	13.44
24	11.58	13.30	11.43	13.38
36	10.85	22.49	10.85	22.59
37	10.30	24.65	10.10	24.75
42	11.31	31.67	11.31	31.76
43	12.18	23.79	12.00	23.98
44	12.24	24.28	12.04	24.38

5.2.4 Lens Coupling Tuning

The principle of lens coupling is shown in Fig.5.2.11a and Fig.5.2.11b. It is a variation of the distance (d) between the lens housing and the girders of the cavity central frame. The different thickness of 7mm, 9mm and 12mm of lens coupling inserts for magnetic lenses 1-3 were available, and additionally a number of 1mm thickness copper sheets. If the lens capacitance coupling distance d (see also Fig.5.2.2a) is smaller, the coupling between the lens and girder is stronger; the fields in neighbouring sections before and behind the according lens are increased. Fig.5.2.12a, 12b and 12c show the effects of lens coupling. The d_1 , d_2 , d_3 are the distances between each triplet lens and the cavity girders. The lens capacitance coupling or lens couplers on both sides of triplets are symmetric. When d_1 , d_3 are kept, d_2 is changed from 12.0mm, 13.0mm and 14.0mm, the field distributions in 1st and 2nd go down, the field at 4th section goes up. This tuning effect will be discussed once more in the tuning of the lens supporting stems.

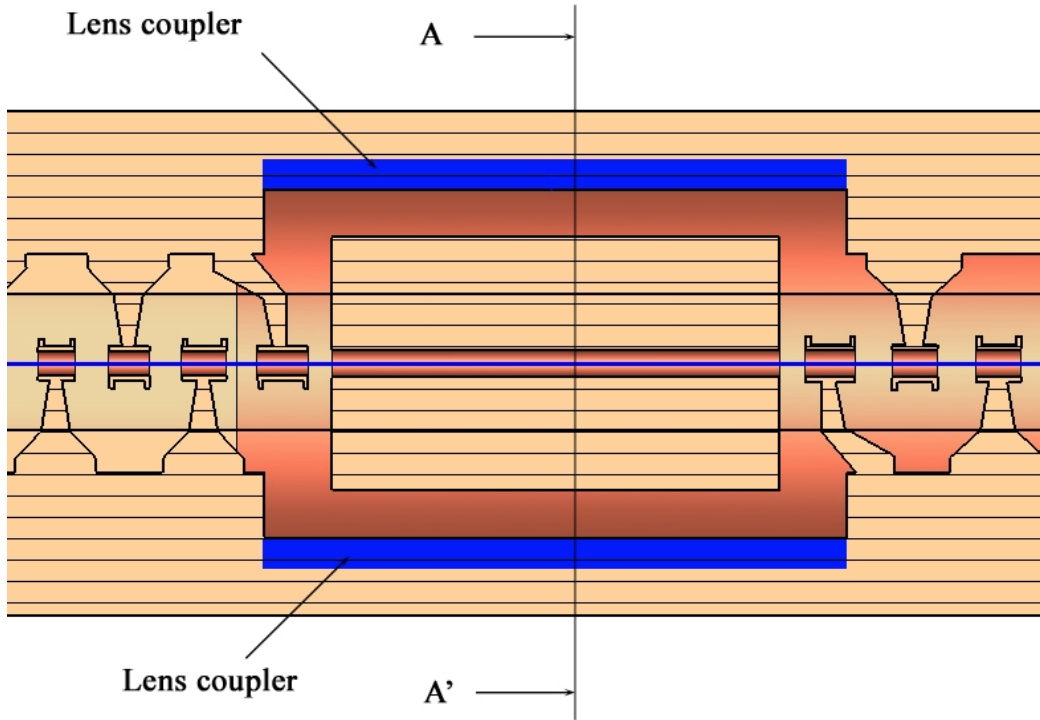


Fig.5.2.11a Lens coupling tuning

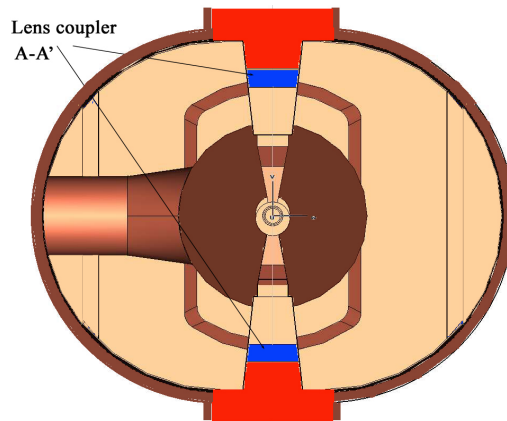


Fig.5.2.11b Sketch of lens coupling tuning

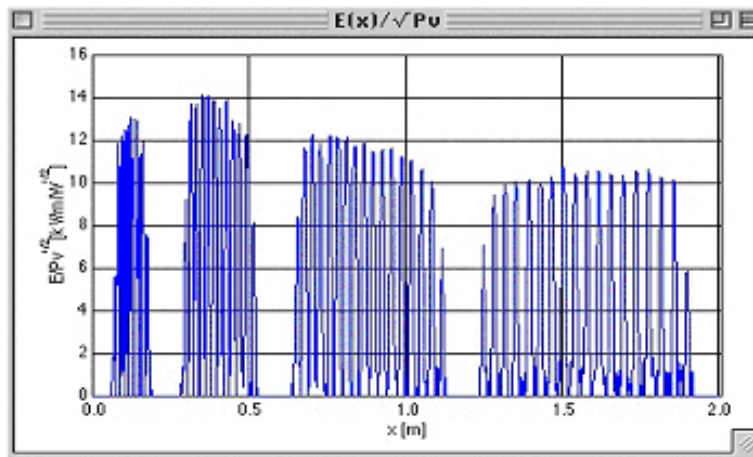


Fig.5.2.12a The field distribution with $d_1=16.0, d_2=12.0, d_3=11.0$ (mm)

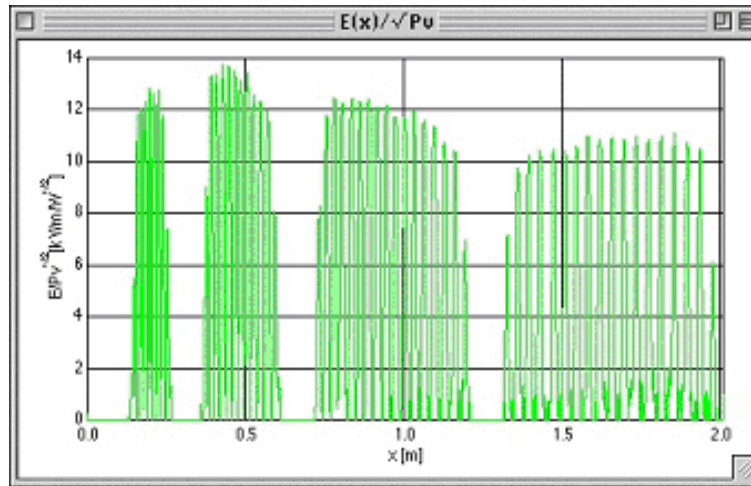


Fig.5.2.12b The field distribution with $d_1=16.0$, $d_2=13.0$, $d_3=11.0$ (mm)

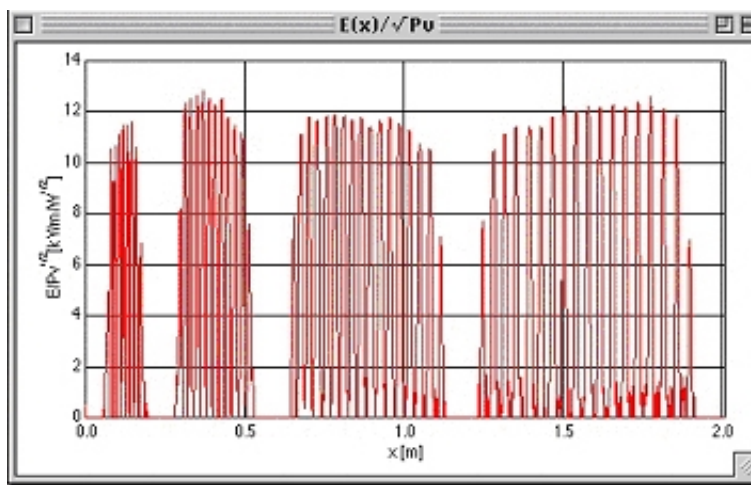


Fig.5.2.12c The field distribution with $d_1=16.0$, $d_2=14.0$, $d_3=11.0$ (mm)

5.2.5 The Undercut Tuning

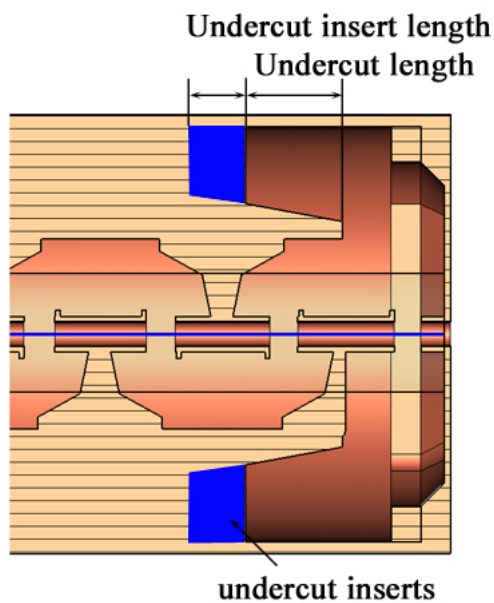


Fig.5.2.13 The concept of undercut tuning

Fig.5.2.13 shows the entrance and exit geometry of HICAT IH-DTL model cavity. It shows also the definition of undercut and its tuning concept. The undercuts tuning means: if the undercuts lengths at low or high energy end are longer or shorter, it can make the field distributions at this end larger or smaller. The undercuts inserts on both sides are symmetric. It is also very important for the model cavity, the length of undercuts for the girders of real RF power cavity should't be changed any more, because the girders are water cooled for the real power cavity. The undercuts tuning in the model cavity could give more details about the sensitivity and its shape for the power cavity design. Here are only two examples shown in Fig.5.2.14a, 14b and Fig.5.2.15a and 15b. In Fig.5.2.14a and Fig.5.2.14b, the lengths of higher energy (abbreviated as HE) undercut inserts are changed only 0.7mm, the field distribution seems no big changes, but it has the effects which is shown clearly in the difference of effective voltage between designed and experimental values. It makes the percentage of the sum of effective voltages in 4th section to the sum of effective voltages for whole cavity change from 0.529% to -0.21%.

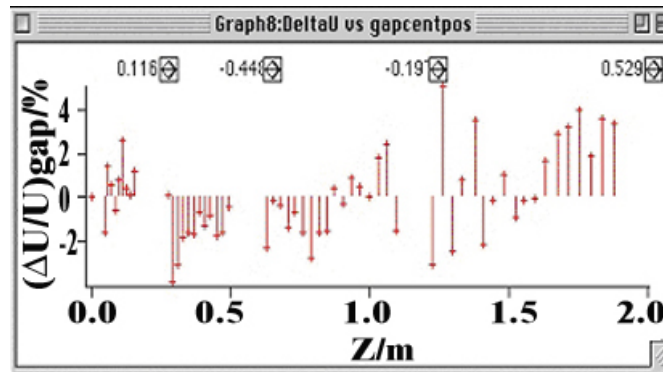


Fig.5.2.14a HE undercut insert lengths 75.3mm

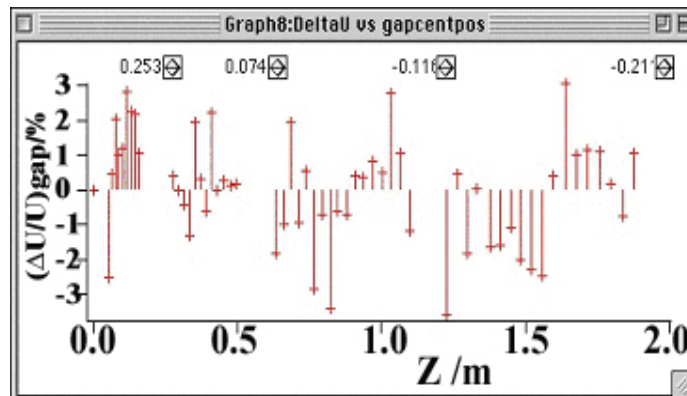


Fig.5.2.14b HE undercut insert lengths 76.0mm

Fig.5.2.15a and Fig.5.2.15b show the big influence of different lengths of high energy undercuts tuning. When the lengths of high energy undercuts inserts are changed from 78.0mm to 75.0mm, the field distribution at exit are increased quite a lot, as discussed before, to flatten the field distribution, the tube tuning

concept is needed. It can be concluded if the lengths of undercut inserts are smaller, the field at this end is larger, while the field at another end is smaller.

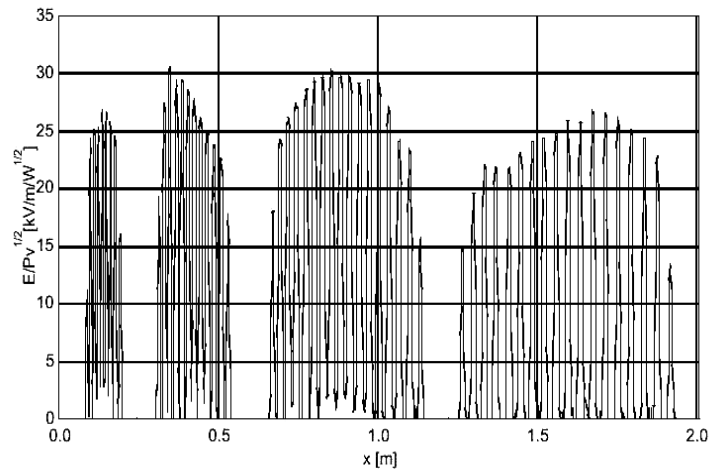


Fig.5.2.15a HE undercut insert lengths 78.0mm

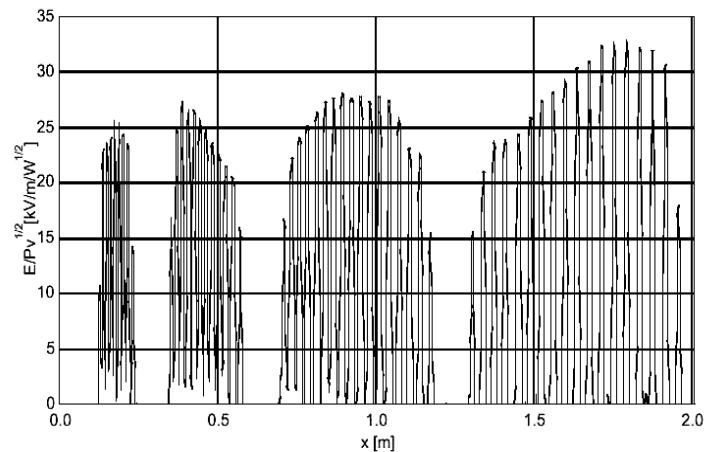


Fig.5. 2.15b HE undercut insert lengths 75.0mm

5.2.6 The Plunger Tuning

The plunger tuning methods are widely used in RF linear accelerators. This tuning concept is using movable metallic bodies, which are driven from outside of the cavity. The motion is transferred into the vacuum by using metal bellows. It is the standard method for controlling the resonance frequency of the cavity during operation by an electronic feed back loop, moreover, using several tuner along multicell structures the drift gap voltage distribution can be readjusted, especially the voltage ratio between drift tube sections as defined by the lens positions. Due to the speciality of the medicine project, the designed electric field distribution should be reached without any plunger, which means the tube and gap parameters were the best fit. Then the tuning abilities of two different types of RF plungers were investigated. The plungers used in 3rd section are shown in Fig.5.2.16 and Fig.5.2.17. Only the plate plunger was tested in section

4. The plate plunger has the height of 73mm and width of 60mm. The block plunger has the height of 74mm and width of 30mm and thickness of 18.0mm. The tuning range of plate plunger in 3rd section is shown Fig.5.2.18. Fig.5.2.19 plots the effective voltage difference for every section related with the total effective voltage of the cavity in percentage for the plate plunger 3. All the figures in this chapter are only for one plunger. The composite effectives were not investigated in this chapter.

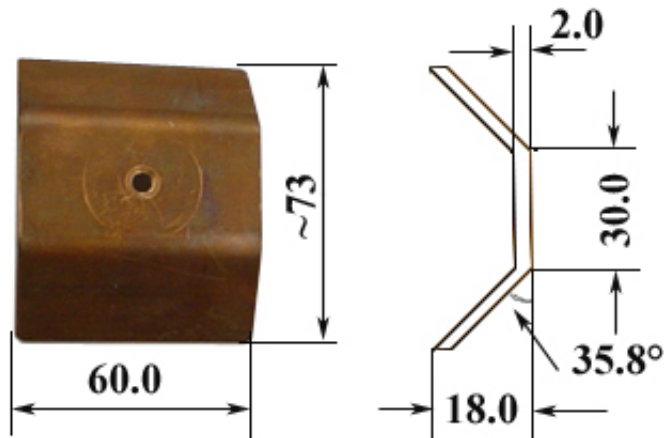


Fig.5.2.16 Plate plunger for section 3 and 4

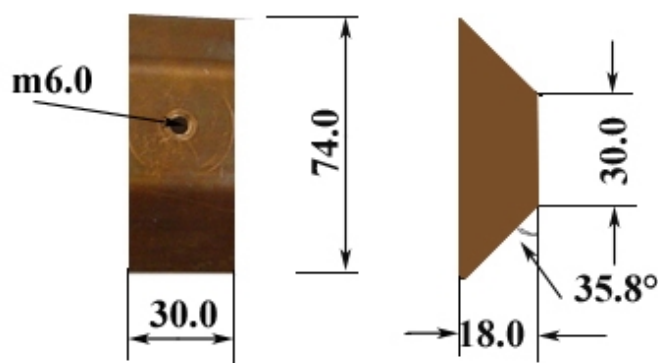


Fig.5.2.17 Block plunger

Tuning range of plate Plunger 3

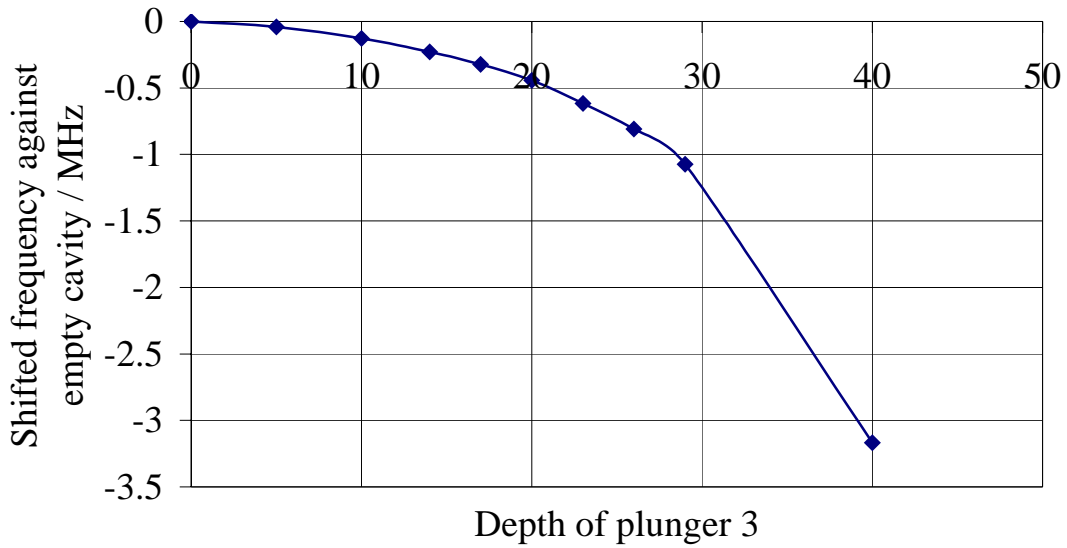


Fig.5.2.18 The tuning range of **plate** plunger 3 (installed in 3rd section)

DeltaU1-4

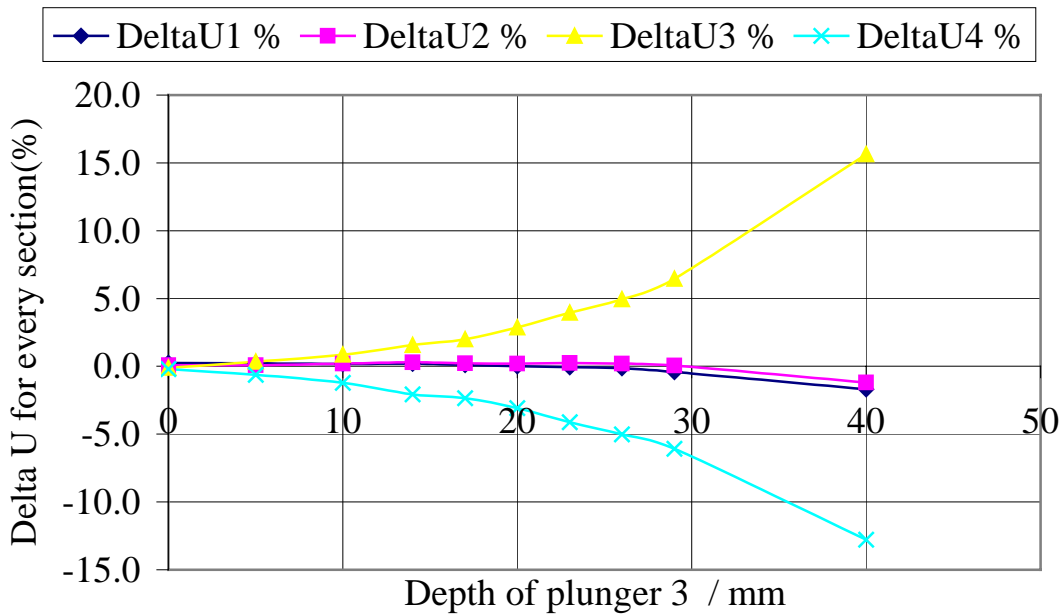


Fig.5.2.19 The influence of different plunger positions on the voltage distribution of sections 1—4

Fig.5.2.20 shows the tuning abilities of the block plunger in 3rd section. Fig.5.2.21 shows the effects of the same plunger on the voltage distribution. Because the block plunger occupies more volume of the cavity than it of the plate plunger, it brings the resonating frequency up at the beginning. It is very interesting that this block plunger give plunger more tuning range because of

inducing of inductance and its special response on the voltage distribution. This effect is very helpful for IH medical cavity. Up to now almost all IH cavities use block plungers with the exception of the HSI-GSI; the weight of the plunger was a main aspect. The characteristics of the plate plunger in section 4 are shown in Fig.5.2.22 and Fig.5.2.23. One can see the strong influence on the voltage distribution when the plunger is mounted at the end section of the cavity, especially.

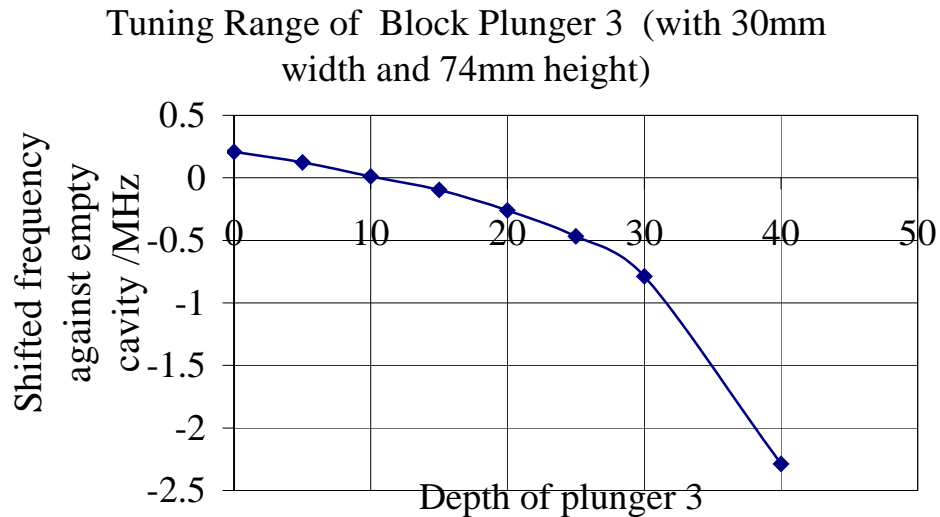


Fig.5.2.20 Tuning range of block plunger 3

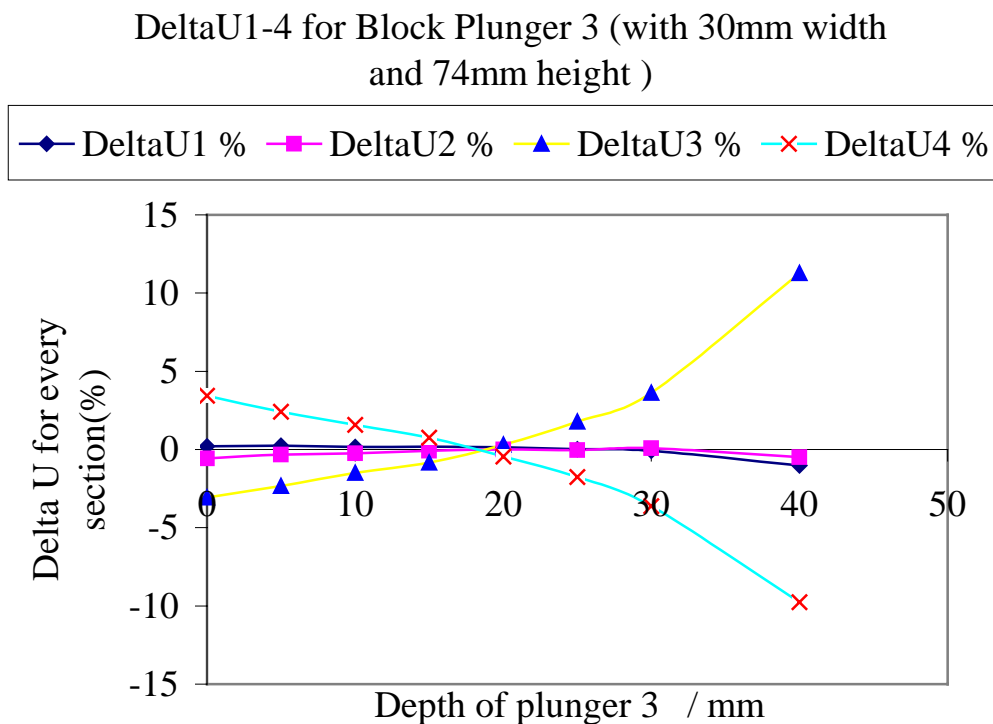


Fig.5.2.21 The effect of different depth of block plunger 3

Tuning Range of Plate Plunger 4 (60mm width and 73mm height)

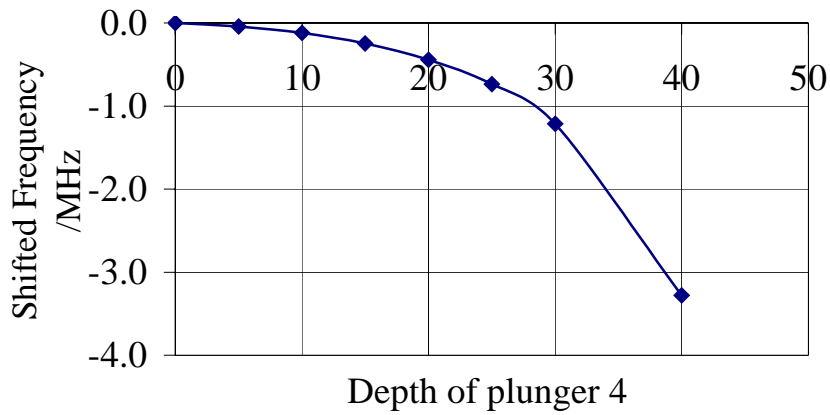


Fig.5.2.22 The tuning range of plate plunger 4

DeltaU1-4 for Plate Plunger 4 (60mm width and 73mm height)

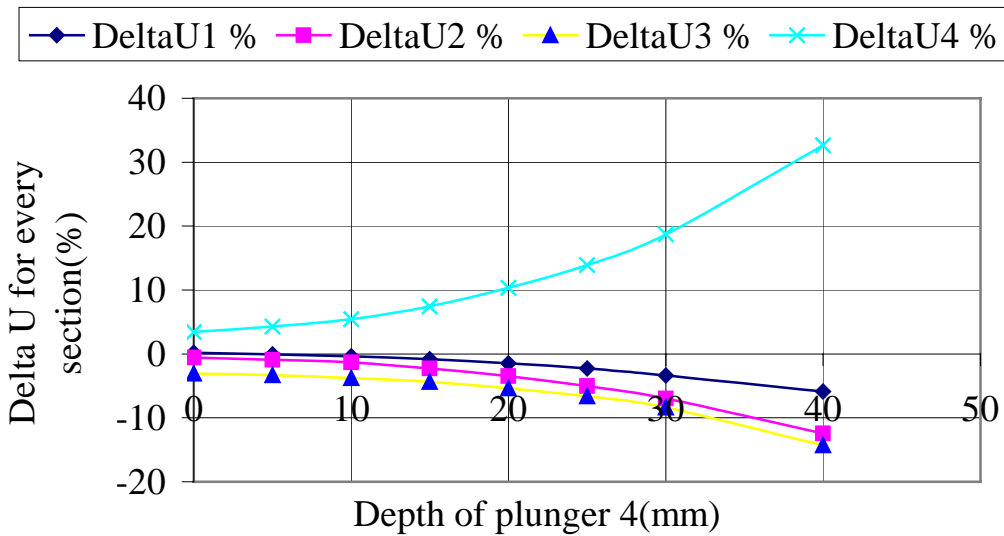


Fig.5.2.23 The effects of plate plunger 4 (installed in section 4)

5.3 The Effects of Lens Supporting Stems

Before we discuss the influence of different lens supporting stems on the field distribution along the structure, it is necessary to show the initial tuning result.

5.3.1 The Initial Tuning Result of the IH Model Cavity in 2002

From the former report “RF Tuning of the IH Model Cavity for the Heidelberg Cancer Therapy”^[4.5] (IAP Internal Note:IAP-ACCC-270103), the tuning results are reviewed here briefly in Fig.5.3.1-4 (^[4.5] P.16-P.17). The lens coupling spaces

between triplets and the girders of central frame are 16mm, 14mm and 11mm (see ^[4.5] P.19), respectively. The undercut lengths for low and high-energy end are 20.8mm and 32.6mm, respectively (i.e.: the lengths of the undercut inserts are 29.2mm and 76.0mm) (P.20). Section 1 and section 2 have volume tuners (Fig.5.3.1). The dimension of volume tuner in section 1 is 90mm(L)*25.0mm(Thickness) (with the same radius of cavity half shell), while in section 2 the according numbers are 120mm(L)*15.0mm(Thickness) (see ^[4.5] P.19)

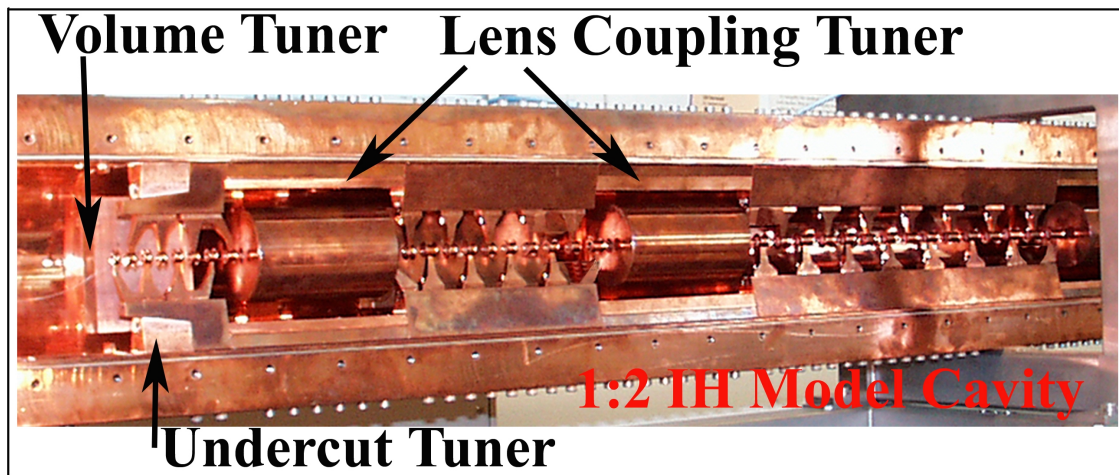


Fig.5.3.1 The 1:2 scaled IH model cavity (3 of 4 sections)

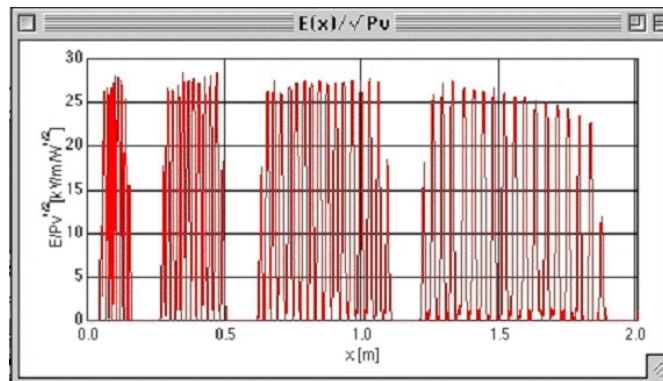


Fig.5.3.2 Electric field distribution

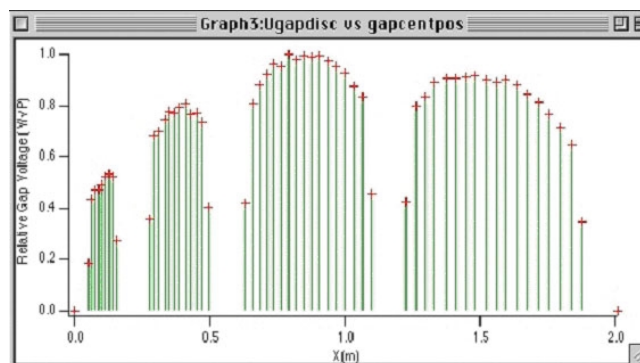


Fig.5.3.3 Effective voltage distribution

The bead pull measurements were done with a 2.5mm diameter copper metal ball. The measuring points are 1598. The resonance frequency is **434.53MHz**. The measured loaded quality factor is 2464.

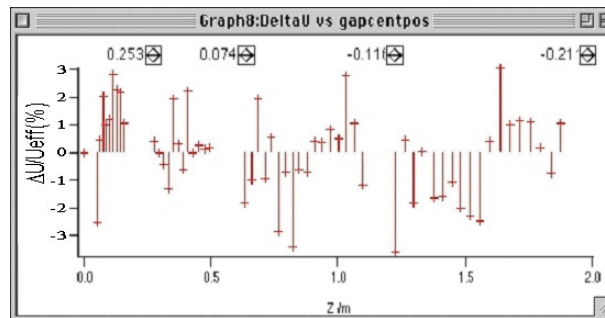


Fig.5.3.4 The remaining differences of the effective voltage distribution for every gap and for the sections when compared to the design distribution

Fig.5.3.4 shows the relative effective voltage differences from measured and theoretical values in %. On the top of this diagram, these four errors in percentage show the voltage difference between the measured and theoretical section gap effective voltage related to the sum of the total cavity effective gap voltages. For example, the sum of effective gap voltages for total cavity is 20.851MV, the theoretical effective gap voltages for the four sections are 1.7363, 3.8738, 7.4973 and 7.7432MV, respectively. After the final tuning, the measured effective gap voltage for different sections is 1.7890, 3.8892, 7.4731 and 7.6992MV, respectively. So the errors for different sections are 0.253%, 0.074%, -0.116% and -0.211% (related to 20.851MV), respectively. Remaining errors are felt to be comparable with errors added by the differing geometric details of the final cavity, so the tuning will be optimised on the real cavity.

5.3.2 The Field Distribution Influence of Triplet Supporting Stems^[5.3]



Fig.5.3.5 Original stem



Fig.5.3.6 New stem geometry

The initial tuning result in 5.3.1 was based on the old supporting stem that consists of two rectangular profiles (Fig.5.3.5). In fact, the supporting stem needs more space for assembling the triplet driving wires, in which there is cooling water flowing. The influence of final designed triplet stem geometry on the field distribution has to be investigated. The new supporting stem geometry (shown in Fig.5.3.6) consists of one cylinder ($\Phi 32*30$) and one elliptical cone (65mm*39mm, side width is 18.0mm). Because of the machining difficulties, they were simplified a little from the GSI drawing during the fabrication in the institute factory at Frankfurt University. The volume of the new supporting stems is considerably larger than the old one. This has two effects: 1, the resonating frequency will be higher than before; 2, the distance between triplet 1 and 2 are shorter than triplet 2 and 3, so the effect will be like a volume tuning. So it will make the field distribution in 3rd section and 4th section much larger than before. This gives a good chance to release the lens coupling problem as shown below. At a starting point, the distances between triplets and girders are 16mm, 14mm and 11mm, respectively. That means the space at the last triplet in the real power cavity is about 22mm, which should stand a RF voltage of amplitude 270kV.

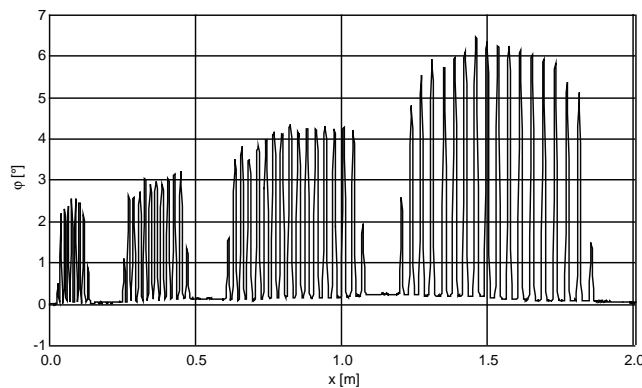


Fig.5.3.7 After assembling new stem geometry, with the lens coupling distances $d_1=16.0, d_2=15.0, d_3=14.0$

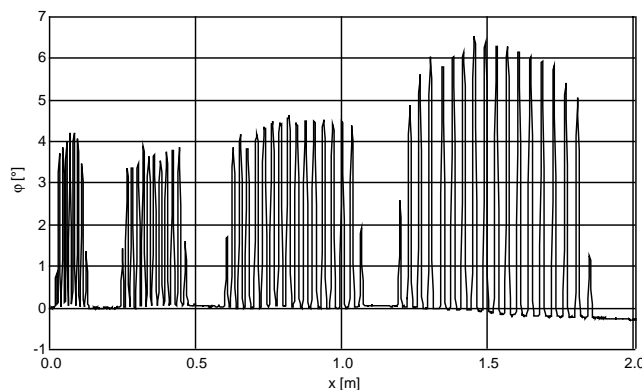


Fig.5.3.8 The lens coupling distances: $d_1=14.0, d_2=15.0, d_3=14.0$, the field distributions in 1st and 2nd sections go up

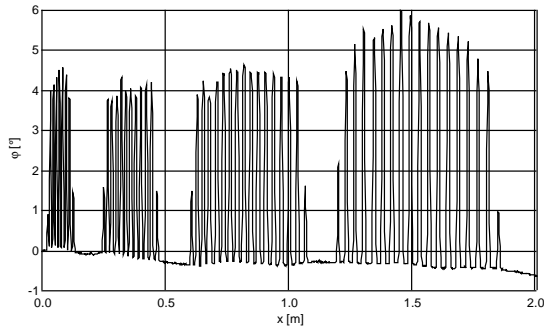


Fig.5.3.9 The lens coupling distances: $d_1=14.0$, $d_2=14.0$, $d_3=14.0$ mm, comparing to Fig.5.3.8, the field distributions neighbouring triplet 2 go up by decreasing d_2 from 15.0mm to 14.0mm

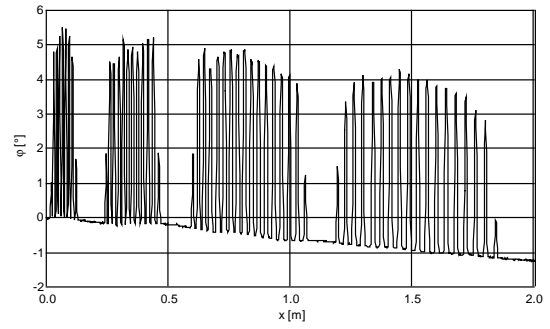


Fig.5.3.10-1, The lens coupling distances: $d_1=14.0$, $d_2=13.5$, $d_3=14.0$ mm, d_2 is decreased from 14.0mm to 13.5mm, the perturbation phase around triplet 2 goes up again

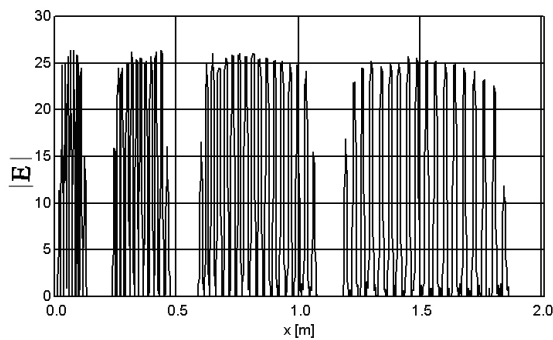


Fig.5.3.10-2 Electric field distributions with lens coupling distances: $d_1=14.0$, $d_2=13.5$, $d_3=14.0$ mm

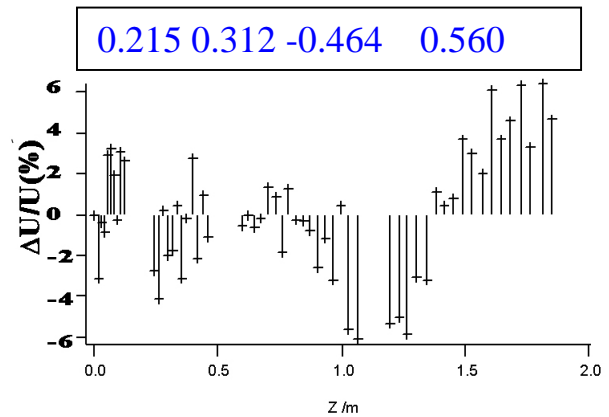


Fig.5.3.10-3 The remaining differences of the effective voltage distribution when the same lens coupling distances with Fig.5.3.10-2

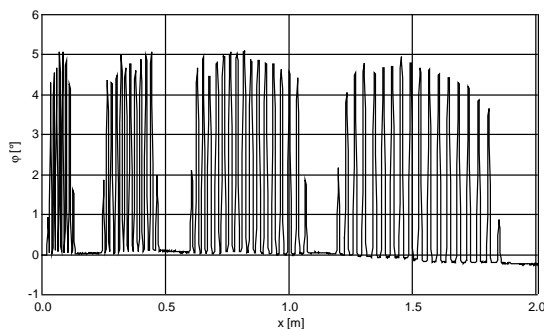


Fig.5.3.11-1 Phase distribution with $d_1=14.0$, $d_2=13.5$, $d_3=13.5$ mm

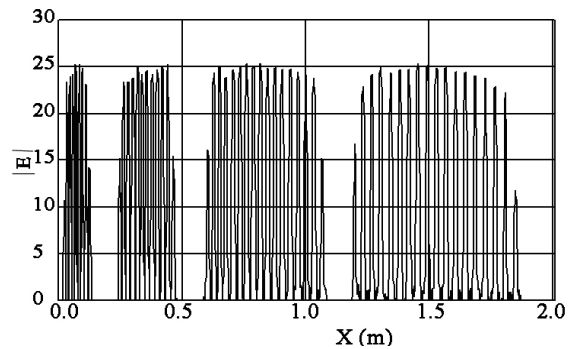


Fig.5.3.11-2 Electric field with $d_1=14.0$, $d_2=13.5$, $d_3=13.5$ mm

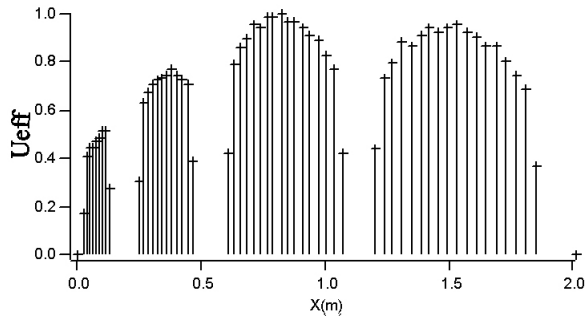


Fig.5.3.11-3 Effective voltage distribution with $d_1=14.0$, $d_2=13.5$, $d_3=13.5$ mm

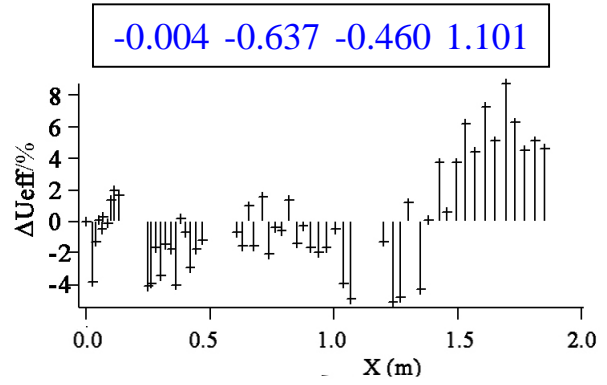


Fig.5.3.11-4 Effective voltage difference with $d_1=14.0$, $d_2=13.5$, $d_3=13.5$ mm

From above measurements, the effects of lens coupling tuning concept are very obviously. The voltage in section 4 is a bit larger, so the high energy undercut inserts are increased to 76.5mm. This will make the field distribution in last section go down. The measurements were shown in Fig.5.3.12-1 to Fig.5.3.12-4.

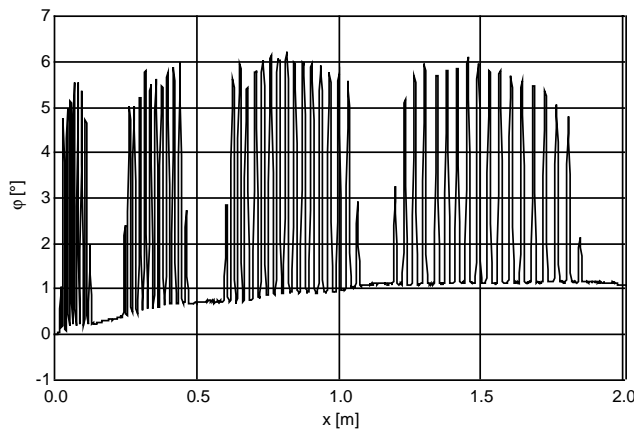


Fig.5.3.12-1 Phase with the lens coupling distances: $d_1=14.0$, $d_2=13.5$, $d_3=13.5$ mm, and high energy undercuts inserts 76.5mm

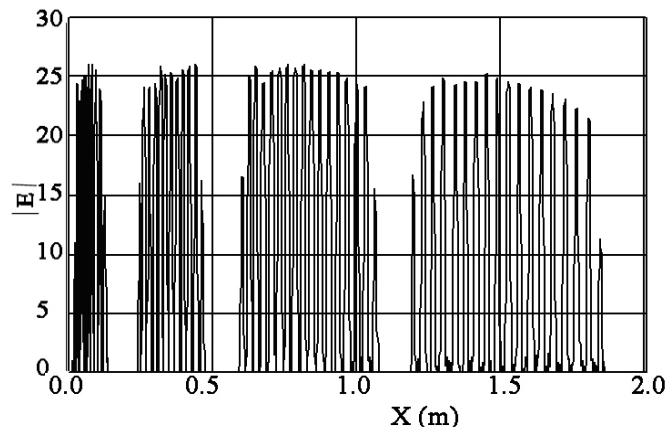


Fig.5.3.12-2 Electric field distribution with the same measurement condition

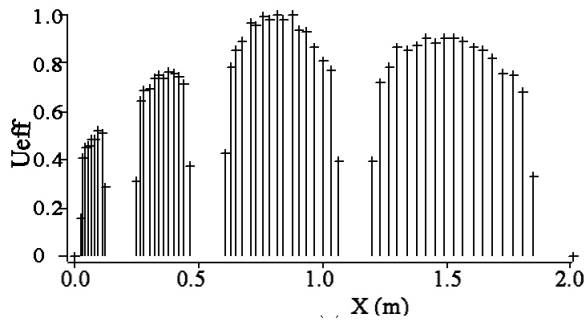


Fig.5.3.12-3 Effective voltage distribution

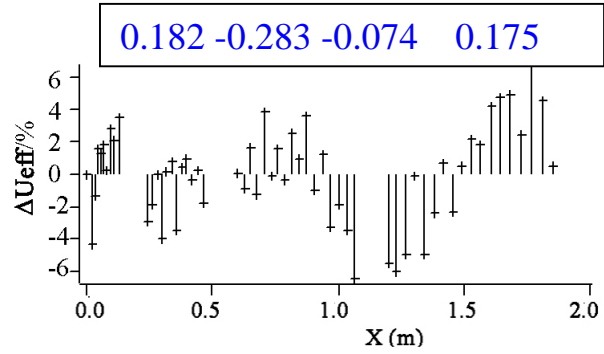


Fig.5.3.12-4 Effective voltage difference

It can be concluded from the model measurements shown in Fig.5.3.9-12, that identical lens girder distances of 14mm (i.e. 28mm for the real power cavity) can be chosen to compensate the new stem enlarging effects and to decrease the RF field between the 3rd triplet and drift tube girders.

5.4 The final end flanges and tuning results

With respect to the needed short drift length at the LE end flange and to technical needs (sealing of tank components) it was necessary to redesign the end wall geometry as shown in Fig.5.4.1, Fig.5.4.2 and Fig.5.4.3.

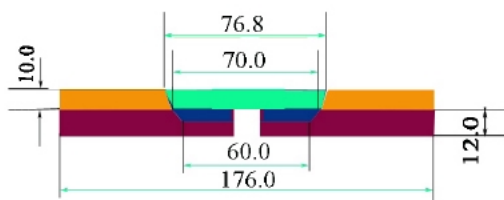


Fig.5.4.1 Final input flange

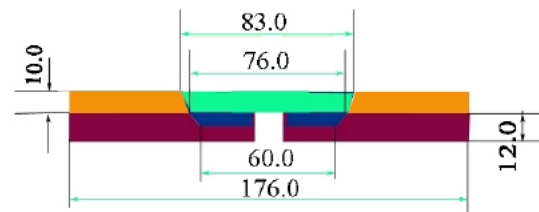
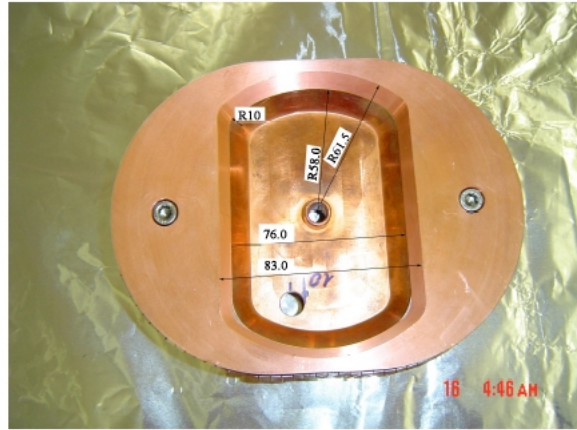


Fig.5.4.2 Final exit flange

The tuning with final cavity end flanges (Fig.5.4.3) has also been done. This shape provides the shortest drift lengths, especially from the RFQ exit to the IH

entrance. Furthermore, this geometry is caused by the tank design with the upper and lower half shells screwed on central frame with 220mm height. By the measurements, the final shape of the volume tuners in section 1 was determined.

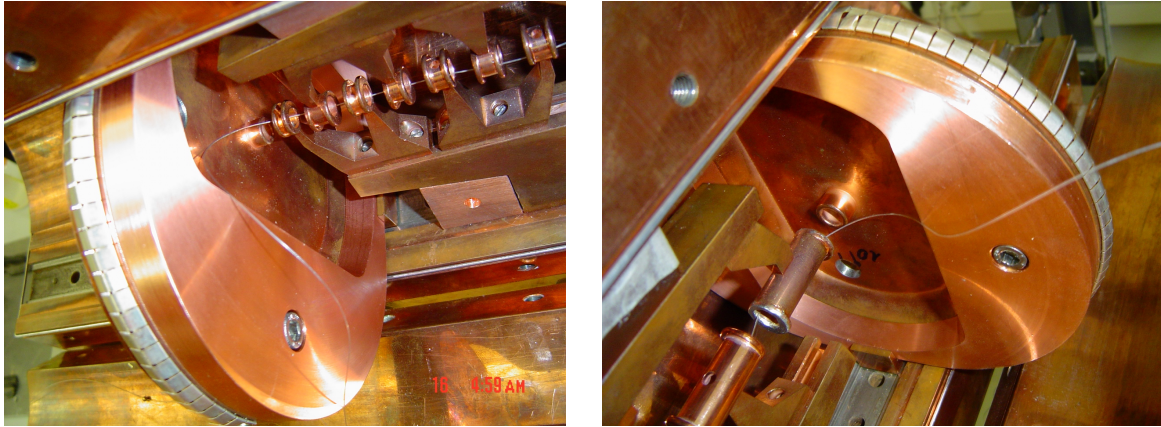


Fig.5.4.3 Final geometry for end flanges

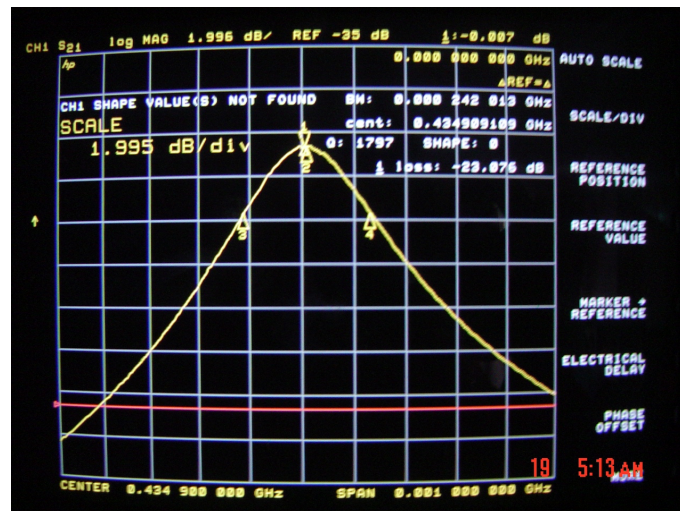


Fig.5.4.4 The resonance measurement, $f=434.9\text{MHz}$

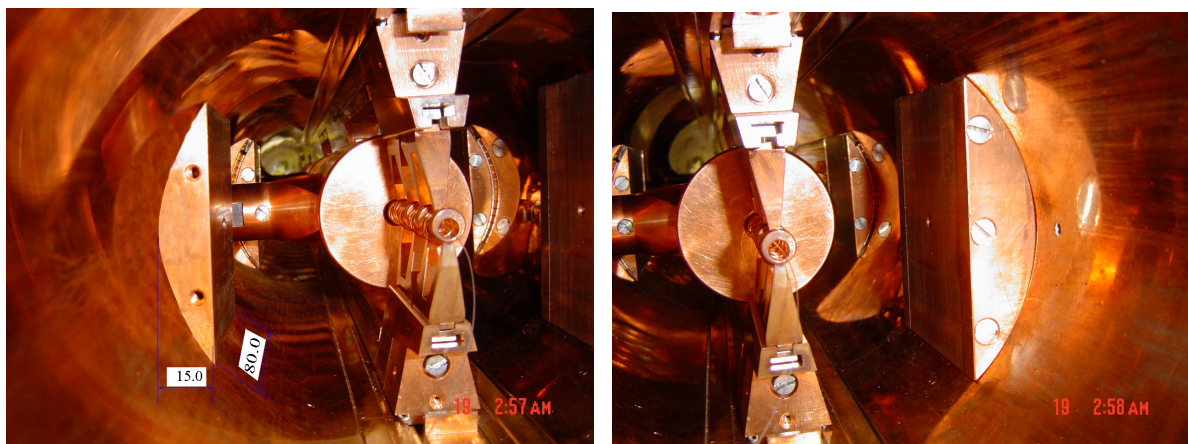


Fig.5.4.5 Volume tuners in section 1 for new designed input and exit flanges (Left: 80mm(L)*15mm(T); Right:90mm(L)*25mm(T))

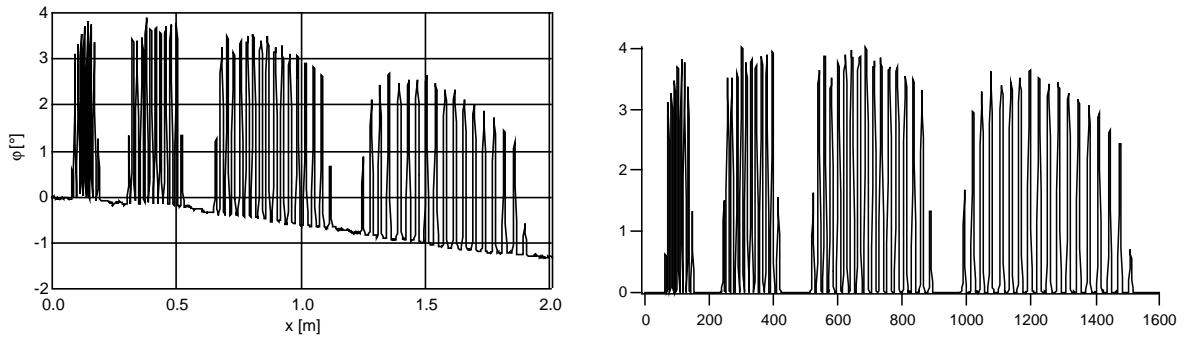


Fig.5.4.6.1 Phase distribution, $f_0=434.9\text{MHz}$ (before (left) and after (right) ground line subtraction)

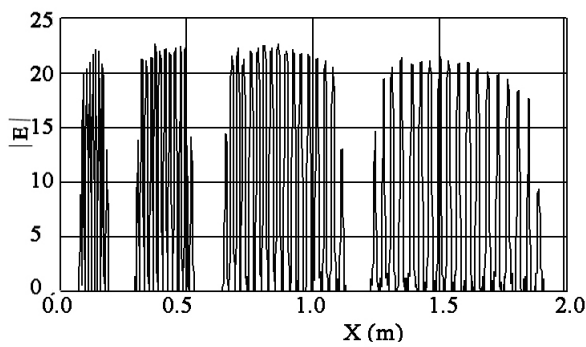


Fig.5.4.6.2 Field distribution

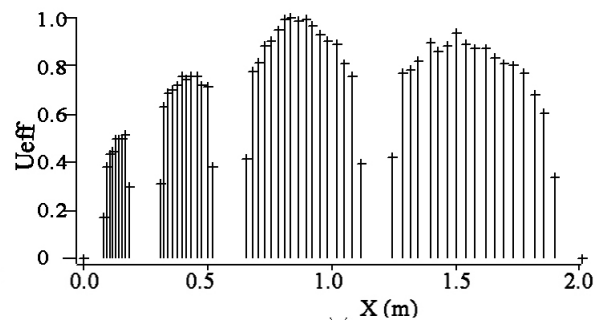


Fig.5.4.6.3 Effective voltage distribution

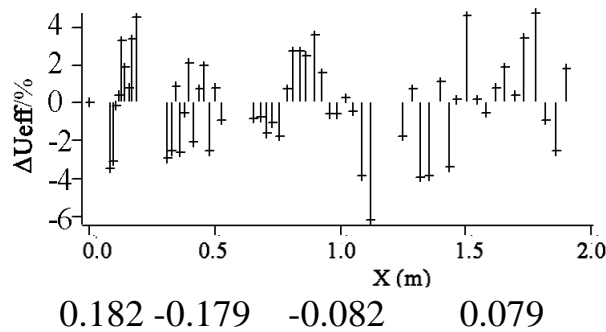


Fig.5.4.6.4 Effective voltage difference

5.5 The Field Distribution of Higher Order Modes

Up to now, several high order modes have been measured after the RF tuning. The amplitude-frequency response is shown in Fig.5.5.1. The field distribution for the fundamental mode (H_{110}) has been shown in Fig.5.4.6.2. Fig.5.5.2-Fig.5.5.5 show the field distributions of modes H_{111} - H_{114} , respectively. It is very remarkable to investigate how to separate the first harmonic, now the frequency separation is only 2.4MHz. This corresponds to about 130 half widths of the fundamental resonance.

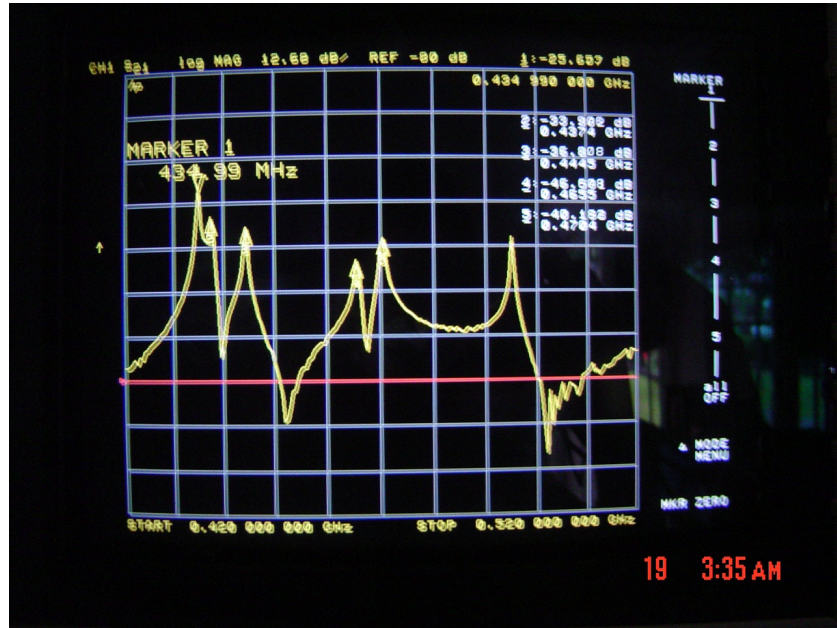


Fig.5.5.1 Amplitude response on frequency, $f_{110}=434.99\text{MHz}$

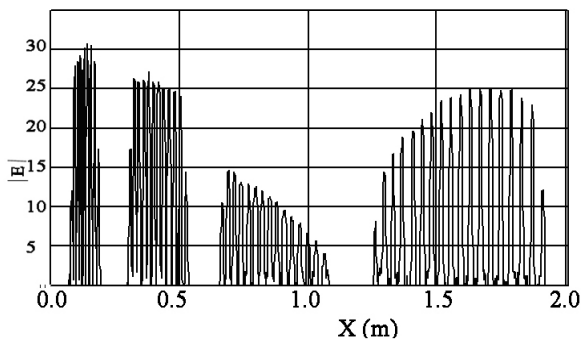


Fig.5.5.2 H_{111} mode, $f_{111}=437.4\text{MHz}$

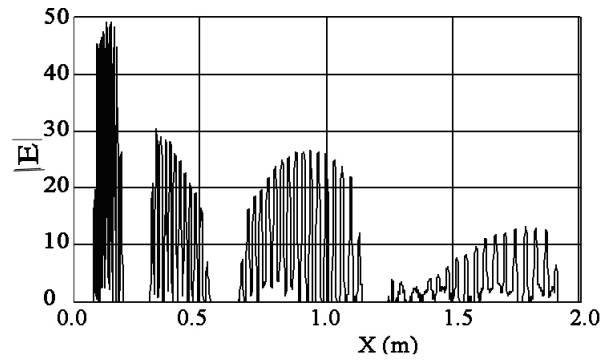


Fig.5.5.3 H_{112} mode, $f_{112}=444.3\text{MHz}$

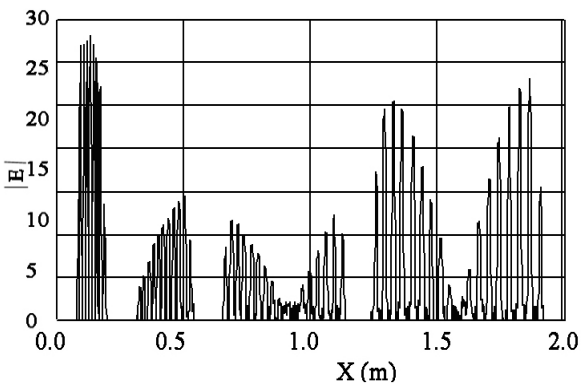


Fig.5.5.4 H_{113} mode, $f_{113}=465.5\text{MHz}$

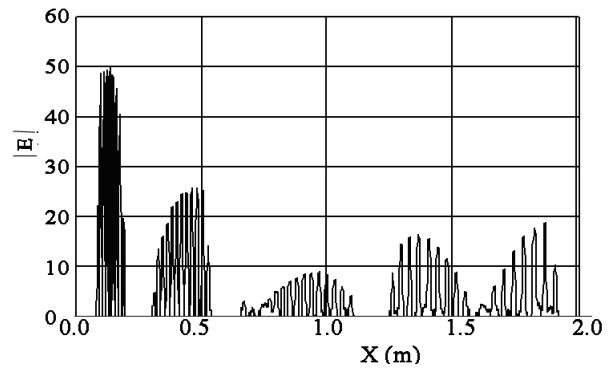


Fig.5.5.5 H_{114} mode, $f_{114}=470.4\text{MHz}$

5.6 Comparison of the Different Tuning Techniques

Six different tuning concepts were explained in this chapter: **Volume tuning** can compensate the unbalanced capacitance distribution in case of extreme $\beta\lambda$ -variation along an IH cavity; **Additional Capacitance Plate** or Copper sheets clamped on drift tube stems are a fast way for checking the tuning sensitivity but not for final use; **Lens Coupling** is an important tool to stabilize the operation mode and to increase the coupling between neighboring sections; Modification of **Tube Tuning** is the fine tuning concept for the flat electric field. It is also the standard tuning method to reach the voltage distribution in every single gap; **Undercut tuning** is the most sensitive tuning to the end sections and to the voltage distribution balance along the structure; for the long medical linac structure, the tuning range by the **plunger** should be very limited (safety), that means additionally stabilization by a well-controlled cooling water temperature. The influence of QT supporting stems and end flanges on the electric field distribution was also investigated and presented in the chapter.

Chapter Six

The Final Proposal of IH Medical Power Cavity

Based on the engineering design of the IH model cavity, RF tuning investigations and its tuning results, which were described in the last chapter, and the KONUS beam dynamics design of LORASR, the final proposal of the IH real power cavity will put more emphasis on the following topics:

- Controlled variation of the cavity cross sectional area by varying the inner half shell contour (milling different profiles into a solid);
- Tuning of rf frequency and voltage distribution by connecting tuner blocks to the plane surfaces on the top and bottom of the upper and lower half shell, respectively;
- Fastening and alignment of the lens housing drift tubes on the lower half shell. This is possible because of the robust half shell design;
- No outer stiffening frames around the cavity to counteract against the vacuum forces, as the forces are controlled by the stiff half shells and by the quadratic outer cavity shape (400*420mm).

6.1 Geometry of the IH Medical Power Cavity

IH Model cavity scaling a factor of 2 would results in an elliptical cavity with half long axis 0.180m, half short axis 0.140m (see Fig.5.2.2a) and inner cavity length of 3.718m. Generally, the elliptical cavity design needs some additional outer stiffening frames to counteract against the vacuum forces, and to decrease the deforming of the cavity and its influence on the cavity operating frequency. Instead of an elliptical cavity, a rectangular power cavity with chamfers is preferred.

Fig.6.1 shows the cross section of the IH power cavity. The cross section area of empty rectangular cavity with chamfers by Fig.6.1 is about $8.26 \cdot 10^4 \text{ mm}^2$, the equivalent circle radius is $R_2=0.162\text{m}$. The empty cavity cross section comes from the 1:2 scaled model cavity by factor of 2. All other parameters, for example, cavity length, drift tubes' parameters, the tube supporting stems and triplet lens, are just scaled by the factor 2 of the model cavity design. The additional heights (+7mm) of upper and lower half shells are needed to get the resonance by final power cavity measurements.

The parameters of the two girders are changed based on the CERN lead IH linac experience. For such scaling, the drift tube capacitance C_d' in the formula (2.3) and distributed capacitance C' in formula (2.5) per unit length will not be changed. C_d' was shown in Fig.2.4. It is worthful to calculate the mean C_d'

(averaged drift tube capacitance per unit length) by the weight of $(U_{ia}/U_a)^2$, U_{ia} is the measured amplitude voltage, U_a is the averaged amplitude voltage. So for the IH-DTL, $C_d'=16.6$ [pf/m]. According to the experience of existing current IH cavity, substituting $R_1=0.038$ [m], $r_a=1.45r_o$, $F=2\pi r_a^2/(R_1^2(\phi_2-\phi_1))=0.379$, $\phi_2-\phi_1=2.819$ and $\epsilon_0=8.85*10^{-12}$ into the formula (2.5), hence : $C'=3.25$ [pf/m], $C_{IHD}'=2C'+C_d'=23.1$ [pf/m], $L'=44.0$ [nHm], $L_{IHD}'=23.3$ [nHm]. So the designed frequency $f_{IHD}=1/(2\pi(L_{IHD}'C_{IHD}')^{1/2})=217.0$ [MHz]. The Microwave Studio simulation in the next chapter will verify this.

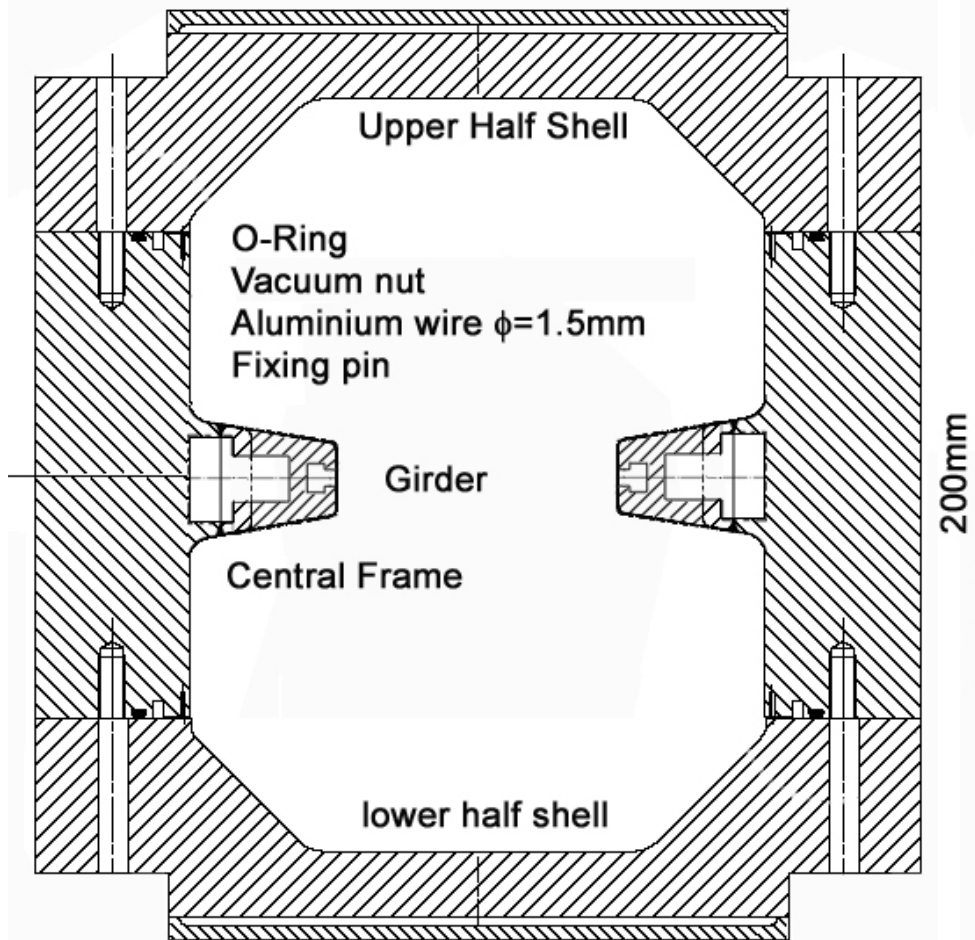


Fig.6.1 Cross section of IH power cavity

Central frame is separated from upper and lower half shell, girders are also good welded into the central frame, the beam entrance and exit can be easily milled in the central frame and freely be vacuum sealed. Cooling water inside cools the central frame and girders. The positions of magnetic lenses (triplets), entrance and exit (LE and HE) undercuts and some example drift tubes are shown in Fig.6.2. This design is very convenient for the mounting of the drift tubes and its alignment.

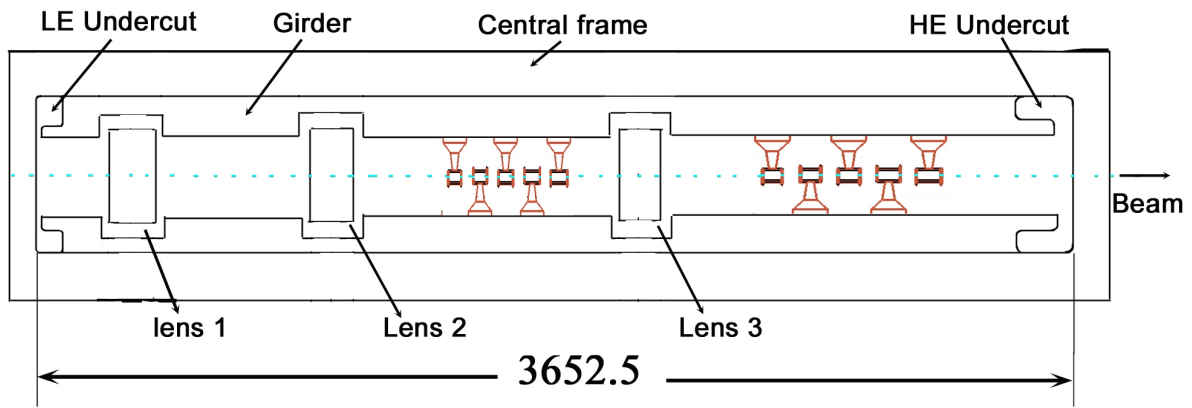


Fig.6.2 Top view on the central frame

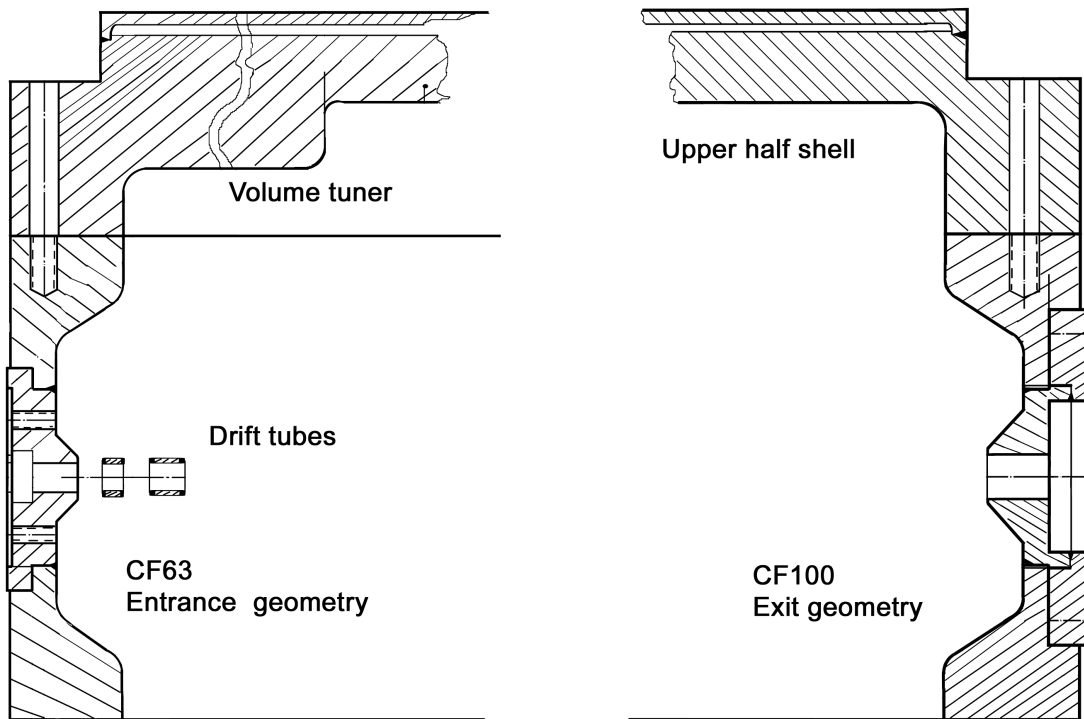


Fig.6.3 End geometry of the IH cavity

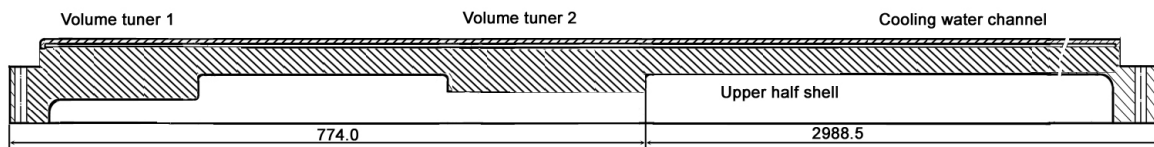


Fig.6.4 Variation of the contour of the upper and lower half shells along the cavity

The proposed entrance and exit geometry are shown in Fig.6.3. Using the standard CF63 and CF100 flanges simplifies the design of the end geometry and the vacuum sealing. The tuning effects of end flanges, which were discussed in

the last chapter (See chapter 5.4), have been taken into account in the end geometry design of IH power cavity.

As discussed in the chapter 5.2 and 5.4, the capacitance per unit length at entrance is much larger than at the exit, it is necessary to vary the cross sectional area of IH medical power cavity along the beam axis, this will decrease the local inductance at entrance section and result in the design of variation contours of the upper and lower half shells along the cavity. It is shown in the Fig.6.4 and Fig.6.5. Fig.6.6 shows the final geometry of the IH power cavity with the magnetic triplets.

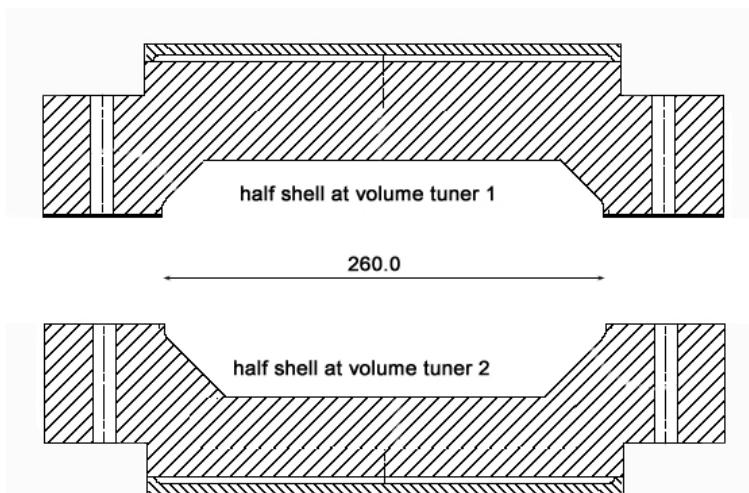


Fig.6.5 Cross sectional view of the half shells with different volume tuner

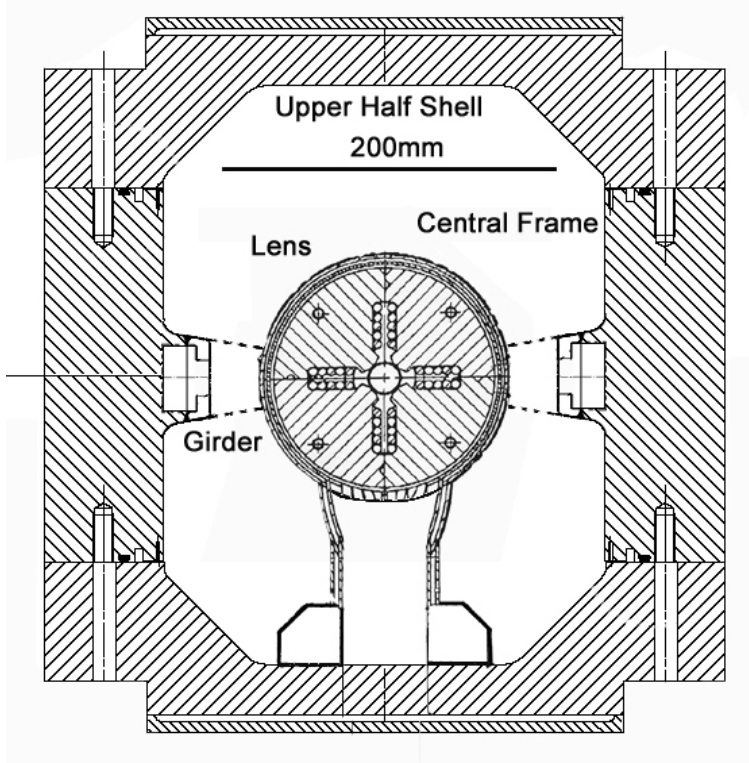


Fig.6.6 Final geometry of the IH power cavity with magnetic triplet

6.2 Calculations of IH cavity parameters

- Operating frequency

Based on the proposed IH power cavity geometry, we got the capacitance per unit length for IH-DTL in last section $C_{IHD}'=23.1\text{Pf}/\text{m}$, from equation (2.6), the equivalent capacitance for whole the cavity $C_e=C_{IHD}'L=23.1*3.72=85.93[\text{Pf}]$, and the equivalent inductance $L_e=L_{IHD}'/L=23.3/3.72=6.26[\text{nH}]$, so the resonance frequency of the IH-DTL power cavity $f=1/(2\pi(L_eC_e)^{1/2})=217.0[\text{MHz}]$.

- Stored energy

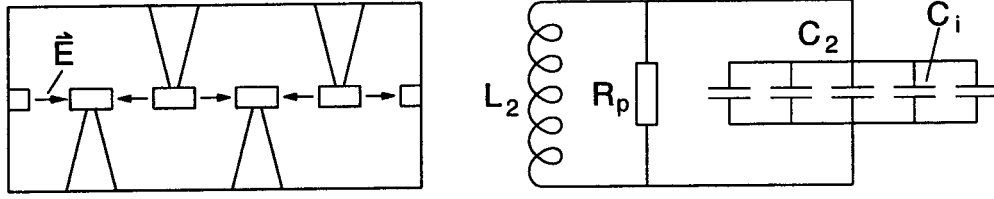


Fig.6.7 The equivalent circuit of IH-DTL

From the designed effective voltage distributions (Fig.4.5) and the transit time factor (Fig.4.4c) which are simulated by the LORASR for the real drift tube parameters, one can get the averaged amplitude voltage U_a of IH cavity:

$$V_{ia} = \frac{V_{ie}}{T_i}, \quad U_a = \frac{1}{N_g} \sum_{i=1}^{N_g} V_{ia}, \quad T = \frac{1}{N_g} \sum_{i=1}^{N_g} T_i \cdot \frac{V_{ia}}{U_a} \quad (6.1)$$

Here V_{ie} , V_{ia} note the effective and amplitude voltage of the i^{th} gap, T_i is the i^{th} gap transit time factor, T is the averaged transit time factor for IH cavity. so $U_a=0.4236\text{MV}$. From the last paragraph and equations (2.10), $C_2=C_e=85.93[\text{pf}]$, the stored energy W :

$$W = \frac{1}{2} C_e U_a^2 = 7.70 [\text{J}] \quad (6.2)$$

then the amplitude driven current:

$$W = \frac{1}{2} L_e I^2, \quad I = \left(\frac{2W}{L_e} \right)^{\frac{1}{2}} = \left(\frac{2 \cdot 7.70}{6.26 \cdot 10^{-9}} \right)^{\frac{1}{2}} = 4.96 \cdot 10^4 [\text{A}] \quad (6.3)$$

- Shunt impedance Z_0

Substituting $c_1=1.1$, $c_2=1.43$, $\beta_i=0.0293$, $\beta_j=0.1219$, $N_m=2$, $R_2=0.162\text{m}$, $\varphi_2-\varphi_1=2.819$ into the equation (2.10), then the shunt impedance:

$$Z_0 = 195.8 \text{ M}\Omega/\text{m} \quad (6.4)$$

- Quality factor

By inserting the above parameters into the equation (2.10), so the quality factor of the IH cavity:

$$Q \cong 13910 \quad (6.5)$$

- Power dissipation

According to the equation (2.9), the power dissipation of IH cavity is about 755kW. After the calculation of the RF dissipation surface areas of cavity wall, girders, drift tubes and its stems, and magnetic triplets, the power dissipation in percentage for the different components of IH-DTL power cavity is shown in Fig.6.8. Table 6.1 lists the RF power dissipation on the different components. Taking an example, if RF dissipation power of IH cavity is 800kW with 1% duty cycle, the cooling of IH cavity, girders, and triplets and so on should stand for correspondent RF power for long time stable operating.

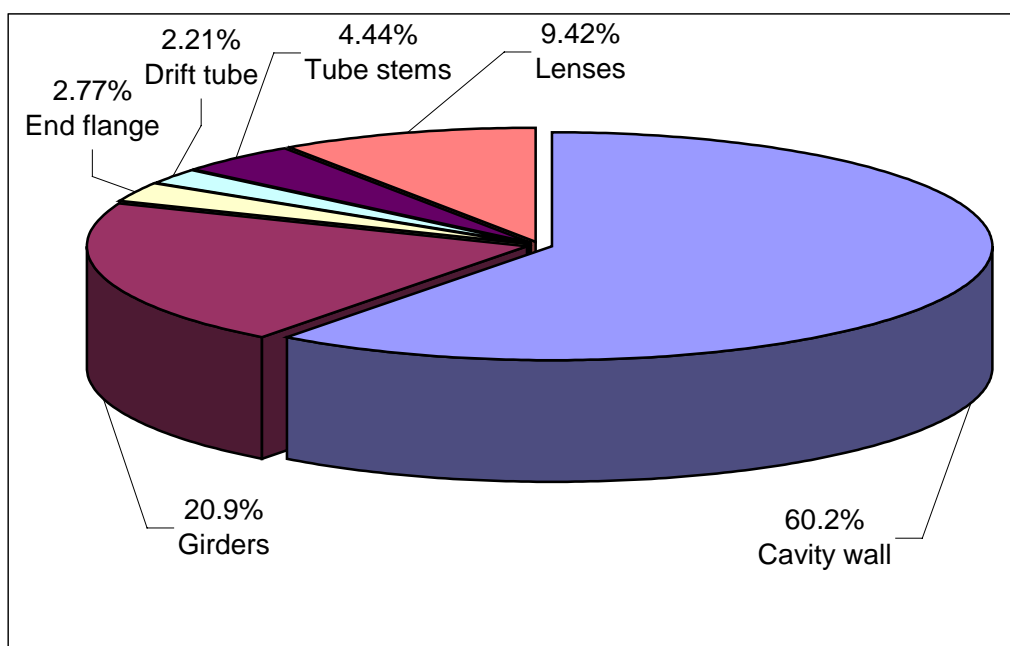


Fig.6.8 Diagram of the power dissipation on the cavity components

Table 6.1 RF power dissipation estimation

Item	Area (m ²)	Percent (%)	Power (kW)
Total	5.96	100.00%	800.0
Tube stems	0.264	4.44%	35.5
End flanges	0.165	2.77%	22.2
Drift tubes	0.131	2.21%	17.7
Lenses	0.561	9.42%	75.3
Girders	1.247	20.93%	167.4
Cavity wall	3.590	60.24%	481.9

6.3 RF feeder design

For the Heidelberg cancer therapy project, the beam power of accelerated heavy ion is small. The input impedance of in-coupling loop was almost not

changed with the accelerating ions. So the in-coupling loop is only designed to create the RF cavity amplitude voltage U_a , which is shown in the formula (6.1). This energy is transferred by the magnetic induction \vec{B} . It should be the same with the magnetic field strength, which is generated by the magnetic in-coupling loop. The B determines the in-coupling loop area together with the RF power dissipation.

To assume that the magnetic field B is homogeneous in the IH cavity, it can be calculated by the following formula (see Fig.2.2 and equations (2.10) and (6.2))

$$W = \frac{1}{2 \cdot \mu_0} \iiint_V B_0^2 \cdot dV \approx \frac{1}{2\mu_0} B_0^2 V \quad (6.6)$$

Here, $W=7.70\text{J}$, the magnetic permeability in vacuum free space $\mu_0=4\pi \times 10^{-7}$, the volume V of the IH cavity is $0.272[\text{m}^3]$, then the magnetic induction $B_0=8.44\text{mT}$.

This can be checked in the following way, the reference [2.1] gives the next formula:

$$B_z = B_0 = \frac{E_0(r) \cdot 2r}{\omega(R_2^2 - r^2)} \quad (6.7)$$

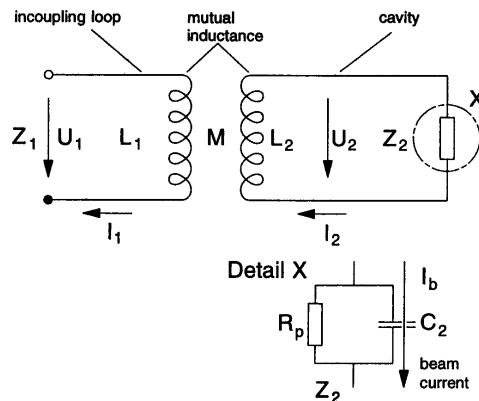


Fig.6.9 In-coupling loop with IH-DTL cavity

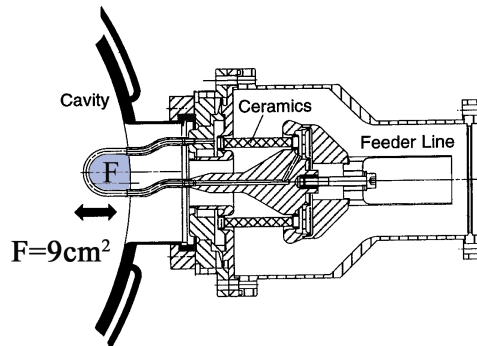


Fig.6.10 The RF feeder structure

Here $E_0(r)$ can be replaced by the electric field strength on the longitudinal axis at r , because there is nearly no magnetic field in the center area.

$$E_0(r) = \frac{U_a \cdot N_g}{L} = 6.38(MV/m) \quad (6.8)$$

Taking the equivalent geometrical average radius R_2 of the IH cavity, from the chapter (6.1) and Fig.2.2 and Fig.6.1, the equivalent circle radius $R_2=0.162m$, $r_a < r < R_1$ in the formula can be figured out by the averaged out radius of drift tubes 10.8mm for all sections ($10.8=(8*9.0+11*10.0+16*11+17*12)/52$), according to the experience of existing IH-DTL cavities, $r=2.15*10.8=23.2mm$, here 2.15 is the radius modification factor. Substituting R_2 , $r=0.0232m$, $f=216.816MHz$ and $E_0(r)$ to the formula (6.7), then $B_0 = 8.46$ mT, it fits above result so well.

As mentioned before, the beam loading effect for the heavy ions is very small in the IH-DTL medicine accelerating cavity, the input impedance Z_1 of the in-coupling loop in the Fig.6.9 must be matched with the characteristic impedance of RF transmission line, RF amplifier and the transmission line are already matched. Z_1 should equal to the characteristic impedance $Z_0=50\Omega$ of RF transmission line (see Fig.6.9). There is no RF power losses when RF power is feed into the IH-DTL cavity, so the amplitude voltage in the in-coupling loop:

$$U_{loop} = \sqrt{2 \cdot P \cdot Z_0} \quad (6.9)$$

Meanwhile it generates the needed B_0 in the IH-DTL cavity through the in-coupling loop area S :

$$U_{loop} = \left| \frac{d\Phi}{dt} \right| = \omega \cdot S \cdot B_0 \quad (6.10)$$

So:

$$S = \frac{U_{loop}}{\omega \cdot B_0} = \frac{\sqrt{2 \cdot P \cdot Z_0}}{\omega \cdot B_0} \quad (6.11)$$

Substituting $P=0.755MW$, $Z_0=50\Omega$, $f=216.816MHz$, $B_0=84.4$ gauss into (6.11), then the in-coupling loop area $S=0.755*10^{-3}m^2=7.55cm^2$.

The RF feeder structure is shown in Fig.6.10. The shape of the loop can be similar with Fig.6.10; needed loop area is $7.55cm^2$. The loop area could be made a bit larger ($9cm^2$) and be readjusted by turning during the cavity input impedance measurement.

Chapter Seven

Microwave Studio Simulation of the IH Cavity

This chapter will present the simulation results of the 1:2 scaled IH model cavity and of the actual power cavity for the Heidelberg Cancer Therapy Project. The following subjects will be discussed:

- The simplification of the simulation for the IH cavities
- The electric and magnetic field distribution
- The shunt impedance comparing to the technical design
- The simulation of the high order modes.

7.1 Introduction of the Simulation Software

The software used for the simulation is CST MICROWAVE STUDIO. It is a general purpose electromagnetic simulator based on the Finite Integration Technique (FIT) ^[7.1]. It has been used to design many projects successfully^[7.2] and upgraded to versions 5.0. Meanwhile FIT discretizes the integral form of Maxwell's equations, rather than the differential equations. It is suitable to simulate various electromagnetic problems, ranging from the static field distributions to high frequency applications in the time and frequency domains. The mesh setting or creating system for the different applications is the key of the simulation; higher mesh density means higher simulation accuracy but longer simulation time and a need for enormous computer resources. The mesh setting and simulation methods are discussed very detailed in the specifications of CST MICROWAVE STUDIO^[7.3]. Nowadays, the personal computer is developing rapidly. Faster CPU and great computer resources provide the possibility to simulate the whole IH cavity by the CST MICROWAVE STUDIO on a standard PC.

7.2 Simplification of the IH cavity for the Microwave Studio Simulation

After setting the structure into the Microwave Studio interface, the 1:2 scaled IH model cavity is shown in the Fig.7.1—Fig.7.3, the blue line is the beam axis, and the sketch of the 1:2 scaled and symmetrized IH power cavity is shown in Fig.7.4—Fig.7.6 (Note the different cavity cross section in Fig.7.6). Y-z plane figures show the drift tubes, their supporting stems, girders and undercuts clearly. X-z plane figures show the triplets and its supporting stems, which are

installed 90 degrees apart from the y-z girder plane, see Fig.7.2 and Fig.7.3. It brings the advantage of ground level RF voltage, but the disadvantage is that it breaks the symmetry of the IH cavity. That was why the IH Microwave Studio simulation was done for full cross section at the very beginning. The 2.5million mesh points were taken, the simulation took about 36 hours for 5 iterations and 10 modes, but the simulation results were often not accuracy enough because of the limitation of mesh points. If taking more mesh points, it makes the simulation too long time and the computer is also overloaded, the simulation will be stopped when no computer resource is available meanwhile no any result is reported in the software result log-files. It leads then very difficult to do the optimisation.

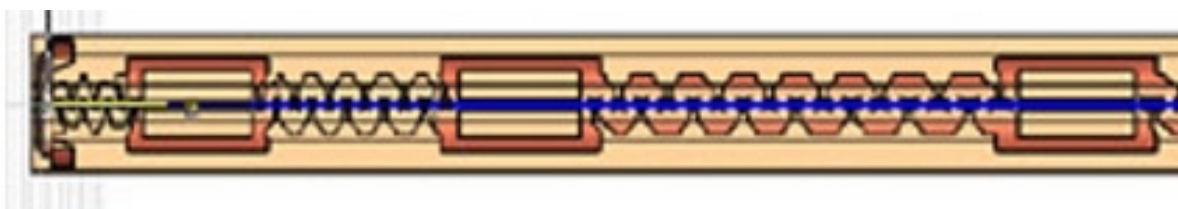


Fig.7.1 Part of y-z plane view of IH 1:2 model cavity

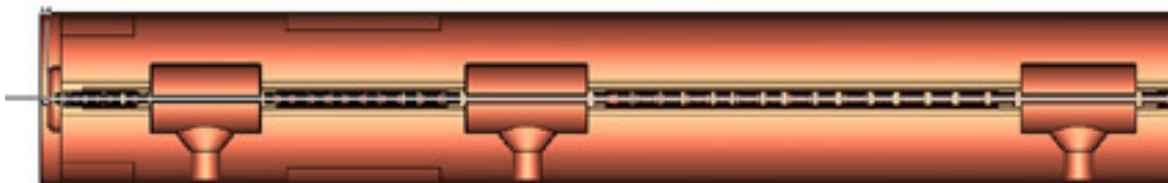


Fig.7.2 Part of x-z plane of IH 1:2 model cavity (asymmetric lens stem)

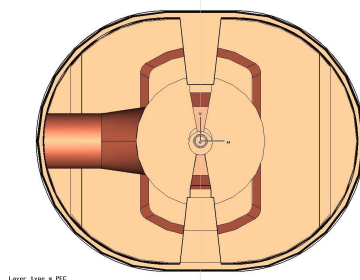


Fig.7.3 Cut of z-plane of IH model cavity (left view of above figure)

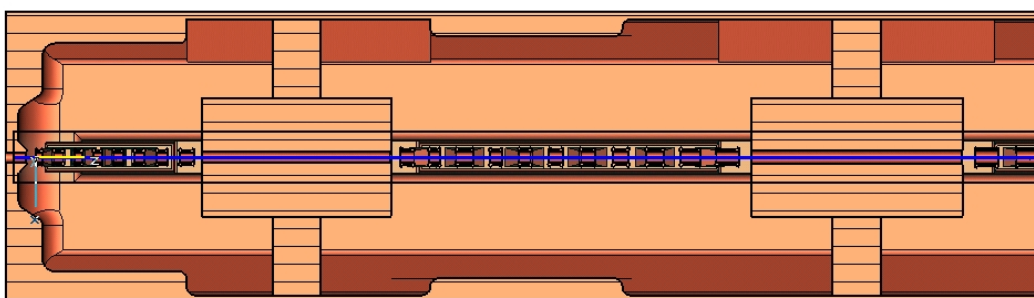


Fig.7.4 X-Z plane of IH power cavity (after symmetrization)

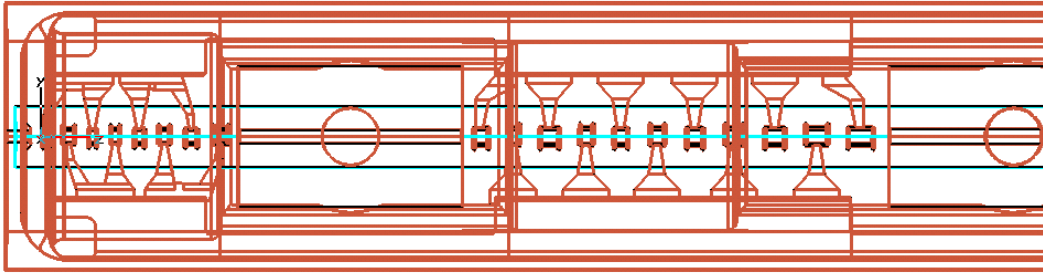


Fig.7.5 Y-Z plane of IH power cavity divided into 3 parts
(blue cylinder volume around drift tubes with highest mesh points density)

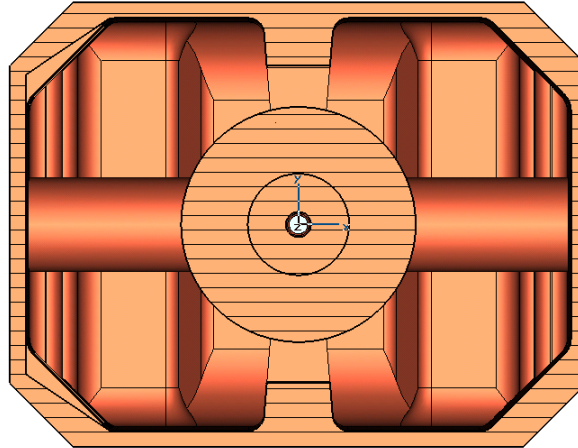


Fig.7.6 Z plane cut view of IH power cavity (after symmetrization)

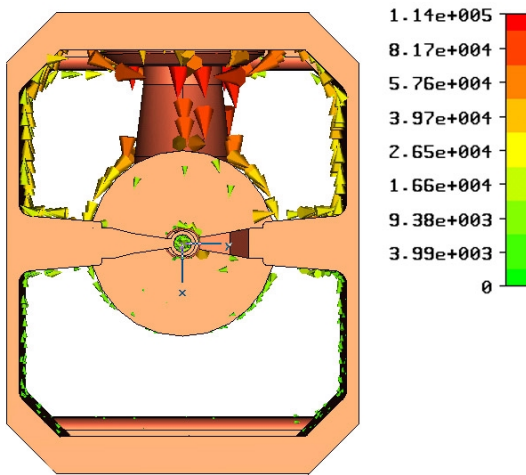


Fig.7.7 Mode 1 (305MHz)
for triplet 1

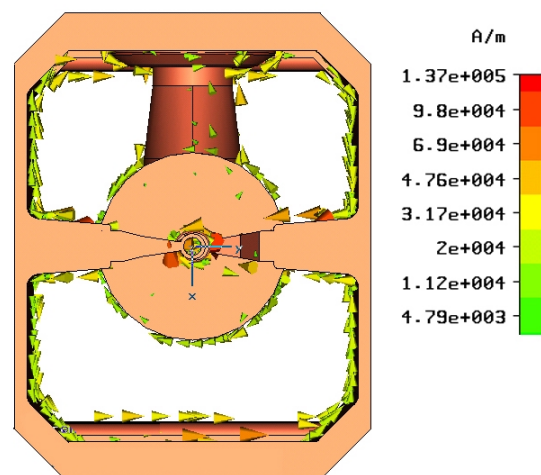


Fig.7.8 Mode 2 (H_{110} 443.4MHz) for
triplet 1

Fig.7.7 and Fig.7.8 show the real geometry at lens position and also the surface current flowing of mode 1 and mode 2 of real supporting stems around the first lens (triplet). Actually, for the correct operating mode Fig.7.8, there is no or less current that is flowing along the lens stems. The surface current flowing is also symmetric in the upper and lower half cavity. That means one

can use the simple symmetric supporting stems to replace the original asymmetrical one.

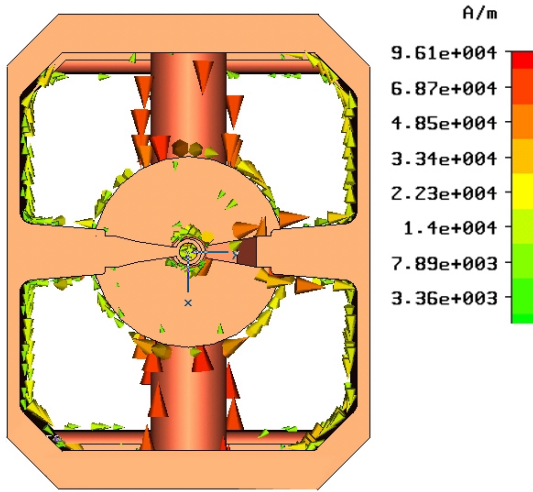


Fig.7. 9 Mode 1 (410.7MHz) for triplet 1

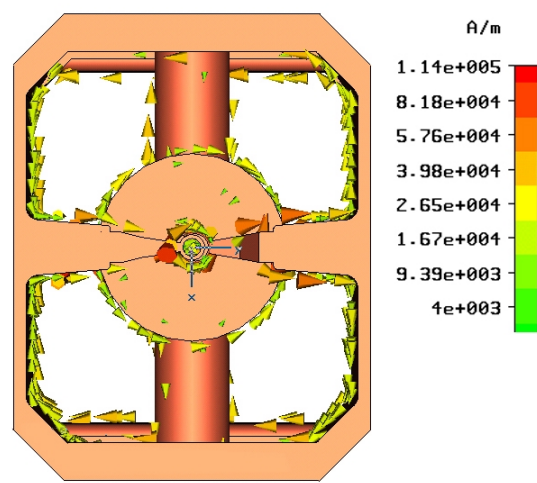


Fig.7. 10 Mode 2 (H_{110} 444.6MHz) for triplet 1

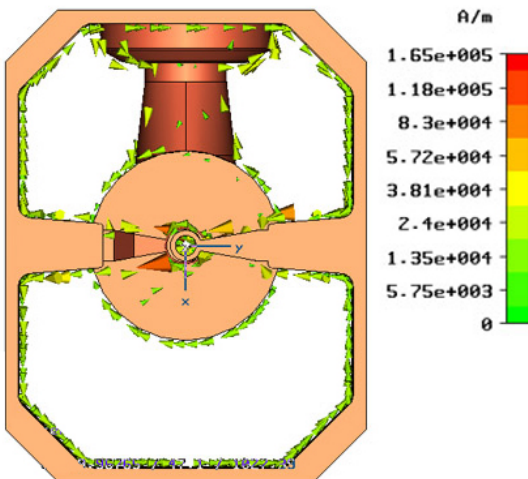


Fig.7.11 H_{110} mode (462.00MHz) for triplet 3 (real stem)

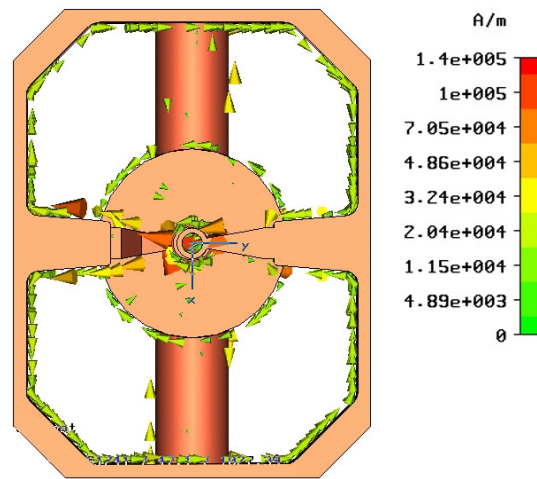


Fig.7.12 H_{110} mode (462.06MHz) for triplet 3 (symmetric stem)

In order to optimise the diameter of symmetric cylinder supporting stems, the triplet's parts including only two gaps at each side are simulated. If the symmetric cylinder stems are used to replace the real lens stem, it should have the frequency as near as possible with the correct mode frequency, while the diameter of the cylinder stem should fit the simulation for the other two triplets too. The boundary condition for such simulation is $H_t=0$ at the cut z end plane of the cavity, that means only H_z exists. The minimum and maximum of x and y

boundaries are $E_t=0$ (that means no fields exist outside of the cavity). After optimization, 30mm is the adopted diameter of the symmetric supporting cylinder stems. The maximum simulated H_{110} mode frequency difference is only 0.28% higher than that of real asymmetric stem (see Fig.7.9—Fig.7.10). Fig.7.11 and Fig.7.12 compare the simulated frequency difference of the triplet 3 for the correct mode H_{110} . Actually, there isn't the mode that was shown in Fig.7.9 for the real model and power cavity.

7.3 The Field Distribution for the 1:2 Scaled IH Model and Power Cavity

After the simplification of the unsymmetrical supporting stems by the 30mm symmetric cylinder stems, the Microwave Studio simulation could be performed for half the cross section of the IH cavity, this leads to a sufficient mesh points number of 2.2 million. It makes the simulation faster (about factor of 2 compared with a 2.5 million mesh points on the whole cavity), and enhances the computing accuracy very efficiently. In order to have a more reasonable mesh point distribution, a mesh cylinder was defined around the drift tubes, where the cubic mesh grid with 1mm increment is used. Fig.7.13 shows the mesh distributions of the IH power cavity. Table 7.1 lists some data concerning the simulations for the model and the 1:2 scaled power cavity.

Table 7.1 Some data concerning the simulation of 1:2 scaled IH-DTL

	IH model cavity	IH power cavity
Cavity Dimensions /mm*mm	180*140	172*130
Length(inner) /mm	1860	1860
Smallest mesh step /mm	1.00	1.11
Biggest mesh step /mm	6.0	11.14
Number of mesh points	2346204	2226048
CPU time	11h29m25s	23h59m26
LE undercuts length /mm	21.5 (no edge blending)	21.5 (edge blended)
HE undercuts /mm	32.5 (no edge blending)	32.5 (edge blended)
Frequency /MHz	433.837	434.167
Computer performance	Intel(R) Xeo 2.4GHz, 2.096GRAM	Intel(R) Xeo 1.4GHz, 1.047GRAM

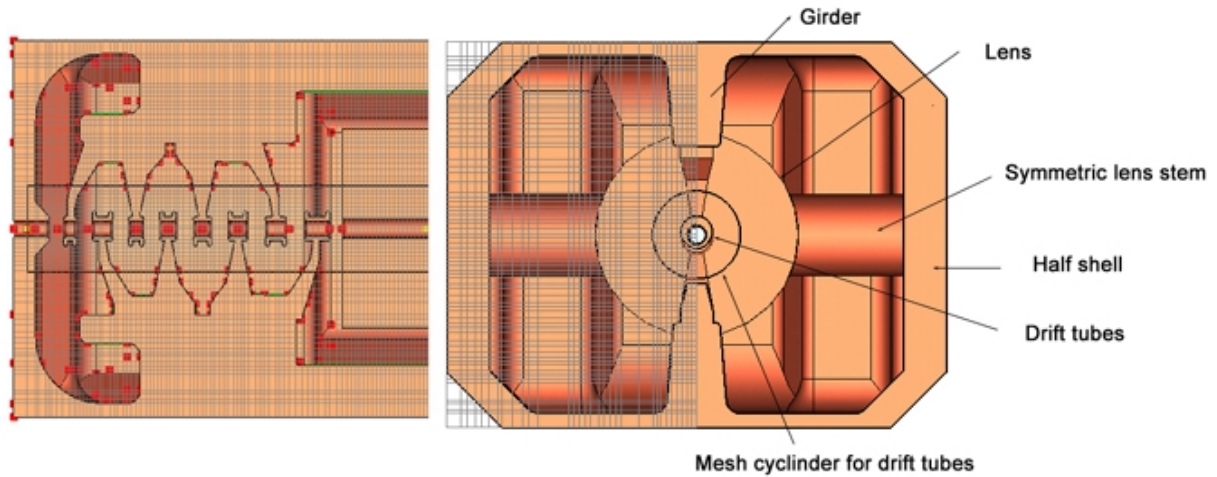


Fig.7.13 Mesh distributions of IH power cavity

The following figures show the microwave studio simulation results of the 1:2 scaled IH model cavity. The electric field distribution along the IH-DTL is shown in Fig.7.14. Fig.7.15 draws the 2d vector view of electric (black and gray) and magnetic field (colour) distributions. The surface current cross sectional view of the IH model is shown in Fig.7.16, this leads to the correct H_{110} magnetic distribution (Fig.7.17).

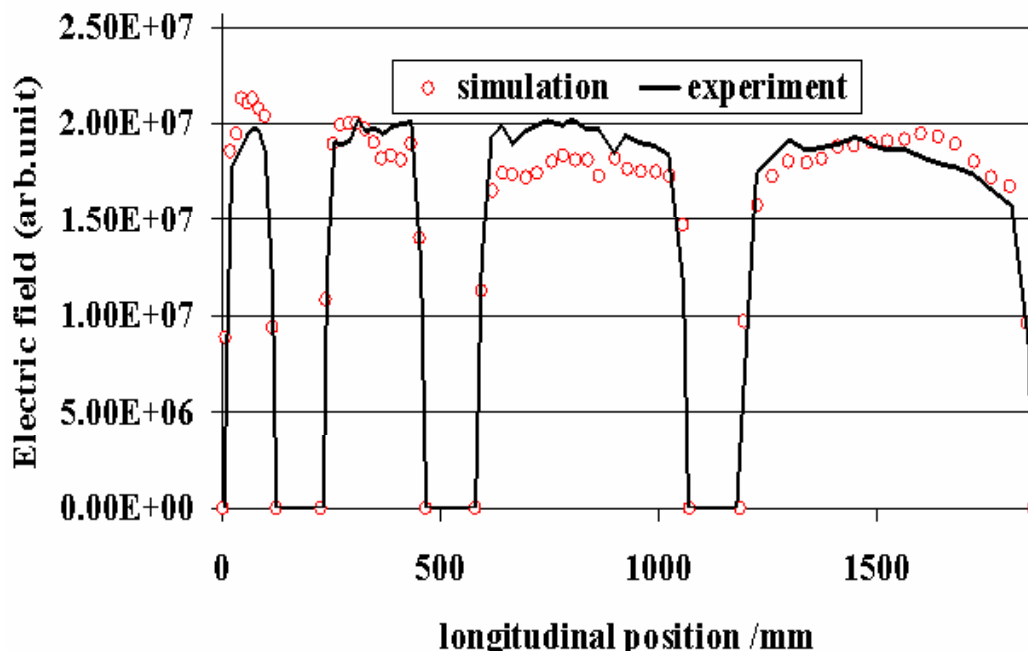


Fig.7.14 The electric field distribution along the IH-DTL (Model)

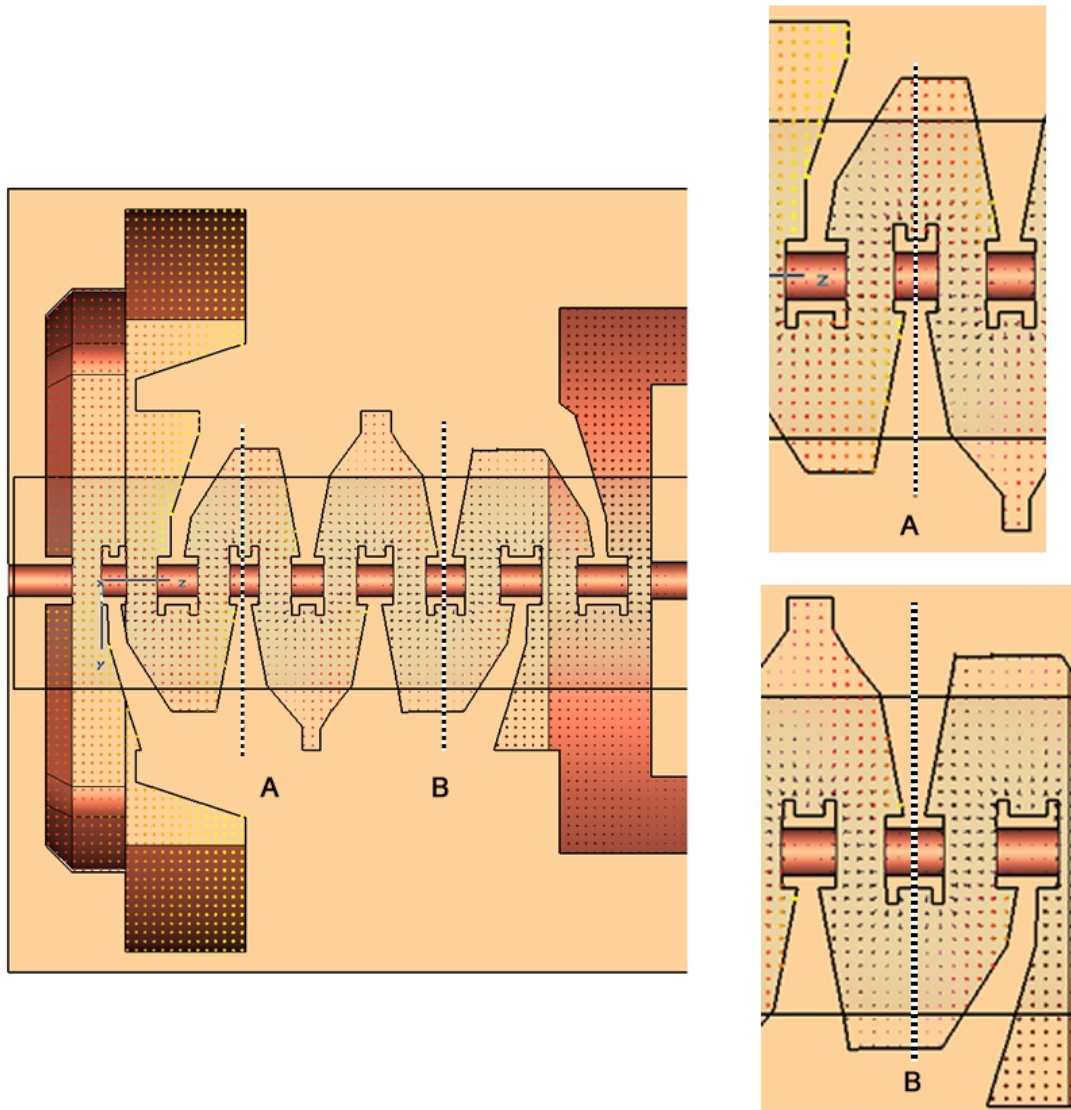


Fig.7.15 Electric (black and gray) and magnetic (colour) field distribution at low energy end (Model Cavity)

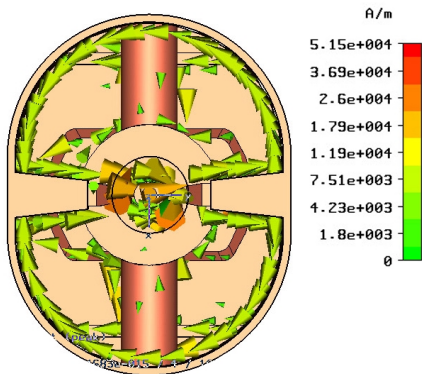


Fig.7.16 Surface current of IH model cavity

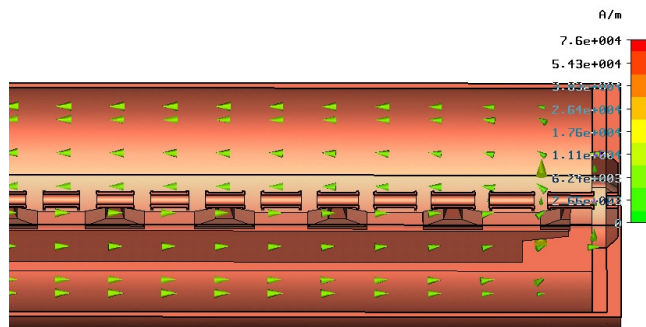


Fig.7.17 Magnetic field distribution (IH model cavity)

The cross section of the IH power cavity is quite different from the model. It is more robust and has more flat plane, which is more easily for manufacturing and provides the convenience of the installing of vacuum and other device. The cross section has been shown in some figures. Both cavities have the similarity of the H-field and surface current flow.

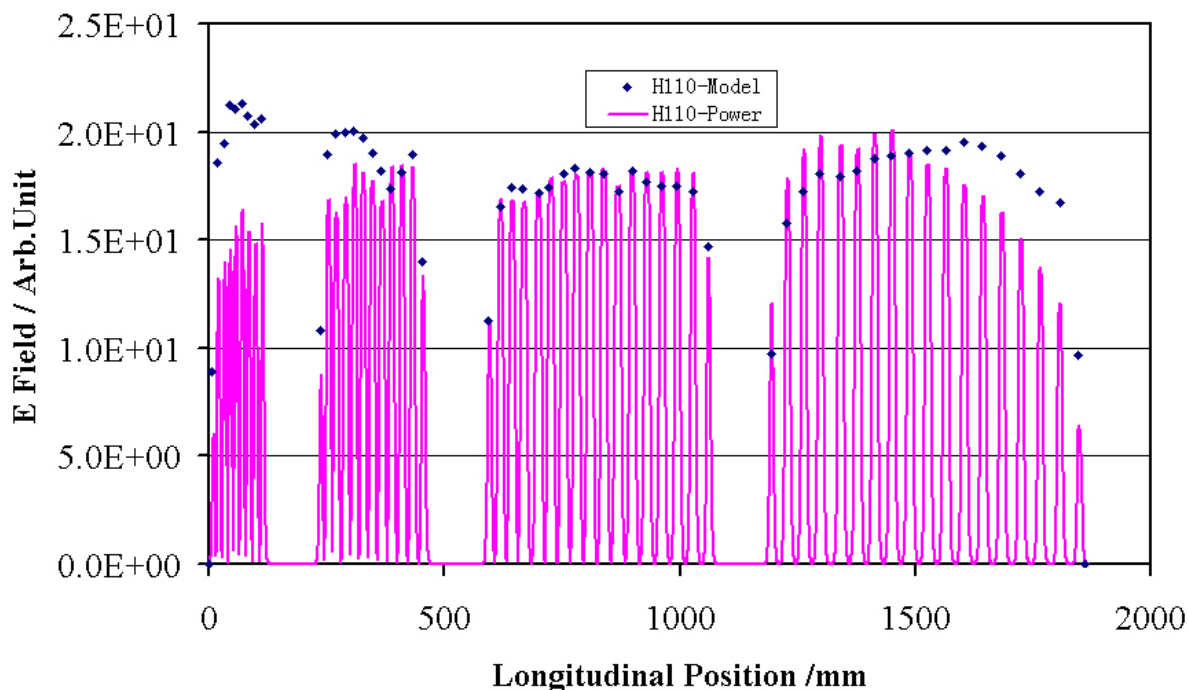


Fig.7.18 The field distributions of IH model and power cavity

The gap effective voltage for each gap equals to the product of the gap integrated amplitude voltage and the transit time factor output by the LORASR software. Fig.7.18 shows the electric fields at both ends are smaller (red curve), that is the reason why the effective voltages at both ends are less than the needed. This can be explained by the size decreasing of the undercuts due to the undercuts curvature. Fig.7.19 shows the simulated and designed effective voltage distributions for the real power cavity. This will be tuned by adding additional capacitance copper blocks on the girders opposite to correspondent drift tubes during the power cavity measurements. The simulations give the guidance of power cavity tuning.

Fig.7.20 shows the magnetic H_z component distribution along the line that is near the cavity wall and parallel to the z-axis. One can exit this data and make the averaged magnetic intensity, it is 6678.5A/m for 1:2 scaled IH power cavity with the stored energy 1.0J, for the real size power cavity by the factor of 2, the volume of the cavity will be 8 times larger, the scaled stored energy will be 8.0J,

actually, the stored energy is 7.70J (see the chapter 6.2 and formula (6.2)), so the simulated magnetic intensity of the real size IH power cavity is:

$$W = \frac{1}{2} \mu_0 H^2 \cdot V, \quad H = \left(\frac{7.70}{8}\right)^{1/2} \cdot 6678.5 = 6556.3 [A/m], \quad B = \mu_0 \cdot H = 82.3[Gauss]$$

This fits the result in the chapter (6.3).

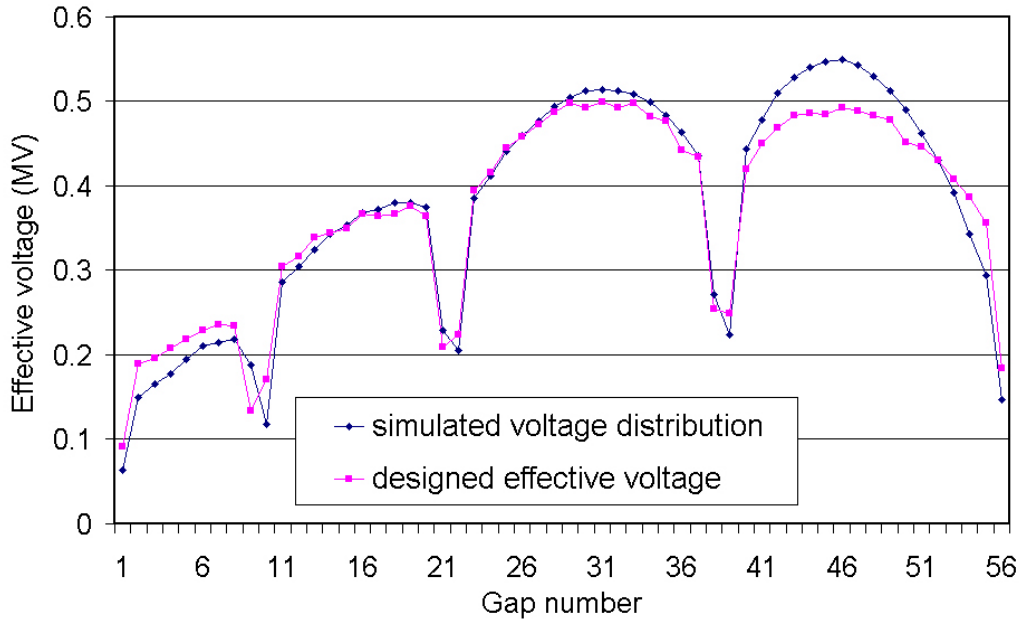


Fig.7.19 The simulated (MWS) and designed effective voltage distributions for the power cavity

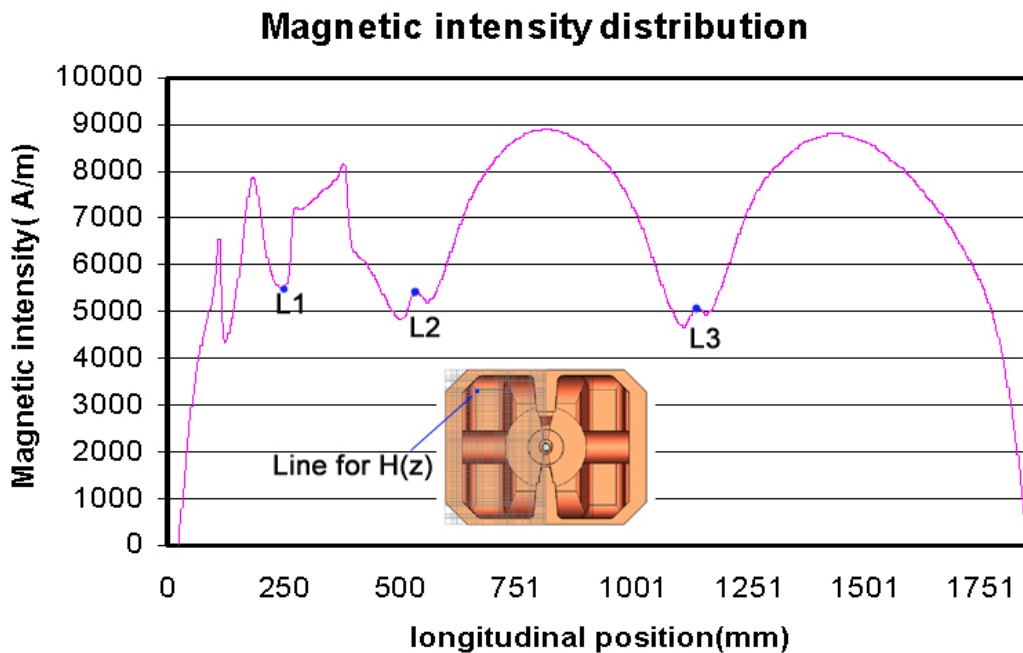


Fig.7.20 The simulated magnetic intensity distribution

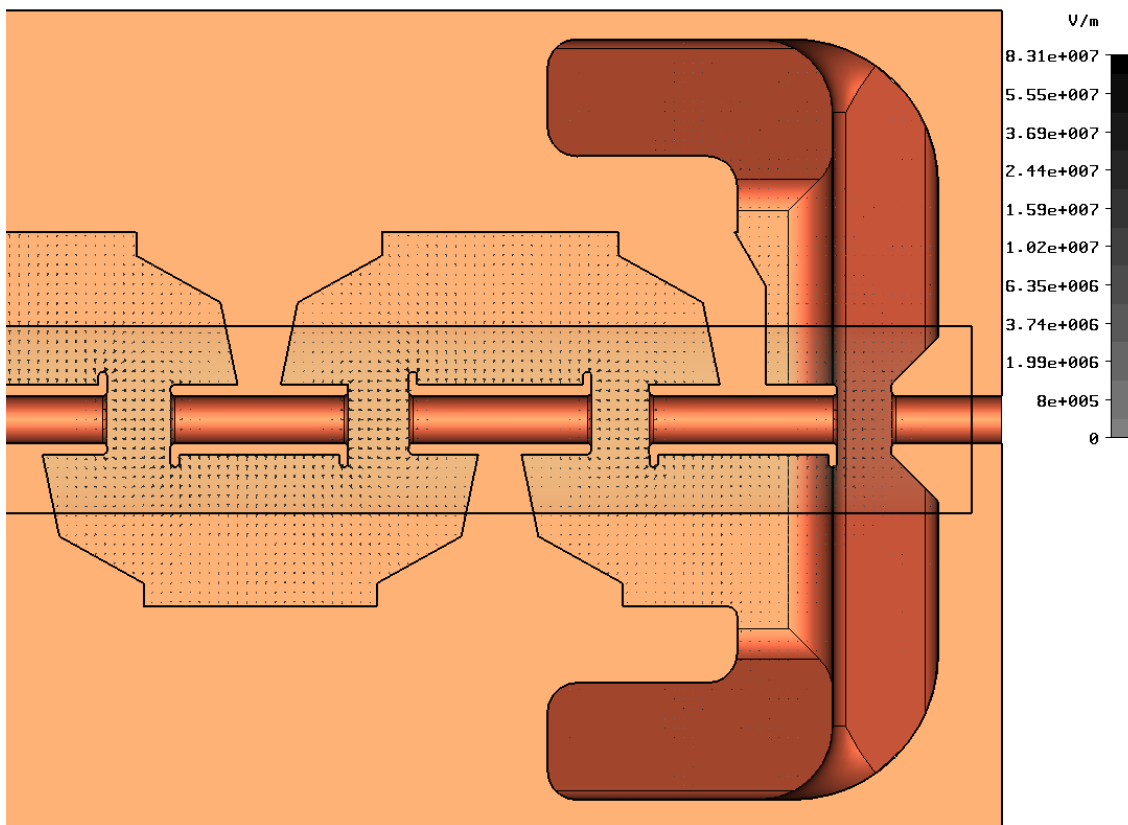


Fig.7. 21 Electric field distribution at high energy end (power cavity)

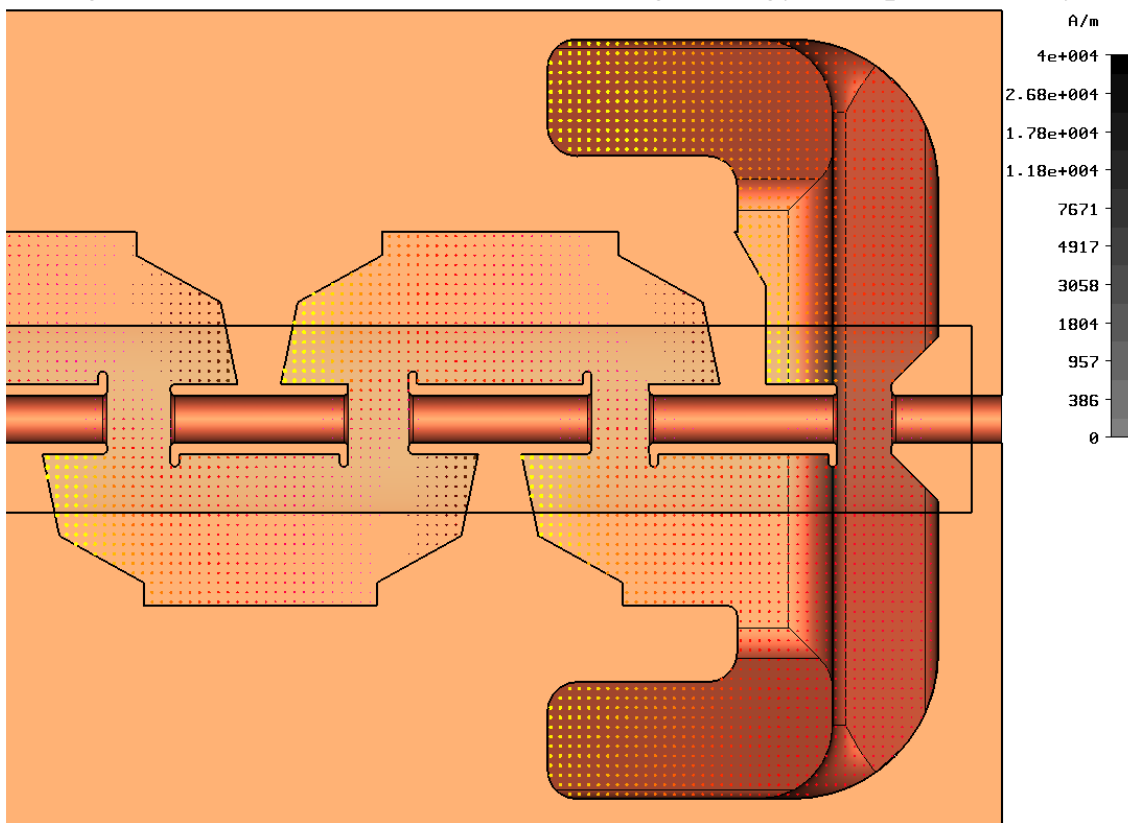


Fig.7. 22 Magnetic field distribution at high energy end (power cavity)

One can see the electric field distribution at high energy end for the IH power cavity in Fig.7.21, while the magnetic distribution is symmetric around every drift tube stem shown in Fig.7.22.

7.4 Shunt Impedance and RF Power Dissipation for IH Real Power Cavity Simulated by MWS

In this section, the shunt impedance and RF power dissipation for the IH real power cavity will be recalculated based on the MWS simulation. It is worth to check the calculation in the last chapter 6.2. From the microwave studio simulation, the peak power dissipation for 1:2 scaled power cavity is about 494.6kW, the reduced conductivity $5.0 \cdot 10^7 \Omega^{-1} \text{m}^{-1}$ has been used from the experience, the integrated amplitude voltage along the axis is 11.42MV, the inner length of 1:2 scaled cavity is 1.86m, so the shunt impedance Z_o is 283.5 M Ω /m, the average transit time factor for the power cavity is about 0.874, so the simulated effective shunt impedance Z_{eff} is 216.5 M Ω /m. The table 7.2 lists the principle parameters of the simulated 1:2 scaled power cavity and the predicted real size IH power cavity.

For the real IH-DTL power cavity, the operating frequency will be nearly half of model frequency 434.11MHz, the shunt impedance is proportional to $R_2^3 \cdot \omega^{7/2}$, R_2 is two times of 1:2 scaled values, but the frequency is only half of that, so the shunt impedance is proportional to the square root of frequency, it will be:

$$Z_{\text{eff}(1:1)} = Z_{\text{eff}(1:2)} \cdot \sqrt{216.816/434.11} = 153.0(\text{M}\Omega/\text{m}) \quad (7.1)$$

$$Z_{o(1:1)} = Z_{o(1:2)} \cdot \sqrt{216.816/434.11} = 200.3(\text{M}\Omega/\text{m})$$

For the real power cavity, the inner cavity length is 3.718m, the predicted RF power dissipation by above shunt impedance (7.1) and needed averaged amplitude voltage $U_a=0.4236\text{MV}$:

$$P = \frac{U_a^2 \cdot N_g^2}{Z_o \cdot L} = \frac{(\sum_{i=1}^{N_g} V_{\text{ieff}} / T_i)^2}{Z_o \cdot L} = 0.755\text{MW} \quad (7.2)$$

Here the copper conductivity used by the Microwave studio is $5.0 \cdot 10^7 \Omega^{-1} \text{m}^{-1}$, which is about 10.7% lower than the theoretical value $5.6 \cdot 10^7 \Omega^{-1} \text{m}^{-1}$. So the shunt impedance Z_o verifies the technical design from the experienced formulas.

When IH cavity is used to accelerate the proton beam, the accelerated beam current is $I_{\text{dc}}=1.5\text{mA}$, the equivalent beam current for the IH cavity:

$$I_{b0} = 2 \cdot T \cdot N_g \cdot I_{\text{dc}} = 146.78(\text{mA}) \quad (7.3)$$

so the accelerated beam power:

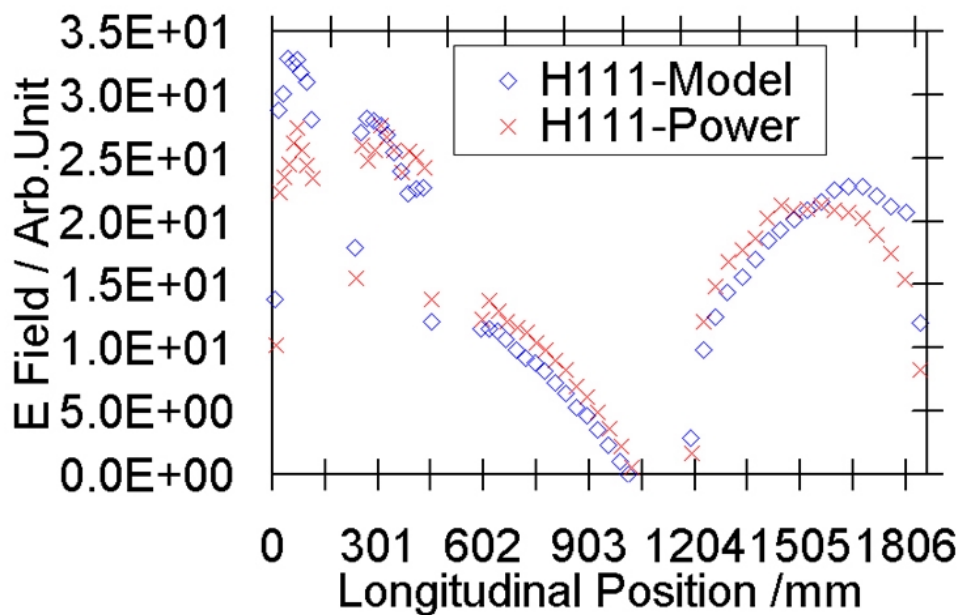
$$P_b = \frac{1}{2} U_{pa} \cdot I_{b0} \cdot \cos \phi_s = \frac{1}{2} \cdot \left(\frac{1}{3} U_a \right) \cdot I_{b0} \cdot \cos \phi_s = 10.4 \text{ (kW)} \quad (7.4)$$

The zero proton current acceleration for IH cavity needs 1/9 of full RF power 755kW, i.e. 83.8kW. So for proton acceleration the in-coupling loop area should be 11% larger to compensate the beam loading effects. Because of the difference of the cavity quality and the performance of the RF amplifier at full power output, for the safety, the RF amplifier should output more than 15-20% of needed RF power. Table 7.2 lists the principle parameters.

Table 7.2 The parameters of therapy IH cavity

	1:2 power cavity (MWS)	Real power cavity (predicted)
Power dissipation	494.61 (peak) kW	755kW(average)
Quality factor	11030	15600
Conductivity	5.00E+07	5.00E+07
Integrate amplitude voltage ($U_a N_g$)	11.42 MV	23.72
Frequency	434.11 MHz	216.816
Inner length (m)	1.86 m	3.72
Outer length (m)		3.77
Shunt impedance Z_0	283.5 MΩ/m	200.3
Effective shunt impedance Z_{eff}	216.5 MΩ/m	153.0

7.5 The Simulations of Higher Order Modes


 Fig.7.23 “H₁₁₁” Mode for the IH model and power cavities

In chapter 5, the field distributions of high order modes for the IH model cavity have been measured and presented (see Fig.5.5.2—Fig.5.5.5). In order to make a comparison, the simulation results for the IH model and power cavities will be presented in this chapter. Fig.7.23—Fig.7.26 draws the simulated field distributions of modes H_{111} - H_{114} , respectively. From these figures, one can see the field distributions for the higher order modes fit the experiments very well. Because the H_{111} is the most dangerous higher order mode, the in-coupling loop is set to the zero field point of H_{111} mode, this is very helpful to excite the needed H_{110} mode.

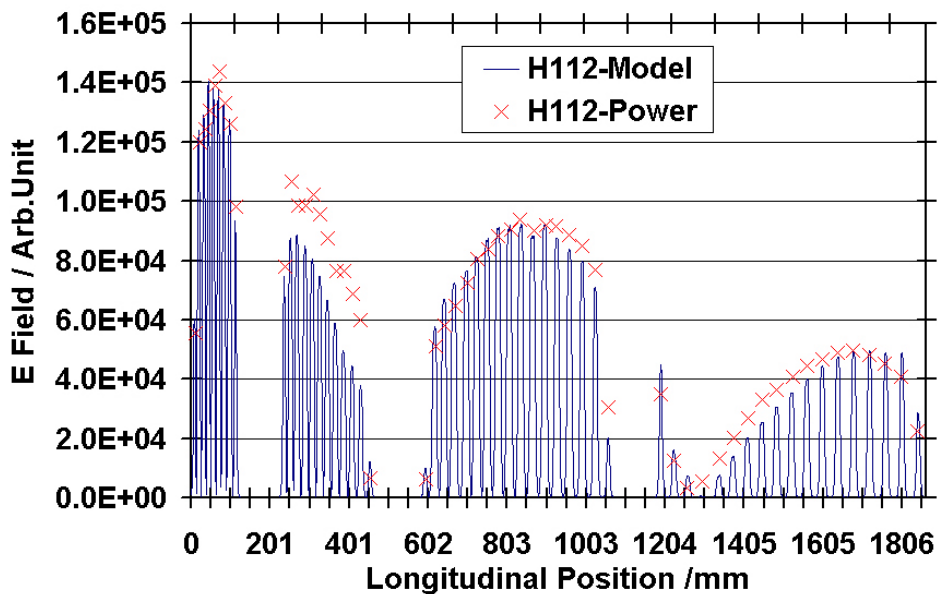


Fig.7.24 “ H_{112} ”Mode for the IH model and power cavities

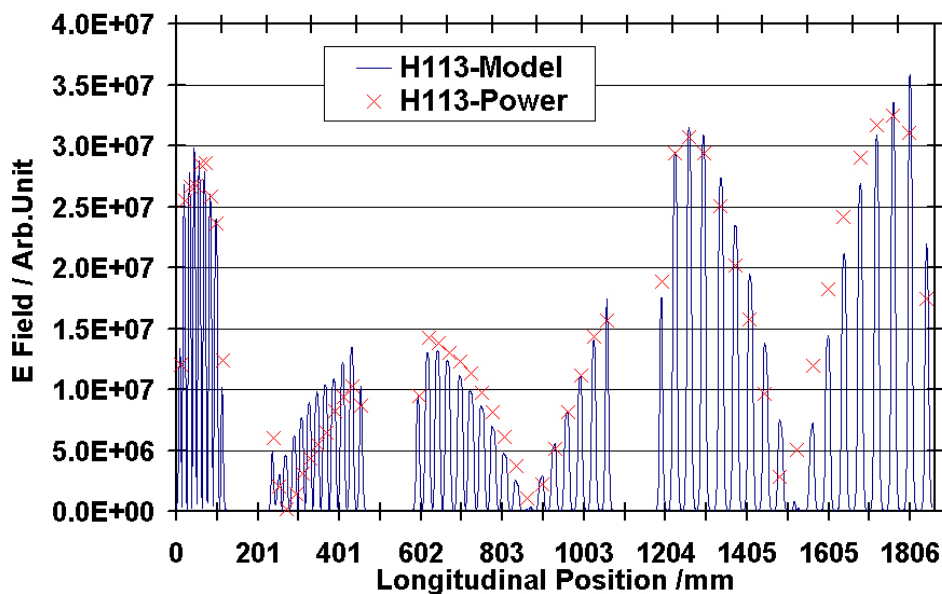


Fig.7.25 “ H_{113} ”Mode for the IH model and power cavities

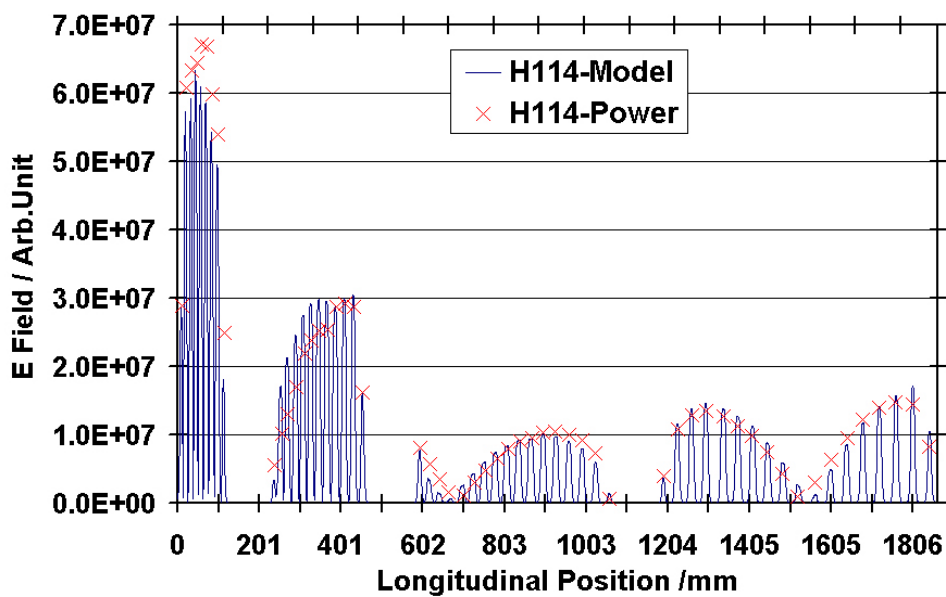


Fig.7.26 “H₁₁₄” Mode for the IH model and power cavities

Chapter Eight

The RF Measurements of the IH-DTL Power Cavity

The RF measurements on the IH-DTL power cavity during production at the company are needed to get the required precision of the gap field distribution as well as the resonance frequency. The following measurements were performed:

- The resonance frequency measurement
- The field distribution without any plunger
- Plungers in the 3rd and the 4th sections additionally

Furthermore, MWS simulations were performed with respect to the cutting of the IH cavity half shells and of volume tuners in the 1st section.

All above mentioned investigations will be presented and discussed in this chapter.

8.1 Assembling of the IH Power Cavity at PINK Company

The HICAT IH-DTL cavity with an additional height of 7mm for the upper and lower cavity half shells with respect to the expected sizes had been manufactured in November 2004 at PINK Company, Germany. All drift tubes were copper plated in the GSI copper-plating laboratory. Fig.8.1 shows some of the copper plated drift tubes. According to technical requirements of the triplets and to cooling needs, the final triplet geometry was redesigned. The lengths of triplets were kept because of the beam dynamics design, but the triplet stems were enlarged once more. The dummy lenses were machined in IAP and copper plated in GSI. One of the un-copper plated dummy lenses is shown in Fig.8.2. The enlarged triplet stems reduce the field in the 1st section, as discussed in chapter 5.



Fig.8.1 Some original drift tubes after copper plating

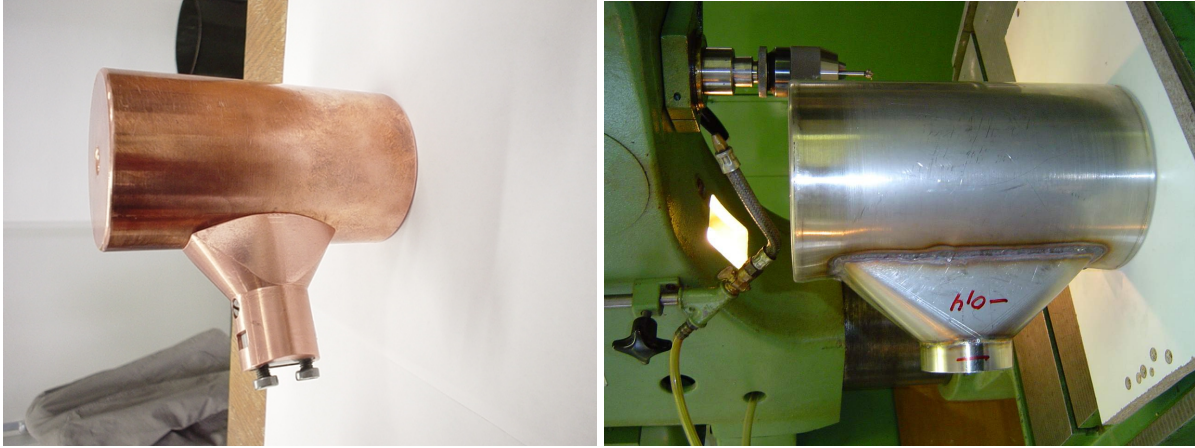


Fig.8.2 Triplet stem for model (left), triplet stem shape for power cavity (right)

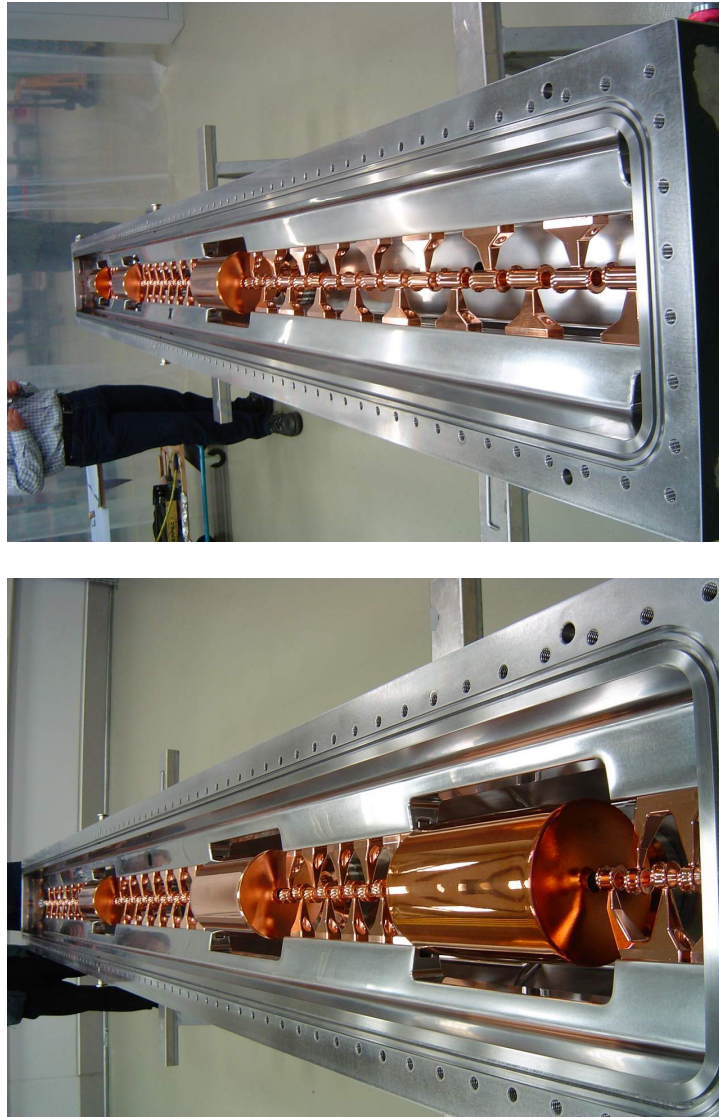


Fig.8.3 View on the drift tube structure of the IH-DTL power cavity, mounted on the central frame

After mounting the drift tubes inside the cavity, the real power cavity looks like shown in Fig.8.3. The cavity central frame, upper and lower half shells are not copper plated yet. This makes the cavity quality factor much lower, but the resonance frequency as well as the relative field distributions is quite independent from the quality factor Q as long as the Q -values are better than 100 in all cases. By the measurements the final cavity geometry with respect to some key parameters was defined.

8.2 The Initial RF Measurements of the IH Power Cavity

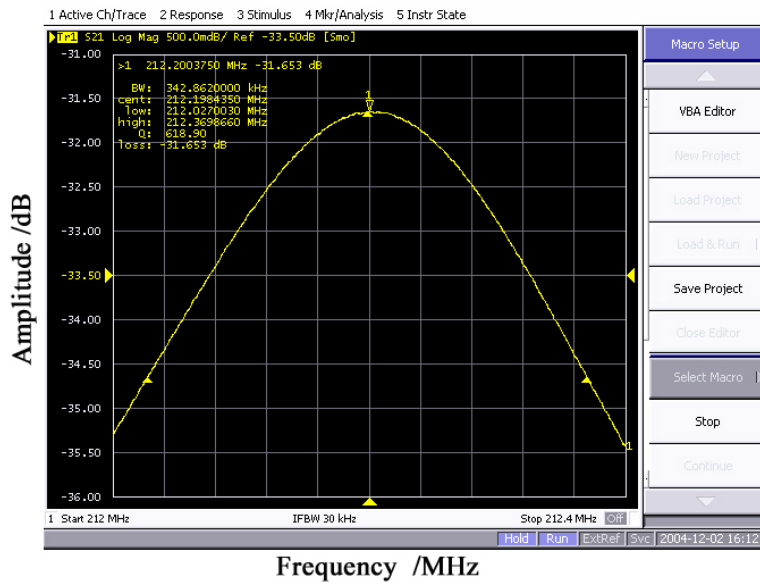


Fig.8.4 The resonance of the IH-DTL power cavity with an additional height of 7mm on the half shells ($f=212.20\text{MHz}$, $Q=618.90$)

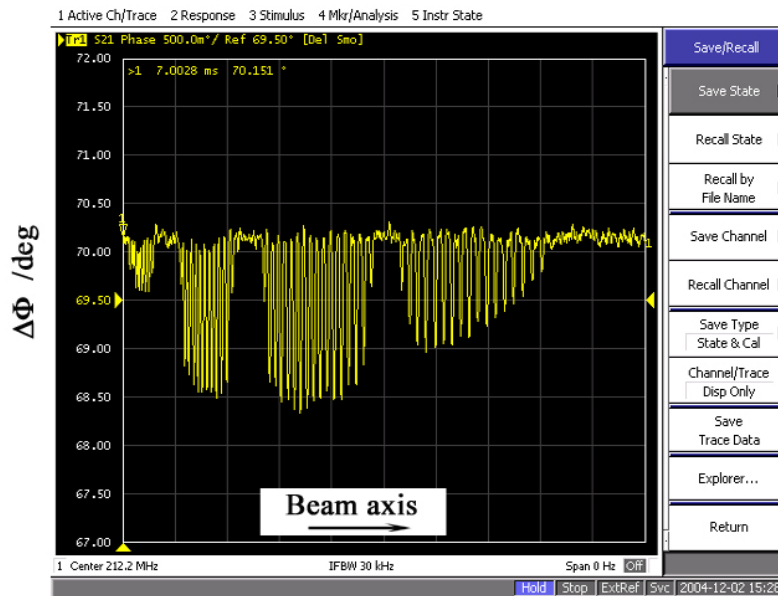


Fig.8.5 The phase measurement at resonance 212.2MHz

The 1st RF measurement was done on 2nd December 2004 at PINK Company. The measured resonance frequency for the IH-DTL cavity with 7mm extra half shell heights was 212.2MHz. The -3dB bandwidth is 342.862kHz, the quality factor is about 618.90. All bead pull measurements were done by a 5mm diameter metal ball. The resonance curve in logarithmic scale is shown in Fig.8.4. Fig.8.5 shows the phase response at above resonance frequency during the bead pull measurement. The corresponding field distribution is shown in Fig.8.6. For 3.8 meters measured length, there were 1600 measured phase points, the sweep time was 35seconds, IF bandwidth 30kHz, the noise was rather high, this was reduced by narrow IF bandwidth 30Hz setting in the later cavity measurements. The narrower or lower IF bandwidth is, the longer sweep time is, that means the phase measurement takes longer time.

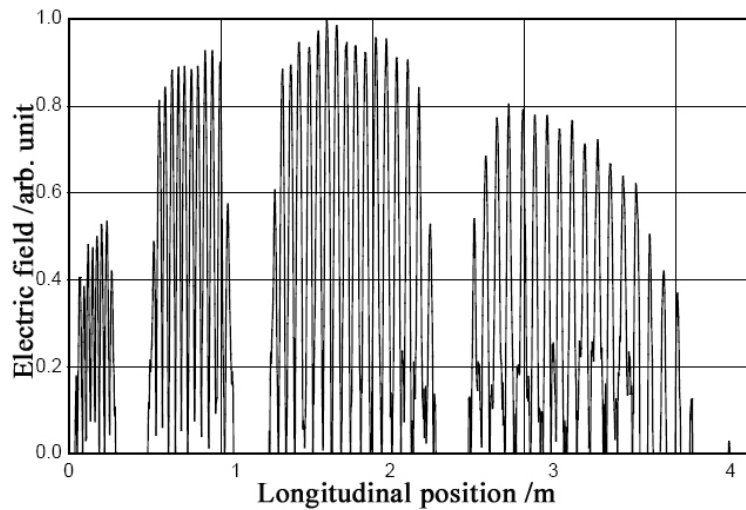


Fig.8.6 Absolute electric field distribution with 7mm additional heights of the IH cavity half shells

The measured resonance frequency fits the value predicted by the formula (2.5). It is lower than the design value of 216.816MHz, and will go up after cutting the additional heights of half shells partly away.

The measured quality factor is defined mainly by the electrical conductivity σ and by the effective magnetic permeability μ_r of the steel at that frequency. The quality factor Q is inversely proportional to the cavity power dissipation P , P is proportional to the surface resistance i.e. to $1/(\sigma \delta)$, δ is the skin depth, $\delta = (2/(\omega \sigma \mu_0 \mu_r))^{1/2}$, the surface resistance of the steel is written in the following :

$$R_{st} = R_{Cu} \sqrt{\frac{\mu_{r,st} \sigma_{Cu}}{\sigma_{st} \mu_{r,Cu}}} \quad (8.1)$$

The cavity material is ST52-3 steel, the surface resistance from Equation (8.1) is much larger than the copper cavity, that is the reason why the quality factor Q is only about 619.

As discussed in chapter 2, the cavity inductance per unit length is proportional to the cavity cross sectional area; it was planned to cut the extra cavity half shells in two steps. After the height of the half shells was cut by 5mm each, the predicted resonance frequency:

$$\frac{\Delta A}{A} = -3.55\% \quad , \quad \frac{\Delta f}{f} = -\frac{1}{2} \frac{\Delta L'}{L'} = -\frac{1}{2} \frac{\Delta A}{A} = 1.775\% \quad (8.2)$$

$$f_n = \left(1 + \frac{\Delta f}{f}\right) f = 216.0 \text{ MHz}$$

8.3 The Second RF Investigation

After cutting the cavity half shells by 5mm on the rectangular flanges, RF measurements were done again in PINK Company on 24th of February 2005. The measured resonance went up to 216.23MHz; it is about 0.586MHz below the operation frequency, the resonance curve without any plunger in the 3rd and 4th sections is shown in Fig.8.7.

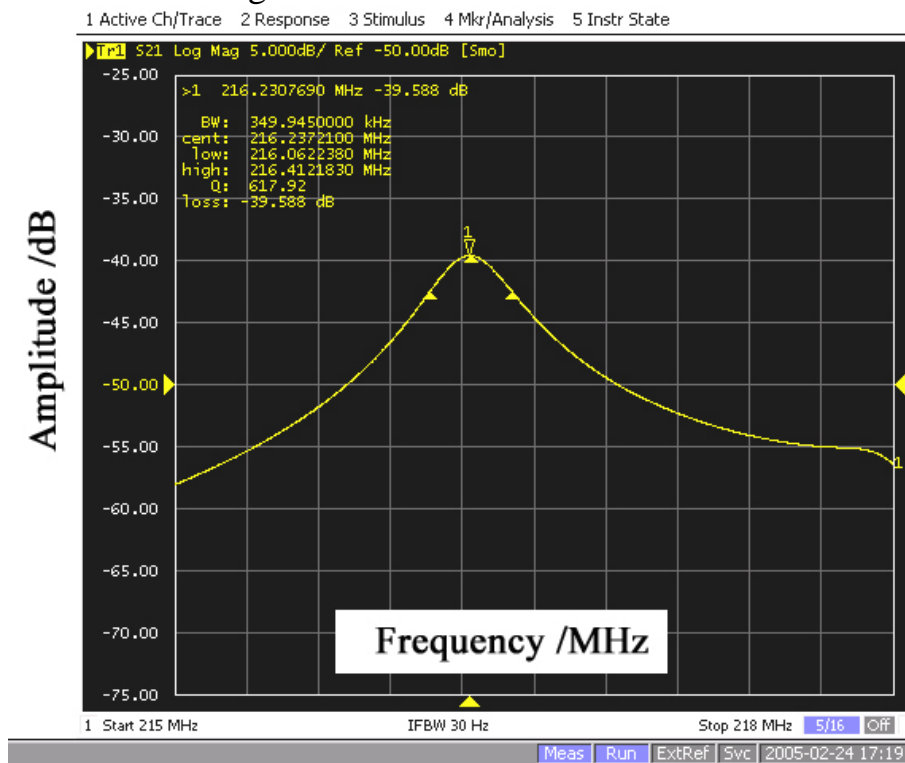


Fig.8.7 Resonance of IH cavity after cutting 5mm ($f=216.23\text{MHz}$, $Q=617.9$)

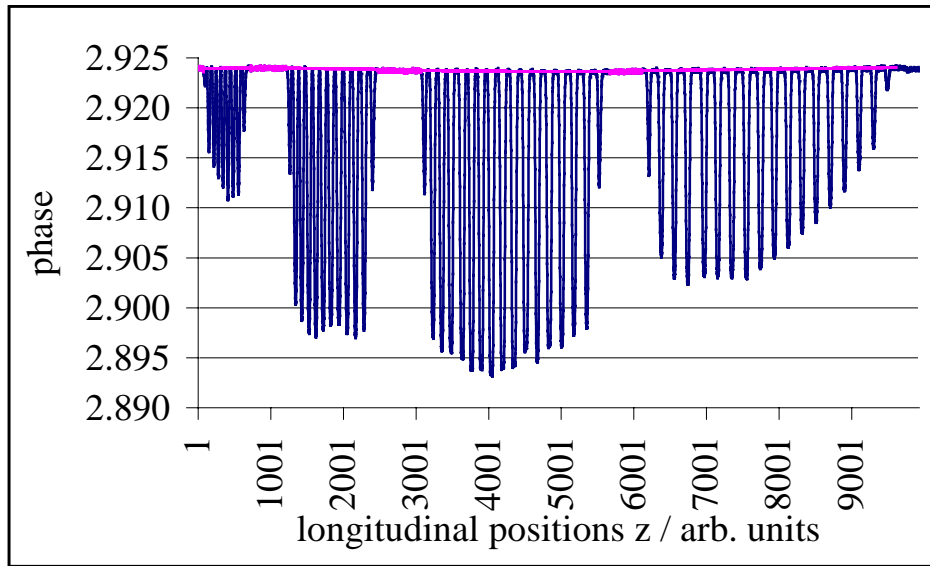


Fig.8.8 The corresponding bead pull measurement

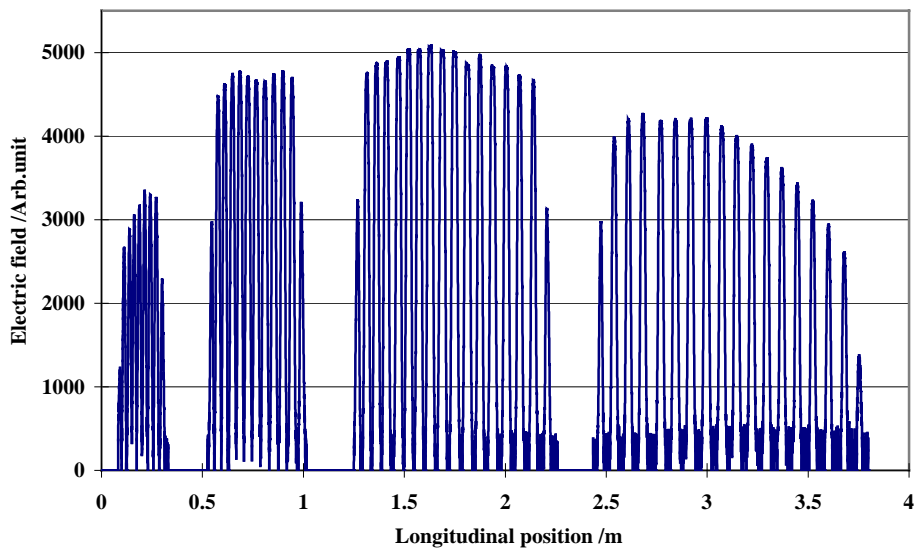


Fig.8.9 The field distribution of IH cavity after cutting 5mm half shells

According to the resolution and noise level of the bead pull measurements, the number of points was increased to 7×1600 (seven cycles measurement), the total measuring time was about 7 minutes. The measurements were performed with the HP8753E network analyzer. The Fig.8.8 shows the measured phase against the longitudinal positions after cutting 5mm cavity half shells each. After subtracting the ground line, the field distribution along the longitudinal axis position is shown in Fig.8.9.

Comparing Fig.8.9 to Fig.8.6, the field distributions in the 1st and 4th sections are going up very obviously, but they are still lower than the fields in the other

two sections. To let the field in the 1st section reach the design level one can in a next step reduce the size of the volume tuners in the 1st section (see Fig.6.3/6.4). The fields in the 4th section can be increased by lowering the movable plunger positions.

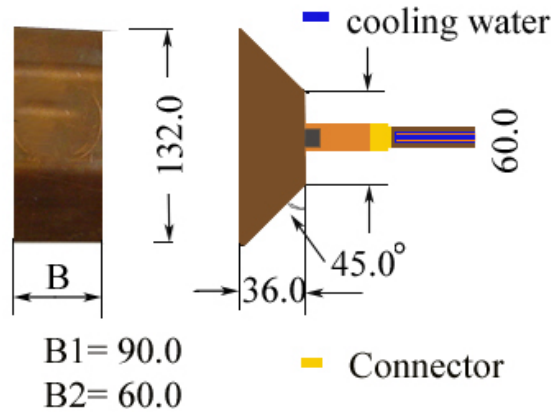


Fig.8.10a The block plungers in the 3rd and 4th sections

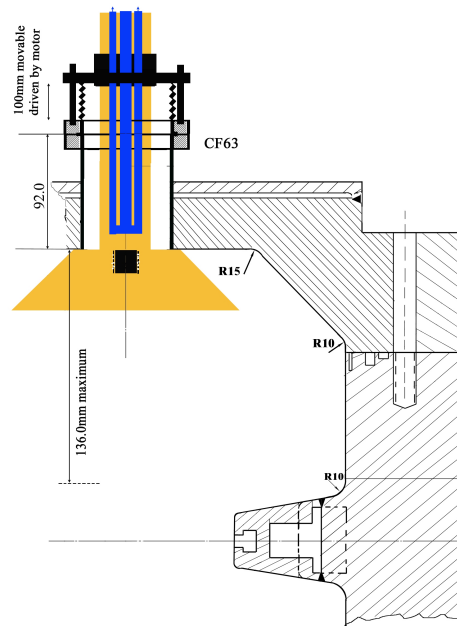


Fig.8.10b The block plunger with a quarter cross section of IH cavity

The plungers in the 3rd and 4th sections are shown in Fig.8.10: The plunger in the 3rd section is 60mm (B_2) long, that is 30mm shorter than the length (B_1) of the plunger in the 4th section. As discussed in chapter 5, the block plungers in Fig.8.10 will make the cavity resonance about 0.5MHz higher than that without any plunger when located in the highest position.

Table 8.1 The resonance frequency shifted by plungers in 3rd and 4th sections

Depth of plungers /mm		Frequency /MHz
Plunger in 3 rd section	Plunger in 4 th section	
0	0	216.7
10	0	216.667
10	10	216.650
20	20	216.614
30	30	216.538
40	40	216.441
45	50	216.336
50	50	216.304
55	50	216.259
55	55	216.204

In order to see an effect at the cavity end from the Additional Capacitance Tuning technique, which was discussed in chapter 5.2.2, two copper blocks (denoted as C_{11} and C_{12}) were set on the girders at the entrance and another two copper blocks (denoted as C_{h1} and C_{h2}) at the exit (see Fig.8.11). These four copper blocks make the cavity resonance lower.

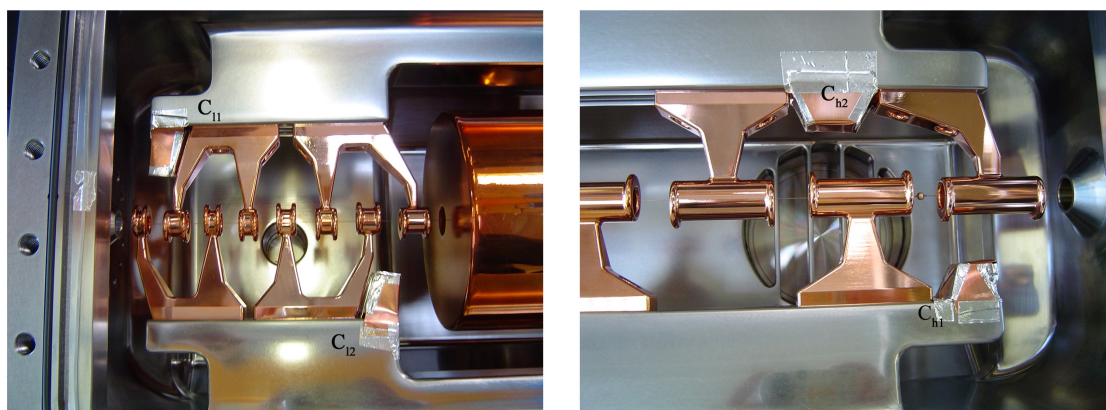


Fig.8.11 The additional capacitance blocks at entrance and exit of IH cavity

The field distribution with the plungers in the 3rd and 4th sections is shown in Fig.8.12. The plungers are at the top position, just near by the cavity wall. After setting the plungers deeper, the field distributions in the 3rd and 4th sections are going up. Fig.8.13 shows the measured phase distribution at 216.2MHz, the corresponding field distribution is shown in Fig.8.14. This experiment proved the possibility of cavity tuning by the plungers in the 3rd and 4th sections.

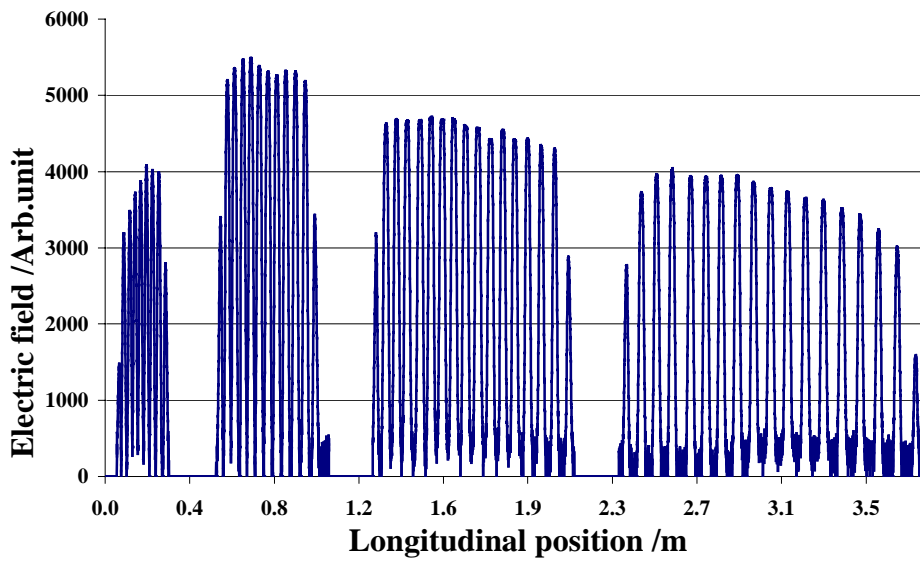


Fig.8.12 The field distributions with the plungers (plunger depth: $P_3=0, P_4=0$, while the effects of two additional capacitance tuning blocks at cavity entrance and exit are included (see Fig.8.11))

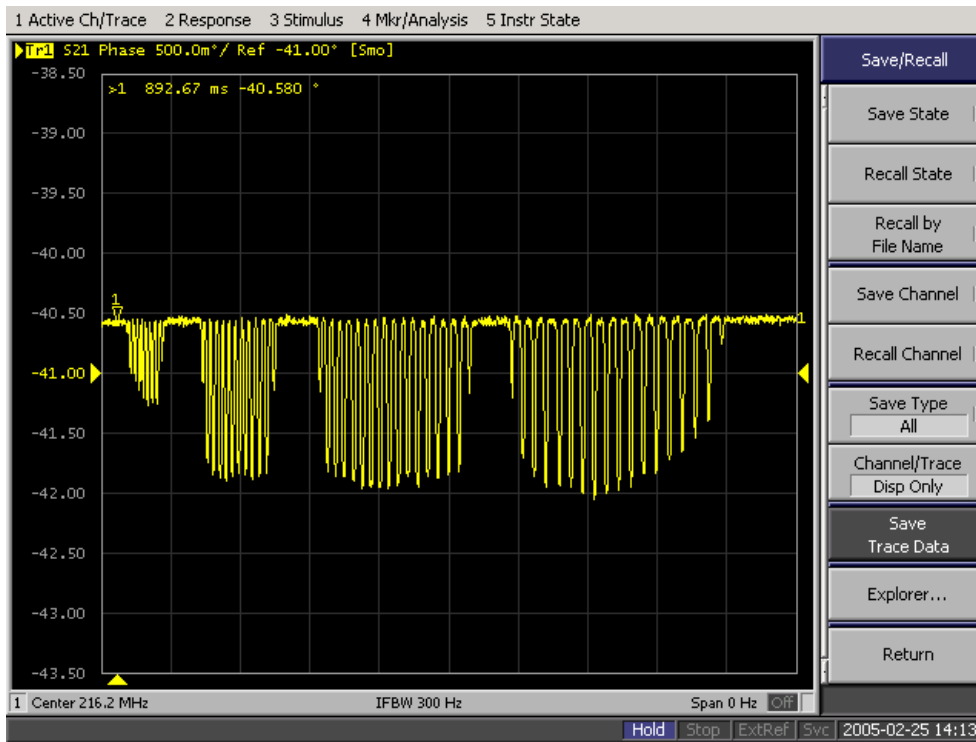


Fig.8.13 The phase distribution with the two plungers 55mm deeper

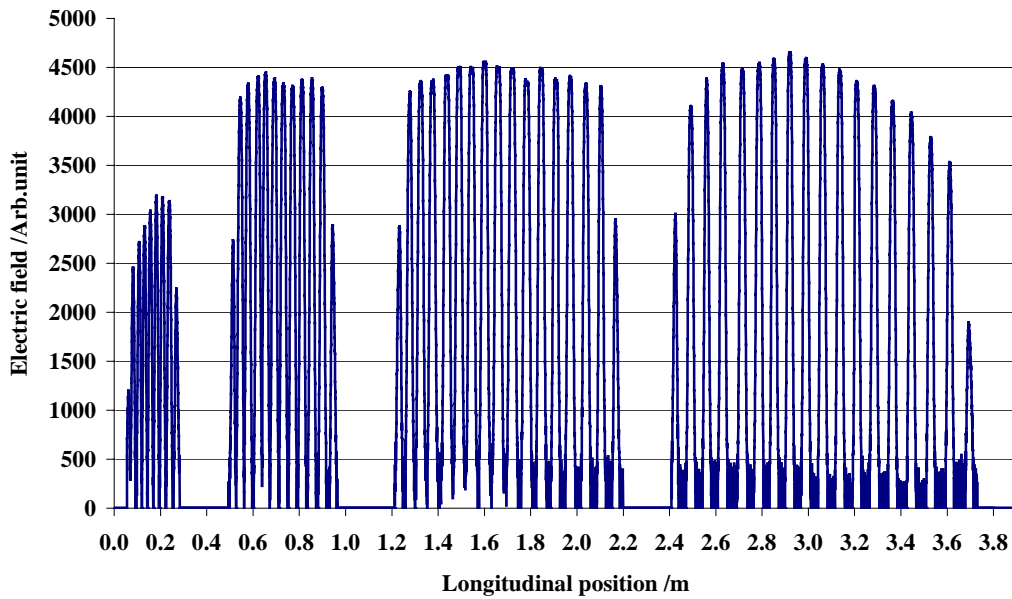


Fig.8.14 The field distribution with the plungers in the 3rd and 4th sections, plunger depth: P3=55mm,P4=55mm, f=216.2MHz

8.4 The Third RF Investigation

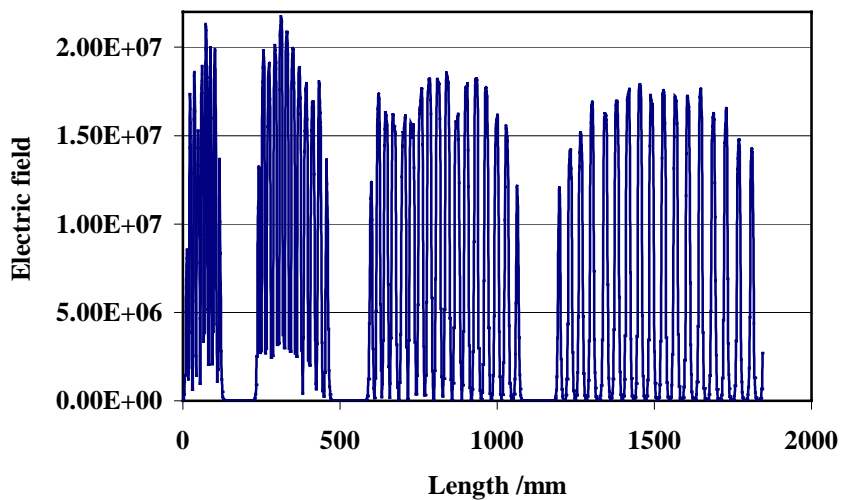


Fig.8.15 The simulated field distribution after cutting volume tuners 11mm (full scale) away in the 1st section and cutting cavity half shells another 1.2mm (full scale) away

As discussed before, the field distribution in the 1st section in Fig.8.14 can be improved by cutting the volume tuners in the 1st section. This has been simulated for the complete 1:2 scaled cavity by the Microwave Studio 5.02 version. As the simulation starting point, the simulation should reach the measured field distribution, which was shown in Fig.8.9. To compensate the

mesh point limitations due to computer resources, the four parameters for drift tube outer diameters in the four sections were readjusted. The volume tuners in the 1st section (see Fig.6.3 /6.4) originally had a thickness of 30mm. Finally, due to the MWS simulations (Fig.8.15), the thickness of volume tuners 1 was reduced to 19mm. Additionally, to reach the needed resonance frequency, the half shells were cut again by another 1.2mm. The MWS simulated field distribution related to these parameters is shown in Fig.8.15.

Table 8.4 The resonance frequency shifted by the plungers in the 3rd and 4th sections (Cavity dimension: 341.6*260, volume tuner in the 1st section: 19mm)

Depths of plungers /mm		H ₁₁₀ Frequency /MHz
Plunger in 3rd section	Plunger in 4 th section	
0	0	217.355
0	60	217.138
40	40	217.20
50	50	217.03
55	60	216.996
57	62	216.96
60	62	216.936
63	66	216.846
66	66	216.816

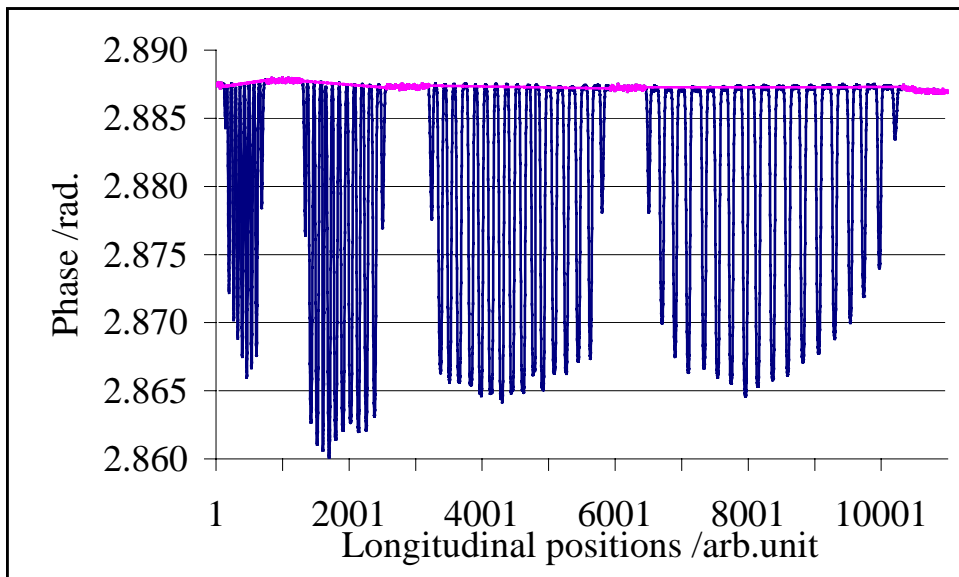


Fig.8.16 The phase distribution with the cavity dimension: 341.6*260; volume tuner in the 1st section: 19mm; with C₁₁, C_{h1} and C_{h2} (see Fig.8.11); and the plunger positions: P₃=66mm, P₄=66mm. The measured frequency: 216.816MHz

After cutting the half shell flanges as well as the volume tuners in the 1st section as described above, RF measurements took place in 11th of May 2005. Main results were: The resonance frequency was in the expected tuning range, as shown by table 8.4, the operating frequency of 216.816MHz as well as a ‘balanced’ field are reached when the plungers are positioned reasonably. The perturbation phase and the field distributions are shown in the Fig.8.16 and Fig.8.17, respectively.

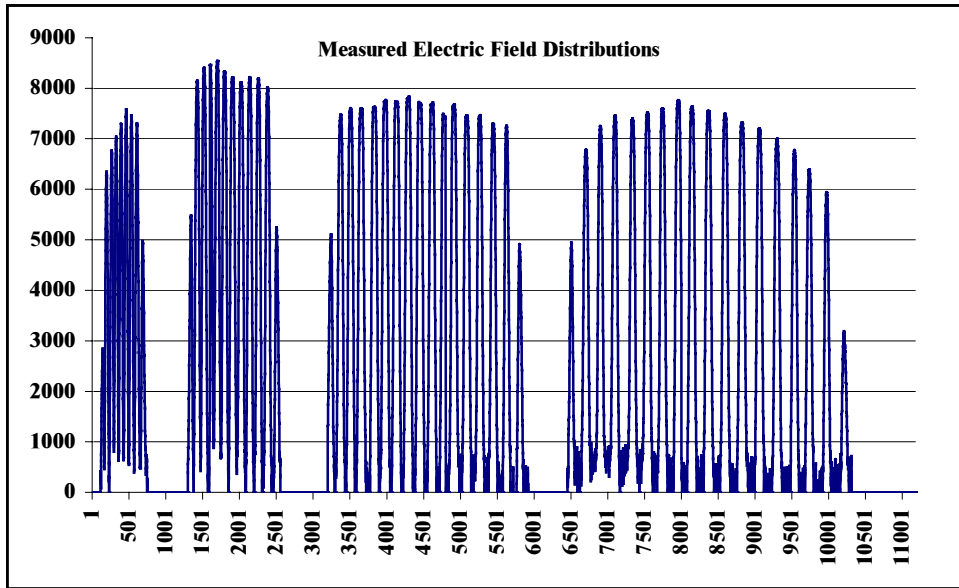


Fig.8.17 The corresponding field distributions

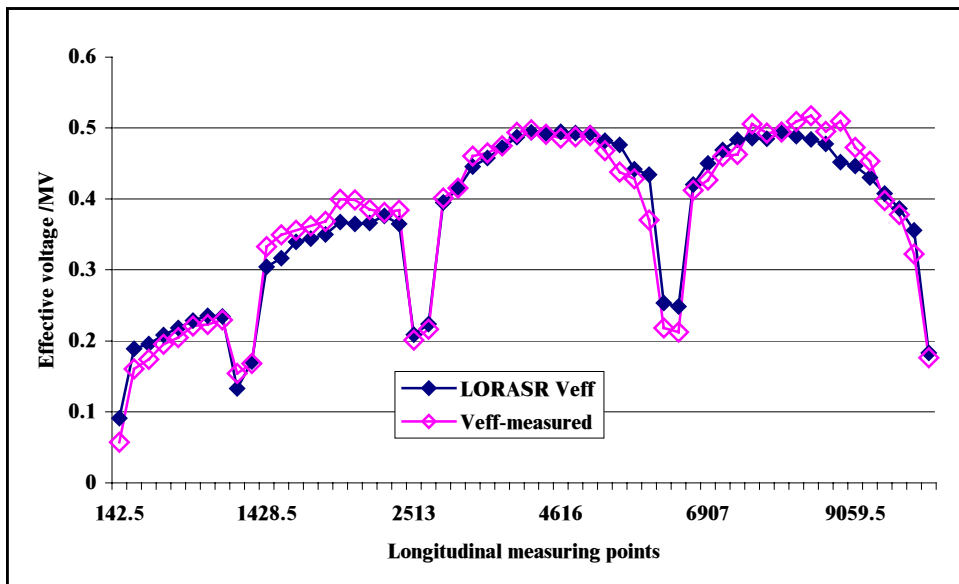


Fig.8.18 The effective voltage distributions along the structure with respect to the above field distributions. The measured frequency: 216.816MHz)

Quite a big difference when compared to the simulation result (Fig.8.15) is seen in the relative amplitude of drift tube section 1: The measured amplitudes are significantly lower! Moreover the measured field distribution became only balanced after adding capacitance by the movable plungers in the 3rd and 4th sections. Moreover the Additional Capacitance Tuning techniques (Fig.8.11 for the HE end and Fig.8.20 left) were applied. The resulting voltage distribution (Fig.8.19) can still not be accepted, mainly because of missing the effective voltages at the very first gaps of section 1. This wouldn't allow for stable beam acceleration.

After these results, it was concluded that the size of the low energy undercuts had to be enlarged. Due to technical reasons a longitudinal extension of 5mm at a width of 24mm was decided after discussions with the manufacturer and due to experience from RF model measurements. This modification is shown in Fig.8.19.

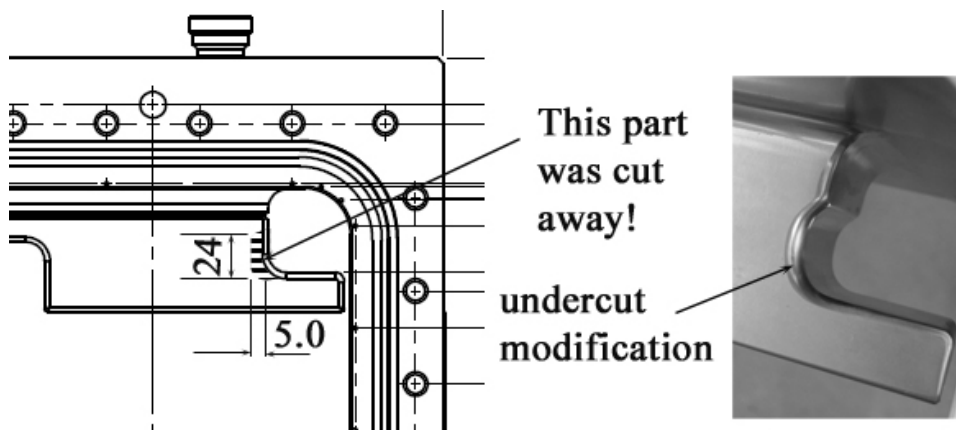


Fig.8.19 The low energy undercut modification

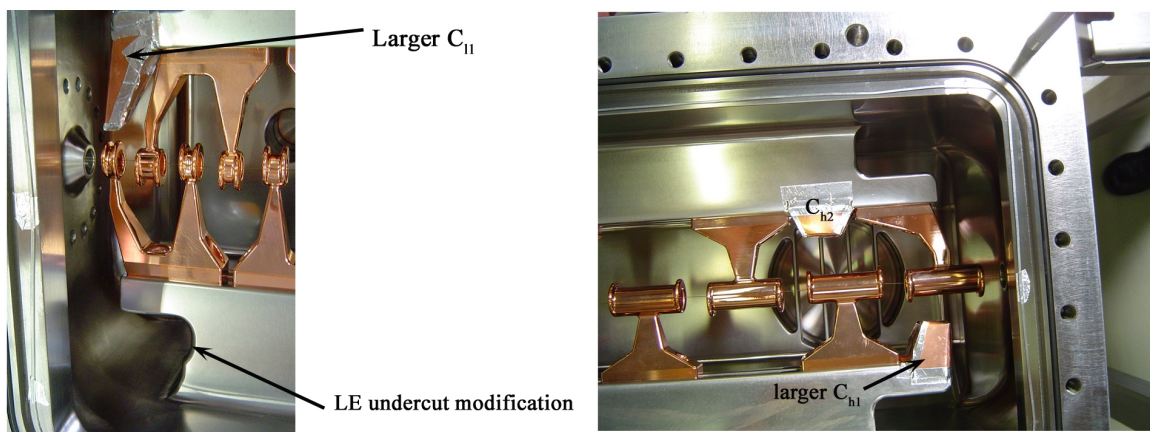


Fig.8.20 New Additional Capacitance Tuning for the two ends

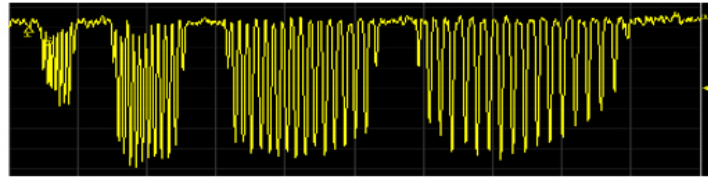
8.5 The Fourth RF Investigation

After re-machining the undercuts on the low energy side, as shown in Fig.8.19, RF measurements were performed again on 27th of May 2005. The measured perturbation phases before and after the undercut modifications are shown in Fig.8.21a and 21b, the ratio of maximum phase in the 1st section to that in the 2nd section is increased from 0.571 to 0.773, i.e. the electric field in the 1st section is improved from 75.6% of maximum to 87.9%. The phase could be further improved by enlarging the round radius at both sides of last undercut modification or by setting an additional copper block (capacitance C_{ll}) on the girder at opposite of the first short drift tube. This is shown in the left Fig.8.20. The phase measurement after C_{ll} setting together with the undercut modification (Fig.8.19/8.20) is shown in Fig.8.21d. Meanwhile Fig.8.21c gives the phase without undercut modification but with C_{ll} setting.

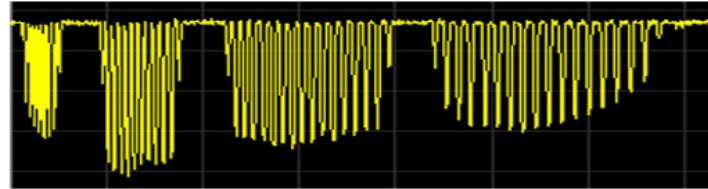
From the Fig.8.21.c, d, e, one can see the perturbation phase distribution can be flatted by moving the plungers in the 3rd and 4th sections, i.e. the design field distributions along the structure can be realized easily. Fig.8.22 shows the field distribution corresponding to the phase distribution in Fig.8.21.d. Comparing the Fig.8.22 to Fig.8.17, the field distribution in the 1st section has been improved. There is no any doubt that the flat field distributions along the structure can be easily realized by setting the plungers in the last two sections. The effective voltage distribution along the structure is shown in Fig.8.23. So the needed gaps' effective voltage distributions can be reached for the HICAT IH-DTL cavity. This is a demonstration, that now the tuning of the cavity ends to sufficient field levels is possible.

This led to two main discussions:

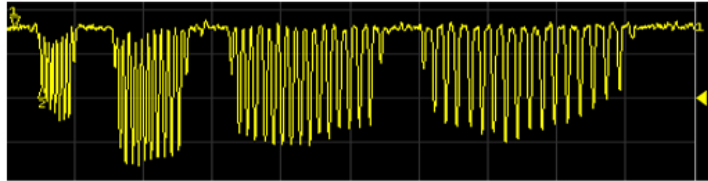
- No more RF measurements during cavity production are needed
- The undercuts on both ends are slightly further extended to replace Additional Capacitance Tuning C_{ll} and C_{hl} partly



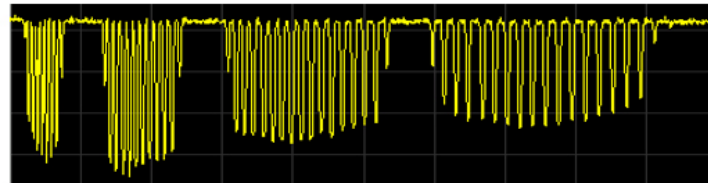
a. without undercut modification, without C_{11} ,
 $p_3=60\text{mm}$, $p_4=62\text{mm}$, $f_1=216.94\text{MHz}$,
 $\Phi_{1\text{max}}=0.571$ $\Phi_{2\text{max}}$, $E_{1\text{max}}=75.6\%$ $E_{2\text{max}}$



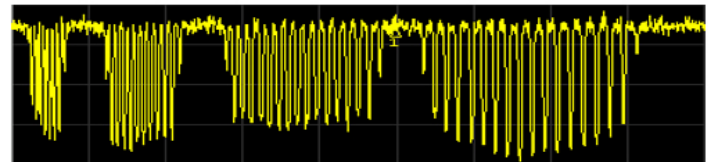
b. with undercut modification, without C_{11} and C_{h1}
 $p_3=60\text{mm}$, $p_4=62\text{mm}$, $f_1=216.90\text{MHz}$,
 $\Phi_{1\text{max}}=0.773$ $\Phi_{2\text{max}}$, $E_{1\text{max}}=87.9\%$ $E_{2\text{max}}$



c. without undercut modification, with old C_{11}
 and C_{h1} , $p_3=60\text{mm}$, $p_4=62\text{mm}$, $f_1=216.90\text{MHz}$,
 $\Phi_{1\text{max}}=0.676$ $\Phi_{2\text{max}}$, $E_{1\text{max}}=82.2\%$ $E_{2\text{max}}$



d. with undercut modification, with new C_{11} and
 C_{h1} , $p_3=71\text{mm}$, $p_4=60\text{mm}$, $f_1=216.60\text{MHz}$,
 $\Phi_{1\text{max}}=0.938$ $\Phi_{2\text{max}}$, $E_{1\text{max}}=96.8\%$ $E_{2\text{max}}$



e. with undercut modification, with new C_{11} and
 C_{h1} , $p_3=66\text{mm}$, $p_4=66\text{mm}$, $f_1=216.575\text{MHz}$

Fig.8.21 The phase effects of LE undercut modifications, old C_{11} and C_{h1} were shown in Fig.8.11, new C_{11} and C_{h1} were shown in Fig.8.20

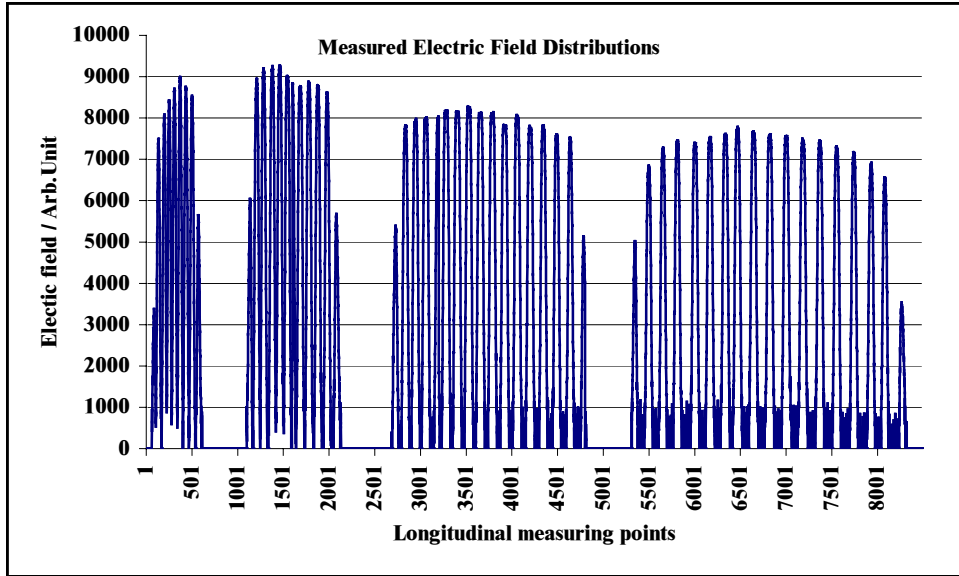


Fig.8.22 The field distribution respects to the phase in Fig.8.21.d

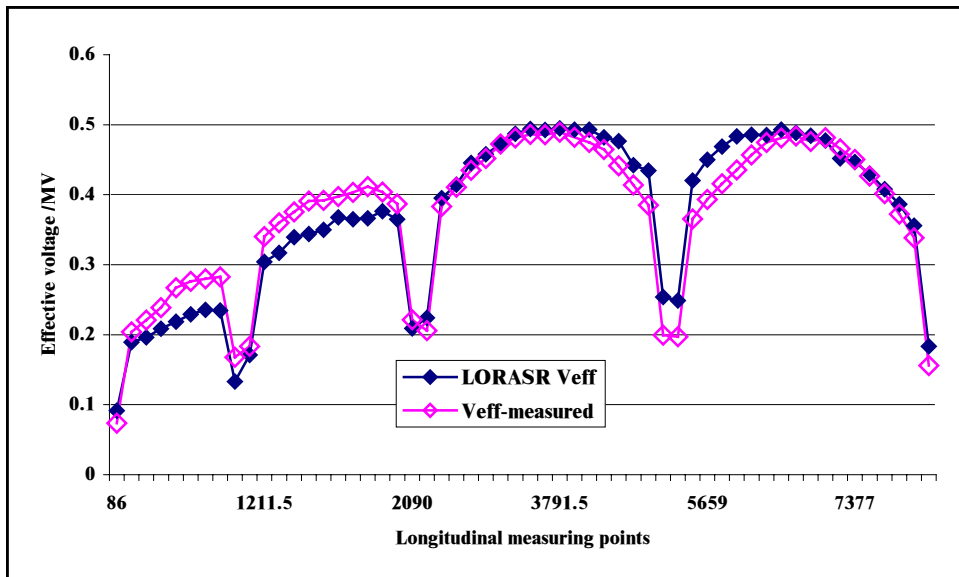


Fig.8.23 The gap effective voltage distribution related to the field in Fig.8.23

Summary

Cancer has become one of the most fatal diseases. The Heidelberg Heavy Ion Cancer Therapy (HICAT) has the potential to become an important and efficient treatment method because of its excellent “Bragg peak” characteristics and on-line irradiation control by the PET diagnostics.

The dedicated Heidelberg Heavy Ion Cancer Therapy Project includes two ECR ion sources, a RF linear injector, a synchrotron and three treatment rooms. It will deliver $4 \cdot 10^{10}$ protons, or $1 \cdot 10^{10}$ He, or $1 \cdot 10^9$ Carbons, or $5 \cdot 10^8$ Oxygens per synchrotron cycle with the beam energy 50-430 A MeV for the treatments. The RF linear injector consists of a 400 A keV RFQ and of a very compact 7 A MeV IH-DTL accelerator operated at 216.816 MHz.

The development of the IH-DTL within the HICAT project is a great challenge with respect to the present state of the DTL art because of the following reasons:

- The highest operating frequency (216.816 MHz) of all IH-DTL cavities;
- Extremely large cavity length to diameter ratio of about 11;
- IH-DTL with three internal triplets;
- The highest effective voltage gain per meter (5.5 MV/m);
- Very short MEBT design for the beam matching.

The following achievements have been reached during the development of the IH-DTL injector for HICAT :

- ▶ The KONUS beam dynamics design with LORASR code fulfills the beam requirement of the HICAT synchrotron at the injection point. The simulations for the IH-DTL injector have been performed not only with a homogeneous input beam, but also with the actual particle distribution from the exit of the HICAT RFQ accelerator as delivered by the PARMTEQ code. The output longitudinal normalized emittance for 95% of all particles is 2.00 A keV ns, the emittance growth is less than 24%, while the X-X' and Y-Y' normalized emittance are 0.77 mmmrad and 0.62 mmmrad, respectively. The emittance growth in X-X' is less than 18%, and the emittance growth in Y-Y' is less than 5%.
- ▶ Based on the transverse envelopes of the transported particles, the redesign of the buncher drift tubes at the RFQ high energy end has been made to get a higher transit time factor for this novel RFQ internal buncher. An optimized effective buncher gap voltage of 45.4 KV has been calculated to deliver a minimized longitudinal beam emittance, while the influence of the effective buncher voltage on the transverse emittance can be neglected.

- ▶ Six different tuning concepts were investigated in detail while tuning the 1:2 scaled HICAT IH model cavity. ‘Volume Tuning’ by a variation of the cavity cross sectional area can compensate the unbalanced capacitance distribution in case of an extreme $\beta\lambda$ - variation along an IH cavity. ‘Additional Capacitance Plates’ or copper sheets clamped on drift tube stems are a fast way for checking the tuning sensitivity, but they will be replaced by massive copper blocks mounted on the drift tube girders finally. ‘Lens Coupling’ is an important tuning to stabilize the operation mode and to increase or decrease the coupling between neighboring sections. ‘Tube Tuning’ is the fine tuning concept and also the standard tuning method to reach the needed field distributions as well as the gap voltage distributions. ‘Undercut Tuning’ is a very sensitive tuning for the end sections and with respect to the voltage distribution balance along the structure. The different types of ‘plungers’ in the 3rd and 4th sections have different effects on the resonance frequency and on the field distribution. The different triplet stems and the geometry of the cavity end have been also investigated to reach the design field and voltage distributions. Finally, the needed uniform field distribution along the IH-DTL cavity and the corresponding effective voltage distribution were realized, the remaining maximum gap voltage difference was less than 5% for the model cavity. The several important higher order modes were also measured.
- ▶ The RF tuning of the IH-DTL model cavity delivers the final geometry parameters of the IH-DTL power cavity. A rectangular cavity cross section was adopted for the first time for this IH-DTL cavity. This eases the realization of the volume tuning concept in the 1st and 2nd sections. Lens coupling determines the final distance between the triplet and the girder. The triplets are mounted on the lower cavity half shell.
- ▶ The Microwave Studio simulations have been carried out not only for the HICAT model cavity, but also for the final geometry of the IH-DTL power cavity. The field distribution for the operation mode H_{110} fits to the model cavity measurement as well as the Higher Order Modes. The simulations prove the IH-DTL geometrical design. On the other hand, the precision of one simulation with 2.3 million mesh points for full cross section area and the CPU time more than 15hours on a DELL PC with Intel Pentium 4 of 2.4GHz and 2.096GRAM were exploited to their limit when calculating the real parameters for the two final machining iterations during production.

- ▶ The shunt impedance of the IH-DTL power cavity is estimated by comparison with the existing tanks to about $195.8\text{M}\Omega/\text{m}$, which fits to the simulation result of $200.3\text{M}\Omega/\text{m}$ with reducing the conductivity to the $5.0 \cdot 10^7 \text{ }\Omega^{-1}\text{m}^{-1}$. The effective shunt impedance is $153 \text{ M}\Omega/\text{m}$. The needed RF power is 755kW . The expected quality factor of the IH-DTL cavity is about 15600.
- ▶ The IH-DTL power cavity tuning measurements before cavity copper plating have been performed. The results are within the specifications. There is no doubt that the needed accuracy of the voltage distribution will be reached with the foreseen fine tuning concepts in the last steps.

References

- [1.1] W. H. Scharf, O.A. Chomicki: Medical Accelerators in Radiotherapy: Past, Present and Future, Phys. Med., No.4, Oct-Dec., 1996
- [1.2] U. Amaldi, M. Silari: The TERA Project and the Centre for Oncological Hadrontherapy, Roma, July 1994
- [1.3] J. Debus et al.: Proposal for a Dedicated Ion Beam Facility for Cancer Therapy, Eds.: K.D. Gross, M. Pavlovic (GSI), Sept. 1998
- [1.4] Roentgen, *Ueber eine neue Art von Strahlen* (On a New Kind of Rays), Proceedings of the Würzburg Physico-Medical Society, 1895
- [1.5] <http://www.aip.org/history/electron/jj1897.htm>
- [1.6] G. Ising, Ark. Mat. Fys. 18(No.30), 1-4(1924)
- [1.7] R. Wideroe, Arch. Electrotech. 21, 387(1928)
- [1.8] E.O. Lawrence and N.E. Edlson, Science 72, 376(1930)
- [1.9] V. Veksler, Doklady U.S.S.R. 44, 444(1944)
- [1.10] E.M. McMillan, Phys. Rev. 69, 145(1945)
- [1.11] R. Wilson, Radiological Use of Fast Protons, Radiology 1946:47:487-91
- [1.12] M. Goitein, M. Jermann, *Clin. Oncol.* **15**, S37 (2003)
- [1.13] H. Eickhoff, Th. Haberer, G. Kraft, U. Krause, K. Poppensieker, M. Richter, R. Steiner, The GSI cancer therapy project, PAC97, P.3801-3803
- [1.14] Jürgen Debus, Daniela Schulz-Ertner, et-al., Five years heavy ion therapy at GSI, GSI annual report 2002. The website: <http://www-aix.gsi.de/annrep2002/files/161.pdf>
- [1.15] http://www.hmi.de/isl/att/att-i_en.html
- [1.16] A. Itano et al, "Hyogo Hadrontherapy Centre Project", Advances in Hadrontherapy, Proc. Int. Week on Hadrontherapy, and 2nd Intl. Symp. on Hadrontherapy, Elsevier (1997) 193.
- [1.17] Satoru Yamada, The progress of HIMAC and particle therapy facilities in Japan, Proceedings of the Second Asian Particle Accelerator Conference, Beijing, China, 2001, P.829-833
- [1.18] H. Eickhoff, et al, HICAT - The German hospital-based light ion cancer therapy project, Proc. of the 2003 Particle Accelerator Conf. (PAC 2003), Portland, Oregon, 2003, pp. 694-698.
- [1.19] J.M. Sisterson, Update on the worldwide proton therapy experience through 1997 in abstracts of the PTCOG Meetings, Sept. 14-16 1998, <http://ptcog.web.psi.ch/Particle%20NewsLetter%2022.html>
- [1.20] Ugo Amaldi, Future trends in cancer therapy with particle accelerators, Elsevier, Zeitschrift fuer Medizinische Physik 14, 2004, 7-16
- [1.21] http://zhizi.com/proton_equipment.htm, <http://www.zhizi.com/>
- [1.22] P. Spaedtke et al.: Ion source development in GSI, Rev. Sci. Instrum. 69/2(1998) 1079.

- [1.23] E. Badura et al.: First patient treated with carbon ions: status report of the heavy ion therapy at GSI, GSI scientific report 1997, GSI-report-98-01, March 1998, 140
- [1.24] A. Bechtold, Eine integrierte RFQ-Driftröhrenkombination für ein Medizin-Synchrotron, Frankfurt dissertation, 2003.
- [1.25] A. Bechtold, et al, Development of an RFQ injector for a therapy synchrotron, Proceeding of EPAC2000, Vienna, Austria, P.2500-2502, 2000.
- [1.26] A. Bechtold, et al, The RFQ-Drifttube-combination for medicine synchrotron in Heidelberg, Proceeding of LINAC2002, P784-787, Korea.
- [1.27] B. Schlitt, et al, Design of the 7 MeV/u, 217 MHz injector linac for the proposed ion beam facility for cancer therapy at the clinic in Heidelberg, Proc. of the XX Int. Linac Conf. (LINAC 2000), Monterey, California, 2000, pp. 226-228.
- [1.28] B. Schlitt et al, Design of a carbon injector for a medical accelerator complex, Proc. of the 6 th Europ. Particle Accelerator Conf. (EPAC 98), Stockholm, 1998, pp. 2377-2379.
- [1.29] S. Minaev, et al, APF or KONUS drift tube structures for medical synchrotron injectors - a comparison, Proc. of the 1999 Particle Accelerator Conf. (PAC 99), New York, 1999, pp. 3555-3557.
- [2.1] U. Ratzinger, H-type Linac structure, CERN Accelerator School, 8th-16th May, 2000, Lufthansa Training Center, Germany
- [2.2] P. Blewett, Proc. Of the CERN Symposium 1956, p. 162
- [2.3] P.M. Zeidlitz, V.A. Yamnitskii, Journ. of Nuclear Energy, Part C, vol. 4(1962), p. 121.
- [2.4] V.A. Bomko, E.I. Revutskii, Soviet Physics Techn. Physics, vol. 9, no. 7(1965), p. 973.
- [2.5] M. Bres et al., IEEE, Trans. Nucl. Sci. vol. NS-16/3 (1969), p. 372.
- [2.6] J. Pottier, IEEE Trans. Nucl. Sci., vol. NS-16/3 (1969), p. 377.
- [2.7] E. Nolte et al., Nucl. Instr. and Meth., vol. 158, p. 311.
- [2.8] J.M. Potter et al., proc. of the 1979 PAC Conf. San Francisco, IEEE, Vol. NS-26, p. 3745.
- [2.9] U. Ratzinger et al., Nucl, Instr. and Meth. A, vol. 263 (1988), p. 261.
- [2.10] Y. Oguri, E. Arai, T. Hattori, Nucl. Instr. and Meth. A, vol. 235 (1985), p. 7.
- [2.11] U. Ratzinger, proc. of the 1988 LINAC Conf., Newport News, Virginia, CEBAF-Report-89-001, p. 185.
- [2.12] U. Ratzinger, Effiziente Hochfrequenz-Linearebeschleuniger fuer leichte und schwere Ionen, Habilitationsschrift, IAP, Frankfurt Universitaet, 1998
- [2.13] U. Ratzinger, K. Kasper, et al, The GSI 36MHz high current IH type RFQ and HIF-relevant extensions, NIMA 415 (1998) 281-286
- [2.14] Hoefl, Passive elektrische Bauelemente, Dr. A. Huething Verlag, 1977
- [2.15] P.M. Lapostolle, Proton Linear Accelerators: A Theoretical and Historical Introduction, Los Alamos Report LA-11601-MS, 1989, P.74

- [2.16] Thomas P. Wangler, Principles of RF Linear Accelerators, John Wiley & Sons, Inc, 1998, P.175
- [3.1] M.L. Good, Phys. Rev. 92, 538 (1953).
- [3.2] J.B. Fainberg, in: Proc. CERN Symposium on High Energy Accelerators and Pion Physics, Geneva, 1956, p. 91.
- [3.3] V.V. Kushin, Atomnaya Energiya 29, 132 (1970).
- [3.4] D.A. Swenson, Particle Accelerators 7, 61 (1976).
- [3.5] A.S. Beley, V.S. Kabanov, S.S. Kaplin, N.A. Khizhnyak and N.G. Shulica, Atomnaya Energiya 49, 294 (1980).
- [3.6] S. Minaev, Proc. EPAC'90, Nice, p.1744.
- [3.7] W.-H. Cheng, R.L. Gluckstern, S. Nath and T.P. Wangler, in Proc. 1992 LINAC Conf., Ottawa, p.193.
- [3.8] U.Ratzinger, et al, The three-harmonics double drift buncher at the Munich heavy ion postaccelerator, NIM 205(1983) 381-386
- [3.9] U.Ratzinger, et al, The Upgrade Munich Linear Heavy Ion Postaccelerator, NIMA 263 (1988) 261-270
- [3.10] U.Ratzinger, High Current IH Structure, Proc. Of the EPAC 1994 Conference, London, vol.1, P.264
- [3.11] U. Ratzinger, RNB-specific linac development, Nuclear Physics A 701 (2002) 641c-646c
- [3.12] H.D. Haseroth, in: Proc. LILNAC 96, Geneva, CERN 96-07, p. 283.
- [3.13] O. Kester, et al, STATUS OF THE REX-ISOLDE LINAC, Proc. Of LINAC98, Japan, 812-814
- [3.14] A.Sauer, PARTICLE DYNAMICS INVESTIGATIONS FOR A HIGH CURRENT D⁺ DTL, Proceedings of the 2001 Particle Accelerator Conference, Chicago, 3182-3184
- [3.15] H. Podlech, et al, Higher Order Mode Investigation of Superconducting CH Structures and Status of the CH-Cavity Prototype, Proceedings of the PAC2003, Portland, OR, USA, P.1335-1337
- [3.16] Requirements for the XADS Accelerator & Technical Answers, DAPNIA-02-302, September 2002, France
- [3.17] U. Ratzinger, The IH-Structure and its Capability to Accelerate High Current Beams, Proc. of the IEEE Particle Accelerator Conf., San Francisco 1991, p. 567.
- [3.18] U.Ratzinger, et al, LORAS—A computer code to calculate the longitudinal and Radial beam dynamics of a drift tube accelerator, GSI internal report 0791
- [3.19] R.Tiede, Development of LORASR, Frankfurt University internal oral report, 7th Nov., 2003
- [3.20] U.Ratzinger, Effiziente Hochfrequenz-Linearebeschleuniger fuer leichte und schwere Ionen, Habilitationsschrift, IAP, Frankfurt Universitaet, 1998, P.135-136
- [4.1] A.Bechtold, U. Ratzinger, A.Schempp, et al, [RFQ development for an injector linac for therapy facility](#). GSI annual report.

- [4.2] A.Bechtold, Dr. Dissertation,2003
- [4.3] B.Schlitt,GSI Notiz, 26.11.03
- [4.4] B.Schlitt, Strukturdaten fuer das 1:2 HF-Modell des IH-Driftroehrenbeschleunigers fuer den Therapieinjektor. GSI Notiz, 29. November 2000
- [4.5] Y.Lu, et al, RF tuning of the IH model Cavity for the Heidelberg Cancer Therapy Project, IAP Internal Report, IAP-ACCC-270103
- [4.6] U.Ratzinger,V.T.Nimje, A computer code to calculate the longitudinal and radial beam dynamics of a drift tube accelerator. Description and Manual of LORASR
- [5.1] C.Peschke, Diplom Arbeit, Frankfurt University, 1995
- [5.2] H.Klein, Basic Concepts I, CERN Accelerator School for Particle Accelerators, 1991,Oxford, 112
- [5.3] Y.Lu, et al, Retuning of IH model Cavity for the Heidelberg Cancer Therapy, IAP Internal Report, IAP-ACCC-100603, Frankfurt University
- [7.1] Weiland,T: A discretization method for the simulation of Maxwell's equations for six component fields: Electronics and Communication, (AEÜ),Vol.31,pp.116-120,1977.
- [7.2] Krietenstein, B.:Zur Numerischen Berechnung von IH-Resonatoren, TU DARMSTADT, Dissertation, 1999
- [7.3] CST Company, Manual of Microwave Studio, HF design and analysis, advanced topics, Chapter four, 2002

Lists of the figures

Chapter one

Fig.1.1	The Bragg peak for different radiation source (after ^[1.18])	5
Fig.1.2	Covering a target volume by stacking several individual Bragg peaks of different carbon beam energy and intensity ^[1.18]	6
Fig.1.3	The layout of the Heidelberg Therapy Facility	11
Fig.1.4	The HICAT injector	11
Fig.1.5	Accelerator components of Heidelberg radiation facility	13

Chapter Two

Fig.2.1	Top view on the 202 MHz drift tube structure of the CERN Pb 25+ IH-DTL tank 2. Below a cross sectional view of this cavity as well as the electric and magnetic field distributions at characteristic regions are plotted. [2.12]	16
Fig.2.2	The cross section of the IH-DTL and parameters relevant for the analytical field approach	17
Fig.2.3	CERN IH-DTL structure and equivalent geometry to calculate the capacitance load	18
Fig.2.4	Equivalent circuit of IH-DTL	18
Fig.2.5	RF drift tube gap for the particle acceleration	19
Fig.2.6	RF power efficiency of H-mode cavities	21
Fig.2.7	Accelerating cells for describing the longitudinal motion	22
Fig.2.8	Longitudinal phase space and potential well	23
Fig.2.9	Longitudinal and radial electric field in an RF gap	24

Chapter Three

Fig.3.1	Sectional view of 2f cavity in Munich Post-accelerator	27
Fig.3.2	Particle velocity relative to 0° synchronous particle in the longitudinal phase space (a) and its transformation in $\Delta E / \Delta \phi$ plane by passing through a 0° synchronous particle of finite length	28
Fig.3.3	Concept of KONUS Dynamics Design	28
Fig.3.4	Schematic sketch of the LORASR structure	29
Fig.3.5	The model of real field distribution for different type of gaps	32
Fig.3.6	One gap is divided into 5 zones; every zone is divided into 6 steps	33
Fig.3.7	IH-DTL structure for GSI HLI project [2.1]	34
Fig.3.8	Beam envelopes of IH-DTL for GSI HLI project	35

Chapter Four

Fig.4.1	RF internal buncher	36
Fig.4.2	Bunched phase width vs. effective bunch voltage [4.2]	36
Fig.4.3	New MEBT geometry	37
Fig.4.4a	The length changes of drift tubes and gaps	39
Fig.4.4b	Capacitance of the drift tube structure per unit length	39
Fig.4.4c	New transit time factor distribution	40
Fig.4.4d	Measured electric field distribution	40
Fig.4.4e	Measured effective voltage distribution	40

Fig.4.4f	Effective voltage difference between theory and experiment	41
Fig.4.5	New designed effective voltage distributions	41
Fig.4.6	RFQ Output beam parameters at the middle of first drift tube	42
Fig.4.7	Geometry parameters of triplet	43
Fig.4.8a	Results of 98% envelopes (3949 particles) at x direction	45
Fig.4.8b	Results of 98% envelopes (3949 particles) at y direction	45
Fig.4.9a	Longitudinal envelopes (98%,3949 particles)	46
Fig.4.9b	Longitudinal phase envelopes along the IH cavity (98%)	46
Fig.4.9c	The phase width (red) refers to the centre particle phase (blue)	46
Fig.4.10	Normalized relative rms emittance growth	46
Fig.4.11	Phase advance per structure period	47
Fig.4.12	Normalized output emittance (with 95% particles)	47
Fig.4.13	Output longitudinal beam emittance (with 95% particles)	47
Fig.4.14	Dependence of the emittance values on the RFQ internal buncher voltage	48
Fig.4.15	Beam envelopes from the first drift tube centre of RFQ internal buncher to the exit of doublet	49
Fig.4.16	Buncher drift tube geometry	50

Chapter Five

Fig.5.1.1	IH model cavity for Heidelberg Cancer Therapy Project	51
Fig.5.2.1	Phase distribution from the first bead pull measurements $f_1=428.73\text{MHz}$ (a), $f_2=436.1\text{MHz}$ (b), $f_3=445.4\text{MHz}$ (c)	54
Fig.5.2.2a	Cross sectional view of IH model cavity	56
Fig.5.2.2b	Volume tuning blocks position at the low energy end of the cavity	56
Fig.5.2.3a	Without volume tuning in section 2	57
Fig.5.2.3b	With volume tuning in section 2	57
Fig.5.2.4a	Length of volume tuning blocks in section 2: 200.0mm	58
Fig.5.2.4b	Length of volume tuning blocks in section 2: 120mm	58
Fig.5.2.5	ACP tuning	58
Fig.5.2.6	Field distribution tuned by ACP	59
Fig.5.2.7	Lengthen tubes by soldering	59
Fig.5.2.8a	The field distributions according to drift tube structures listed in table 5.2.1 (a, 17th Sept.)	60
Fig.5.2.8b	The field distributions according to drift tube structures listed in table 5.2.1 (b, 19th Sept.)	61
Fig.5.2.9	Tube tuning effects in 3rd section (example 2), comparing to the Fig.5.2.8b.	62
Fig.5.2.10	Example 3 of tube tuning a, 31st Oct., before changing. b, 7th Nov. after changing tube	62
Fig.5.2.11a	Lens coupling tuning	64
Fig.5.2.11b	Sketch of lens coupling tuning	64
Fig.5.2.12a	The field distribution with $d_1=16.0, d_2=12.0, d_3=11.0$ (mm)	64
Fig.5.2.12b	The field distribution with $d_1=16.0, d_2=13.0, d_3=11.0$ (mm)	65
Fig.5.2.12c	The field distribution with $d_1=16.0, d_2=14.0, d_3=11.0$ (mm)	65
Fig.5.2.13	The concept of undercuts tuning	65
Fig.5.2.14a	HE undercuts inserts lengths 75.3mm	66
Fig.5.2.14b	HE undercuts inserts 76.0mm	66
Fig.5.2.15a	HE undercuts inserts 78.0mm	67
Fig.5. 2.15b	HE undercuts inserts 75.0mm	67

Fig.5.2.16	Plate plunger for section 3 and 4	68
Fig.5.2.17	Block plunger	68
Fig.5.2.18	The tuning range of plate plunger 3 (installed in 3rd section)	69
Fig.5.2.19	The influence of different plunger positions on the voltage distribution of sections 1 ³ / ₄	69
Fig.5.2.20	Tuning range of block plunger 3	70
Fig.5.2.21	The effect of different depth of block plunger 3	70
Fig.5.2.22	The tuning range of plate plunger 4	71
Fig.5.2.23	The effects of plate plunger 4 (installed in section 4)	71
Fig.5.3.1	The 1:2 scaled IH model cavity (3 of 4 sections)	72
Fig.5.3.2	Electric field distribution	72
Fig.5.3.2	Electric field distribution	72
Fig.5.3.3	Effective voltage distribution	72
Fig.5.3.4	The remaining differences of the effective voltage distribution for every gap and for the sections when compared to the design distribution	73
Fig.5.3.5	Original stem	73
Fig.5.3.6	New stem geometry	73
Fig.5.3.7	After assembling new stem geometry, the lens coupling distances d1=16.0,d2=15.0,d3=14.0	74
Fig.5.3.8	The lens coupling distances: d1=14.0,d2=15.0, d3=14.0, the field distributions in 1st and 2nd sections go up	74
Fig.5.3.9	The lens coupling distances: d1=14.0, d2=14.0, d3=14.0mm, comparing to Fig.5.3.8, the field distributions neighboring triplet 2 go up by decreasing d2 from 15.0mm to 14.0mm	75
Fig.5.3.10-1	The lens coupling distances: d1=14.0, d2=13.5, d3=14.0mm, d2 is decreased from 14.0mm to 13.5mm, the perturbation phase around triplet 2 goes up again	75
Fig.5.3.10-2	Electric field distributions with lens coupling distances: d1=14.0, d2=13.5, d3=14.0mm	75
Fig.5.3.10-3	The remaining differences of the effective voltage distribution when the same lens coupling distances with Fig.5.3.10-2	75
Fig.5.3.11-1	Phase distribution with d1=14.0,d2=13.5,d3=13.5mm	75
Fig.5.3.11-2	Electric field with d1=14.0, d2=13.5, d3=13.5mm	75
Fig.5.3.11-3	Effective voltage distribution with d1=14.0, d2=13.5, d3=13.5mm	76
Fig.5.3.11-4	Effective voltage difference with d1=14.0, d2=13.5, d3=13.5mm	76
Fig.5.3.12-1	Phase with the lens coupling distances: d1=14.0, d2=13.5, d3=13.5mm, and high energy undercuts inserts 76.5mm	76
Fig.5.3.12-2	Electric field distribution with the same measurement condition	76
Fig.5.3.12-3	Effective voltage distribution	77
Fig.5.3.12-4	Effective voltage difference	77
Fig.5.4.1	Final input flange	77
Fig.5.4.2	Final exit flange	77
Fig.5.4.3	Final geometry for end flanges	78
Fig.5.4.4	The resonance measurement, f=434.9MHz	78
Fig.5.4.5	Volume tuners in section 1 for new designed input and exit flanges. Left: 80mm(L)*15mm(T); Right: 90mm(L)*25mm(T)	78
Fig.5.4.6.1	Phase distribution, f0=434.9MHz (before (left) and after(right)ground line subtraction)	79
Fig.5.4.6.2	Field distribution	79
Fig.5.4.6.3	Effective voltage distribution	79

Fig.5.4.6.4	Effective voltage difference	79
Fig.5.5.1	Amplitude response with the frequency	80
Fig.5.5.2	H111 mode , f111=437.4MHz	80
Fig.5.5.3	H112 mode, f112=444.3MHz	80
Fig.5.5.4	H113 mode , f113=465.5MHz	80
Fig.5.5.5	H114 mode , f114=470.4MHz	80

Chapter Six

Fig.6.1	Cross section of IH power cavity	83
Fig.6.2	Top view on the central frame	84
Fig.6.3	End geometry of IH cavity	84
Fig.6.4	Variation of the contour of the upper and lower half shells along the cavity	84
Fig.6.5	Cross sectional view of the half shells	85
Fig.6.6	Final geometry of IH power cavity with magnetic triplet	85
Fig.6.7	The equivalent circuit of IH-DTL	86
Fig.6.8	Diagram of the power dissipation on the cavity components	87
Fig.6.9	In-coupling loop with IH-DTL cavity	88
Fig.6.10	The RF feeder structure	88

Chapter Seven

Fig.7.1	Part of y-z plane view of IH 1:2 model cavity	91
Fig.7.2	Part of x-z plane of IH 1:2 model cavity	91
Fig.7.3	Cut of z-plane of IH model cavity (left view of above figure)	91
Fig.7.4	x-z plane of IH power cavity (after symmetrization)	91
Fig.7.5	y-z plane of IH power cavity divided into 3 parts	92
Fig.7.6	z plane cut view of IH power cavity (after symmetrization)	92
Fig.7.7	mode 1 (305MHz)	92
Fig.7.8	mode 2 (H110 443.4MHz) for triplet 1	92
Fig.7.9	mode 1 (410.7MHz) for triplet 1	93
Fig.7.10	mode 2 (H110 444.6MHz) for triplet 1	93
Fig.7.11	H110 mode (462.00MHz) for triplet 3	93
Fig.7.12	H110 mode (462.06MHz) for triplet 3	93
Fig.7.13	Mesh distributions of IH power cavity	95
Fig.7.14	The electric field distribution along the IH-DTL (Model)	95
Fig.7.15	Electric (black and gray) and magnetic (colour) field distribution	96
Fig.7.16	Surface current of IH model cavity	96
Fig.7.17	Magnetic field distribution (IH model cavity)	96
Fig.7.18	The field distributions of IH model and power cavity	97
Fig.7.19	The simulated (MWS) and designed effective	98
Fig.7.20	The simulated magnetic intensity distribution	98
Fig.7. 21	Electric field distribution at high energy end (power cavity)	99
Fig.7. 22	Magnetic field distribution at high energy end (power cavity)	99
Fig.7.23	“H111”Mode for the IH model and power cavities	101
Fig.7.24	“H112”Mode for the IH model and power cavities	102
Fig.7.25	“H113”Mode for the IH model and power cavities	102
Fig.7.26	“H114”Mode for the IH model and power cavities	103

Chapter 8

Fig.8.1	Some original drift tubes after copper plating	104
Fig.8.2	Triplet stem for model (left), triplet stem shape for power cavity (right)	105
Fig.8.3	View on the drift tube structure of the IH-DTL power cavity, mounted on the central frame	105
Fig.8.4	The resonance of the IH-DTL power cavity with an additional height of 7mm on the half shells ($f=212.20\text{MHz}$, $Q=618.90$)	106
Fig.8.5	The phase measurement at resonance 212.2MHz	106
Fig.8.6	Absolute electric field distribution with 7mm additional heights of the IH cavity half shells	107
Fig.8.7	Resonance of IH cavity after cutting 5mm ($f=216.23\text{MHz}$, $Q=617.9$)	108
Fig.8.8	The corresponding bead pull measurement	109
Fig.8.9	The field distribution of IH cavity after cutting 5mm half shells	109
Fig.8.10a	The block plungers in the 3rd and 4th sections	110
Fig.8.10b	The block plunger with a quarter cross section of IH cavity	110
Fig.8.11	The additional capacitance blocks at entrance and exit of IH cavity	111
Fig.8.12	The field distributions with the plungers (plunger depth: $P_3=0, P_4=0$, while the effects of two additional capacitance tuning blocks at cavity entrance and exit are included (see Fig.8.11))	112
Fig.8.13	The phase distribution with the two plungers 55mm deeper	112
Fig.8.14	The field distribution with the plungers in the 3rd and 4th sections, plunger depth: $P_3=55\text{mm}, P_4=55\text{mm}$, $f=216.2\text{MHz}$	113
Fig.8.15	The simulated field distribution after cutting volume tuners 11mm (full scale) away in the 1st section and cutting cavity half shells another 1.2mm (full scale) away	113
Fig.8.16	The phase distribution with the cavity dimension: $341.6*260$; volume tuner in the 1st section: 19mm; with C_{l1}, C_{h1} and C_{h2} (see Fig.8.11); and the plunger positions: $P_3=66\text{mm}$, $P_4=66\text{mm}$. The measured frequency: 216.816MHz	114
Fig.8.17	The corresponding field distributions	115
Fig.8.18	The effective voltage distributions along the structure with respect to the above field distributions. The measured frequency: 216.816MHz)	115
Fig.8.19	The low energy undercut modification	116
Fig.8.20	New Additional Capacitance Tuning for the two ends	116
Fig.8.21	The phase effects of LE undercut modifications, old C_{l1} and C_{h1} were shown in Fig.8.11, new C_{l1} and C_{h1} were shown in Fig.8.20	118
Fig.8.22	The field distribution respects to the phase in Fig.8.21.d	119
Fig.8.23	The gap effective voltage distribution related to the field in Fig.8.23	119

Acknowledgements

I would like to thank my supervisor, Prof. Dr. U. Ratzinger, who offered me the chance to carry on this study in the LINAC group, in the Institute for Applied Physics of Frankfurt University. His kindness, encouragement, profound knowledge and careful guiding were very helpful for me to accomplish this study.

I would also thank Prof. Dr. H. Klein, Prof. Dr. A. Schempp and Dr. Deitinghoff for their help to live in Frankfurt and for useful collaborations and discussions on the accelerator physics and RFQ accelerators.

I should thank Dr. H. Podlech, who gave me his experience and useful suggestions for the Microwave Studio simulations of the IH cavity by using his faster computer. Thanks a lot to R.Tiede for his help during the model cavity measurements, and the valuable discussions in the KONUS beam dynamics and the software of LORASR. I should also thank the secretary, Ms. Harji, she gave me much help in the daily affairs needed by the university.

I would like to thank Dr. N. Angert, Dr. H. Eickhoff, and Dr. B. Schlitt, who gave me much help and great supports in the study of HICAT IH-DTL cavity. Especially, Dr.B.Schlitt helped me to arrange all the measurement events in the PINK Company and made his best to set the measurements in the schedule. I also thank GSI colleagues in the GSI RF group, especially, G.Hutter, W.Vinzenz, W.Gutowski . I feel really glad to have worked with them during my stay at GSI.

Many thanks go to all the collaborators of the institute: all the professors, the other colleagues in LINAC group, Dipl. Phys. G.Clemente, J.Dietrich, H.Liebermann, and Dr. A. Sauer, the colleagues in RFQ accelerator group, mechanical engineers in IAP workshop, and the people I cannot mention here individually.

The study was supported by the IAP, GSI and DKFZ (Deutsche Krebsforschungszentrum Heidelberg) and based on the good collaborations between them.

Curriculum Vitae of the author

First name: Yuanrong

Family name: Lu

Date of Birth: 17 June 1965

Date of Place: Jiangsu

Nationality: P. R. China

Marriage: Married

Social position: Member of Chinese Accelerator Technology Committee



Education:

What	When		Where
Primary School	March 1972	July 1977	前进桥(Qianjinqiao), yuejiang, jingjiang city, Jiangsu Province, P.R.China
Middle School	Sept. 1977	July 1979	前进桥(Qianjinqiao), yuejiang, jingjiang city, Jiangsu Province, P.R.China
Diploma or Bachelor of Science	Sept. 1979	July 1982	靖江高级中学 (Jingjiang Gaoji Zhongxue), Jingjiang city, Jiangsu Province, P.R.China
Master of Science	Sept. 1982	July 1986	Peking University, Nuclear Physics, Dept. of Technical Physics, Beijing 100871, P.R.China
	Sept. 1990	July 1993	Peking University, Nuclear Physics and Application, Major: Accelerator, Institute of Heavy ion Physics, Beijing 100871, P.R.China

Experience:

1. From Aug. 1986 to July 1991, Research assistant, IHIP (Institute of Heavy Ion Physics), Peking University
2. From Aug. 1991 to July 1997, RF Engineer, IHIP, Peking University
3. From Sept.1994 to Mar. 1996, guest scientist at RF group, GSI (Gesellschaft fuer SchwerIonenforschung MBH)
4. From Sept.1997 to now, Vice Professor and senior Engineer, IHIP, Peking University
5. From July 2001 to July, 2002, guest scientist at GSI RF group, GSI, Germany
6. From Aug. 2002 to now, IAP (Institute for Applied Physics), Johann-Wolfgang-Goethe Universitaet (Frankfurt University), Germany

Prize:

1. One of the winners of the excellent scientific achievements at Peking University in 1994.
2. Guanghua perfect teaching prize at Peking University in 1997

3. The second prize of „希望杯“ (Xiwang Bei) in China in 1998
4. The prize of excellent younger accelerator scientist at Peking University in 1999

Since I got my diploma and a position at the Institute of Heavy Ion Physics in Peking University in 1986, I have been working on RF linear accelerators and RF controlling for 18 years. I met and solved many problems by myself during these 18 years and became one of the important research members in our RFQ group. There are two RFQ accelerators in IHIP, one is designed for N^+ to be accelerated to 300KeV, another is 1MeV for O^+ , and I am responsible of RF systems and beam tests of these two RFQ accelerators. I have also the experience on the RFQ beam dynamics design by the PARMTEQM software. I designed the experiments and did my great contributions to complete the project “Experimental research on simultaneous acceleration of positive and negative ions with equal q/m in an ISR RFQ”, which was supported by NSFC during 1996 to 1998.

I made a collaboration with HITACHI works in 1997, as a project leader, I organized one group to finish the related theoretical design works and to explore the possibility to produce 7MeV Proton Injector for therapy in China. I have taught the course “ Accelerator Physics” for undergraduate students for about eight years exclude the years when I was/am in Germany. I guided several students and their diploma works as well as the younger staff members in our group. Before I left for Europe I was ever the vice group leader of high current accelerators at IHIP in Peking University and one of the members of Chinese Accelerator Technology Committee in China.

From Sept. 1994 to Mar. 1996, I was responsible for the upgrade of RF systems in GSI high current project, main works there were concluded in three GSI internal reports. I made almost all the 27MHz and 36MHz analog and digital phase shifters for the wideroe and IH-DTL accelerators, as well as the 108MHz phase shifters for the 108MHz RFQ and Alvarez cavities. I modified the broad-band 300W solid state amplifiers to be capable of running up to 40MHz.

During the last three years, I followed Prof. Dr. U.Ratzinger (IAP) to work for the Heidelberg Heavy Ion Cancer Therapy Project (HICAT). All works for HICAT IH-DTL injector are presented in this thesis.

Publications of the author (only since 1996):

- [1] Y.R.Lu, S.Minaev, U.Ratzinger, B.Schlitt, R.Tiede, The Compact 20MV IH-DTL for the Heidelberg Therapy Facility, Proc. of LINAC conference, Luebeck,2004,Germany
- [2] B. Schlitt, G. Hutter, F. Klos, C. Muehle, W. Vinzenz, A. Bechtold, Y.R. Lu, U. Ratzinger, A. Schempp, STATUS OF THE 7 MEV/U, 217 MHZ INJECTOR LINAC FOR THEHEIDELBERG CANCER THERAPY FACILITY, Proc. of LINAC conference, Luebeck, 2004, Germany
- [3] Z.Y. Guo, J. Chen, J. Fang, Y.R. Lu, C. Zhang, K. Zhu, A.Schempp, Design of a Deuteron RFQ for Neutron Generation, Proc. of LINAC conference, Luebeck, 2004, Germany
- [4] Y.R.Lu,C.E.Chen,J.X.Fang,S.L.Gao,J.F.Guo,Z.Y.Guo,D.S.Li,W.G.Li,O.J.Pan,X.T.Ren,Y.Wu,X.Q.Yan,J.X.Yu,M.L.Yu,U.Ratzinger,H.Deitinghoff, H.Klein,A.Schempp,Investigation of high duty factor ISR RFQ-1000, Nuclear Instruments and Methods in Physics Research A 515 (2003)394–401
- [5] Lu Yuanrong, U.Ratzinger, N. Angert, An Adapter for Beam Loading Compensation of IH Linear Accelerators, Acta Scientiarum Naturalium Universitatis Pekinensis, Vol.39,No.3, P.322-330, (May, 2003)
- [6] X.Q.Yan, C.E.Chen, J.X.Fang, Z.Y.Guo, W.G.Li, Y.R.Lu, Y.Wu, Exploring the feasibility of a separated function RFQ with mini-vane structure, Nuclear Instruments and Methods in Physics Research A 506 (2003)1–6
- [7] Lu Yuanrong, W.Gutowski, Analog Phase Shifter, Acta Scientiarum Naturalium Universitatis Pekinensis,Vol.38,No.1,P.49-56,(Jan,2002)
- [8] Yan Xueqing, Lu Yuanrong, Wu Yu, Zhang Honglin, Gao Shuli, Fang Jiaxun, RFQ Electrode Parameter Calculation and Machining Program---RFQPOLE, Acta Scientiarum Naturalium Universitatis Pekinensis,Vol.38,No.1,P.39-43,(Jan,2002)
- [9] B. Schlitt, G. Hutter, B. Langenbeck, C. Mühle, W. Vinzenz, A. Bechtold, Y. Lu, S. Minaev, U. Ratzinger, A. Schempp, R. Tiede, DEVELOPMENT OF A 7 MEV/U, 217 MHZ CARBON INJECTOR LINAC FOR THERAPY FACILITIES, LINAC02,Korea
- [10] Yu Jinxiang, Chen Jiaer, Ren Xiaotang, Song Zhizhong, Wang Zhongyi,Zhang Zhengfang, Lu Yuanrong, Li Weiguo and Fang Jiaxun, INVESTIGATION OF ION SOURCES AND INJECTOR USED IN RFQ ACCELERATOR, APAC01,Beijing, P.R.China
- [11] Y.R.Lu, C.E.Chen, J.X.Fang, et al, RF and BEAM TESTS of A 1MEV

- 26MHZ RFQ AT PEKING UNIVERSITY, EPAC2000, Austria
- [12] Y.R.Lu, J.F.Guo, et al. Investigations of 26MHz ISR RFQ Accelerators, Nuclear Instruments and Methods in Physics Research A 420, 1999,1-5
- [13] Jufang Guo, Yuanrong Lu, Weiguo Li, Jinxiang Yu, Xiaotang Ren, Yu Wu, Zhongyi Wang, Jiaxun Fang, Chia-erh Chen, Investigation of 26MHz RFQ Accelerators, Proc. Of 1-st Asian Particle Accelerator Conference, 1998, KEK, Japan. (大字报)
- [14] X.T.Ren, Y.R. Lu, J.X.Yu, et al. Experimental Research on Simultaneous Acceleration of Positive and Negative ions with the same q/m in an ISR RFQ. High Energy Physics and Nuclear Physics, Vol.24, No.4, P.347-351, 2000.
- [15] 于金祥, 陈佳洱, 方家驯, 陆元荣, 等, RFQ 加速器同时加速同荷质比正负离子的实验研究, 原子能科学技术 (Nuclear Science and Technology), 2001 年 3 月
- [16] C.E.Chen, J.X. Fang, J.X.Yu, Y.R.Lu, et al, Progress of RFQ for Ion Implantation at Peking University, EPAC2000, Austria
- [17] 陆元荣(Lu Yuanrong), 李纬国, 郭菊芳, 任晓堂, 于金祥, 方家驯, 陈佳洱, 整体分离环 RFQ 加速器的研究(Investigations of ISR RFQ Accelerators), 原子核物理评论(Nuclear Physics Review), 第十五卷第三期, 1998, 144
- [18] 陆元荣 (Lu Yuanrong), 赵渭江, 美国离子束物理新进展(New Development of American Ion Beam Physics), 物理(Physics), 第 27 卷第四期, 250-251, 1998
- [19] 方家驯, 陆元荣, 李纬国, 郭菊芳, 于金祥, 吴瑜, 于茂林, 陈佳洱, 26MHz 整体分离环 RFQ 加速器的研究, 第二届全国加速器技术学术交流会论文集, 宁波, 98-101, 1998
- [20] 陆元荣, W.Gutovski, 李坤, 方家驯, 李纬国, 张保澄, 陈佳洱, 加速器控制用模拟压控移相器的研制(Analog Phase Shifter for RF Accelerators), 第二届全国加速器技术学术交流会论文集, 宁波, 352-355, 1998
- [21] 陆元荣, Ratzinger, 1/4 波长可变特性阻抗高频高功率传输线——交叉指型加速器束载效应的阻抗匹配研究(Ferrite Dominated Transmission Line---An Adapter for Beam Loading Compensation of IH linear Accelerators), 第二届全国加速器技术学术交流会论文集, 宁波, 347-351, 1998
- [22] Yu Jinxiang, Chen Jiaer, Jiaxun Fang, Yuanrong Lu, et al. ,Trends in Nuclear Physics,1996,13(2),P.34
- [23] EPAC96